

THREE-DIMENSIONAL STRUCTURE OF THE CRUST AND
MANTLE BENEATH THE ISLAND OF HAWAII

by

William Leslie Ellsworth

B.S., Stanford University (1971)

M.S., Stanford University (1971)

SUBMITTED IN PARTIAL FULFILLMENT
OF THE REQUIREMENTS FOR THE
DEGREE OF DOCTOR OF PHILOSOPHY

at the

MASSACHUSETTS INSTITUTE OF TECHNOLOGY

November, 1977

Signature of Author.....
Department of Earth and Planetary Sciences
November, 1977

Certified by.....
Thesis Supervisor

Accepted by.....
Chairman, Departmental Committee on Graduate Students

Lindgren
~~WITHDRAWN~~
DEC 1977
MIT LIBRARIES

THREE-DIMENSIONAL STRUCTURE OF THE CRUST
AND MANTLE BENEATH THE ISLAND OF HAWAII

by

William Leslie Ellsworth

Submitted to the
Department of Earth and Planetary Sciences
on November 4, 1977, in partial fulfillment of the
requirements for the degree of
Doctor of Philosophy

ABSTRACT

The Island of Hawaii is the youngest and southeasternmost member of a quasi-linear, age-ordered, chain of volcanic islands and seamounts which extends for 3500 km across the northwestern Pacific sea floor. Similarities between the Hawaiian chain and at least six other linear island chains of the Pacific basin, including their nearly unidirectional and uniform rate of extension, WNW orientation, and formation atop comparatively ancient Pacific lithosphere far from plate boundaries, strongly imply a common mode of formation for these mid-plate island chains. This study addresses the question of the origin of Hawaiian-type shield volcanoes through analysis of the deep internal velocity structure of the Island of Hawaii.

The velocity structure of the crust and mantle underlying the Island of Hawaii is investigated using the arrival times of P-waves recorded by a seismograph network located on that island. Relative travel times of these waves contain abundant evidence for the existence of lateral heterogeneities within both crust and mantle beneath the island. Although lower mantle structural variations can explain limited aspects of these data, requisite structures are found to be improbable. Absolute travel time residuals for both P and PKP average 0.4 sec late, which indicates that the cumulative effect on all departures in velocity from the mean earth encountered by these teleseismic rays is small. Inconclusive evidence does suggest that the steepest rays are delayed by up to 1.5 sec.

A flexible modeling technique for these data is developed to give a quantitative image of laterally heterogeneous structure beneath Hawaii. This method extends the three-dimensional inversion modeling of Aki et al. (1977) by incorporation of ray tracing in three-dimensionally heterogeneous media, and through allowance for a wide variety of medium characterizations.

Iterative convergence of the solution is found to be rapid when using either initially homogeneous or heterogeneous models. Solutions generated using this technique also agree well with single-step solutions.

Application of this method to P-wave travel time data collected from seismographs on the Island of Hawaii determines a high resolution, three-dimensional image of crust and mantle structure to depths in excess of 160 km. Crustal structure of this young volcanic island is dominated by the presence of high velocity intrusive dikes and sills in the summit complexes and radial rift zones of the five shield volcanoes. Mantle structure within the underlying lithosphere, or to about 75 km depth, contains a centralized low velocity zone with typical horizontal dimensions of about 50 km which is flanked by higher velocities in the surrounding offshore zone. The velocity contrast between the low velocity zone and the encircling highs averages 3 to 4%. This contrast increases markedly in the asthenosphere to upwards of 10% $\Delta V/V$. However, the most intense low velocity region lies to the east of the island, and coincides with the axis of the Hawaiian Island chain as extrapolated from the older islands.

The validity of the three-dimensional structure determined by teleseismic data is tested through modeling of crust and uppermost mantle structure using travel times of local earthquakes. A broad and statistically significant correlation exists between these independently determined velocity models, although some significant discrepancies also exist.

The structural relationships indicated by the lateral velocity heterogeneities supports other geophysical and geochemical evidence that the tholeiitic basalts erupted on Hawaii are derived from a source region below the lithosphere. The vertical continuity of the centralized low velocity zone in the lithosphere, which underlies the principal volcanic summits, with more intense low velocity zones in the asthenosphere indicates that the basalts originate no shallower than about 100 km and may be in transit through both asthenosphere and lithosphere from a deeper mantle source.

The deepest-seated lateral heterogeneities resolvable by the data align in a broad low velocity zone which is elongated parallel to the Hawaiian chain axis. Because the most intense regions of this low velocity feature are not directly associated with any overlying volcanism, lie ahead of the island chain along the direction of chain growth, and extend well over 80 km into the asthenosphere,

these results support the hot spot, or plume, hypothesis for the origin of the Hawaiian Islands.

Thesis Supervisor: Keiiti Aki, Professor of Geophysics

ACKNOWLEDGEMENTS

I wish to express my sincere appreciation and gratitude to my advisor, Keiiti Aki, for the excellent and insightful guidance he provided throughout the course of my study, and for his encouragement when difficulties seemed insurmountable. It has truly been a pleasure and an honor to work under him.

My interest in pursuing this topic grew out of discussions I had with Peter Ward of the U.S. Geological Survey who initially made available to me data that John Unger collected from the U.S.G.S. seismograph network on Hawaii. After preliminary analysis of the data proved the project to be feasible, Peter arranged for me to spend the summer of 1975 at the Hawaiian Volcano Observatory. During my stay there Robert Koyanagi generously assisted me in all phases of my work, and kept me supplied with new and additional data after my return to M.I.T.

Among the many others who assisted me in this project I would like to single out George Zandt and Steve Roecker for their deeply appreciated cooperation in developing several of the computer programs used in the thesis, and for their critical commentary on all phases of the research. I also gratefully acknowledge Jerry Eaton, Dave Hill, Fred Klein, Al Lindh and Alan Steppe, all at the National Center for Earthquake

Research, for their most welcome counsel and support. Ken Anderson, Raymond Brown, Raul Madariaga, Randy Richardson, Jim Scheimer, and Sean Solomon also provided encouragement and many helpful suggestions.

The burden of preparing the theses was greatly eased by my wife Nancy, who not only drafted virtually all of the figures, but also did much to keep my humors in balance. I also deeply appreciate the sacrifices she cheerfully and readily made which allowed this work to progress.

Ellen Loiselle's fast and accurate transformation of often illegible draft copy into typescript is also gratefully acknowledged. I also thank Sara Brydges for the many ways she assisted me over the past three years and for her friendship which has meant much to both Nancy and me.

During most of my tenure as a graduate student I was supported under the Federal Manpower Training Act, Training Orders 4-9930-0458, 6-9930-0413, and 6-9930-0489. I also wish to thank my colleagues at M.I.T. supported by U.S.G.S grant 14-08-0001-G-339 for assistance and aid which they generously made available to me. I also gratefully acknowledge my use of computation facilities at the Applied Seismology Group, Lincoln Laboratory, provided through the generosity of Mike Chinnery and Dick Lacoss.

TABLE OF CONTENTS

	<u>Page</u>
Abstract	2
Acknowledgements	5
Chapter 1: Introduction	12
1.1 Summary of Geologic Structure	14
1.2 Origin of the Hawaiian Islands: A Review	18
1.3 Outline of Work Performed	21
Figures	24
Chapter 2: Observation of Teleseismic P-Waves	27
2.1 Seismograph Station Network	27
2.2 Character of Body Wave Arrivals	29
2.3 Teleseismic Sources Studied	31
2.3.1 Teleseismic Travel Time Residuals	31
2.3.2 Hawaiian Station Residuals	36
2.4 Azimuthal Variation of Travel Time	38
2.4.1 Apparent Slowness and Azimuth of Teleseismic Body Waves Across the HVO Array	38
2.4.2 Teleseismic Travel Times to Stations on Other Islands	43
2.4.3 Azimuthal Variation of Relative Residuals	47
2.5 Origin of Travel Time residuals	48
2.5.1 Structure Inferred from Absolute Travel Time Residual	49
2.5.2 Broad Scale Heterogeneous Structure	56

2.5.3	Near Receiver Structure	64
2.5.4	Three-Dimensional Structure Within the Lithosphere	67
Tables		71
Figures		80
Chapter 3:	Determination of Three-Dimensional Velocity Structure Using Distant Sources	107
3.1	Inverse Solution for Structure from Travel Time Data	108
3.1.1	Overview	109
3.1.2	Formulation of the Model	111
3.1.3	Computation of the Inverse Solution	115
3.2	Characterization of the Medium	120
3.2.1	Quantized Model of Aki, Christof- fersson, and Husebye	121
3.2.2	Block Model	124
3.2.3	Continuous Velocity Models	125
3.2.3.1	Hanning Basis Functions	125
3.2.3.2	Model Representation Using Fourier Series	127
3.3	Strategies for Modeling the Earth	128
3.3.1	Network Geometry and Source Distribution	128
3.3.2	Effect of Earth Structure Outside the Model	130
3.3.3	Non-Modelable Local Structure	132
3.3.4	Model Resolution - The Big Picture	135
3.4	Iterative Refinement of the Three- Dimensional Solution	137
3.4.1	Ray Tracing in Heterogeneous Media	138
3.4.2	Application to the Hanning Model	143

Table	144
Figures	145
Chapter 4: Three-Dimensional Crust and Mantle Structure Beneath Hawaii from Teleseismic Waves	148
4.1 Model Framework for Three-Dimensional Inversion Studies	148
4.1.1 Initial Vertical Velocity Structure	150
4.1.2 Depth of Modeling	151
4.1.3 Selection and Specification of Model Framework	152
4.1.4 Model Performance	155
4.2 Three-Dimensional Models on a Coarse Grid	157
4.2.1 Four Layer Models	158
4.2.2 Smoothed Model	162
4.2.3 Five Layer Model	162
4.3 Detailed Deep Structure Models	163
4.3.1 Four Layer Model	164
4.3.2 Five Layer Model	164
4.4 Detailed Lithosphere Model	165
4.5 Crust and Upper Mantle of Kilauea	167
4.6 Synthesis of Mantle Structure Beneath Hawaii	170
4.6.1 Structure of the Upper Lithosphere	172
4.6.2 Structure of the Lower Lithosphere	173
4.6.3 Structure of the Uppermost Asthenosphere	174
4.6.4 Deepest Structure Resolvable by the Data	175
4.6.5 Structural Summary	176
4.7 Further Examination of Three-Dimensional Model Performance	177
Tables	179
Figures	186

Chapter 5: Simultaneous Determination of Velocity Structure and Local Earthquake Focal Parameters	206
5.1 Simultaneous Inversion Method for Hypocenters and Velocity Structure	207
5.1.1 Formulation of the Model	208
5.1.2 Application to the Earth	211
5.2 Local Sources for Travel Time Inversion Studies	213
5.3 One-Dimensional Velocity Structure for Hawaii	217
5.4 Three-Dimensional Velocity Structure Determined from Local Travel Time Data	220
5.5 Comparison Between Structures Determined Using Teleseismic and Local Sources	222
5.5.1 Comparison Between Solutions for Crustal Parameters	224
5.5.2 Comparison Between Solutions in the Upper Mantle	227
5.5.3 Teleseismic Models Which Use the Structure Determined from Local Sources as a Starting Model	230
5.5.4 Summary of Model Comparisons	233
Tables	234
Figures	238
Chapter 6: Summary and Conclusions	250
Figures	238
References	263
Appendices	
A. Estimation of the Average Form of a Function from Multiple Observations in the Presence of Noise	278
B. Test Problems for Three-Dimensional Modeling Using Teleseismic Sources	282

B.1	Damped Least Squares Solution for Linear Algebraic Systems	282
B.2	Recovery of a Simple Inhomogeneity Using an Idealized Array	294
B.2.1	Single Iteration Solutions	295
B.2.2	Convergent Iterative Solution	297
B.2.3	Solution Using a Mis-Aligned Grid	298
B.3	Volcanic Pipe Model for Mauna Loa	300
B.3.1	Single Iteration Solutions	301
B.3.2	Convergent Iterative Solutions	302
B.3.3	Solutions Using a Mis-Aligned Grid	303
B.4	Guidelines for Evaluating Inverse Solutions	303
	Tables	307
	Figures	308
	Biographical Note	326

CHAPTER 1: Introduction

Youthful mid-oceanic islands which are well removed from plate boundaries provide an ideal natural laboratory for the study of volcanism and tectonism. When situated atop stable and relatively ancient lithosphere, the volcanoes which compose these islands, together with their mantle roots, form the active elements of a comparatively simple and closed tectonic system. Because these mid-plate "hot spots" are not kinematically tied to plate tectonic processes in a unique way, a fundamental understanding of their origin potentially provides constraints upon the underlying mechanisms of plate tectonics.

Much of the essential observational data about mid-ocean islands was recognized by the earliest scientific observers, including Dana (1849) and Darwin (1851). These islands characteristically occur as relatively long and linear rows or double rows of regularly spaced basaltic shield volcanoes. Within each island chain, volcanoes often appear to have a unidirectional age distribution suggesting that these chains propagate across the sea floor (Dana 1849, 1871). Among these island chains, the Hawaiian Islands have been the most thoroughly and systematically studied. Consequently, it is not surprising that these islands play an important role in theories of the formation of mid-ocean islands and plate tectonics.

The Island of Hawaii, which is the youngest island in the Hawaiian chain, is, perhaps, the archtypical example of a hot spot and has been studied almost continuously since the earliest scientific expeditions into the North Pacific Ocean. However, after nearly 150 years of careful scrutiny fundamental questions of its origin and internal structure remain unanswered. It is the object of this study to apply new and classical seismological methods to these problems with the hope of extending our understanding of this volcanic center.

The primary data to be examined are teleseismic P waves recorded on Hawaii by a network of short period seismographs. Although there are many features of these waves which might provide valuable insight into the structure of Hawaii, attention is restricted here to their travel times across the island. Using the modeling technique introduced by Aki, Christofferrsson and Husebye (1977a) these data determine a high resolution three-dimensional velocity structure for the crust and mantle beneath Hawaii.

Before launching into the details of this analysis, a brief overview of the geology of Hawaii and the Hawaiian chain is in order. This is followed by a summary of current hypotheses which describe the formation and evolution of linear island chains.

1.1 Summary of Geologic Structure

The Hawaiian Island chain is a quasi-linear topographic ridge composed of tholeiitic shield volcanoes which extends over 3500 km across the North Pacific WNW from the island of Hawaii to where it joins the southern end of the WNW-trending Emperor seamount chain (Figure 1.1). The volcanoes are organized in an approximately age-ordered sequence (Dana, 1849; McDougall, 1964) formed during the past 40 m.y. (Clague and others, 1975). They lie atop comparatively old Pacific lithosphere of Cretaceous age which increases in thickness from about 80 km near the youngest volcanoes on the Island of Hawaii to perhaps 90 km near the Hawaiian-Emperor bend (Yoshii and others, 1976; Forsyth, 1977).

The load of the volcanoes on the lithosphere produces a flexural deep (Dana, 1889; Dietz and Menard, 1953; Walcott, 1970) off the northeastern coast of the younger islands at the southeast end of the chain. The ridge and deep are superposed upon a broad (1000 km), low amplitude (1 km) rise of the sea floor which is known as the Hawaiian Swell (Betz and Hess, 1942; Dietz and Menard, 1953).

The volcanoes themselves are relatively simple geologic structures which exhibit little, if any, systematic variation along the length of the chain (Powers 1935, 1955). The mass of each volcano is composed almost in its entirety of a broad, low relief shield

built of a stratigraphic sequence of thin, tholeiitic basalt flows. The tholeiitic basalts are of remarkably uniform composition along the entire length of the chain (Cross, 1915; Powers 1935, 1955). The shields are typically transected by two or more tabular rift zones which radiate from a central summit complex. During the rapid shield building phase of the volcanic life cycle these rift zones transport magma from the summit complex many tens of kilometers down rift through a connected subterranean plumbing system for eventual eruption or intrusion (Eaton and Murata, 1960). Consequently, volcano topography is typically elongated along the rift zones.

Although once believed to represent primary fractures in the lithosphere, the rifts are now recognized to be crustal features (Swanson and others, 1976). They most probably form within the breakaway zone of massive seaward slumps of the unbuttressed flanks of the shield (Wilson, 1963). Once formed, the forceful injection of magma into the rift wedges the unstable flank seaward, which in the case of the south flank of Kilauea volcano occasionally results in a catastrophic subsidence event (Swanson and others, 1976).

By the end of the shield building phase, which lasts about 0.5 m.y. (McDougall, 1964), the larger volcanoes stand well over 10 km above the now depressed sea floor and extend for over 100 km from summit to rift

zone terminus. Following or accompanying the waning stages of tholeiitic volcanism, a more alkalic series of basalts are emplaced on the upper parts of the shield (MacDonald and Katsura, 1964). Mauna Kea, on the Island of Hawaii, is an example of a volcano which has reached this stage in its evolution. After a hiatus of 1 to 2.5 m.y. nephelinitic tuffs and lavas may possibly erupt from widely scattered vents of the erosionally-dissected shield (Jackson and Wright, 1970). The Honolulu volcanic series on Oahu are an example of these chemically diverse magmas.

The Island of Hawaii, with which we will be primarily concerned in the following chapters, is formed by the confluence of five shield volcanoes: Kohala, the oldest (<0.8 m.y.) which is now dormant; Mauna Kea, which has been active during this interglacial stage; Hualalai, which last erupted in 1801; Mauna Loa, last active in 1975; and Kilauea, which erupted along its east rift zone in September, 1977. Figure 1.2 shows the general geology and topography of the island. Present-day eruptive activity adds about $0.1 \text{ km}^3/\text{year}$ to the mass of the island (Swanson, 1972; Shaw, 1973). In response to this rapid loading, the island subsides at a rate of about 0.5 cm/yr (Moore, 1970). Equilibrium is apparently achieved within a few m.y., as Oahu (<3 m.y.) appears to be stable.

The intensive study of the young volcanoes on Hawaii, notably Kilauea, has led to a coherent and fairly detailed

description of crustal structure and uppermost mantle processes associated with tholeiitic volcanism. Magma rises slowly from depths of at least 60 km and accumulates in shallow (1-3 km) reservoirs in the summit prior to eruption (Eaton and Murata, 1960). There is also some evidence for intermediate storage and differentiation of the magma during its ascent (Wright, 1971), possibly at depths of 20 to 30 km (Mogi, 1958; Koyanagi and others, 1975). Chemical variability of historic lavas of Kilauea and of Mauna Loa can be explained by variations in their olivine content (Powers, 1955), possibly through fractionation during slow ascent (Wright, 1971). Systematic differences between lavas from the two volcanoes, although minor, imply chemically distinct mantle sources.

In addition to being one of the most active volcanic centers on earth, Hawaii is among the most seismically active localities as well. The number of earthquakes large enough to be detected by sensitive seismographs number in the tens of thousands annually (Koyanagi, 1968). These earthquakes are undeniably by-products of volcanism, occurring most frequently beneath or near the Island of Hawaii (Eaton, 1962). Many earthquakes appear to be causally related to eruptive activity and may outline magmatic pathways through the crust and upper mantle (Eaton and Murata, 1960; Koyanagi and others, 1976). Another form of seismic disturbances intimately associated with Hawaiian volcanism is volcanic tremor (Wood, 1913;

Jaggar, 1920; Eaton, 1962; Shimozuru and others, 1966). Although this phenomenon is inadequately understood at present, it is temporally connected with eruptive processes and very probably results from subterranean magma transport (Aki and others, 1977b).

The description of Hawaiian volcanoes summarized above unfortunately contains few details of their internal structure, especially within the mantle. Knowledge of their internal constitution is ultimately as fundamental to the understanding of oceanic islands as is revelation of the underlying forces responsible for their creation.

1.2 Origin of the Hawaiian Islands: A Review

Modern hypotheses advanced to explain the origin of linear island chains share many common points but generally divide into three genetically related groups: (1) propagating fracture; (2) hot spot or plume; and (3) thermal instability. The essential features of each of these models have been discussed by many authors, including the recent summary of Dalrymple and others (1973), and no attempt will be made here to describe them in detail. Several recent contributions do, however, constrain or refine these hypotheses, and it is instructive to review the current status of these models in light of these developments.

The oldest hypothesis for the formation of linear island chains is the propagating fracture model. This

theory was suggested at an early data (Dana, 1871, 1888; Woodworth, 1896; Powers, 1917) and has been expanded and refined by many others (Betz and Hess, 1942; Jackson and Wright, 1970; Green, 1971; McDougall, 1971; Marsh and Marsh, 1976; Turcotte and Oxburgh, 1976; and Walcott, 1976). Perhaps the primary feature of this model, in its present form, which distinguishes it from the other categories is the assumption that volcanoes are derived from magma which rises from relatively shallow depths in the asthenosphere.

The alternative hypothesis is that the volcanoes are genetically related to deep mantle processes. The hot spot, or plume, model (Wilson, 1963, 1965; Morgan, 1971, 1972a, 1972b) proposes that linear island chains are manifestations of deep mantle convection and mark the upwelling of hot and comparatively primitive material from deep in the mantle. This model succeeds in explaining at least three observational features which are not predicted by the propagating fracture model.

Significant differences between the trace element chemistries of ocean floor basalts and oceanic island basalts (Hedge and Peterman, 1970; Hoffman and Hart, 1975) require distinct mantle sources for mid-ocean ridges and volcanic islands. Because island basalts are regarded as being more primitive (less depleted in large ion lithophiles), a sub-asthenospheric source is strongly implied by their geochemistry. Secondly, convective upwelling suggests a probable mechanism for

the Hawaiian swell and the long term subsidence of islands through thermally-induced reduction of density within the basal lithosphere and asthenosphere (Detrick and Crough, in press). Finally, the plume hypothesis predicts that island chains of the Pacific plate extend at an equal and constant rate. Although there are some uncertainties in the dating of specific volcanic edifices, the recent compilations of Duncan and McDougall (1976) and Jarrad and Clague (1977) appear to bear out Morgan's (1971) hypothesis that hot spots remain fixed with respect to one another.

The third class of hypotheses, termed thermal instability (Shaw, 1973; Shaw and Jackson, 1973), proposes that shear melting caused by plate motion produces the magmatism at the head of linear island chains. At least two fundamental objections can be raised to this model. The first is that shear heating is negligible for reasonable mantle viscosities and strain rates (Mercier and Carter, 1975). Secondly, if melting does occur in the shear zone between lithosphere and asthenosphere, the derived melt fraction would most probably not satisfy the geochemical trace element constraints.

Viewed critically, the available evidence favors at least certain aspects of the plume hypothesis. However, the details of its application to Hawaii are vague, at best.

1.3 Outline of Work Performed

The primary objective of this thesis is the development of a quantitative velocity structure for the crust and mantle underlying the Island of Hawaii. In Chapter 2 the primary data analyzed in this study, the relative arrival times of P-waves from sources at teleseismic distances, are analyzed using simple, classical seismological methods. These data are found to contain substantial evidence for heterogeneous structures in the crust and mantle. Detailed examination of the nature of these travel time anomalies reveal that much of these data require explanation by structures near Hawaii and that lower mantle structures which could satisfy limited aspects of the data are improbable. Qualitative interpretation of the observations indicates that crustal velocity structure directly reflects the distribution of major intrusive complexes within the volcanic pile. Velocities within the underlying mantle appear to be low directly beneath the island when compared with the surrounding offshore regions. However, their distribution and fractional contrast cannot be measured with precision.

A collection of methods determining a high resolution, three-dimensional velocity structure for these data is developed in Chapter 3. Included in these methods is a new technique which extends the basic modeling of Aki and others (1977a) by allowing iterative refinement of models and heterogeneous initial models.

In Chapter 4 these techniques are applied to the Hawaiian data. Three-dimensional variations at depths in excess of 100 km are found to be required by the observations. Lateral variations in the mantle are broadly similar throughout the lithosphere and indicate that the mantle beneath the young volcanoes averages 3-4% lower than the surrounding mantle. Contrasts as great as 10% are indicated in the asthenosphere where low velocities occupy an elongate zone which lies northeast of the island.

In Chapter 5 the three-dimensional structure of the upper half of the lithosphere is studied using independent data. Travel times from crust and mantle earthquakes occurring beneath the island are modeled to verify the structure determined by the teleseismic travel times. A broad and statistically significant correlation is found to exist between these independent velocity structures, although some significant discrepancies also exist. The model derived from the local travel times does not satisfy the teleseismic data as adequately as equivalent portions of the models from Chapter 4. However, it is found that its use as the initial model in the inversion for teleseismically-determined structures does not significantly modify the three-dimensional solution at greater depths.

Chapter 6 discusses the implications of the three-dimensional velocity structure determined for the Island of Hawaii. The overall distribution of low

velocities suggests that they outline magmatic pathways from a source region within the asthenosphere to the active volcanoes. The deepest resolvable low velocity features (~ 135 km) lie east of Hawaii and locate more nearly along the trend extrapolated from older islands than does the Island of Hawaii. This suggests that the origin of these deep features is related to a deeper mantle source.

Chapter 1 - Figure Captions

Figure 1.1 Map showing generalized bathymetry of the northwest Pacific Ocean, after Chase and others (1971). Subaerial land masses are shaded. Submarine contours at 3 km and 5 km are shown.

Figure 1.2 Sketch map of the Island of Hawaii showing the five volcanoes which make up the island. Thick lines indicate major rift zones of volcanoes and volcanic centers. Dashed lines are contacts between lavas from adjoining volcanoes.

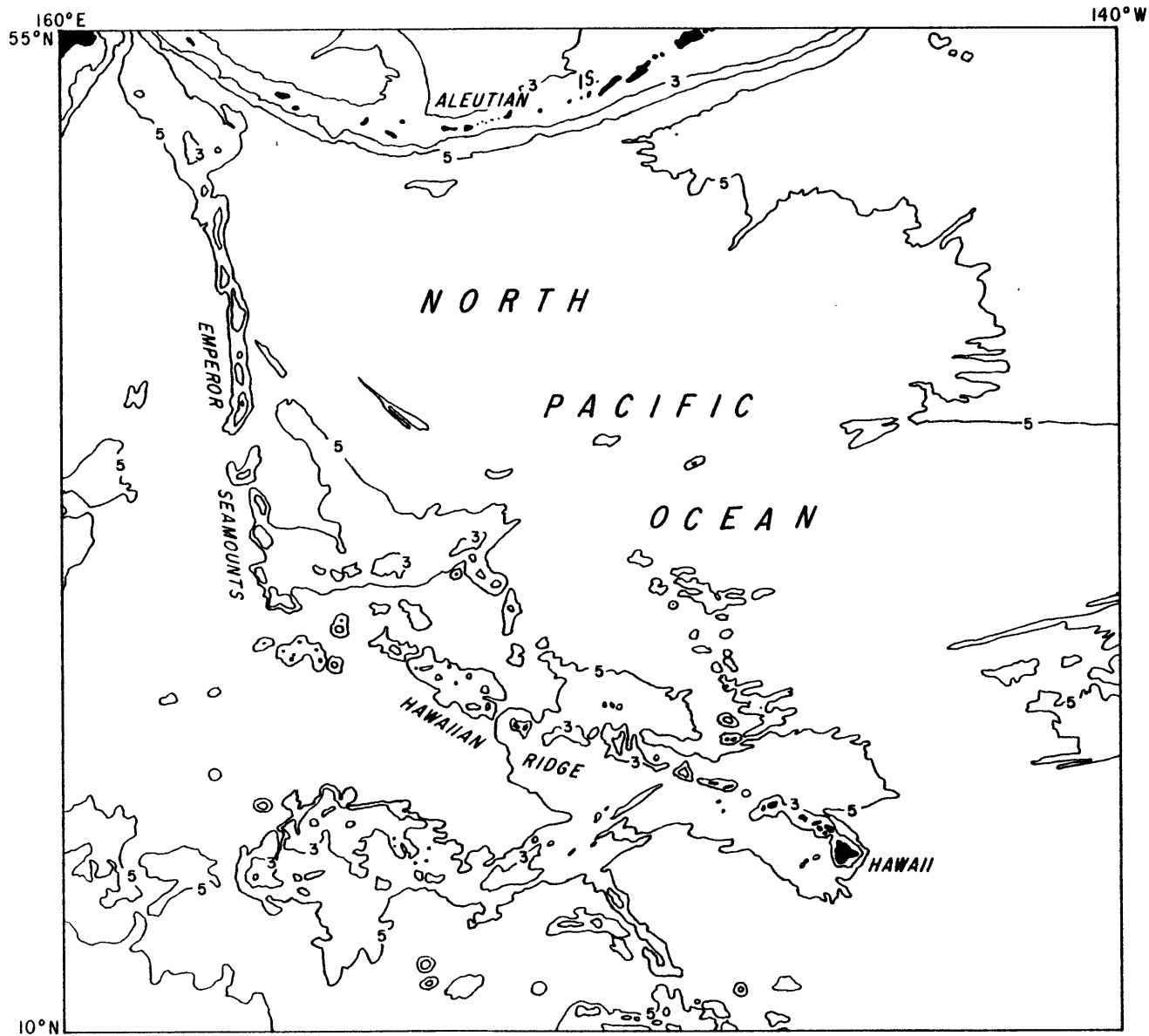
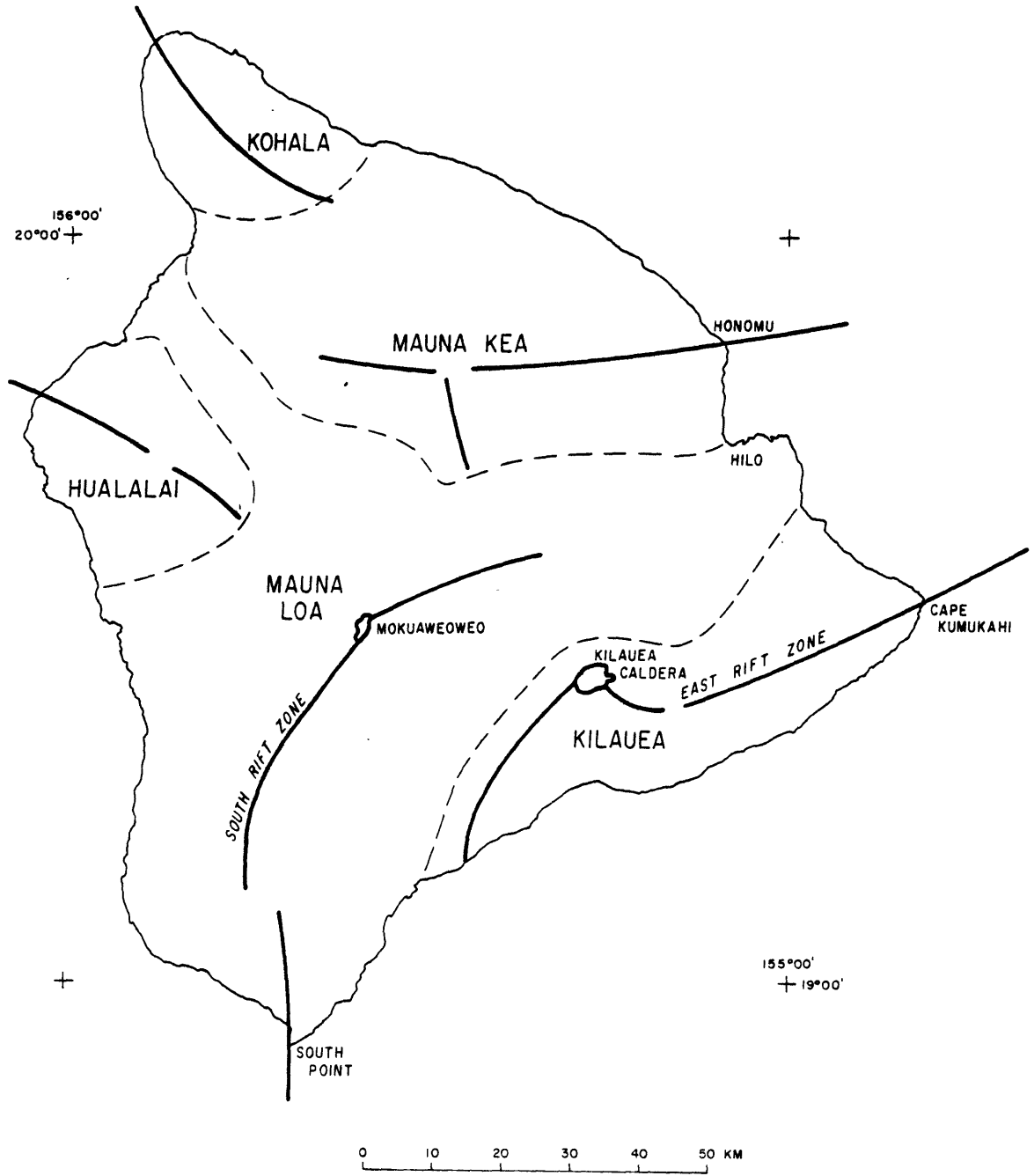


Figure 1.1

Figure 1.2



CHAPTER 2: Observation of Teleseismic P-waves

Knowledge of the composition and physical properties of the earth below a few km depth are limited to the surface measurement of physical quantities such as gravity, magnetic field and displacement of the earth's surface, and to analysis of rocks inferred to have risen from depth. Among these measurable quantities, elastic body waves are perhaps the most useful for high resolution studies of properties deep within the earth. This is because the medium both near and far from the point of observation effects the travel time to a similar degree. In contrast, potential field data rapidly loses sensitivity to small scale features with increasing separation between source and receiver.

In this chapter the nature of teleseismic P-waves recorded on Hawaii is described to provide a framework for three-dimensional modeling presented in Chapter 4. Array recordings of these short period body waves are especially well suited for the study of upper mantle structure beneath the instruments principally because ray theory adequately describes these waves along most of their travel path.

2.1 Seismograph Station Network

We are fortunate that the island of Hawaii is covered by a dense network of telemetered short period seismograph

stations operated by the Hawaiian Volcano Observatory (HVO) of the U.S. Geological Survey (Figure 2.1). The array spans an approximately equidimensional region, about 1° in diameter, and includes over 40 1-Hz vertical component seismometers with standardized response characteristics (Figure 2.2) which are telemetered to the Volcano Observatory and recorded on a common time base. Although these instruments are primarily designed to study local seismicity in the band between 1 and 20 Hz they also write excellent records of teleseismic P-waves. Complete system magnification is about 10^4 at 1 Hz (Koyanagi and others, 1974).

Two formats of the recorded seismograms were analyzed in this study. The first format, direct optical recording in strip chart mode on 16 mm film, of eighteen seismic signals together with two chronometer traces were used for 126 of the 144 events analyzed. The remaining 18 events were analyzed from high-speed ink-jet playbacks of FM tape recordings of the multiplexed seismic signals. Seismograms analyzed using the film records were projected onto a ground glass viewing screen equipped with movable hairline and viewed at a time scale of 1 cm/sec. Image magnification was corrected for each event so that the scale error was less than 0.1%. Optical distortion of the image was also found to be less than 0.1%. Ink-jet playbacks were prepared in a format similar to that used to record the film records with time code written at the top and bottom of the strip-chart paper records. Playback scale for these records was also about 1 cm/sec. These seismograms were read using a

variable length scale. The precision with which times could be measured from either type of record exceeds 0.05 sec or 0.05 cm.

2.2 Character of Body Wave Arrivals

Teleseismic P-waves recorded by the HVO network display a remarkably uniform waveform character throughout the array (Figure 2.3) indicating that strong scattering of the incident waves is not occurring near the array within the frequency band of the signal. Attenuation of frequencies greater than 1 or 2 Hz by the earth and suppression of longer period waves by the seismometer and recording system leaves a record with signal strongly peaked near 1 Hz. The time interval separating prominent arrivals in the P-wave coda was commonly observed to be coherent across the network for several seconds. Together, these facts indicate that strong arrivals in the P-wave train may be adequately represented using geometrical ray theory.

The simple character of the observed waves facilitates the measurement of arrival times. Although the initial onset is often emergent at even the best stations, the phase coherence of the wave train enables us to select a single prominent wavelet for timing. The measured time of this arrival, strictly a phase delay time, is equivalent to the relative arrival time of the initial onset. The actual onset time can be recovered by subtracting from each measured time the interval between the onset time and the measured time as determined at a reference station.

The reading of arrival times involved several steps. Tracings were made of the first 5-10 seconds of record for 3 to 5 stations with representative waveforms. A prominent peak or trough appearing as early as possible in the record and common to all traces was identified and timed using a ruler calibrated in 0.5 mm units. Times were reported to at least the nearest 0.05 sec. For most events, the maxima appeared in the first 1-2 sec of record. As an aid in the identification of the selected phase on stations with poorer signal-to-noise ratios, the seismograms were visually correlated using the tracings as overlays. Misidentification of the proper phase would introduce an easily detectable error of 2π (approximately 1 sec for waves measured) or multiples thereof.

Reading quality classes, designed to be an estimate of the confidence of the readings, were assigned to all readings. Impulsive waveforms were assigned qualities according to the accuracy with which the measurement could be repeated and correspond to estimated standard errors of a single observation of 0.05 sec for quality class "0" and 0.1 sec for class "1". Emergent arrivals with poorer signal-to-noise ratios were assigned quality classes of "2", "3", and "4", corresponding to estimated uncertainties of 0.15, 0.2, and 0.3 sec, respectively. Only data with qualities of "2" or better have been included in subsequent analyses.

2.3 Teleseismic Sources Studied

Events selected for analysis were chosen on the basis of their geographic location, quality of P-wave arrival, and number of readable stations. The first criterion is perhaps the most important from the standpoint of estimation of lateral variations in mantle structure underlying the array. Ideally we would like a suite of sources with ray paths to the array evenly distributed in both azimuth and angle of incidence. Such a distribution optimizes the determination of three-dimensional structures by providing a uniform crossfire of rays through all elements in the region of interest. As can be seen in Figure 2.4 and Table 2.1, the analyzed events cover a wide distance range and are azimuthally well distributed.

2.3.1 Teleseismic Travel Time Residuals

Measured phase arrival times are converted into a form suitable for analysis by comparing them with predicted arrival times given by a reference earth model. Because the data derived from this comparison can be cast into one of several useful forms, we will first define reductions used in the analysis.

The primary datum is the arrival time of a wavelet at station j for event i , which will be denoted by T_{ij}^{meas} . This calendar time (UTC) is related to its corresponding absolute travel time residual, T_{ij} , by

$$T_{ij} = T_{\text{meas}_{ij}} - \Delta T_i - T_{c_{ij}} - OT_i$$

where ΔT_i is the interval between the initial P-wave onset and the measured wavelet, as determined at a single reference station, $T_{c_{ij}}$ is the predicted travel time of the P-wave between source and receiver as given by a specific earth model and OT_i is the event origin time (UTC).

The absolute event residual \bar{T}_i , is defined as the mean of the absolute station residuals

$$\bar{T}_i = \frac{\sum_j T_{ij}}{n_i}$$

where n_i is the number of observations for event i .

Relative travel time residuals, R_{ij} are determined by removing the absolute event residual \bar{T}_i from T_{ij} .

$$R_{ij} = T_{ij} - \bar{T}_i$$

Grouping these data by station, we obtain the average station residual

$$\bar{R}_j = \frac{\sum_i R_{ij}}{n_j}$$

where n_j is the number of observations for station j .

Reduction of the measured arrival times to forms suitable for analysis follows two parallel paths. The first method reduces the data to an absolute travel time residual T_{ij} using reported hypocentral coordinates and the travel time appropriate for each source-receiver pair $T_{c_{ij}}$ as given in either the Jeffreys-Bullen (J-B) table or the Herrin table. Calculated travel times are corrected for the effect of ellipticity on epicentral distance and its effect upon travel time, the latter using the tables of Dziewonski and Gilbert (1976), but not the elevation of the seismograph station. These absolute travel time residuals are then converted into relative travel time residuals R_{ij} by removing the absolute event residual \bar{T}_i , thereby eliminating the dependence of R_{ij} upon the computed origin time or the total travel time. The lone observation of the phase PKP (event #133, Table 2.1) was found to have an apparent velocity appropriate for the AB branch of the travel time curve. Appropriate times from the tables were used in calculating residuals for this event. In the second reduction, a plane is fit to the measured arrivals using least squares and residual travel times are calculated relative to the arrival of the plane wavefront.

The mean of the absolute event residuals, as given by the J-B table, is 0.38 ± 0.08 sec. The small magnitude of the mean residual value is partly due to the fact that the hypocenters and origin times used to determine the travel times are calculated using the J-B table. It also

demonstrates that the average travel time for teleseismic P-waves to the island of Hawaii is not greatly anomalous. If the mean absolute residual is further corrected for the average station elevation of 1.2 km using a vertical velocity of 6 km/sec the average absolute residual is reduced to 0.20 sec. Clearly if there is a systematic delay common to all ray paths between 35° and 95° and exceeding 0.2 to 0.4 sec, it must be compensated for elsewhere along the travel path.

Although the average absolute teleseismic residual is nearly zero, the J-B residuals do correlate with epicentral distance. The residuals of Table 2.1 appear in Figure 2.5 as a function of distance normalized to a focal depth of 33 km. The smooth curve in the figure is the systematic residual curve as determined by a least squares cubic spline fit to the data. The overall behavior of the smooth curve is quite similar to the systematic J-B residual curve determined in recent years by many studies (Carder and others, 1966; Herrin and others, 1968; Cleary and Hales, 1966; Lilwall and Douglas, 1970; Sengupta and Julian, 1976). Each of these systematic residual curves (Figure 2.6) shows a rise in residual between 30° and 40° to 45° from where it decreases to a minimum value at about 60° , and beyond which it increases again.

Since the baseline value for each curve is arbitrary (Herrin et al., 1968) we may shift each by a constant value and compare the shape of the curves. Rather than

compare the smooth residual curve found for the Hawaii array with each of the other studies, we choose to compare the Hawaii result with the average curve defined by

$$\bar{C}(\Delta) = \sum_i (C_i(\Delta) + d_i)w_i(\Delta)$$

where $C_i(\Delta)$ is the i th systematic residual curve of Figure 2.6, d_i is the baseline shift for the i th curve, and $w_i(\Delta)$ is the weight applied to each $C_i(\Delta)$.

It is not difficult to find the baseline shifts d_i which minimizes the variance of each $C_i(\Delta)$ with respect to the mean curve. Equations to find the desired $\bar{C}(\Delta)$ are developed in Appendix 1.

Agreement between the Hawaii systematic residual curve and the mean curve (Figure 2.7) when fit in the interval between 35° and 99° using the method of Appendix 1 is quite good. Note, however, that the Hawaii curve is early for all $\Delta < 65^\circ$ and late for all $\Delta > 65^\circ$, suggesting that travel times measured on Hawaii for sources between 65° and 95° are systematically delayed relative to sources at shorter distances. Ray paths corresponding to these distances not only bottom deeper in the Pacific mantle than those from closer sources, but also sample the deepest regions of the upper mantle directly underlying the array. If the apparent delay is in fact real we cannot, at this point, distinguish between a low velocity zone underlying Hawaii or a regional effect related to the lower Pacific

mantle. This question will be examined more carefully in §2.5.1.

2.3.2 Hawaiian Station Residuals

Average station residuals \bar{R}_j are characterized by rapid geographic variability and depend only weakly upon the elevation of the receiver, despite over 4 km of relief within the array (Figure 2.9). A regression line fit to all average station residual-station elevation data yields an improbably high vertical phase velocity of 10.0 km/sec. Prospects for determining the lateral structural variations in the upper mantle seem dimmed by the apparently random, large amplitude (+.47 to -.33 sec) variation in station residual. Fortunately, the origin of the rapid spatial variation in residuals has a simple explanation.

The strong site dependence of \bar{R}_j indicates the presence of strong lateral velocity contrasts at shallow depth. Consideration of the geologic setting of each site (Figures 2.9 and 2.10) reveals that stations situated upon volcanic summits or within rift zones are fast relative to stations located upon the non-rift flanks of the volcanoes. Summit and rift zone stations are relatively fast because of the presence of reinforcing dikes (Wentworth and Jones, 1940) of high velocity diabase. Regression lines fit to the mean residual data grouped on the basis of geologic setting give vertical phase velocities of 7.46 km/sec for

summit and rift and 6.65 km/sec for the unreinforced shield. These regression lines crossover at a depth of 16.9 km which lies within the range of estimates for crustal thickness (Eaton, 1962; Ryall and Bennett, 1968; Hill, 1969).

If we assume that the excess elevation may be represented by a constant velocity layer with thickness varying according to station elevation, the velocity of the medium, V , is related to the vertical phase velocity by

$$V = V_z (1 + (pV_z)^2)^{-1/2}$$

when p is the slowness of the ray. Table 2.3 compares values for the equivalent layer velocity calculated using the measured V_z and representative p values for teleseismic sources. Clearly, the value of $V_z = 10.0$ km/sec given by all the data is unacceptable. However, velocities corresponding to the grouped stations are reasonable values for crustal rocks underlying Hawaii (Hill, 1969). Alternatively, since differences in vertical phase velocity between the two station groups are small, the average difference between summit or rift and non-rift shield sites may be interpreted as a constant offset of about 0.3 sec superimposed upon an elevation trend with a phase velocity of about 7 km/sec. In either case, it is probable that the spatial variation in mean residual has its origin in the volcanic pile and does not directly

reflect deeper seated structures (Ellsworth and Koyanagi, in press). Further evidence which supports this conclusion is presented in the next section.

2.4 Azimuthal Variation of Travel Time

Evidence for the existence of heterogeneous structure in the crust and upper mantle underlying the HVO seismograph array comes primarily from departure in relative arrival times from those predicted by the wave slowness and azimuth appropriate for the source. These departures themselves constitute direct evidence for heterogeneous structure along the raypath from source to receiver. However, demonstration that the structural inhomogeneity lies along a particular segment of the raypath is usually not possible unless residuals from many sources are considered jointly. In this section, the observational evidence for three-dimensional structure is presented by considering, in turn, average properties of the relative travel time residuals and site-by-site variations in average station residual.

2.4.1 Apparent Azimuth and Slowness of Teleseismic Body Waves Across the HVO Array

The average slowness or phase velocity and azimuth of body waves crossing an array has been used in recent years to study not only average properties of the mantle (Niazi and Anderson, 1965; Johnson, 1967, 1969) but also to infer the presence of inhomogeneous structure in the

lower mantle (Toksöz et al., 1967; Davies and Sheppard, 1972; Powell, 1977) and directly underlying the array (Otsuka, 1966; Engdahl and Felix, 1971; Berteussen, 1975; Okal and Kuster, 1975). If the earth were a radially symmetric, isotropic body, the phase velocity and direction of approach of teleseismic body waves crossing an array would be given by the great circle azimuth to the source, the angular separation between source and receiver, and the focal depth of the source. Departures in observed phase velocity and/or azimuth from that predicted for a radially symmetric earth model indicate the existence of structural variations along the raypath, although they do not uniquely identify its source.

Phase velocity (or slowness) and azimuth of approach for the teleseismic P waves of Table 2.1 were estimated by fitting a plane wave to the observed arrival times using least squares. Two different estimates of slowness and azimuth were made for possible biases introduced by the large variations in near surface structure discussed in §2.3.3. The first estimate was made by correcting the arrival times at each station by a constant factor

$$\Delta t = h/V_z \quad (2.1)$$

where h is the station elevation above sea level. With $V_z = 5.5$ km/sec, this factor approximately corrects the arrival times for the effect of excess elevation caused

by a variable thickness layer with a medium velocity of 5.25 km/sec. The resulting estimates of slowness and azimuth appear in an array diagram in Figure 2.11. An array diagram displays the "mislocation of the source", as a vector connecting the estimated location (vector tail) to the theoretical value (vector head). Although this analysis explains some of the variance of the data, mean travel time residuals for many stations are still significant. Because these large station residuals might bias the estimate of the wavefront azimuth and slowness, we would like to correct the data for these systematic residuals. A comparison between the average station residuals computed using plane waves and J-B travel times which have also been corrected for elevation using (2.1) shows a very high degree of correlation (Figure 2.12). This indicates that the average station residual is insensitive to the choice of reference teleseismic wavefront and can successfully be accounted for by correcting the arrival times at each station by the average J-B station residual.

Plane waves calculated by removing the \bar{R}_j values of Table 2.2 (uncorrected for elevation) are given in Table 2.1 and are displayed in Figure 2.13. These new estimates of the best plane wave slowness and azimuth generally agree well with mislocation vectors calculated using (2.1). The principal difference between these mislocation diagrams (Figure 2.11 and 2.13) is the reduction of the scatter between the nearby vectors for the station corrected plane

waves, especially in the northwest and southwest quadrants where the vector lengths are of comparable magnitude to the measurement error. One standard deviation of the azimuth and slowness are typically 1° and 0.1 sec/deg, respectively. Thus, it appears that the primary effect of algebraic station corrections on the array diagram is to improve precision without distorting the overall pattern.

The agreement between the two array diagrams (Figures 2.11 and 2.13) is significant for several reasons. Use of average residuals as station corrections removes from the diagram effects of the average lateral structure underlying each station. Simple, broadscale trends, such as a regional thickening of the crust, therefore do not contribute significantly to the array diagram for Hawaii. However, more localized variations in crust and upper mantle structure may assert an important influence upon the diagram. Specifically, correlation of azimuth and slowness errors from widely separated sources indicates the presence of heterogeneous structures sampled by rays to many stations.

A notable example of such a correlation is the west-southwest alignment of all vectors with slowness values of about 8 sec/deg between $N10^\circ W$ and $N60^\circ E$ in Figure 2.13. Sources corresponding to these vectors range from the Aleutian Is. to Southern California. A lower mantle or near receiver structure would seem to be required to

explain these mislocation vectors since no single tectonic structure is common to the source regions of these events. Other examples of spatially coherent mislocations include the 5° clockwise azimuth error for Central American sources at an azimuth of $N80^\circ E$ and the nearly radial error vectors found for most sources between $N70^\circ E$ and $S40^\circ E$ with J-B slowness values between 4.5 and 6.0 sec/deg. These vectors correspond to events from the Caribbean through South America to the South Pacific Cordillera.

The two regions with very small, randomly oriented mislocation vectors between $S20^\circ W$ to $S70^\circ W$ and $N70^\circ W$ to $N20^\circ W$ (Figure 2.13) correspond to regions examined in detail by Powell (1976) using the Montana LASA and the USGS Hanford, Washington, array. The pattern of mislocation vectors for the first zone corresponds to events in the South Pacific between Kemradec Is. and New Guinea while the second group includes events from Japan to Kamchatka. For the first group, Powell's results show a strongly oriented pattern of vectors with tails displaced clockwise by as much as 10° and slowness values overestimated by 0.3 sec/deg. The apparent discrepancy between the array mislocations from LASA and Hanford and Hawaii actually strengthens Powell's conclusion that near-source structure cannot explain mislocation errors exceeding 2° or 0.3 sec/deg (Powell, 1976). The absence of remarkable mislocation vectors for these two regions at Hawaii strongly suggests that lower mantle structure encountered by rays from these sources differs little

from the mean earth. The question of whether or not the significant mislocations from other regions can be explained by lower mantle structure is deferred to §2.5.2. However, constraints can be placed upon the amount of the mislocation explainable by lower mantle structure through consideration of travel times to stations at regional distances.

2.4.2 Teleseismic Travel Times to Stations on Other Islands

Short period seismograph stations in the Hawaiian Islands are located not only on Hawaii, but also on Maui and Oahu (Figure 2.14, Table 2.4). Together with HVO network stations, these stations form an elongated array with an aperture of over 400 km along the island chain. By using this extended array we hope to improve our estimates of plane wave slowness and azimuth anomalies and to place constraints on the location of structures responsible for the array mislocations of Figures 2.11 and 2.13.

Arrival time readings for 75 events from Table 2.1 appear in the Bulletins of the International Seismological Centre (ISC) and from Earthquake Data Reports (EDR) published by the U.S. Geological Survey and by NOAA. Although arrival times are usually reported to the nearest second or half second, the increased aperture of the array more than compensates for the loss of time precision. Average J-B travel time residuals for the five Oahu

stations and the single Maui station agree well with average residuals from Hawaii (Table 2.4).

Computation of plane waves for the extended array requires a slight modification of the approach used earlier because curvature of the travel time curve ($dp/d\Delta$) is no longer negligible. Three possible approaches could be used to remedy this problem. First, one could compute plane waves in the usual manner, ignoring the curvature, and compare the results with new, average, predicted slowness and azimuth values. The disadvantage of this approach is the non-uniform distribution of stations which bias the mean epicentral distance well to the Hawaii side of the array center. The second alternative would be to estimate curvature of the travel time curve together with average slowness and azimuth. Since nearly all the stations cluster at the extremes of the array, little control over curvature can be expected from this array configuration. Finally, the curvature can be removed by assuming a $dp/d\Delta$ relation. This is not too extreme an assumption, especially over distances of a few degrees, since $dp/d\Delta$ is nearly constant between $\Delta = 30^\circ$ and 90° . This correction is easily made by constructing arrival times from relative travel time residuals using the average predicted slowness determined for the Hawaii array. Arrow head locations on the array diagram are retained by this method. This method was used together with relative J-B travel time residuals to

estimate the plane waves shown in Figure 2.15. Numerical values are given in Table 2.1.

Comparison between the extended array diagram (Figure 2.15) and the Hawaii array diagram (Figure 2.13) reveals several interesting features. Together the two diagrams verify the absence of any discernable trend in either slowness error or azimuth error from sources to the northwest and to the south-southwest of the island chain. Mislocation vectors for events in the northeast quadrant and at western azimuths retain their relatively uniform alignments indicating that a common structure is sensed by both the smaller and larger array configurations. Two regions of the diagram also show considerable differences between the two plane wave estimates. Small randomly oriented vectors at southwest azimuths in Figure 2.13, which correspond to sources in the Solomon Is. and the New Hebrides Is., point inward in Figure 2.15 and are approximately parallel to vectors at western azimuths. A more dramatic change in vector orientation occurs for events from South and Central America, at eastern and southeastern azimuths. The strongly oriented vector field in Figure 2.13 collapses to a randomly oriented set of short vectors in Figure 2.15.

These significant changes in the array diagram strongly imply that the structure responsible for the mislocations lies near the array and not in either the lower mantle or near the source. This follows since the

distant stations on Oahu and Maui share a common raypath with Hawaii everywhere except immediately beneath the array. A significant reorientation of the vector pattern can only occur when structural variations are encountered. Thus, it appears certain that the large, systematic vectors at eastern and southeastern azimuths in Figure 2.13 arise from structures near Hawaii and not in the lower mantle.

It is tempting to conclude that the correlation of mislocation vectors at northeastern and western azimuths at the extended array and the smaller Hawaii array implies that the responsible structures lie in the lower mantle. However, this is incorrect, since a structural trend common to the entire array would give the same effect. Circumstantial evidence points to this alternative in the case at hand.

The array diagram formed by the extended array is approximately symmetric about a line trending $N50^{\circ}W$. This direction corresponds to the line connecting the islands of Hawaii and Oahu and nearly parallels the mean trend of the island chain (Figure 2.15). Vectors from sources with azimuths falling ahead or along the island chain are small and are distributed randomly. However, vectors from sources at azimuths perpendicular to the chain are themselves approximately perpendicular to the line joining Hawaii and Oahu. A synclinal structure centered upon the island chain but terminating at Hawaii

is compatible with this pattern. Downwarping of the Moho and/or flexure of the lithosphere by the load of the islands represent plausible geological features capable of reproducing the array diagram. Others might include a tabular low velocity zone or an abnormally thin lithosphere underlying the island chain.

To conclude, average mislocation directions for all available Hawaiian Islands stations demonstrate that some of the strong mislocations of Figure 2.13 arise from structures near Hawaii. The significant trends evident in Figure 2.15 may be related to lower mantle structure, but are explainable by realistic structures for either crust or upper mantle below the Hawaiian Ridge.

2.4.3 Azimuthal Variation of Relative Residuals

Departures in average azimuth and slowness, together with mean station residuals, explain most of the variance of the relative travel time residuals. However, significant information escapes explanation by either of these techniques which model chiefly average properties of the wavefront or the recording site. Rapid azimuthal variations in relative residual at a single station (Figure 2.16) characterizes this, as yet, unexplained information. Neither removal of mean station residuals nor correction of slowness and azimuth to the least squares plane wave materially affects the fundamental form of this residual pattern (Figure 2.17). Thus, this azimuthally-varying

residual appears to contain useful information about local three-dimensional structure.

Interpretation of the azimuthal residual pattern is not altogether straightforward since the reference residual is weighted artificially toward Kilauea's summit where the station density is greatest. Thus, it is not too surprising that Kilauea stations such as OTL show smaller variations than distant, isolated stations such as SPT (Figure 2.16). A complete understanding of the origin of the azimuthal residual awaits application of the three-dimensional modeling developed in §3 and applied in §4.

2.5 Origin of Travel Time Residuals

The preceding analysis of the travel time of teleseismic P-waves across the Island of Hawaii identified four principal components to the travel time residual. They are: (1) absolute teleseismic residual for each event \bar{T}_i ; (2) plane wave azimuth and slowness mislocation; (3) mean station residual \bar{R}_j ; and (4) azimuthal dependence of relative travel time residuals at each station. Remarkably, the interaction between these four classes of residual are minimal, each not greatly influencing the others (if at all). We take advantage of the separability of these four residual components in this section and examine the limits each places upon the origin of the overall residual.

2.5.1 Structure Inferred from Absolute Travel Time Residual

The average teleseismic P-wave travel time curve observed on Hawaii (Figure 2.5) agrees in overall shape with recent global estimates of travel time (Figure 2.7). Hawaiian travel times, however, are skewed significantly toward late arrivals with increasing distance. This systematic departure in travel time from the average earth is readily apparent when the mean earth travel time curve of Figure 2.6 is used as the reference travel time. Although the absolute travel time cannot be determined for the Hawaiian data, the proper base line for comparing relative travel times can be established. The base line is just the (J-B) average difference between the old reference travel time and the new standard (mean earth). This follows because the locations of virtually all distant sources observed on Hawaii are controlled by well distributed teleseismic P-wave arrival times. While origin times and total travel times so determined are fixed by the earth model used to locate the event, residuals computed using that origin time and earth model tend to be unbiased because the average travel time residual for all observations is zero. It is for this reason that a systematic residual curve with a shape distinct from the earth model used to calculate it can be recovered.

The systematic residual difference between the Hawaiian observations and the mean earth, with a base line correction of 2.05 sec applied, appears in Figure 2.18.

The nearly monotonic increase in residual with increasing epicentral distance is clearly evident and, to a first approximation, rises linearly with a slope of 0.025 sec/deg. The data suggest that the residual levels off at +1.2 sec beyond 75°.

Source event mislocation can be ruled out as a possible explanation for the systematic residual error because ray paths to stations used to locate the sources traverse most of the earth's mantle. Therefore, the locations and origin times must reflect the average structure of the mantle, which is used here as the reference. Ray paths to Hawaii, however, are rather unique since only a handful of stations (Table 2.4) are located within 30°, and their cumulative effect on the location is minimal. Additionally, comparable residuals are found for the Hawaii network whether or not any Hawaiian stations appear in the solution.

The skewed residual curve for Hawaii can be explained by postulating that P velocities in the Pacific lower mantle are slightly below normal. Mean earth residuals for a mantle with velocities 40 m/sec (0.3%) below normal between 1700 and 2500 km depth and tapering linearly to normal velocity over a 300 km distance adequately models the overall behavior of the observed residual (Figure 2.18). The required perturbations to lower mantle velocity conflict with the whole-earth three-dimensional velocity inversion of Dziewonski and others (1977). Their solution

for the lower Pacific mantle traversed by raypaths to Hawaii shows essentially normal velocities between 1500 and 2200 km (0 ± 15 m/sec) and somewhat higher than average velocities between 2200 km and the core-mantle boundary ($+15$ m/sec). Sengupta (1975) has also estimated three-dimensional mantle heterogeneity for the entire mantle. His perturbations for lower Pacific mantle traversed by raypaths to Hawaii average 0.0% between 1500 and 2000 km and 0.15% above normal between 2000 and 2500 km. On the basis of these comparisons, a lower mantle explanation for the systematic delay of the more distant arrivals at Hawaii is unlikely. An upper mantle explanation appears to be required.

The sense of the residuals of Figure 2.18 implies that a high-velocity, layered upper mantle structure is needed to explain the residual curve. This is because rays from more distant sources are steeper and spend relatively less time in the high velocity upper layers than rays from nearer sources. To match the observed 1.5 sec skewness unrealistically high velocities (>9 km/sec above 200 km) are required. Travel times for these models are also unacceptable, arriving 5.0 sec early. More realistic models, such as the high velocity, Jurassic age Pacific lithosphere and upper mantle model of Asada and Shimamura (1976) ($V_p \geq 8.6$ km/sec below 120 km), are not skewed sufficiently to explain the observations (Figure 2.18). Layered uppermost mantle structure alone therefore cannot reasonably explain the systematic residual curve for Hawaii.

A simple upper mantle structure capable of explaining the observations is a radially symmetric low velocity structure underlying Hawaii at sufficiently great depth so that the steepest rays penetrate it while shallower rays miss it. Geometrical considerations require such a structure to lie below about 50 km. No maximum depth can be placed upon the body by these data.

An alternative explanation for the very late arrivals is the possibility that the first break of the P-wave was not correctly identified for the more distant sources. Re-examination of tracings of the seismograms reveals that the initial onset is very emergent for many of the distant sources and is distinct for a much smaller percentage of the arrivals. Additional evidence on the travel times of teleseismic P-waves to Hawaii is needed to resolve this problem.

Fortunately, many teleseismic arrival times for the Honomu earthquake of April 26, 1973, and the foreshock of the Kalapana earthquake of November 29, 1975, appear in the EDR reports and the ISC Bulletin. A cubic spline fit to J-B residuals for these travel time data, computed relative to hypocentral parameters determined exclusively from stations on Hawaii (Table 2.5, Figure 2.19) show a systematic residual similar in form to that for Hawaii (Figure 2.5) and from global studies (Figure 2.6). In particular, the systematic residual for the Kalapana foreshock fluctuates about the mean earth

systematic residual with a root mean square (rms) error of only 0.2 sec compared to the 0.5 sec rms error of the curve obtained from teleseismic observations on Hawaii. Rms errors relative to the J-B table for these same curves are 0.4 sec and 0.8 sec, respectively. Systematic residual curves for these two travel time data sets are clearly closer to the mean earth than to J-B, and travel times from the Kalapana foreshocks are the more normal of the two. Because the coverage of the focal sphere by rays leaving the Kalapana foreshock to teleseismic stations is far more uniform than coverage of the focal sphere by rays to Hawaii from the sources of Table 2.1 (Figure 2.4), the better agreement between mean travel time residuals from the Kalapana foreshock and both reference travel times underscores the possibility that the skewed nature of the Hawaiian teleseismic residual curve is an artifact. A similar comparison of rms error for the Honomu earthquake is inconclusive with an rms error of 0.4 sec found in both comparisons.

Absolute travel times for P-waves from the two earthquakes are potentially meaningful because the focal parameters for each are well controlled by the local network. The average J-B residual between 35° and 95° for the Honomu earthquake is 0.6 sec and for the Kalapana foreshock is 0.4 sec. Both are considerably later than the absolute travel times found by many recent studies (Carder and others, 1966; Cleary and Hales, 1966; Herrin

and others, 1968). For example, the mean travel time residual over the same distance range is -2.5 sec for the Herrin table. This large baseline error for these two Hawaiian earthquakes is not necessarily significant because teleseismic arrivals for these two events are most frequently reported with an 'e' (emergent) notation. Travel time residuals in Figure 2.19 are also bounded from below by an error of -2.5 sec. Additionally, the fact that travel times to Hawaii from circum-Pacific sources average only 0.4 sec late contradicts the existence of a 3 sec baseline error between travel times from Hawaii and the global average travel time.

The core phase PKP also provides useful constraints upon possible travel time anomalies associated with Hawaii. Owing to its very high surface phase velocity, this wave samples the deepest regions directly underlying the seismograph array of all short period body waves. Absolute travel times and travel time residuals for 44 observations of PKP (DF branch) for the April 26, 1973, Honouliuli earthquake indicate that structure along these nearly vertical raypaths is not greatly anomalous. The average travel time residual relative to Bolt's (1968) table is +1.5 sec after the proper depth correction is made for Hawaiian crust and upper mantle structure. This value is consistent with the 1.2 sec residual for P waves at distances beyond 75°. However, an alternative set of focal coordinates given by Ward and Ungar (written communication, 1975) with

an origin time 0.4 sec later and a focal depth 5 km shallower than those of Table 2.5, reduces the discrepancy to 0.2 sec. Absolute travel times for PKP observations reported to the ISC for this earthquake in the distance range 110° to 135° (Figure 2.20) average 1.2 sec later than travel times from Bolt (1965) and 0.7 sec later than Jeffreys and Bullen's (1958) estimates. Given the scatter in the data and the complex signature of the body wavelet for this earthquake (Butler and Langston, 1976) these data clearly do not represent significant evidence for an anomalous travel time. The travel time data also agree well with absolute travel times of PKP for Pacific nuclear explosions (Figure 2.20).

The mean residuals for the lone observation of PKP on Hawaii (event 133, Table 2.1) is -0.2 sec relative to J-B and 2.2 sec relative to Bolt, the differences resulting from the 2.0 sec offset between these tables for the AB branch of PKP at 145° . Since there is no near station control of the solution for this earthquake, the residual for this event must be considered normal. Insufficient travel time data for the November 29, 1975, Kalapana earthquake or its foreshock prevent any useful conclusions to be drawn for this event in spite of excellent control on the hypocenters and origin time.

In summary, total teleseismic travel times for both P and PKP are essentially normal on Hawaii. Available evidence allows, but does not require, a systematic delay of up to 1.5 sec along raypaths with the steepest

angles of incidence. Larger delays are ruled out by both P and PKP travel times. Comparison of lower mantle structures consistent with a delay of this magnitude and other studies of lateral variations in mantle structure indicates that the possible delay most likely occurs near Hawaii rather than in the deep Pacific mantle.

2.5.2 Broad Scale Heterogeneous Structure

The existence of heterogeneous structure near Hawaii, only hinted at by total travel time data, finds much stronger support in departures in the measured azimuth and slowness of teleseismic P-waves from values predicted by laterally homogeneous earth models. As discussed in §2.4.2, some of these array mislocations arise from structures near the array while others are consistent with either nearby structure or lower mantle heterogeneity.

Let us first address the question of lower mantle structures consistent with slowness and azimuth measurements on Hawaii. The observations to be explained divide approximately into two classes. The first group corresponds to sources at northeastern azimuths with mislocation vectors directed approximately inward and with slowness error of about 0.8 sec/deg (Figures 2.11, 2.13, and 2.15). The other corresponds to sources west of the array with mislocation vectors also directed inward and with a slowness error of about 0.6 sec/deg. Given only these

few measurements of slowness error we cannot find a unique lower mantle structure consistent with them. However, by jointly considering the total travel time and measured slowness we can construct families of models which exactly satisfy individual measurements. Although models so obtained do not impose strict bounds upon possible mantle structures, they do provide useful information on the size and magnitude of velocity heterogeneities required. Because the principal mislocation error is radial we will consider only structures with lateral homogeneity normal to the ray direction, so that the velocity-depth profile depends only upon depth.

Construction of velocity structure consistent with a single observation of slowness, p at a distance Δ with an arrival time t is easily accomplished using the function $\tau(p) = t(p) - p\Delta(p)$. For convenience, the spherical earth is transformed into a horizontally stratified earth by

$$x = R\Delta$$

$$z = R \ln(R/r)$$

$$u(z) = r/(RV(r))$$

where R is the radius of the earth and $V(r)$ is the velocity at radius r . Physically, $\tau(p)$ is the time intercept at $\Delta = 0$ of the tangent to the travel time curve where $dt/d\Delta = p$. In transformed coordinates

$$\tau(p) = t(p) - px(p)$$

and in integral form

$$\tau(p) = 2 \int_0^{Z(p)} [u(z)^2 - p^2]^{1/2} dz \quad (2.2)$$

where $Z(p)$ is the depth at which the ray with ray parameter p bottoms (Gerver and Markushevich, 1966). The inverse solution for (2.2) is

$$Z(p) = \frac{1}{\pi} \int_0^{\tau(p)} [v^2(\tau) - p^2]^{-1/2} d\tau \quad (2.3)$$

where $v(\tau)$ and $\tau(p)$ are mutual inverse functions (Bessonova and others, 1976). Before applying (2.3) to the problem at hand, several important features of $\tau(p)$ need to be illuminated.

The power of the function $\tau(p)$ lies in its "unfolding" of the travel time curve $t(x)$ into a single-valued, monotonically decreasing function of p . Since

$$\frac{d\tau}{dp} = -x \quad (2.4)$$

$t(x)$ can be completely recovered from $\tau(p)$. Furthermore, by specifying a point $\tau(p_0)$ in the $\tau(p)$ plane and $d\tau/dp$ at that point, the function $\tau(p)$ for all velocity structures consistent with those values must pass through $\tau(p_0)$ with that slope. Thus, by equivalently specifying $t(x)$ and $p(x)$ at one distance, all models consistent with those observations can be generated using (2.3).

Numerical evaluation of the inverse solution (2.3) for arbitrary velocity functions requires treatment of a square-root singularity at $\tau = \tau(p)$. Let

$$u = v(\tau)$$

so

$$-xdu = d\tau.$$

Then (2.3) becomes

$$z(p) = \frac{-1}{\pi} \int_{p_{\max}}^p [u^2 - p^2]^{-1/2} x(u) du. \quad (2.4)$$

This is just the familiar Herglotz-Wiechert formula.

Now let

$$u = p \sec\theta$$

and (2.4) becomes

$$z(p) = \frac{1}{\pi} \int_0^{\cos^{-1} p/p_{\max}} x(p \sec\theta) \sec\theta d\theta \quad (2.5)$$

which is non-singular everywhere since $\theta < \pi/2$ always. This solution must be modified by inclusion of terms corresponding to low velocity zones crossed by the ray, when present.

In applying (2.5) to the slowness estimates from Hawaii the velocity model and travel time table of Herrin and others (1968) is used as the standard for comparison. The close agreement between the mean earth travel time curve and the Herrin model (rms error of 0.2 sec, Figure 2.6) indicates that it is a suitable reference model. Total travel times to Hawaii were found to be within 1.5 sec of normal, so Herrin travel times are used in constructing $\tau(p)$ values to be modeled together with Hawaiian slowness observations. As is shown in Figure 2.18 realistic variations in upper mantle structure have only a minimal effect on p values. Consequently, choice of a Herrin upper mantle model will not unduly bias the results. Possible models are therefore restricted to those arising from $\tau(p)$ curves which connect Herrin $\tau(p)$ values to a single measurement for Hawaii at the minimum p value.

Solutions for two measured slowness errors, one from each group discussed above appear in Figures 2.21 and 2.22. Other solutions for these two events (#113 and #82, Table 2.1) give similar results for both travel time and velocity profile. In the case of the Nevada Test Site explosion (Figure 2.21), a very high velocity mantle is required to match the observed slowness and travel time to Hawaii. Between 400 km and 700 km the velocity averages 370 m/sec (4%) faster than the reference model. Travel times are as much as 7 sec early near 26° .

The solution for the Halmahera earthquake (Figure 2.22) is generally similar to the result for the explosion although the magnitude of the velocity perturbations and travel time errors are smaller by a factor of 2 to 3. In either case it is evident that lower mantle velocity perturbations of at least a few hundred m/sec are required to match slowness observations on Hawaii.

Velocity variations of this magnitude with a lateral scale length of a few degrees to a few tens of degrees are, perhaps, allowed by current evidence on lateral heterogeneity in the mantle (Sengupta and Toksöz, 1976; Dziewonski and others, 1977). However, it is remarkable that absolute travel times to Hawaii are individually not more than 2 or 3 sec in error (Table 2.1) in view of large (>5 sec) travel time residuals corresponding to models which fit individual slowness and travel time data at Hawaii. Therefore, while we cannot conclusively demonstrate that the slowness anomaly pattern for the extended Hawaiian Islands array (Figure 2.15) has its origin in structures near the array, lower mantle structures required to explain the anomalies border upon the improbable.

Several simple models of local structure are consistent with the array mislocations of Figure 2.15. As noted in §2.4.2, the observed pattern implies a structural trend parallel to the island chain axis with lower average velocities occurring near the island center and

higher velocities on the northeast and southwest flanks of the area spanned by the array.

The first possible structure to be examined is a moho dipping towards the symmetry axis. An elongate crustal basin of this shape with a central depth of a few km is consistent with isostasy for a Hawaiian-type volcano. Refraction studies by Furumoto and others (1968) indicate that this type of elongate moho basin dipping 4° to 5° inward is present under Oahu. Given a crust-to-mantle velocity ratio of 0.73 a moho dip of 5° to 10° is required to match the mislocation vectors of Figure 2.13 or 2.15. However, these figures are misleading as the actual effect of a synclinal warp on the moho or slowness measured by an array which spans the structure is smaller by about a factor of 10 (Powell, 1976). Figure 2.23a illustrates this problem. Although ray paths to stations on the side of the array nearest the source cross the moho in the down dip direction, rays to stations on the other side of the array experience the opposite effect, with a net result that the perturbation of the measured slowness is very small. This cancellation is pronounced in Hawaii because of the large diameter (100 km) and shallow moho (12-15 km). Furthermore, measurements of crustal thickness on Hawaii indicate that the amplitude of any possible moho depression beneath the island is too small to account for the measured mislocation vectors (see Figure 2.24).

An alternative model in acceptable agreement with

the data is a thinning of the lithosphere by a maximum of about 45 km, assuming a P-wave velocity contrast of 0.94 between asthenosphere and lithosphere (Figure 2.32b). This model succeeds where the moho basin model failed because the structure is deep enough so that the entire array senses one limb of the structure at a time. An equivalent description of this model would be a low velocity core to the island within the lower half of the lithosphere.

The rapid reorientation of mislocation vectors seen at eastern azimuths (Figure 2.13) was earlier attributed to structural heterogeneities near Hawaii on the basis of comparison with extended array diagrams (Figure 2.15). A possible structure consistent with these mislocation vectors is a tabular low velocity zone displaced northeastward from the island (Figure 2.23c). Arrival times of rays from near teleseismic sources ($\Delta = 40^\circ$) to the far side of the island are delayed relative to arrivals on the near side of the island. This results in an apparent velocity which is too low and appears on an array diagram as an inward pointing vector. As the teleseismic sources become more distant, arrival times across the array are affected more equally until at distances of approximately 80° ray paths to the nearest stations sense the body while those on the far side of the array travel beneath it. This results in too high an apparent velocity and an outward pointing vector on the array diagram.

2.5.3 Near Receiver Structure

Two features of the relative travel time data suggestive of near receiver structure are the rapid geographic variation in average station residual \bar{R}_j and azimuthal variations in relative residual R_{ij} unexplained by either standard earth models or plane wave reductions. The former undoubtedly arises from localized geologic structural variations as is indicated by the strong correlation between \bar{R}_j and geologic setting (Figure 2.9 and 2.10). These mean station residual values cannot alone distinguish between variations in average crustal velocity, average crustal thickness, or a combination of the two as the causal structure. Fortunately this difference in interpretation will not influence the three-dimensional inverse solutions presented in §4.

Of greater concern is the possibility that the rapid azimuthal variations in relative travel time residual at a particular site (Figures 2.16 and 2.17) arise from either rapid fluctuations in crustal thickness or very strong lateral heterogeneity within the crust. Unless the modeling described in §3 adequately allows for such rapid changes, the residuals may potentially be explained by phantom structures elsewhere in the model (see §3.3.3). It is therefore important to examine the magnitude of travel time residuals arising from very localized structures.

Consider first the effect of a uniformly dipping moho under a single site. The maximum variation in travel time to this site occurs along the azimuth of the dip and is given approximately by

$$\Delta T = 2hp \left(1 - \frac{\cos \theta}{V_1 \sqrt{1/V_2^2 - p^2}} \right) \alpha \quad (2.6)$$

where h is the vertical depth from station to interface, p is the ray parameter, α is the dip angle on the interface, V_1 and V_2 are the velocities in the lower and upper media, respectively, and $\sin \theta = pV_1$. This formula follows from a small angle expansion of the exact solution and agrees to within 0.01 sec for $\alpha \leq 40^\circ$. Taking $h = 12$ km, $V_1 = 8.2$ km/sec, and $V_2 = 6.0$ km/sec as representative values for Hawaii, the maximum azimuthal variation in travel time to a station underlain by a moho with $\theta = 30^\circ$ is only 0.31 sec for a source at $\Delta = 40^\circ$ and 0.19 sec for a source at $\Delta = 80^\circ$. A dip of 10° produces a variation of only 0.10 sec and 0.06 sec, respectively. Referring to Figures 2.16 and 2.17, the observed relative residuals require localized dip angles of up to 40° (at station KPR, for example) to satisfy the data.

Available data on crustal thickness on and near Hawaii is compiled in Figure 2.24 from refraction studies by Pollard and Eaton (1964), Ryall and Bennett (1968) and Hill (1969). This compilation indicates an east to west thickening of the crust with local gradients as high as 10°

along the western flank of Mauna Loa and between Kilauea and Hilo, and an average gradient of a few degrees. Although there are large areas of the island without crustal thickness estimates, the uniformity of the depth to moho along profile lines of 50 km is striking, especially on the flanks and summit of Kilauea. Moho dip directions indicated by the azimuthal residual diagrams (Figures 2.16 and 2.17) conflict with the crustal thickness gradients indicated by the refraction data. Station CAC, on the west coast of Mauna Loa has an apparent dip direction of $S60^{\circ}E$, almost 180° out of phase with that indicated by Figure 2.24. The refraction line from South Point to Hilo of Ryall and Bennett (1968) passes through station KPR and indicates a 1° southwest dip on the moho between Kilauea and South Point (Figure 2.24) in complete disagreement with the 40° northeast dip suggested by relative residuals at KPR. Examination of moho relief required by other stations such as HUA, KHU, and KKA leads to similar disagreements. Other stations such as HLP, KAA, MLO, MOK, and SPT, to name a few, show rapid changes of up to 0.4 sec in relative residual over an azimuth range of 30° or less. These rapid variations require improbably rugged relief on the moho of up to 8 km in a distance of 3 km. Furthermore, it is questionable as to how sensitive the long wavelength teleseismic P waves (5 to 8 km in the crust) would be to these sharp features. It therefore appears unlikely that topography on the moho is the explanation for the observed azimuthal

dependence of the residuals. A formal inverse solution testing this conclusion is presented in §4.5.

Lateral variations in crustal velocities are even less likely as an explanation because teleseismic P waves traverse the crust at very steep incidence angles. Since all sources share a common raypath through the upper 4-6 km of the crust, variations in the lower half of the crust needed to match the observations exceed the range of reasonable crustal velocities. Deeper-seated structural heterogeneities appear to be the most likely explanation for the azimuthally-dependent residuals.

2.5.4 Three-Dimensional Structure Within the Lithosphere

Interpretative analysis of both array mislocations and the azimuthal dependence of relative residuals suggest the presence of significant three-dimensional structures in the uppermost mantle underlying Hawaii. This is not at all surprising in view of voluminous volcanism and the youthful age of the islands. In this section we relate azimuthal variations in relative residuals to possible structures of volcanic origin. Although non-unique, this analysis provides a classical interpretative framework for comparison with the formal inverse solutions of §4. Throughout the following discussion the diagrams displaying relative residual versus azimuth to the source as given by the J-B tables (Figure 2.16) are used as the fundamental

observations. For convenience, the azimuth to the summit of Mauna Loa, Mauna Kea, and Kilauea are indicated in Figure 2.16. The pertinent features to be analyzed do not undergo significant changes, in terms of this analysis, when the residuals are based upon alternative reductions (Figure 2.17).

Consider first a broad scale pattern observed by all stations located west of Mauna Loa's summit, including CAC, HUA, KAA, KHU, KOH, and SPT. Residual times are early at westerly azimuths at all stations which, in part, is reflected in the array diagram (Figure 2.13). This azimuth corresponds to the direction the majority of all island stations (on the summit and central shield of Kilauea) look through Mauna Loa. Although azimuthal diagrams for the Kilauea stations suggest a delay of about 0.1 sec at western azimuths, the large number of Kilauea stations control the mean residual. Thus, these observations strengthen the earlier conclusion, based upon analysis of the array mislocation diagram, that lower than average velocities occur deep in the lithosphere beneath the island.

Relative residuals at stations MLO and MLX, located on the eastern flank of Mauna Loa, increase sharply by about 0.2 sec at western azimuths. As this direction corresponds to Mauna Loa's summit it strongly suggests that the abrupt increase in travel time corresponds to magmatic processes at about 50 km depth, where the raypaths

pass beneath Mokuaweoweo. Rays to Kilauea stations pass below Mokuaweoweo at about 80 km and do not show an abrupt rise in relative residual. This suggests that rays to these stations pass below the structure.

Delayed arrivals at azimuths corresponding to Mauna Kea are also seen in Figure 2.16. Both stations MOK and MLO show an increase in residual at the appropriate azimuth. Rays to these stations pass below Mauna Kea at about 60 km depth. Residuals at several stations, notably KKU and KPR are late through an azimuth range spanning both Mauna Loa and Mauna Kea. Other stations such as NAG and PPL show possibly delayed residuals for all azimuths traversing the island, indicative of a low velocity zone deep in the lithosphere or in the upper asthenosphere.

The difficulties with the descriptive analysis are twofold. First, it provides little quantitative information about the size, shape or velocity contrasts of heterogeneous structures suggested by the data. Secondly, and perhaps most seriously, the analysis is hard pressed to explain azimuthal residual patterns which differ markedly from the simplified predicted behavior. For example, station HLP located south of Kilauea caldera has its latest arrivals not from the northwestern azimuths, but from eastern to southwestern azimuths. Station CAC, west of Mauna Loa has early arrivals for eastern sources, crossing below both Mauna Loa and Kilauea, but late arrivals

for sources crossing below Mauna Kea. At station WHA, located east-southeast of Kilauea, residuals are, perhaps, slightly delayed along azimuths through Mauna Loa, Kilauea, and Mauna Kea, and are greatly delayed at eastern azimuths. These three examples illustrate some of the complexities involved in forward modeling of these data and recommend the application of an inverse modeling which is unbiased in its treatment of the data.

DATE	ORIGIN TIME	LOCATION	DEPTH	M	DELTA	RES	AZM P		AZM P		AZM P		NUMBER
							J-B	TABLE	LEAST SQUARES	PLANE WAVES	HAWAII ONLY	ALL ISLANDS	
700527	1205	06.0 27.7 N 140.1 E	382	6.2	61.39	0.73	291.06	6.75	290.24	6.72	293.04	6.54	# 154
700729	1016	19.3 26.0 N 95.4 E	59	6.5	97.82	0.93	300.94	4.55	299.16	4.94	298.06	4.86	# 157
700731	1708	5.4 1.5 S 72.6 W	651	7.1	86.00	0.70	93.83	4.91	93.85	4.09	96.72	4.59	# 158
700824	1230	19.5 56.6 S 142.5 W	33	5.9	76.57	0.01	172.77	5.64	180.63	5.93	170.17	5.55	# 20
710209	1400	41.6 34.4 N 118.4 W	13	6.2	35.70	-0.36	57.85	8.48	58.64	9.12	58.02	9.39	# 42
710319	0612	31.9 17.1 N 95.1 W	83	5.5	57.47	-2.12	81.84	7.07	81.23	7.47			# 167
710405	0904	42.8 53.4 N 170.6 W	153	5.8	36.70	-0.70	344.36	8.42	348.99	7.64	342.38	8.28	# 169
710509	0825	01.7 39.8 S 104.8 W	33	6.2	75.53	-0.54	142.10	5.73	138.74	4.49			# 21
710517	1104	07.1 1.6 S 77.7 W	176	5.7	79.38	1.12	95.68	5.40	93.75	4.61	96.52	5.60	# 196
710530	0708	38.1 19.1 S 169.4 E	255	5.3	53.61	-0.43	224.14	7.39	226.89	7.63	224.42	7.90	# 171
710611	1256	04.3 18.0 N 69.8 W	57	6.1	80.15	2.50	74.39	5.34	73.13	4.83	79.42	5.21	# 172
710701	0116	16.8 6.4 S 130.3 E	133	5.8	78.02	2.22	258.59	5.52			256.87	5.96	# 173
710709	0303	18.7 32.5 S 71.2 W	58	6.6	95.38	8.38	122.41	4.54	118.79	3.90	126.45	4.53	# 55
710727	0202	49.6 2.7 S 77.4 W	135	6.3	79.68	1.05	96.61	5.38	96.48	4.84	99.34	5.24	# 197
710807	0653	27.0 13.9 S 167.2 E	178	5.4	50.25	0.50	230.79	7.62	229.27	7.70	230.80	7.93	# 175
710902	0633	20.7 11.1 S 166.3 E	175	5.4	49.33	0.33	234.35	7.69	231.67	7.68	233.20	8.12	# 176
710916	0622	37.6 5.9 S 130.7 E	115	6.2	77.52	1.37	258.87	5.56	256.51	6.05	257.09	5.99	# 177
710930	2124	11.0 0.5 S 4.8 W	33	6.0	145.6	1.17	59.2	3.81	64.89	3.88			# 133
711030	1416	23.6 32.1 N 137.7 E	393	5.6	62.87	1.02	296.47	6.61	295.74	6.69	292.50	6.78	# 192
711106	2200	00.1 51.5 N 179.1 E	2	6.8	37.26	-1.12	333.89	8.39	334.72	8.27	334.89	8.32	# 73
711121	0557	11.9 11.8 S 166.5 E	115	6.4	49.08	1.22	233.57	7.71	232.16	7.99			# 182
711202	1718	21.8 44.8 N 153.5 E	24	6.2	49.07	2.08	312.88	7.70	312.86	7.59	312.91	7.77	# 184
720108	0527	52.9 20.9 N 120.2 E	33	6.2	78.26	3.07	288.12	5.50	286.83	5.54			# 66
720125	0206	23.3 22.5 N 122.3 E	33	6.3	75.93	1.59	289.13	5.69	283.63	5.58			# 65
720306	1850	18.2 50.2 N 148.8 E	592	5.4	57.89	-0.32	318.61	7.03	319.86	7.09			# 188
720320	0733	49.6 6.8 S 76.8 W	64	6.1	81.71	2.15	100.25	5.19	98.34	4.80	101.71	5.29	# 79
720322	1027	41.9 49.1 N 153.6 E	134	6.3	50.55	-0.14	318.35	7.60	315.61	7.77	318.97	7.54	# 58
720502	0656	23.4 5.2 N 100.3 W	33	5.8	55.50	0.16	97.24	7.23	95.16	7.26	96.54	7.49	# 48
720527	0406	50.4 55.0 N 156.3 E	409	5.7	53.15	-0.30	326.27	7.42	326.84	7.28	325.18	7.23	# 189
721020	0817	48.6 18.8 N 106.7 W	38	5.7	45.81	0.40	82.36	7.93	81.93	8.29	78.77	8.52	# 45
721204	1751	22.4 1.5 S 136.7 E	33	6.0	69.75	1.92	260.83	6.10	259.64	6.36	258.62	6.19	# 89
730105	1354	29.1 39.0 S 175.2 E	150	6.2	64.33	-2.05	205.07	6.48	204.38	6.52	203.12	6.45	# 60
730130	2101	12.5 18.5 N 103.0 W	43	6.2	49.34	-1.03	81.97	7.69	78.94	7.95			# 44

TABLE 2.1. Teleseismic Sources Studied

DATE	ORIGIN TIME	LOCATION	DEPTH	M	DELTA	RES	AZM P		AZM P		AZM P		NUMBER	
							J-B TABLE	LEAST SQUARES	LEAST SQUARES	PLANE WAVES	PLANE WAVES			
							HAWAII ONLY		ALL ISLANDS					
730304	1757	43.5 54.8 N	161.6 E	32	6.1	47.99	0.21	327.89	7.78	326.42	7.68	326.68	7.41	# 57
730309	1006	37.7 6.3 N	127.3 E	55	6.0	75.95	12.05	271.79	5.68	269.69	6.35			# 64
730319	1141	07.7 52.8 N	173.8 E	81	5.8	41.18	1.28	331.70	8.23	331.17	8.28	331.14	8.13	# 71
720320	2331	48.8 51.3 N	179.2 W	46	6.0	37.02	0.58	335.07	8.41	335.76	8.32	335.04	8.34	# 72
730323	0655	33.1 51.3 N	174.2 E	27	5.8	39.83	0.46	330.21	8.29	330.30	8.24	330.54	8.33	# 70
730403	1354	01.8 4.7 N	75.6 W	158	6.2	79.18	1.04	88.93	5.42	88.26	5.08	89.58	5.38	# 54
730529	0614	22.3 54.0 N	163.8 W	30	6.0	35.09		351.43	8.52	352.49	8.83			# 69
730530	0438	01.8 2.3 S	78.5 W	111	5.7	78.60	0.98	96.61	5.47	94.18	4.95			# 80
730616	1443	47.5 45.0 N	125.8 W	33	5.6	35.37	-1.96	37.19	8.50	41.21	9.44	39.48	9.60	# 41
730617	2037	57.3 42.7 N	146.0 E	50	6.0	54.20	1.36	309.06	7.33	310.03	7.38	309.93	7.23	# 56
730624	0243	25.5 43.3 N	146.4 E	50	6.3	53.92	2.11	309.83	7.35	309.39	7.52	309.53	7.07	# 59
730701	1333	34.6 57.8 N	137.3 W	33	6.1	40.56	1.18	14.79	8.27	18.23	8.67	16.02	8.79	# 40
730703	0703	43.9 12.2 N	125.3 E	33	6.1	76.18	1.34	278.23	5.67	270.02	5.44			# 63
730703	1659	35.1 58.0 N	138.0 W	33	6.0	40.61	0.40	14.18	8.27	16.98	8.64			# 39
730708	0403	34.5 6.8 N	73.0 W	156	5.7	80.68	2.20	86.13	5.29	79.39	4.98			# 51
730716	1812	57.5 17.3 N	100.7 W	44	5.6	51.70	0.26	82.94	7.52	77.66	7.65	80.30	7.89	# 43
730728	2006	36.0 50.5 N	148.8 E	592	5.5	57.94	-1.51	319.00	7.02	319.31	7.00	319.89	6.83	# 77
730813	0828	19.7 4.5 S	144.0 E	112	6.0	64.04	-0.72	254.91	6.50	250.50	6.54	252.46	6.79	# 88
720821	0623	48.9 49.5 N	147.0 E	578	5.9	58.34	-0.48	317.44	6.99	318.20	6.98	317.46	7.03	# 78
730822	1814	37.2 57.1 N	154.1 W	38	5.9	37.62	0.27	1.14	8.37	4.75	8.75	3.64	8.95	# 68
730830	1825	43.1 7.3 N	72.8 W	181	5.7	80.80	0.47	85.55	5.27	84.24	5.03	87.06	5.38	# 50
730910	0743	30.5 42.5 N	130.9 E	532	6.0	67.68	-0.16	308.59	6.25	310.18	6.34	309.36	6.27	# 76
730920	2043	39.8 9.0 N	123.8 E	560	6.0	80.57	1.01	275.54	5.29	275.63	5.61	271.59	5.11	# 62
730921	0713	34.0 4.4 S	102.0 W	33	6.1	57.52	-0.05	108.60	7.05	109.14	7.50	109.39	7.34	# 47
730929	0044	00.8 41.9 N	130.9 E	575	6.5	68.07	-0.18	307.93	6.23	307.12	6.35	306.71	6.27	# 75
731106	0936	05.0 51.6 N	175.4 W	34	5.8	35.73	-0.40	338.55	8.47	339.36	8.63			# 67
731129	1759	21.3 53.3 N	153.4 E	491	5.2	54.76	-0.49	323.43	7.28	322.61	7.23	322.43	7.13	# 74
731130	0809	55.4 15.2 S	167.4 E	124	6.0	50.56	1.95	229.42	7.60	228.47	7.60	230.45	7.61	# 96
740102	1042	29.9 22.5 S	68.4 W	105	6.4	94.84	1.48	112.11	4.55	109.89	4.71	111.84	4.89	# 53
740105	0833	50.7 12.3 S	76.4 W	98	6.3	84.30	1.45	105.25	5.01	104.39	4.79			# 52
740110	0851	13.3 14.4 S	166.9 E	34	6.7	50.11	0.36	230.65	7.63	229.69	7.79	229.30	8.11	# 97
740131	2330	5.3 7.5 S	155.9 E	34	6.0	54.92	-0.51	245.54	7.27	245.18	6.96	244.73	6.95	# 87
740222	0036	53.8 33.2 N	136.9 E	385	6.0	63.29	0.11	297.79	6.57	299.08	6.74	298.12	6.13	# 61

TABLE 2.1 (continued)

DATE	ORIGIN TIME		LOCATION		DEPTH M		DELTA RES		AZM P		AZM P		AZM P		NUMBER			
									J-B TABLE		LEAST SQUARES		PLANE WAVES					
										HAWAII ONLY		ALL ISLANDS						
740306	0140	26.4	12.3	N	86.4	W	110	5.8	66.85	0.99	84.75	6.31	79.11	6.00	#	49		
740318	1056	12.4	14.9	S	172.8	W	27	5.9	38.14	0.75	207.83	8.35	206.87	8.57	#	200		
740504	1247	28.3	13.9	S	172.6	E	602	5.5	50.33	-0.70	225.98	7.62	224.70	7.70	226.16	7.78	#	95
740513	0211	29.7	10.1	N	124.1	E	592	5.3	80.25	1.81	276.53	5.31	271.45	5.40	#	38		
740516	2000	01.5	27.2	N	140.1	E	471	5.3	62.06	1.60	290.59	6.69	289.88	6.91	#	86		
740517	2306	44.1	26.1	S	179.5	E	494	5.3	54.59	-0.21	209.21	7.30	208.78	7.37	#	94		
740713	0118	22.8	7.7	N	77.7	W	12	6.4	75.84	1.86	86.71	5.68	85.73	5.39	87.32	5.65	#	37
740718	1104	43.2	15.2	S	173.6	W	33	5.9	38.80	1.31	208.72	8.32	208.76	8.48	#	93		
740823	0450	34.6	7.5	S	127.5	E	136	5.8	80.50	1.23	258.57	5.30	253.66	5.60	253.49	5.77	#	85
740829	0959	55.5	73.4	N	55.1	E	1	6.4	84.61	1.41	351.59	4.98	355.21	5.01	354.48	5.18	#	36
740921	0555	57.6	44.4	S	168.1	E	49	5.8	71.83	0.41	206.72	5.95	209.45	6.16	#	35		
740927	0310	07.9	33.6	N	141.1	E	46	5.8	57.84	0.53	297.97	7.02	297.50	7.16	296.33	7.19	#	84
741008	0950	58.1	17.3	N	62.0	W	47	6.6	87.64	1.20	72.68	4.82	73.75	4.75	75.43	4.95	#	34
741011	1411	56.1	23.2	N	121.4	E	44	5.3	76.60	1.41	290.07	5.63	288.90	5.25	#	33		
741025	0005	34.1	15.8	N	93.1	W	120	5.5	59.64	-2.32	82.86	6.88	79.73	6.65	#	32		
741015	2127	42.5	30.7	S	178.0	W	59	5.7	54.58	-0.03	204.02	7.30	203.89	7.33	#	91		
741102	0459	56.7	70.8	N	54.1	E	1	6.7	87.56	1.11	350.62	4.82	355.90	4.67	353.84	4.95	#	31
741111	0629	21.1	23.9	S	177.6	W	196	5.6	49.41	-1.17	207.63	7.68	206.29	7.73	#	90		
741202	0151	37.0	11.0	S	166.4	E	153	5.2	48.97	0.81	234.43	7.72	233.98	7.58	#	98		
741203	0306	35.2	5.0	S	129.8	E	33	6.2	77.40	0.87	260.08	5.57	256.19	5.93	255.82	5.94	#	83
741205	0316	05.7	18.6	N	145.5	E	185	5.0	56.52	0.57	279.62	7.14	272.80	7.27	#	30		
741205	1157	31.3	7.7	S	74.5	W	162	6.0	84.54	1.15	100.32	5.00	98.39	4.55	#	29		
741214	2007	10.0	2.6	N	128.4	E	218	5.5	77.53	0.80	267.84	5.56	265.13	6.05	263.80	5.92	#	82
741220	1638	55.6	49.8	N	149.7	E	416	5.0	55.04	-0.83	318.31	7.26	318.22	7.32	#	28		
741224	0210	25.4	14.3	N	90.1	W	155	5.4	62.84	1.14	83.70	6.62	79.83	6.50	#	27		
741230	0333	16.6	62.0	N	149.7	W	62	5.1	42.73	0.02	3.94	8.17	5.67	8.55	#	26		
750202	0843	39.1	53.1	N	173.5	E	10	6.1	41.49	0.90	331.82	8.22	331.61	8.21	329.79	8.04	#	1
750207	0451	44.0	7.3	S	149.5	E	33	6.3	60.41	-0.93	249.33	6.82	247.06	6.87	246.39	6.93	#	81
750222	0836	07.4	51.4	N	179.4	W	48	6.3	37.18	-0.21	334.94	8.39	335.02	8.38	333.96	8.32	#	3
750222	2204	37.7	24.9	S	179.1	W	375	6.2	52.14	-0.31	208.59	7.49	209.48	7.19	#	5		
750223	0258	41.0	8.0	N	124.1	E	623	5.6	81.00	2.51	274.47	5.25	274.96	5.52	271.91	5.05	#	4
750305	0022	19.7	2.4	S	126.1	E	33	6.4	79.98	3.61	263.87	5.35	260.31	5.78	259.55	5.90	#	8
750305	1027	09.8	19.5	S	168.9	E	55	5.6	52.36	0.28	224.14	7.48	224.22	7.65	#	7		

TABLE 2.1 (continued)

DATE	ORIGIN	TIME	LOCATION	DEPTH	M	DELTA	RES	AZM	P	AZM	P	AZM	P	NUMBER
								J-B	TABLE	LEAST SQUARES	PLANE WAVES	HAWAII ONLY	ALL ISLANDS	
750313	1526	42.5	29.9 S	71.3 W	4	6.2	94.30	1.67	119.97	4.58	113.87	4.93		# 9
750313	1845	29.5	21.8 S	170.5 E	85	6.1	53.21	0.67	220.83	7.42	221.73	7.52	220.96	7.38 # 10
750322	1854	26.7	54.5 N	161.6 E	33	5.2	47.89	0.91	327.53	7.79	325.76	7.66		# 25
750323	0732	36.5	22.7 N	122.8 E	21	6.2	75.47	1.54	289.23	5.71	292.47	6.28		# 24
750328	0231	05.7	42.1 N	112.5 W	5	6.1	42.55	2.01	48.35	8.16	50.15	9.09		# 22
750411	0047	15.3	54.1 N	163.2 W	20	5.5	35.10	-0.28	351.95	8.53	354.37	9.10		# 23
750416	0127	18.7	71.5 N	10.4 W	13	6.1	85.88	1.17	10.57	4.91	16.75	4.97		# 18
750420	1140	39.9	36.4 S	98.8 W	33	6.0	76.97	-0.06	136.36	5.60	136.40	5.01		# 19
750514	1400	00.4	37.2 N	116.5 W	1	6.0	37.69	-0.53	54.10	8.37	55.89	9.06		# 113
750618	1632	29.7	13.7 S	167.2 E	208	5.5	50.57	0.04	231.03	7.60	229.71	7.73	230.56	7.66 # 14
750619	1300	00.1	37.4 N	116.3 W	1	6.1	37.91	-0.89	53.87	8.35	55.45	8.95		# 15
750626	0952	19.9	31.9 N	138.1 E	389	5.4	62.64	1.72	296.22	6.63	296.98	6.75		# 16
750626	1230	00.2	37.3 N	116.4 W	1	6.2	37.80	-0.48	53.99	8.36	54.69	9.27		# 112
750708	2246	19.6	32.8 N	142.2 E	51	5.8	56.89	-0.30	296.98	7.10	295.54	7.05		# 17
750710	1829	20.6	7.3 N	126.8 E	33	7.2	76.57	2.18	272.22	5.61	270.39	6.01		# 99
750721	0238	57.1	6.9 S	155.4 E	58	6.2	55.27	-0.29	246.47	7.25	246.68	7.12	246.37	7.12 # 104
750724	1901	42.6	23.5 S	179.8 W	579	5.6	53.08	-1.01	210.23	7.43	210.31	7.49		# 102
750725	1040	25.0	55.1 N	160.4 W	17	5.8	35.54	-0.59	355.08	8.48	357.37	8.78		# 101
750728	0844	55.3	6.9 S	154.5 E	38	5.7	55.84	-1.95	247.00	7.19	245.70	7.05		# 100
750801	2020	12.9	39.4 N	121.5 W	8	5.7	34.94	0.35	48.41	8.53	52.02	9.02		# 108
750802	1018	17.9	53.4 N	161.5 W	33	6.2	34.25	0.94	353.51	8.58	355.45	8.79		# 107
750807	1328	24.2	3.8 S	139.7 E	65	5.6	68.06	0.42	257.38	6.23	254.10	6.53		# 103
750807	2012	15.2	22.9 S	178.9 E	626	5.4	53.87	-1.28	212.01	7.37	211.77	7.39		# 105
750810	1025	43.3	22.6 S	66.6 W	166	6.2	96.64	1.26	111.66	4.55	110.13	4.56		# 106
750812	1421	04.7	32.0 N	137.7 E	391	5.7	62.88	0.02	296.37	6.61	296.55	6.80	295.09	6.64 # 109
750815	0728	18.9	54.9 N	167.8 E	4	6.0	44.69	-0.32	330.74	8.01	332.03	7.78		# 110
751021	1159	57.3	73.4 N	55.1 E	1	6.5	84.61	1.90	351.58	4.98	355.52	4.99		# 111
751226	1556	38.7	16.3 S	172.5 W	33	6.4	39.31	0.06	206.51	8.31	207.83	8.50	206.69	8.48 # 114
760114	1556	34.9	29.2 S	177.9 W	33	6.5	53.04		204.80	7.43	204.64	7.29		# 115
760114	1647	33.5	28.4 S	177.7 W	33	6.5	52.19	1.48	205.01	7.48	204.98	7.45	206.54	7.57 # 116
760123	0545	30.5	7.5 S	119.9 E	614	6.4	90.03	2.13	261.21	4.69	256.87	4.79		# 117
760203	1227	30.1	25.1 S	179.7 E	477	5.8	53.75	0.09	209.69	7.38	209.69	7.39	209.86	7.38 # 118
760204	0901	43.3	15.3 N	89.08 W	5	7.5	62.98	-0.88	82.34	6.61	76.86	6.55		# 119

TABLE 2.1 (continued)

DATE	ORIGIN TIME	LOCATION	DEPTH	M	DELTA	RES	AZM P		AZM P		AZM P		NUMBER
							J-B TABLE	LEAST SQUARES	HAWAII ONLY	PLANE WAVES	ALL ISLANDS		
760204	1440	0.2 37.1 N 116.0 W	1	5.7	38.09	-0.79	54.44	8.35	57.55	8.80	56.08	9.03	# 120
760215	0154	23.1 13.0 N 125.8 E	33	6.1	75.42	1.61	278.83	5.73	276.72	5.88			# 121
760304	0250	0.5 14.7 S 167.1 E	90	6.4	50.22	0.39	230.14	7.63	229.15	7.84	229.25	7.84	# 122
760310	0905	1.1 16.8 N 61.1 W	77	5.9	88.80	2.60	72.87	4.76	72.39	4.31			# 123
760314	1230	0.2 37.3 N 116.5 W	2	6.3	37.73	-0.40	53.94	8.36	55.48	9.05			# 124
760324	0446	4.4 29.9 S 177.9 W	33	6.4	53.65	-1.01	204.40	7.39	204.63	7.49	204.11	7.44	# 126
760407	0710	15.8 17.6 N 145.5 E	217	5.5	56.75	0.15	278.48	7.12	275.48	7.21			# 127
760505	0452	51.0 29.9 S 177.8 W	35	6.2	53.62	-0.77	204.31	7.39	204.51	7.34			# 128
760521	0411	15.2 3.7 N 125.1 E	173	5.9	79.33	1.02	270.02	5.40	268.78	5.70			# 129
760603	1644	38.7 5.2 S 153.4 E	88	6.1	56.44	-0.26	249.43	7.15	248.20	7.00			# 130
760605	0820	7.2 10.1 S 161.0 E	61	6.2	52.15	-0.85	239.48	7.49	238.96	7.46	236.79	7.46	# 131
760629	1830	7.5 33.8 S 177.9 W	33	6.1	57.12	-0.93	202.29	7.08	201.41	7.08			# 132

TABLE 2.1 (concluded)

TABLE 2.2. Telemetered Seismograph Stations on the Island of Hawaii

STATION	LATITUDE	LONGITUDE	ELEV	J-B RESIDUAL *
AHU	19N22.40	155W15.90	1070	-0.11
AIN	19N22.50	155W27.62	1524	0.25
CAC	19N29.29	155W55.09	323	-0.12
CPK	19N23.70	155W19.70	1038	-0.14
DES	19N20.20	155W23.30	815	-0.12
ESR	19N24.68	155W14.33	1177	-0.14
HLP	19N17.96	155W18.63	707	0.12
HPU	19N46.85	155W27.50	3396	0.25
HSS	19N36.31	155W29.13	2445	0.47
HUA	19N41.25	155W50.32	2189	0.18
CAA	19N15.98	155W52.28	524	0.09
KAE	19N17.35	155W 7.95	37	0.13
KHU	19N14.90	155W37.10	1939	0.08
KII	19N30.56	155W45.90	1841	0.47
KKU	19N53.39	155W20.58	1863	0.21
KOH	20N 7.69	155W46.77	1166	-0.13
KPN	19N20.10	155W17.40	924	-0.04
KPR	19N16.40	155W26.70	610	0.04
LUA	19N24.55	155W 4.25	622	-0.33
MLO	19N29.80	155W23.30	2010	0.19
MLX	19N27.60	155W20.70	1475	0.17
MOK	19N29.28	155W35.98	4104	0.23
MPR	19N22.07	155W 9.85	881	-0.15
MTV	19N30.25	155W 3.75	409	0.08
NAG	19N42.12	155W 1.72	18	0.01
NPT	19N24.90	155W17.00	1115	-0.25
OTL	19N23.38	155W16.94	1038	-0.20
PAU	19N22.62	155W13.10	994	-0.17
PHH	19N22.45	155W12.66	988	-0.12
PHO	19N28.90	154W53.40	215	-0.33
POL	19N17.02	155W13.47	169	0.05
PPL	19N 9.50	155W27.87	35	-0.10
RIM	19N23.90	155W16.60	1128	-0.12
SCA	19N28.20	155W35.08	4048	0.22
SPT	18N58.91	155W39.92	244	-0.31
SWR	19N27.26	155W36.30	4048	0.15
TAN	19N27.79	154W58.51	315	-0.28
UWE	19N25.40	155W17.60	1240	-0.16
WHA	19N19.90	155W 2.92	29	0.01
WLG	19N25.49	155W15.69	1067	-0.13
WPT	19N24.70	155W17.50	1115	-0.14

* UNCORRECTED FOR ELEVATION

TABLE 2.3. Mean Crustal Velocities
 Implied by Measured Vertical Phase Velocities
 for Several Slowness Values.

V_z (km/sec)	Slowness (sec/deg)		
	8.4 ($\Delta=38^\circ$)	7.0 ($\Delta=58^\circ$)	5.0 ($\Delta=85^\circ$)
10.0 (all stations)	7.98 (km/sec)	8.46	9.12
7.46 (summit rift zone)	6.50	6.75	7.07
6.65 (non-rift flank)	5.94	6.13	6.37

TABLE 2.4. Regional Seismograph Station Data

Name	Latitude	Longitude	Elevation (m)	\bar{R}_j (sec)
HLK	20°N46.0'	156°W15.0'	2090	.69
HON	21°N19.3'	158°W 0.5'	24	.52
KIP	21°N25.4'	158°W 0.9'	70	.11
KPH	21°N34.6'	158°W16.5'	0	.04
MOK	21°N27.4'	157°W44.2'	0	-.22
OPA	21°N41.4'	158°W 0.7'	150	.24

TABLE 2.5. Focal Parameters for Hawaiian Earthquakes Recorded at Teleseismic Distances

Honomu Earthquake

Origin time: 26 April 1973, 20:26:30.8

Epicenter: 19°N54.2', 155°W 7.8'

Focal Depth: 46.0 km

Magnitude: $m_b = 6.0$

Source: P.L. Ward, written comm., 1976

Kalapana Earthquake (foreshock)

Origin time: 29 November 1975, 13:35:40.5

Epicenter: 19°N22.2', 155°W 3.0'

Focal Depth: 8.5 km

Magnitude: $m_b = 5.8$

Source: F. Klein, written comm., 1977

Chapter 2 - Figure Captions

Figure 2.1 Map of Island of Hawaii showing seismograph stations. Elevation contour interval 1 km.

Figure 2.2 Standard total system response for HVO seismograph stations.

Figure 2.3 Seismogram.

Figure 2.4 Epicenters of earthquakes and explosions studied.

Figure 2.5 Absolute event residuals (squares) versus normalized epicentral distance. Smooth curve is a least squares cubic spline fit to data.

Figure 2.6 Systematic travel time residuals for teleseismic P-waves from five recent studies.

Figure 2.7 Comparison between mean earth systematic travel time curve and spline curve determined from Hawaiian travel time observations.

Figure 2.8 Map of Island of Hawaii showing epicenters of two recent earthquakes observed at teleseismic distances.

Figure 2.9 Average station residuals versus station elevation.

Figure 2.10 Map showing distribution of average station residuals. Dashed lines outline principal rift zones.

Figure 2.11 Array mislocation diagram for Hawaii array computed using a simple elevation connection.

Figure 2.12 Correlation diagram for average station residuals to least squares plane waves and J-B tables.

Figure 2.13 Array mislocation diagram for Hawaiian array computed using average station residuals as station corrections.

Figure 2.14 Map of Hawaiian Islands showing regional seismograph stations (triangles) reported in EDR and ISC bulletins. Seismograph stations on the Island of Hawaii (small triangles) are also shown.

Figure 2.15 Array mislocation diagram for all Hawaiian Island stations computed using average station residuals as station corrections.

Figure 2.16 Azimuthal plot of relative travel time residuals versus azimuth to source. Labeled arrows mark azimuths to volcanic summits: H - Hualalai, K - Kilauea, KO - Kohala, MK - Mauna Kea, ML - Mauna Loa.

Figure 2.17 Azimuthal plots of relative residuals versus azimuth to source for selected stations illustrating effect of different data reductions on the relative residuals.

Figure 2.18 Top: Systematic absolute travel time residuals relative to mean earth. Bottom: Upper mantle velocity structures corresponding to systematic residuals illustrated above.

- Figure 2.19 Absolute travel time residuals for a) Honomu earthquake of April 26, 1973 and b) Foreshock of Kalapana earthquake of November 29, 1975. Smooth curve is least squares cubic spline fit to data.
- Figure 2.20 Reduced travel time plot of PKP travel times for Honomu earthquake and Pacific nuclear explosions. Solid curve is PKP travel time curve from Bolt (1968). Dashed curve is PKP travel time curve from Jeffreys and Bullen (1958).
- Figure 2.21 Radial earth model satisfying travel time and slowness observation for NTS explosions. Top: $\tau(p)$ versus p . Middle: Radial velocity model. Bottom: Systematic travel time residual to Herrin model.
- Figure 2.22 Radial earth model satisfying travel time and slowness observations for Halmahera earthquake (#82, Table 2.1). Graphs are same as in Figure 2.21.
- Figure 2.23 Simplified structural models for Hawaiian crust and upper mantle (no vertical exaggeration).
- Figure 2.24 Crustal thickness from seismic refraction studies. Contour interval 2 km. Triangles mark volcanic summits.

Figure 2.1

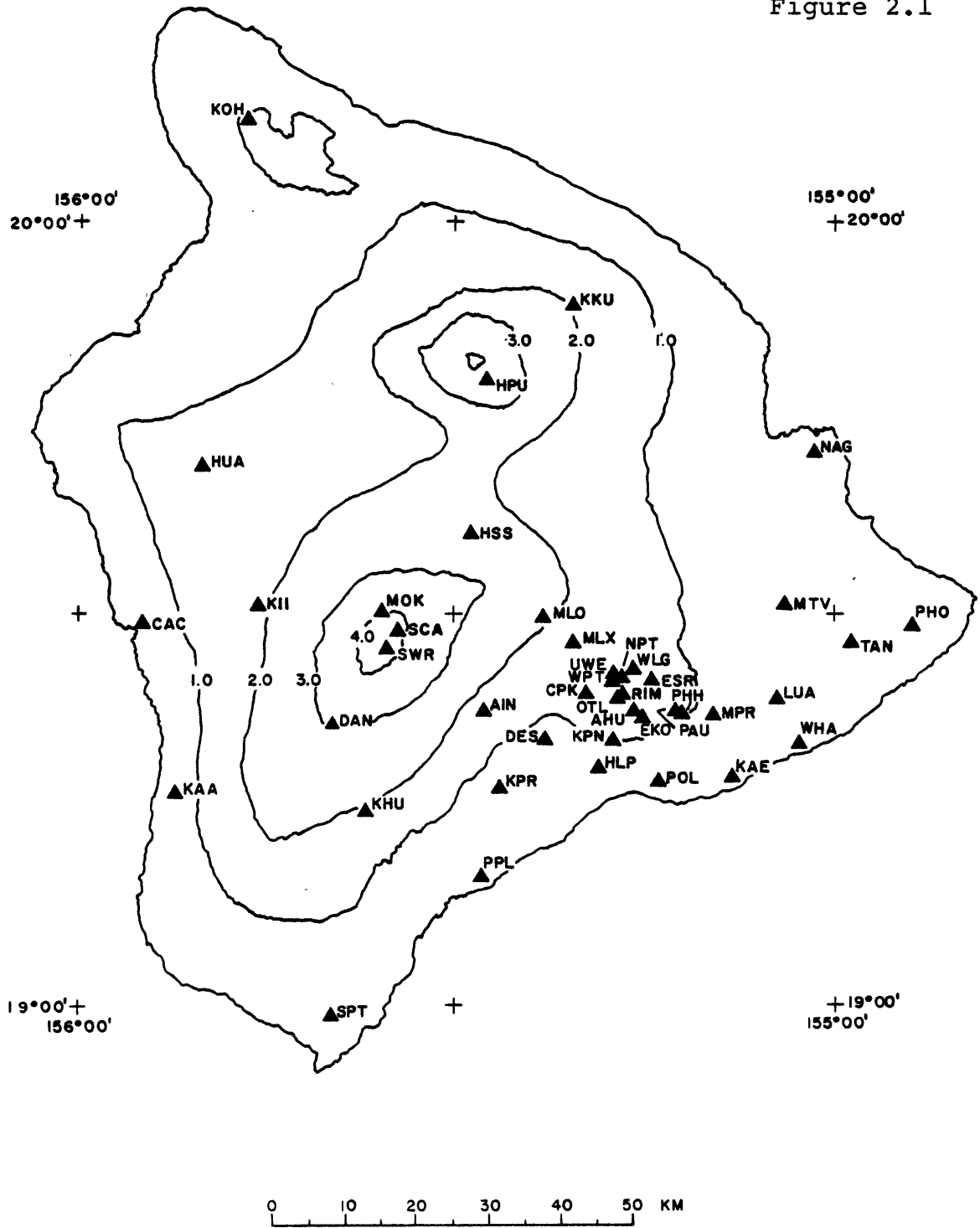
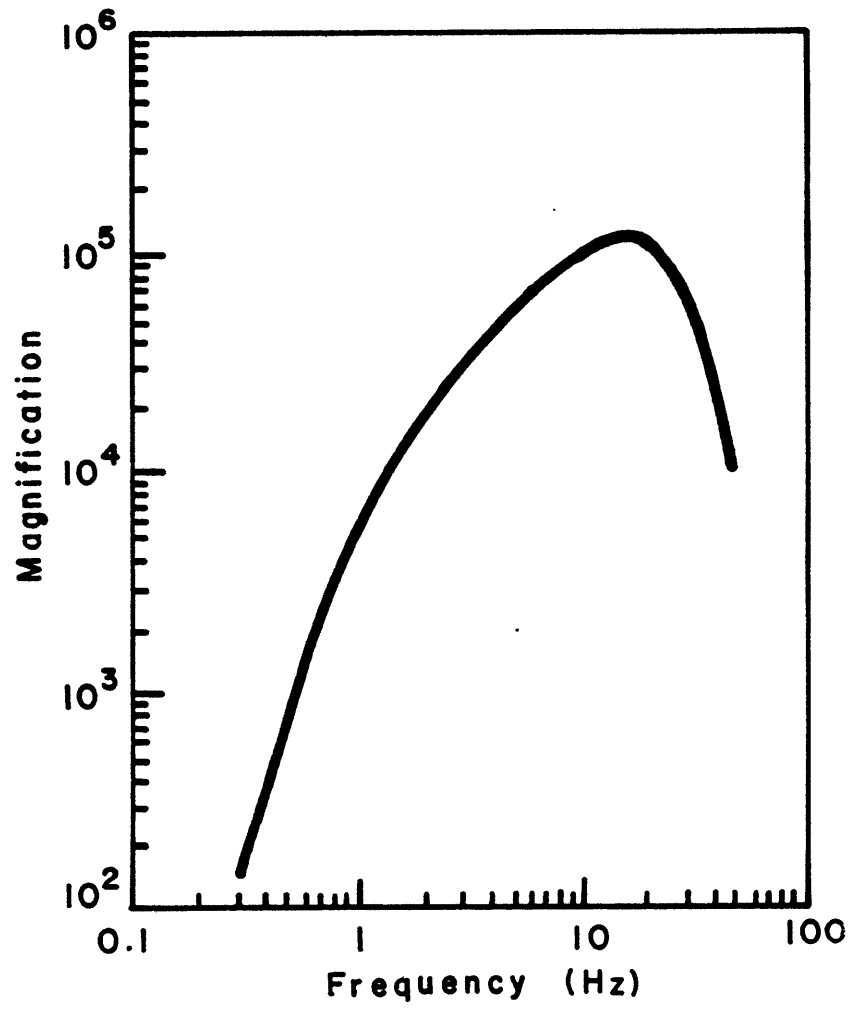
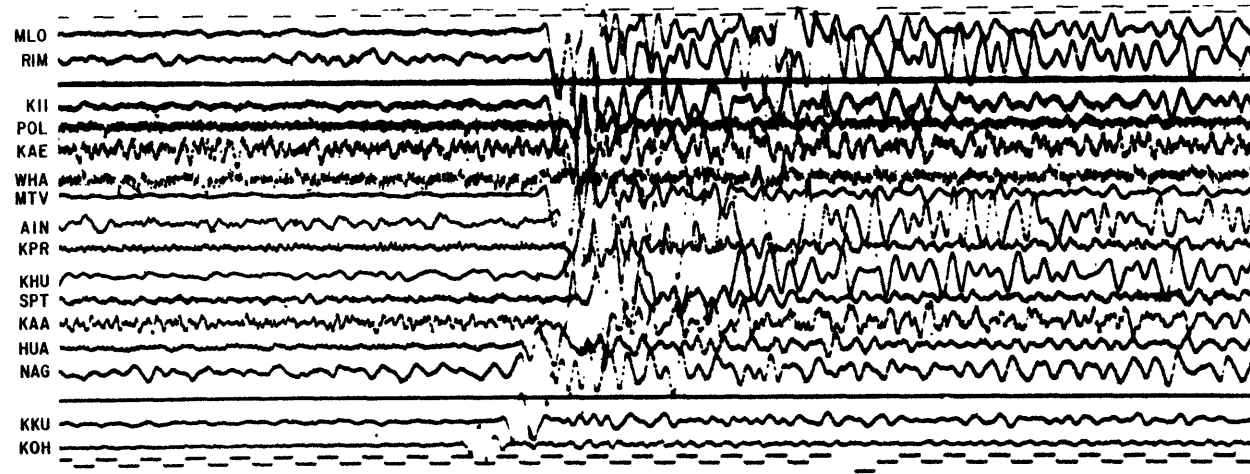
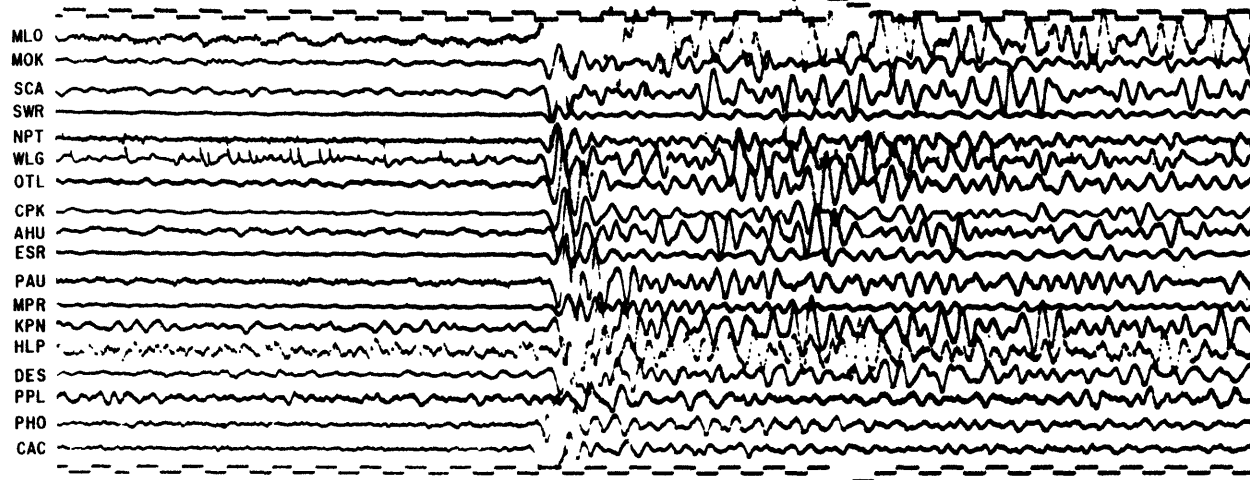


Figure 2.2



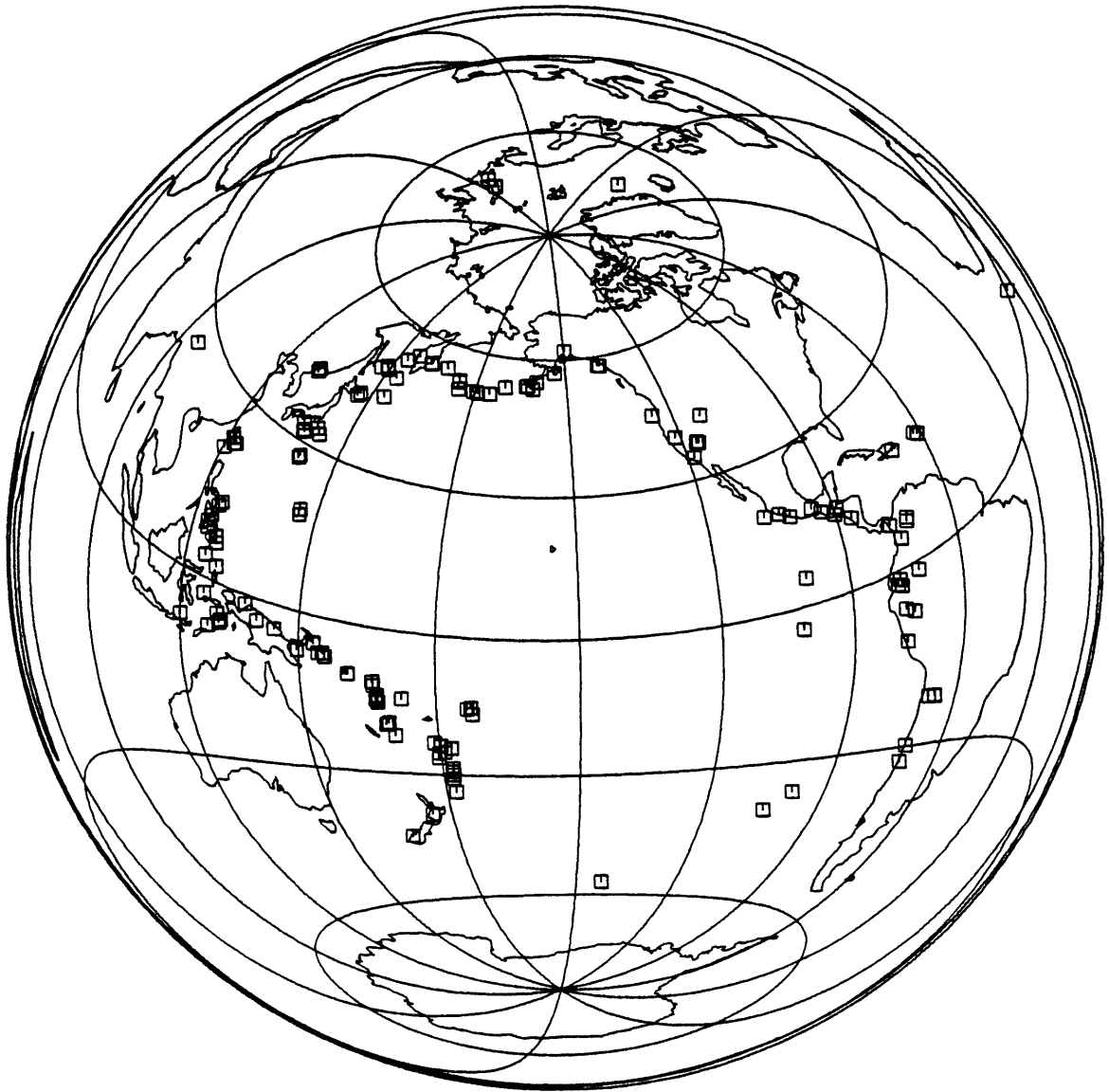
NOVAYA ZEMLYA 751021 1159 $\Delta = 85^\circ$ m = 6.5



10 SECONDS

Figure 2.3

Figure 2.4



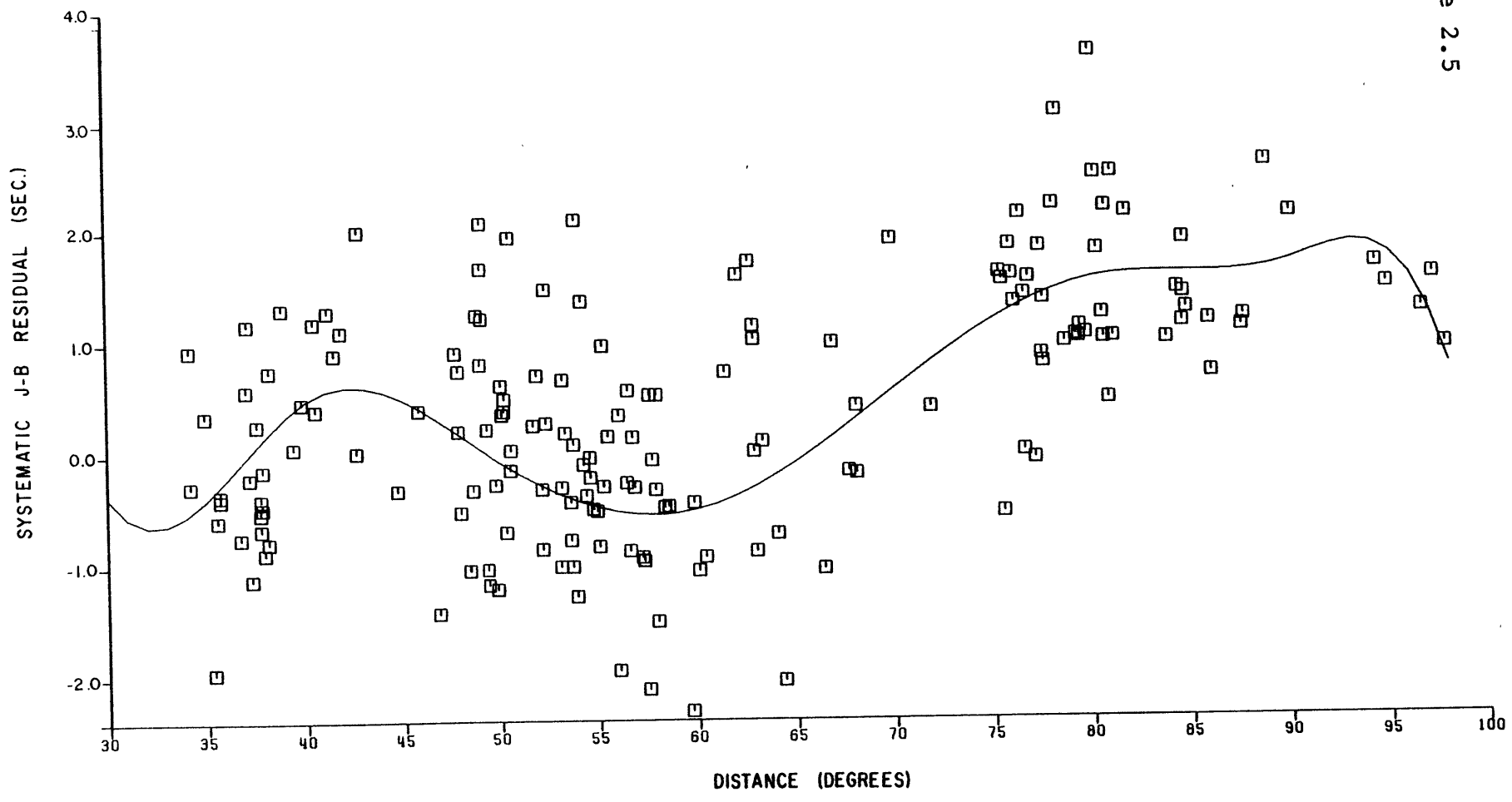


Figure 2.5

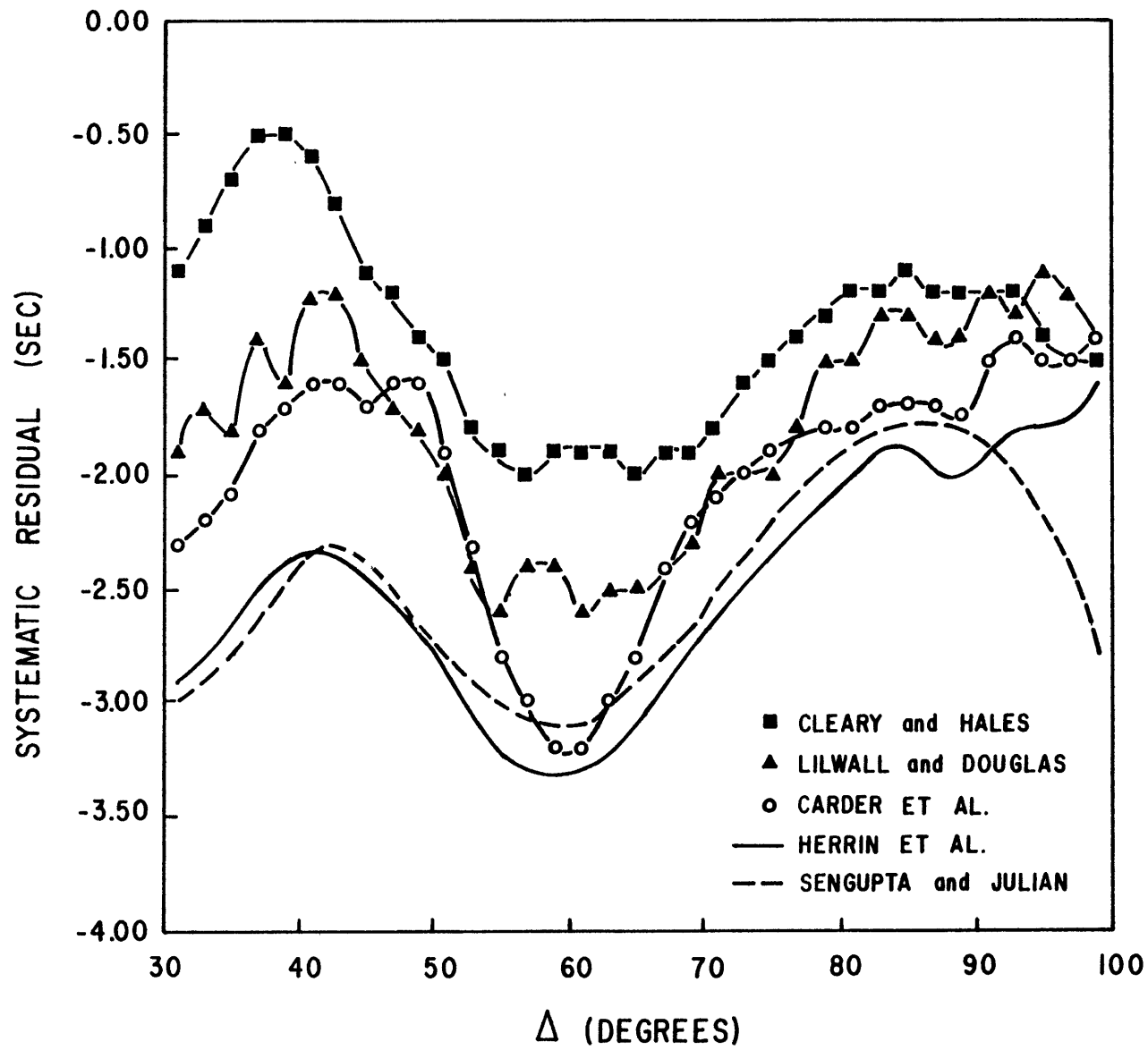


Figure 2.6

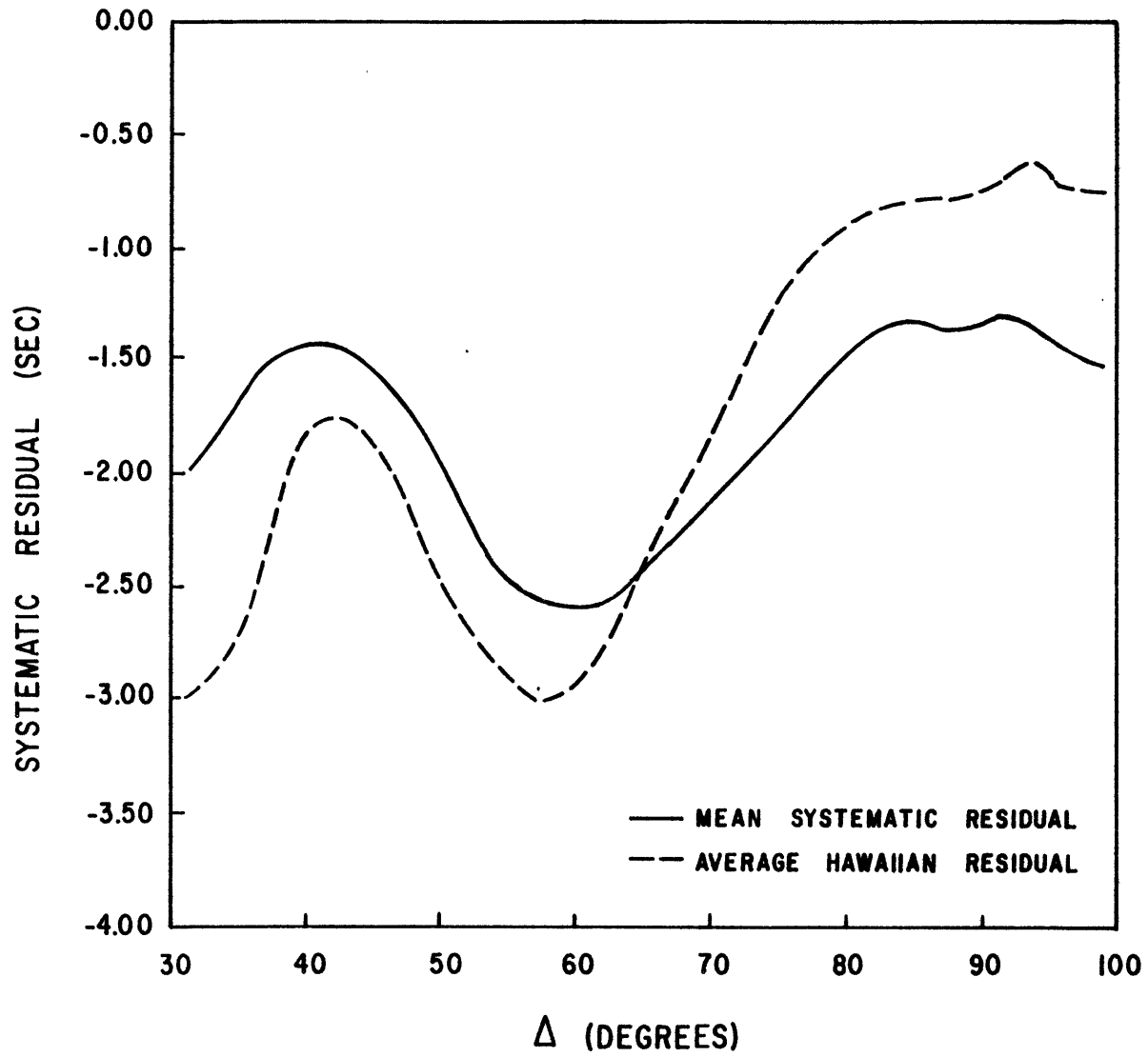
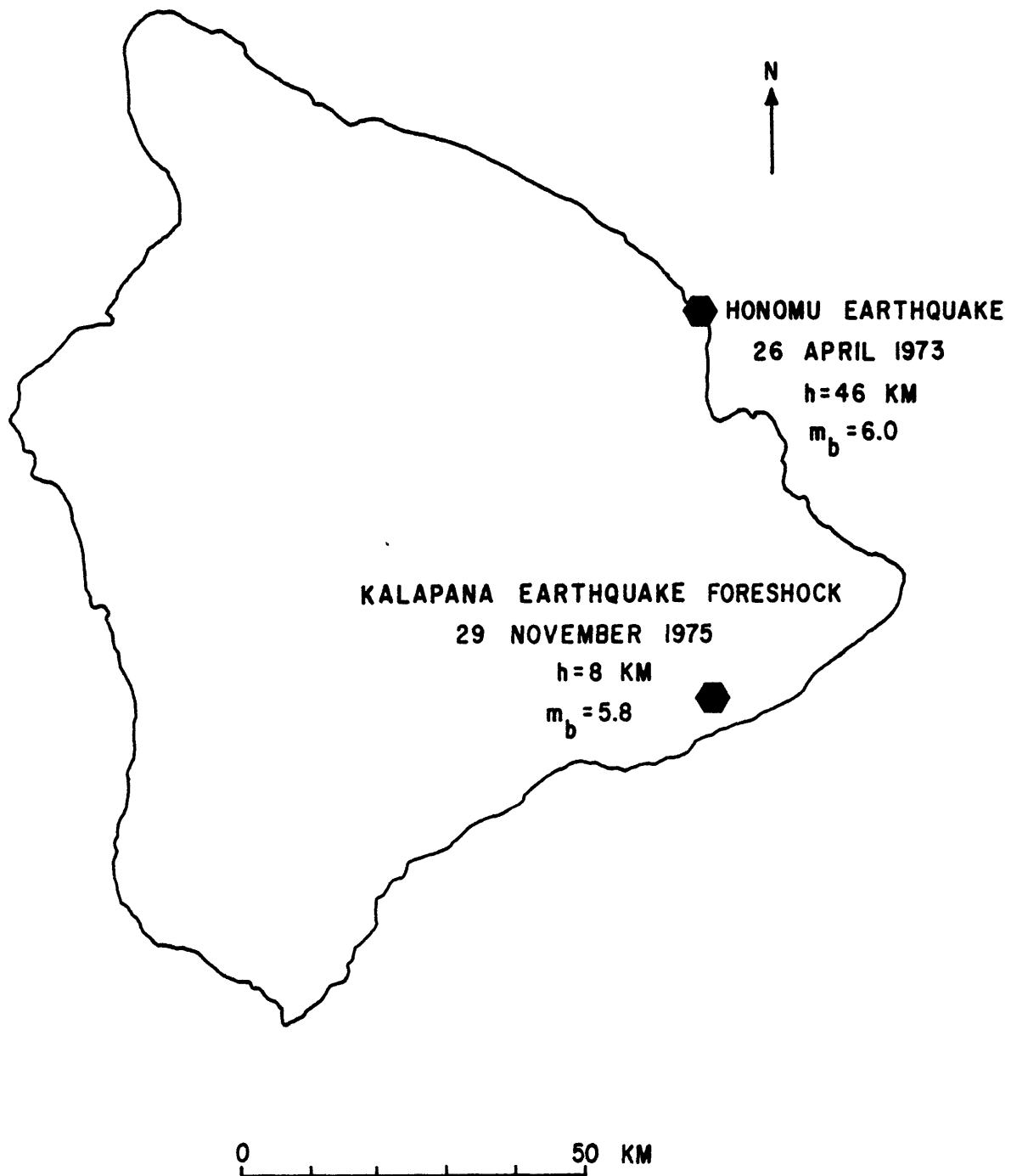


Figure 2.7

Figure 2.3



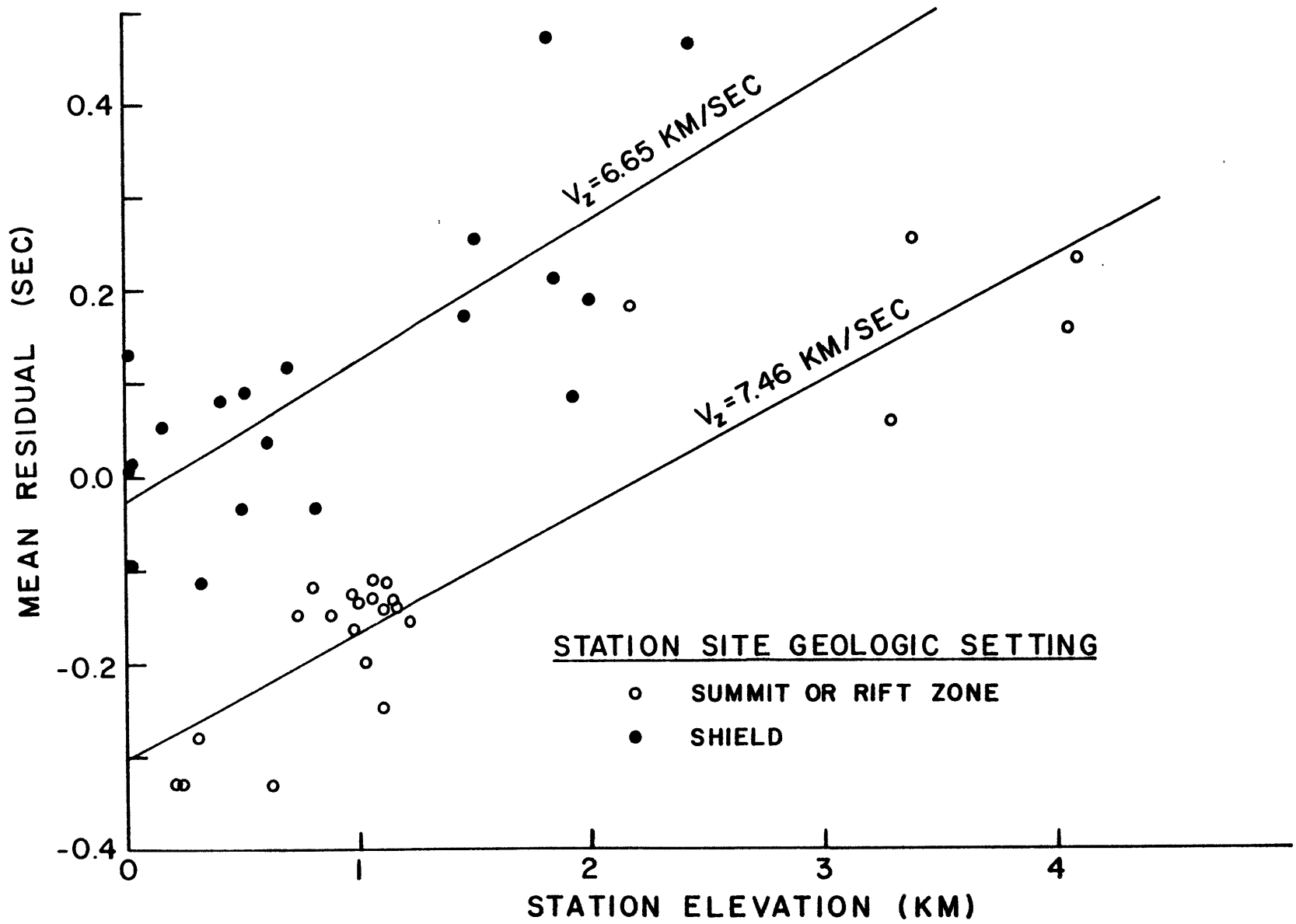
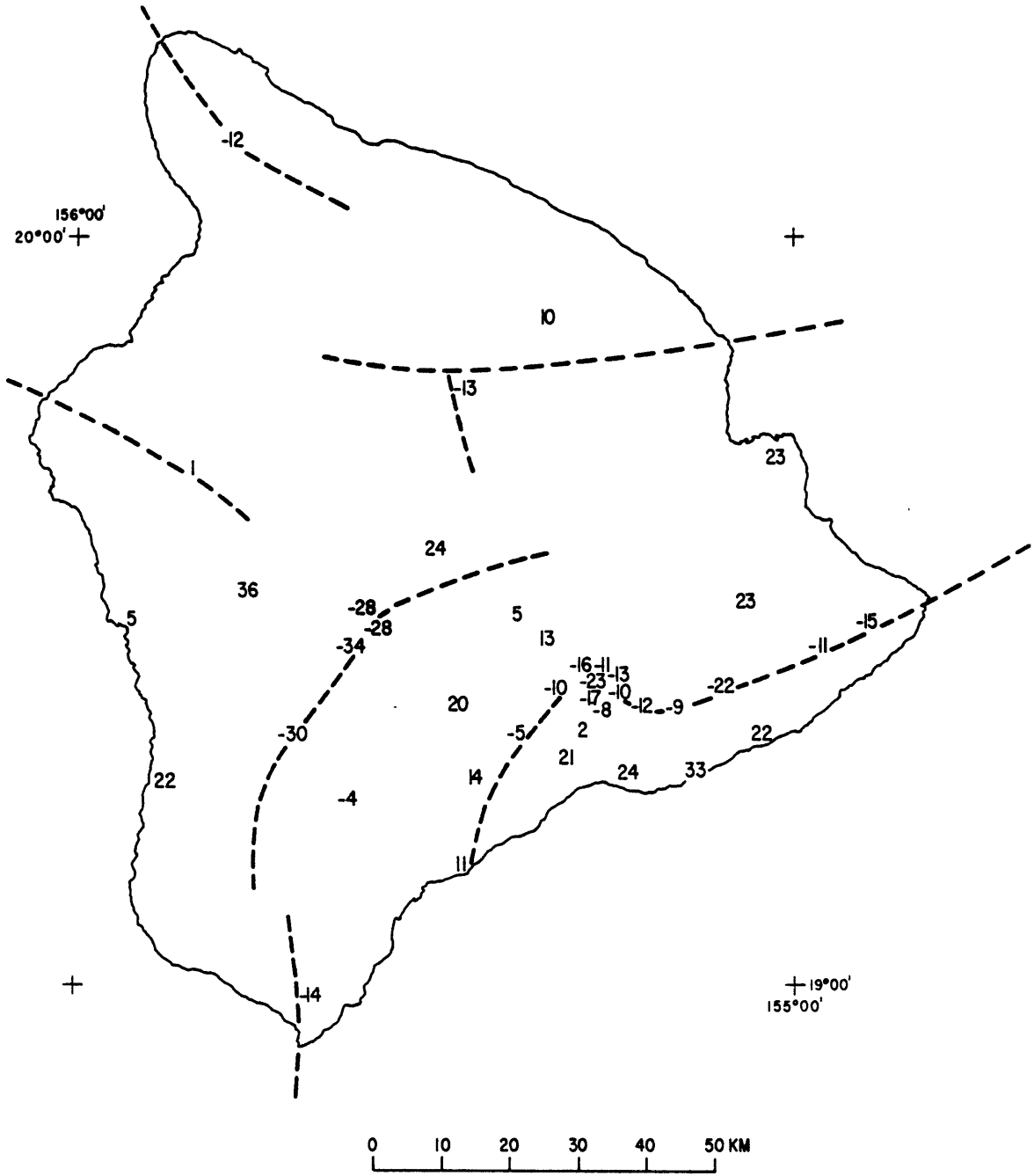


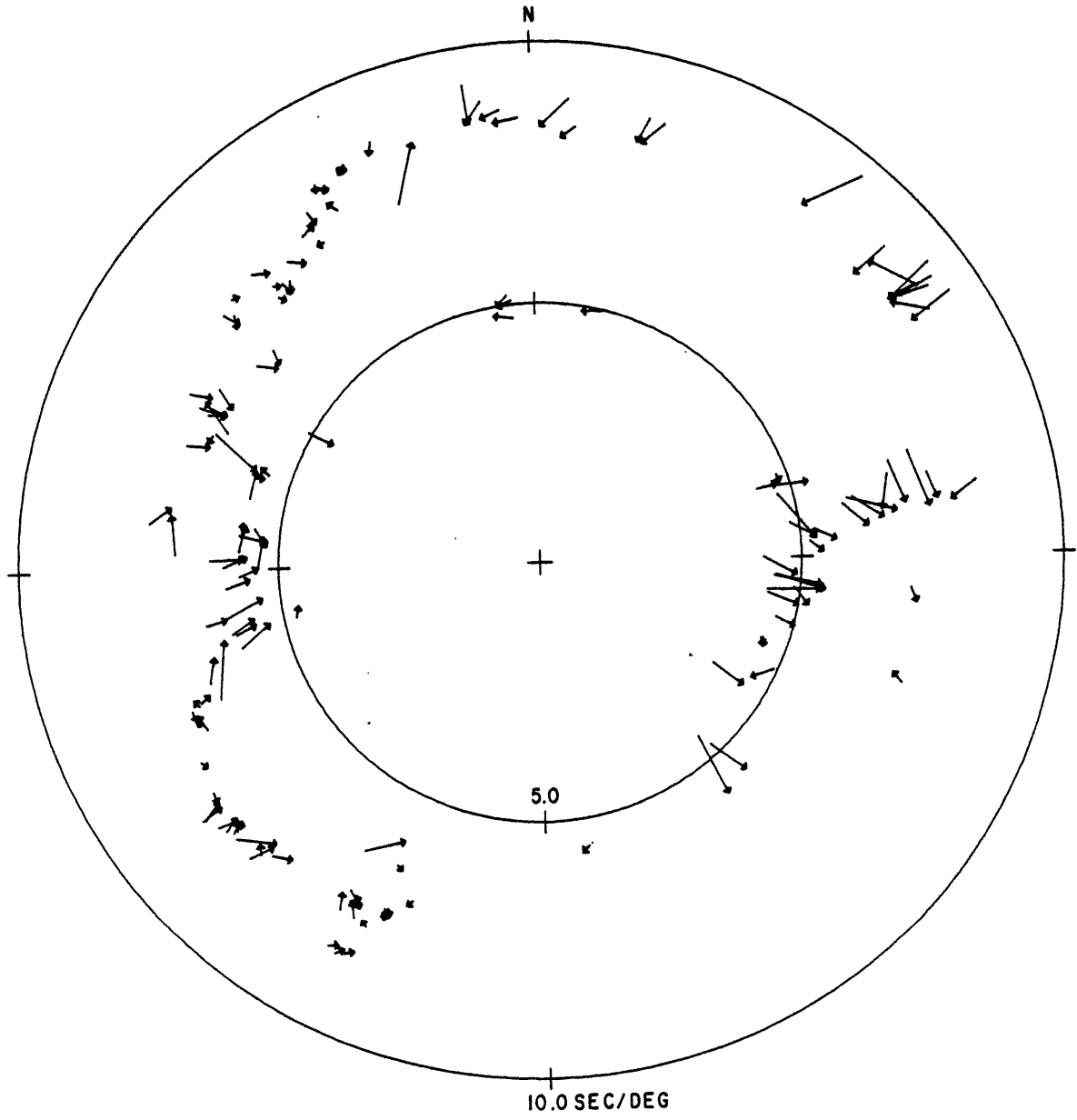
Figure 2.9

Figure 2.10



AVERAGE TRAVEL TIME RESIDUALS TO J-B TABLES
(CORRECTED FOR ELEVATION)

Figure 2.11



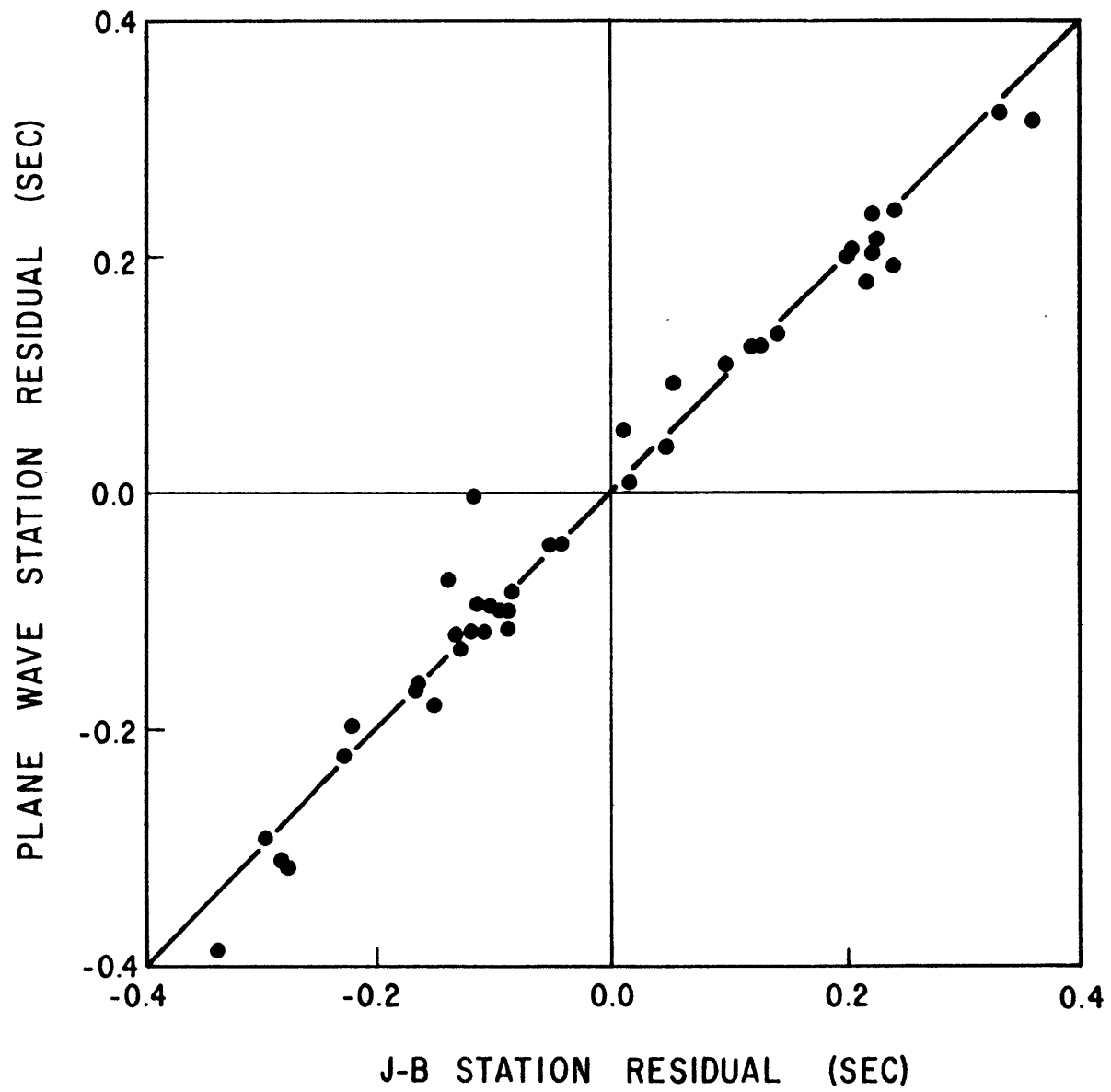
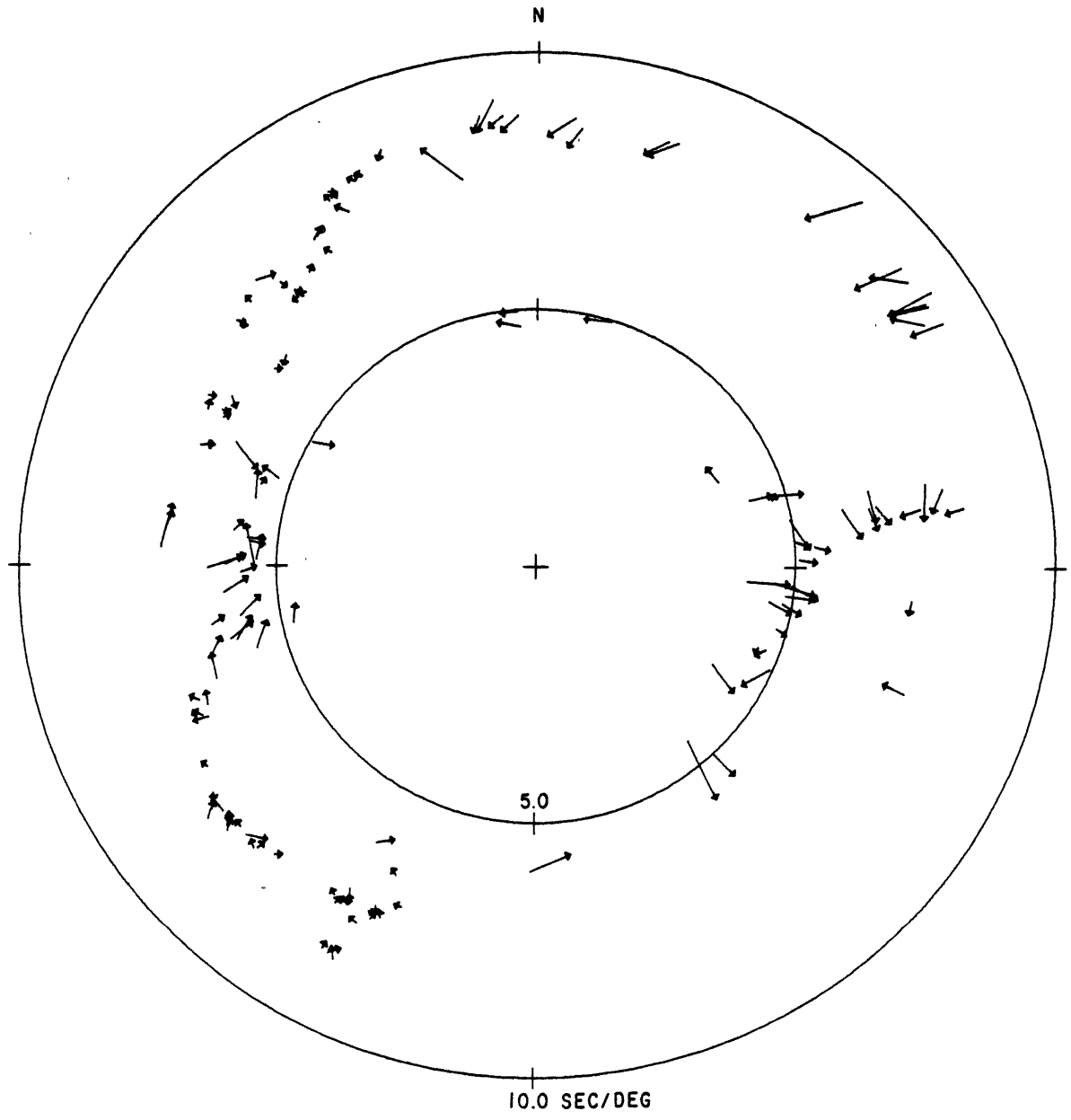


Figure 2.12

Figure 2.13



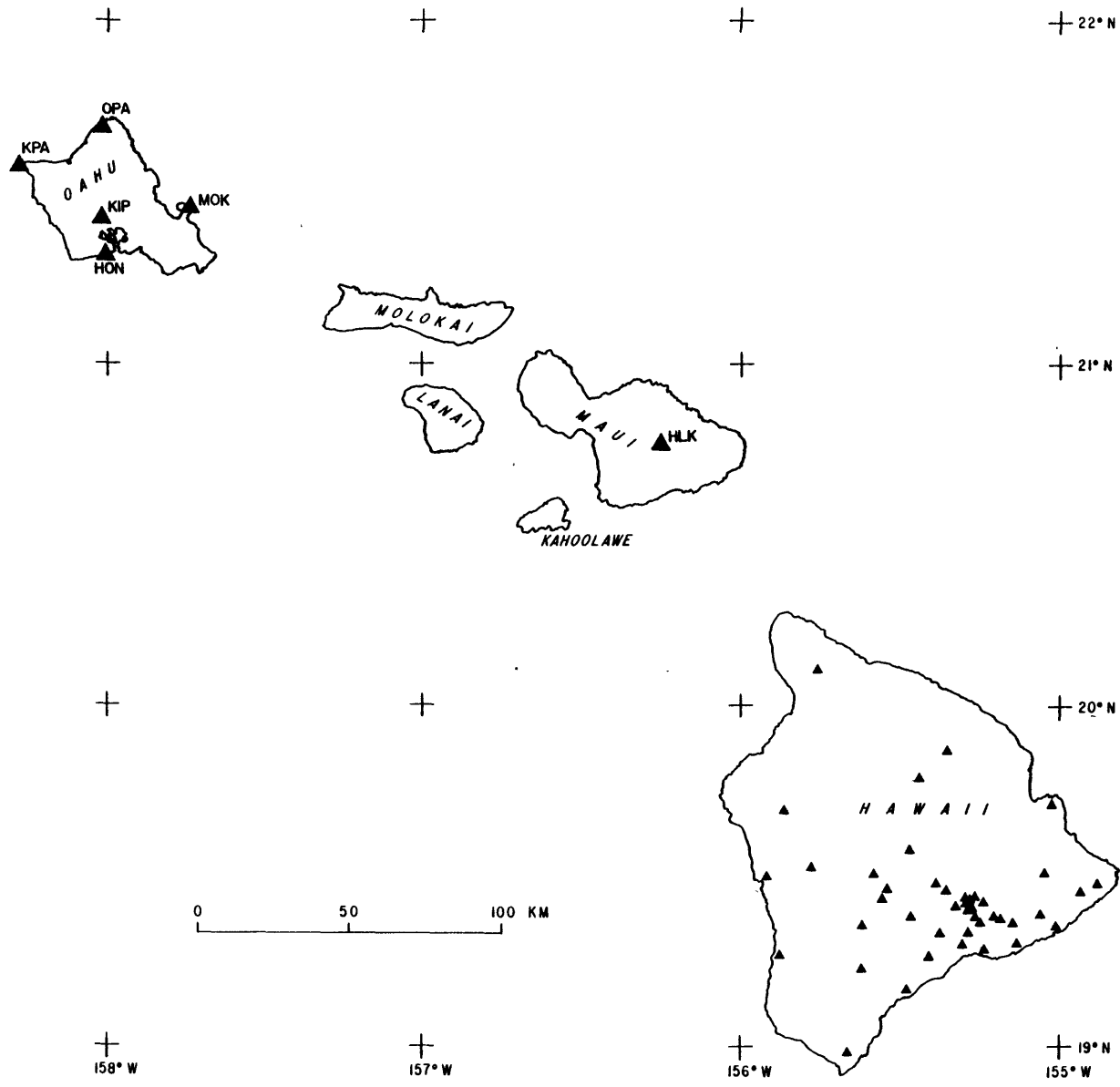


Figure 2.14

Figure 2.15

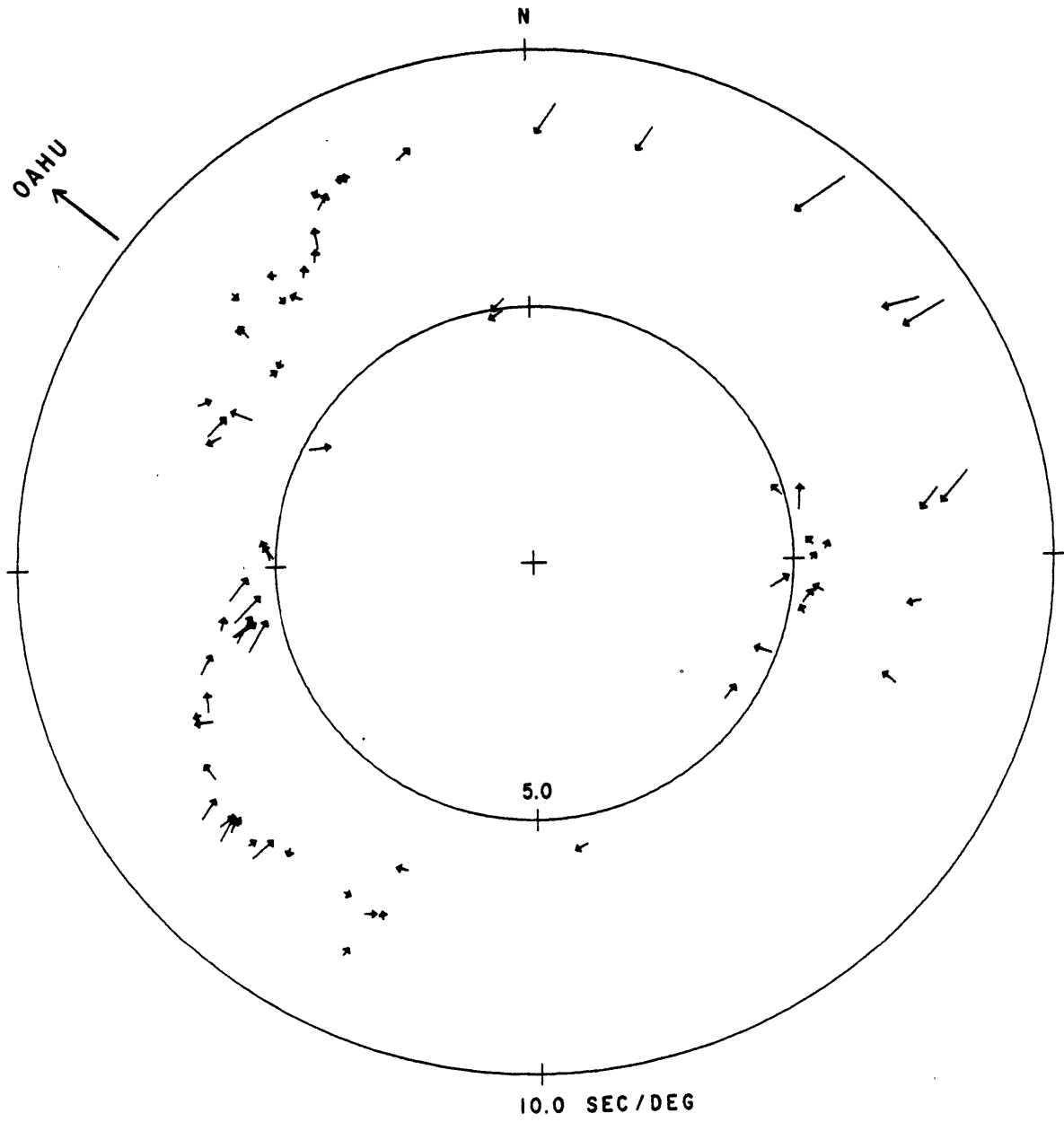
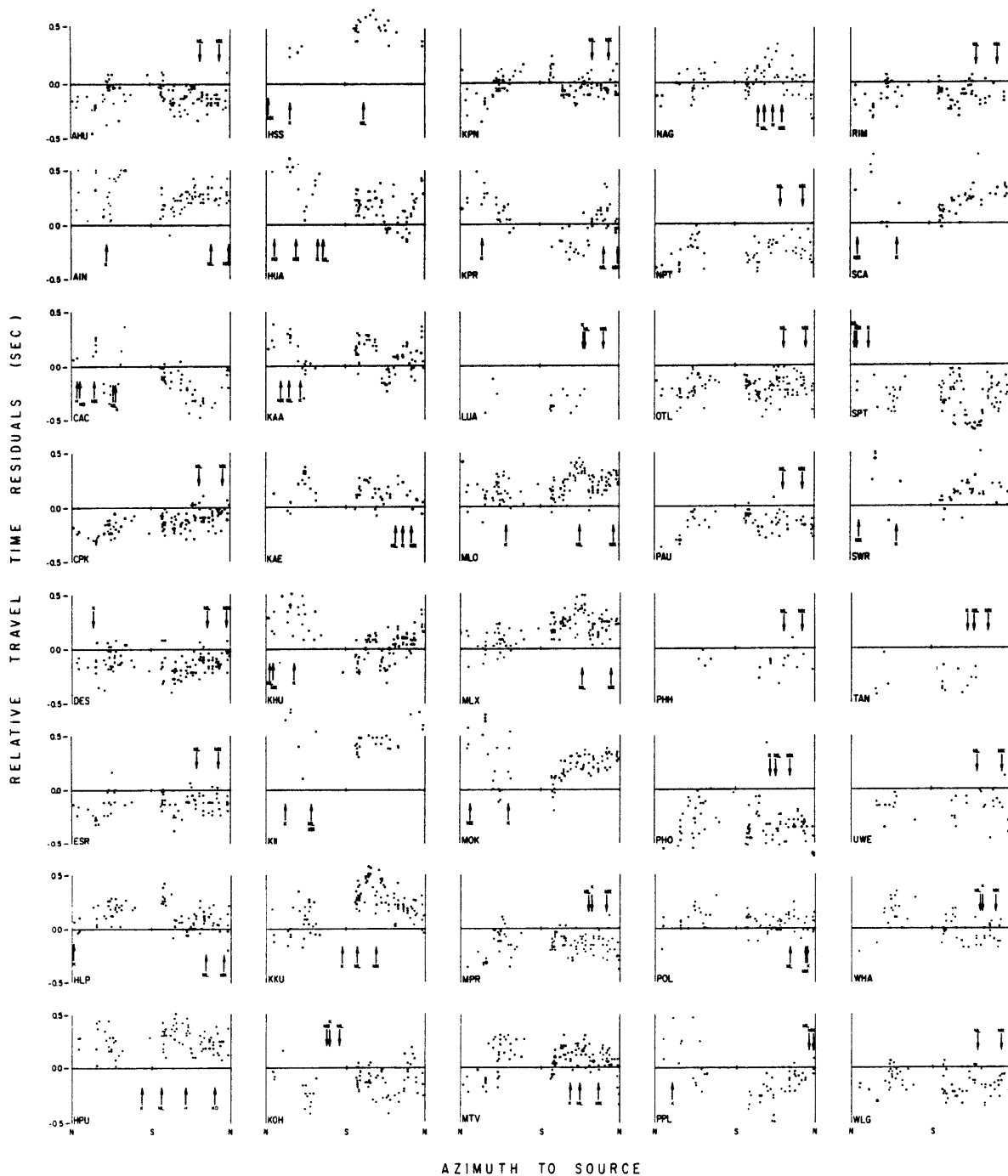


Figure 2.16



RELATIVE TRAVEL TIME RESIDUALS (SEC.)

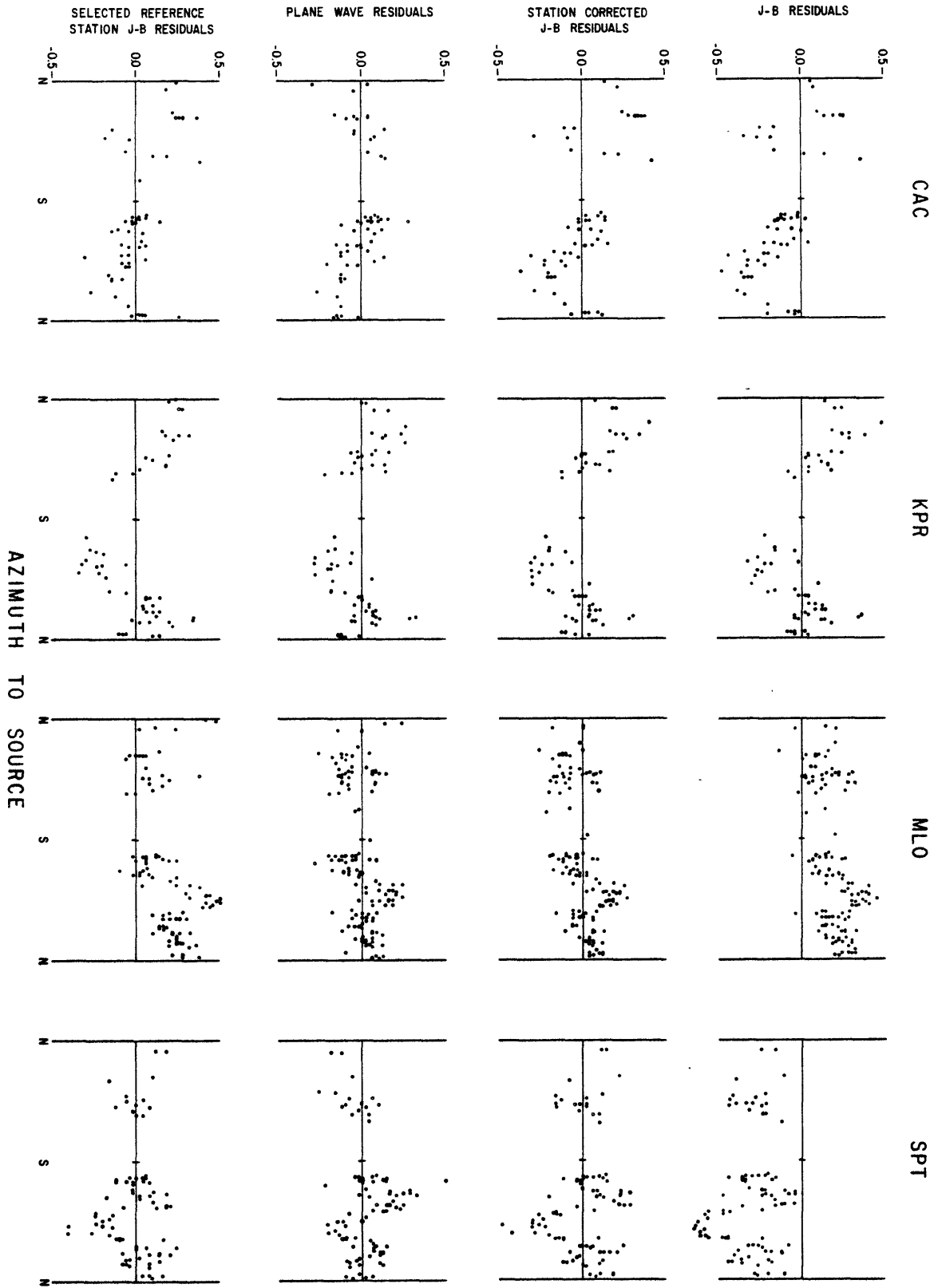
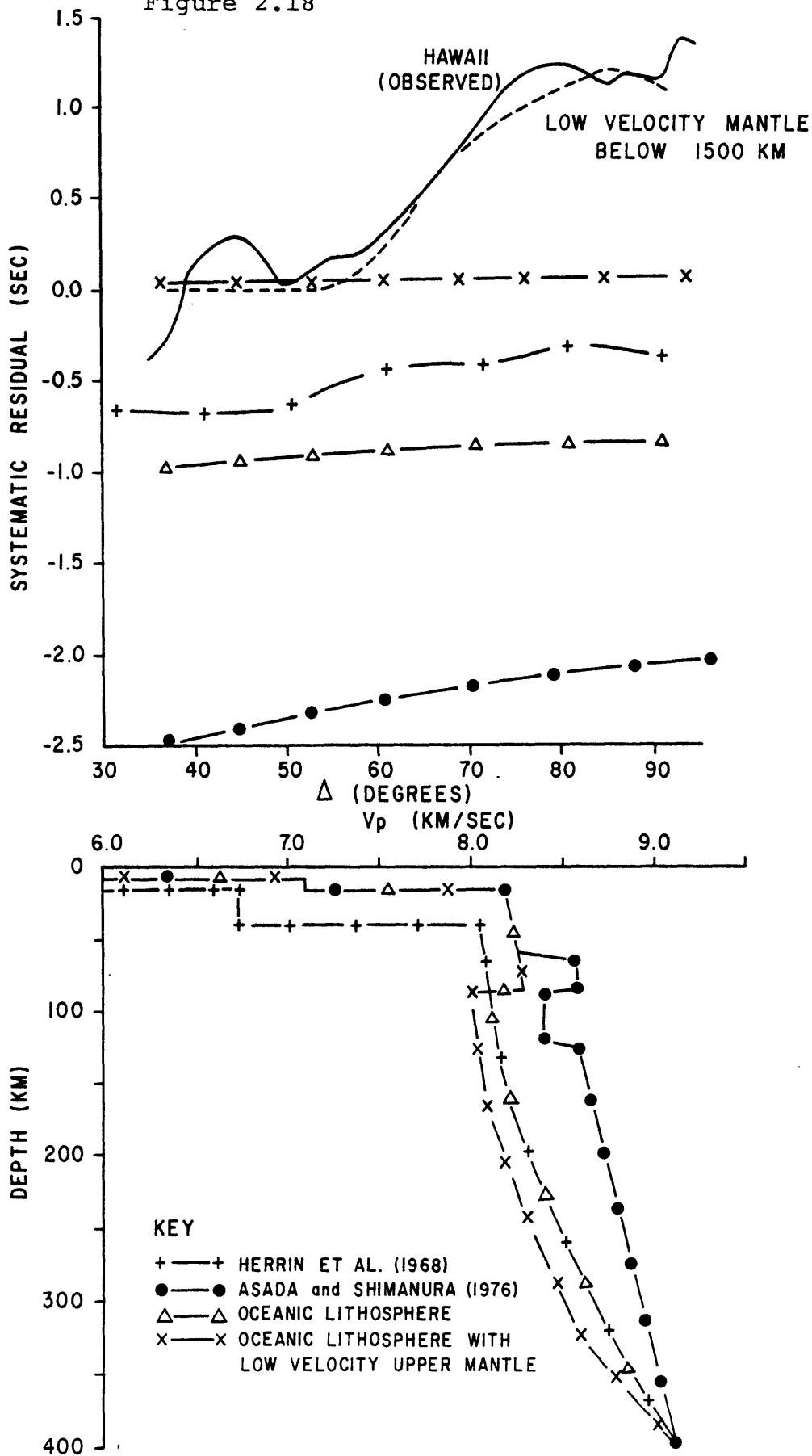
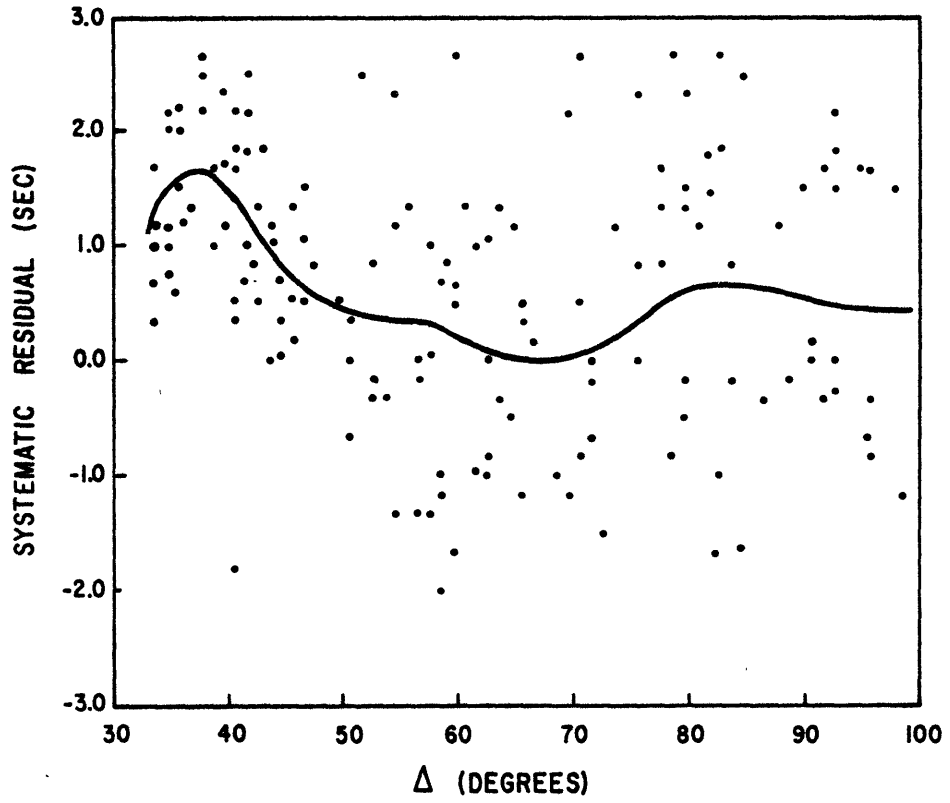


Figure 2.17

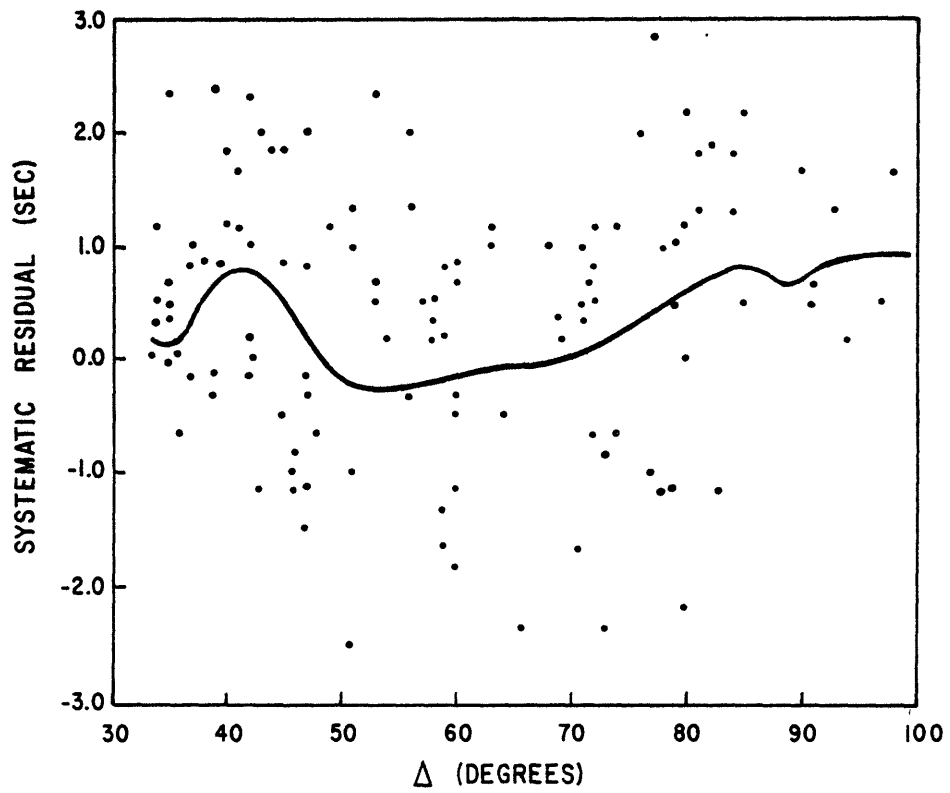
Figure 2.18



HONOMU EARTHQUAKE



KALAPANA EARTHQUAKE FORESHOCK



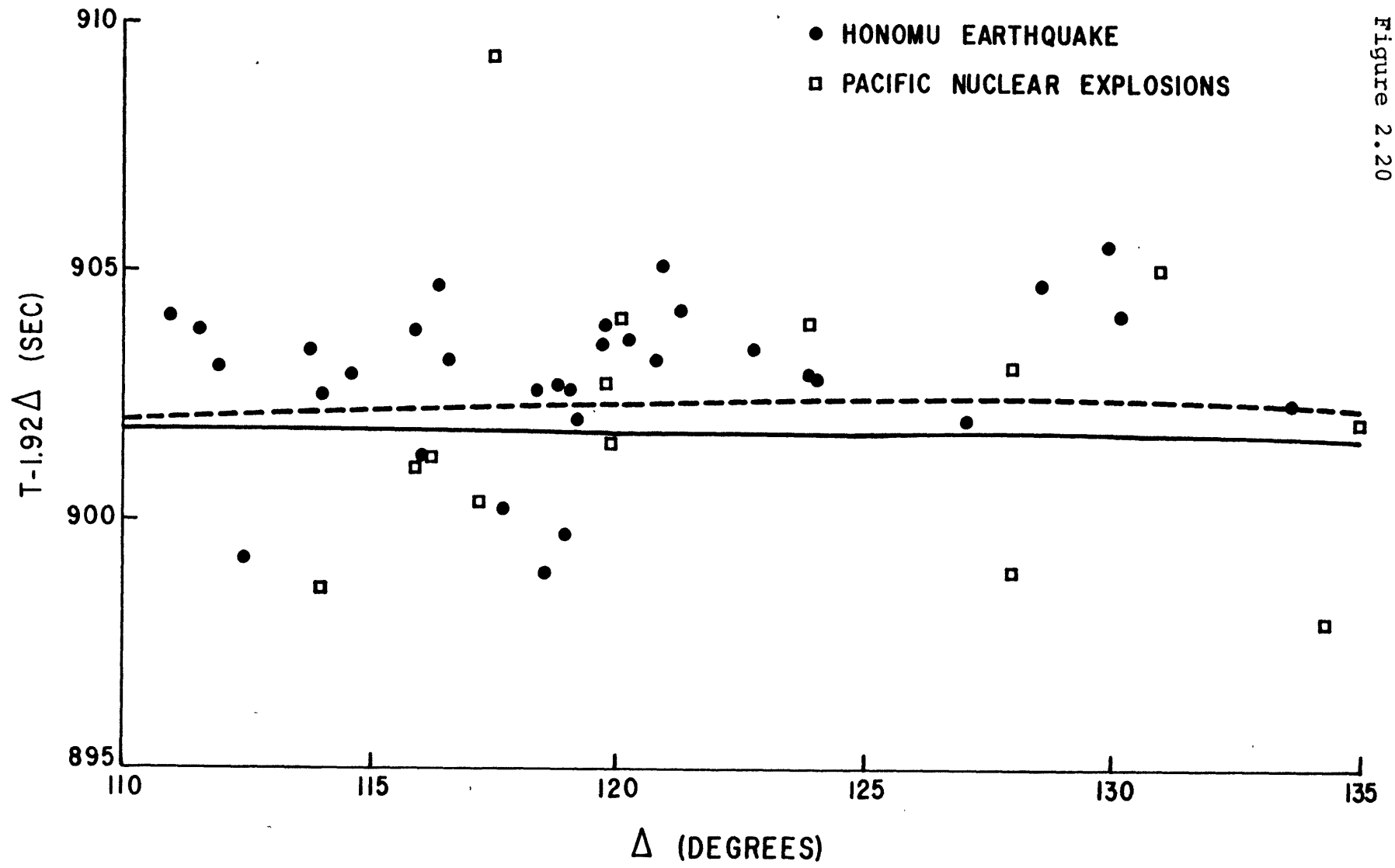


Figure 2.20

NTS EVENT (#113)

Figure 2.21

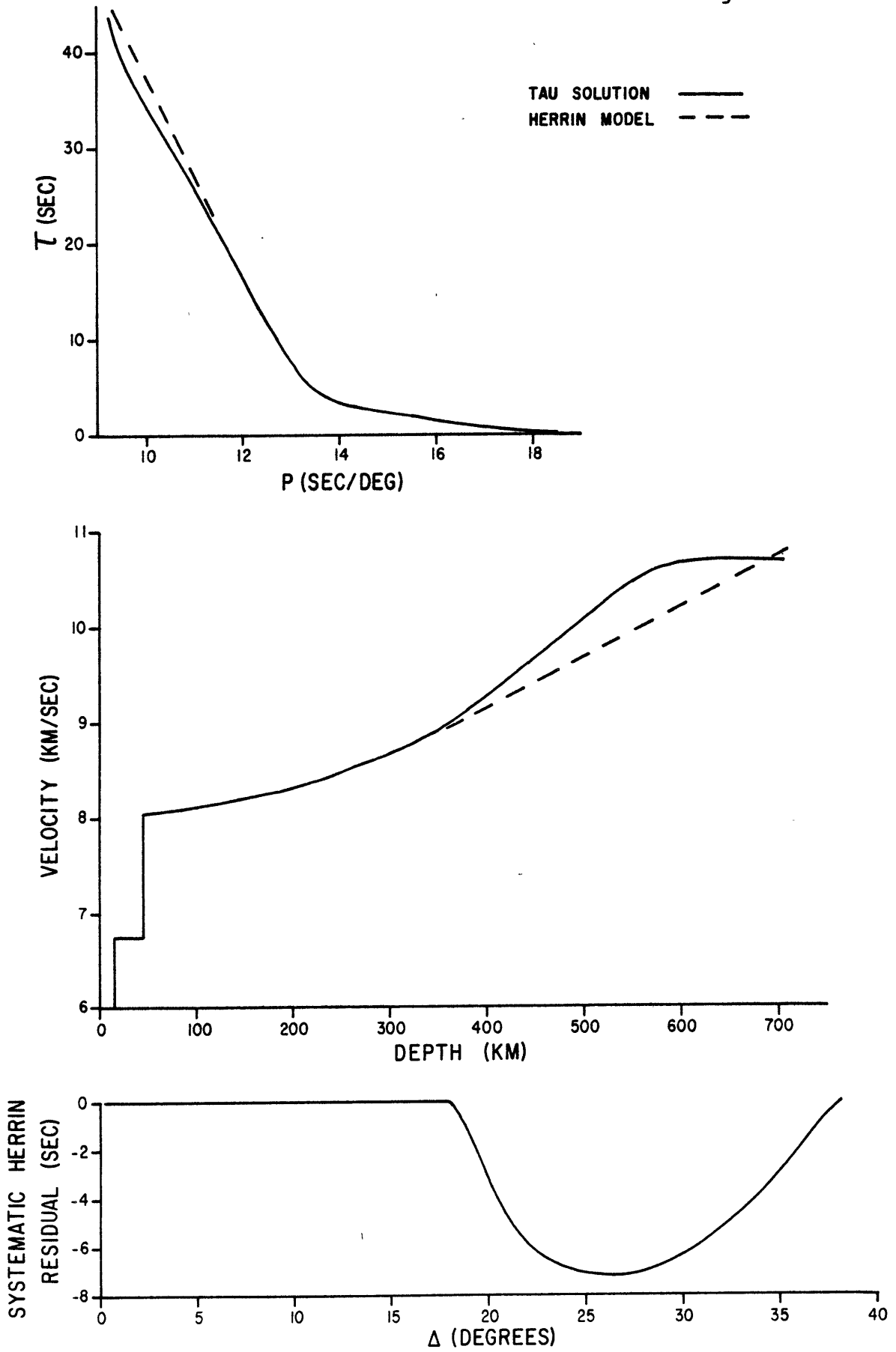
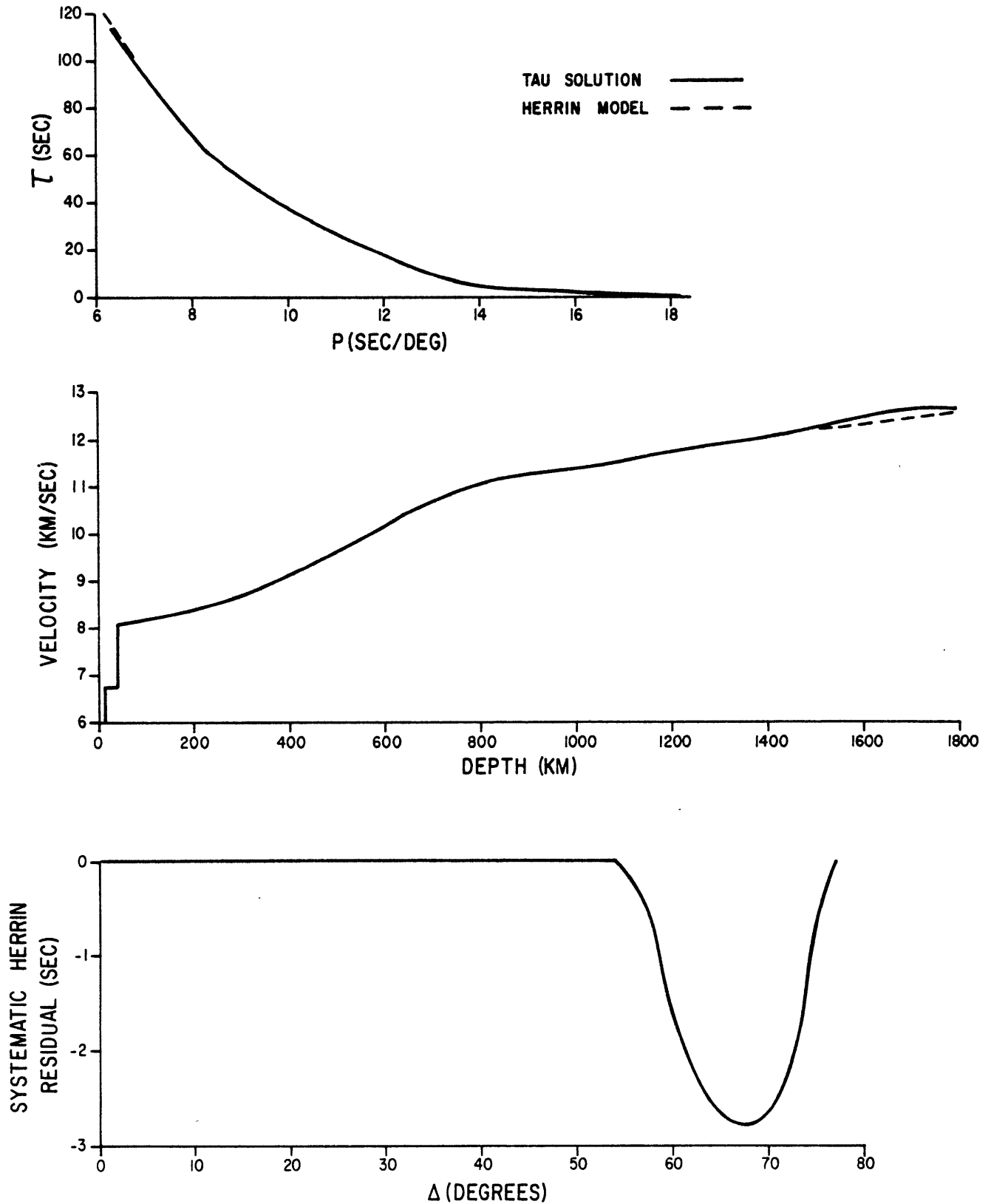
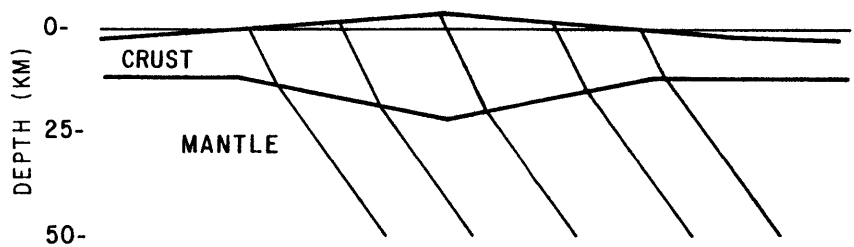


Figure 2.22

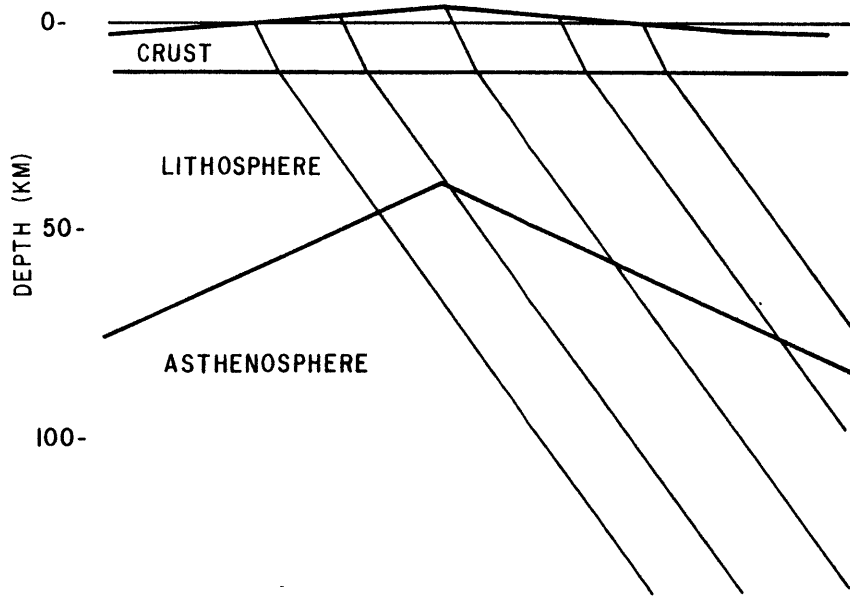
HALMAHERA EARTHQUAKE (#82)



a. MOHO BASIN



b. THINNED LITHOSPHERE



c. OFF AXIS LOW VELOCITY BODY

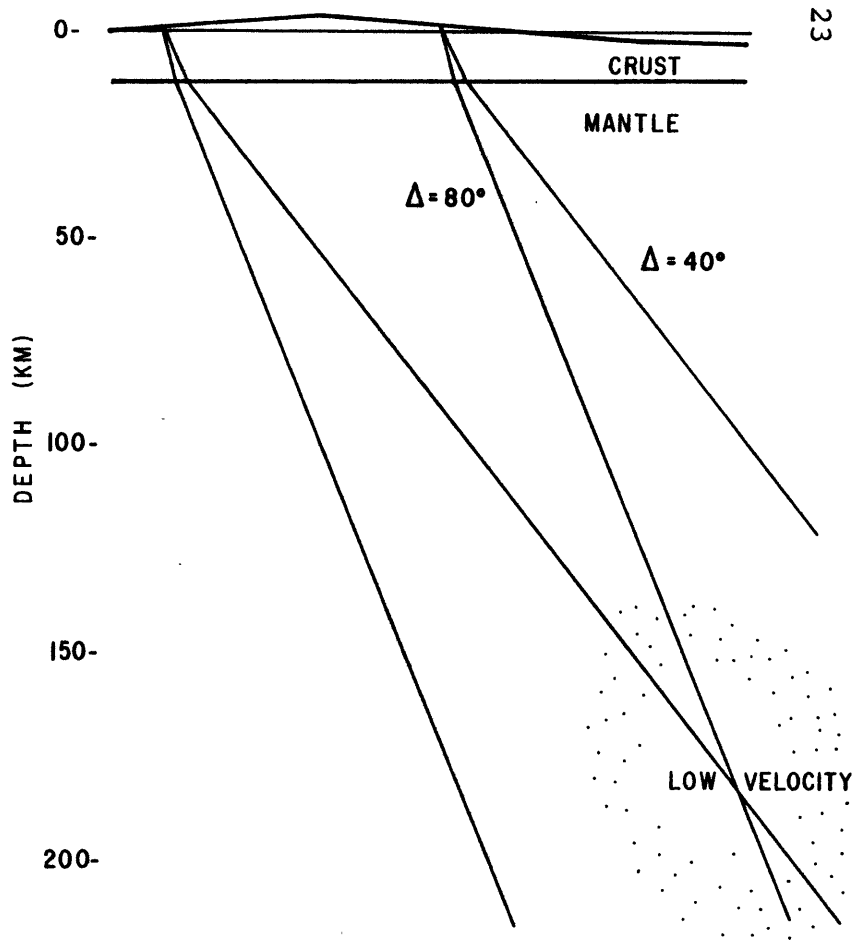
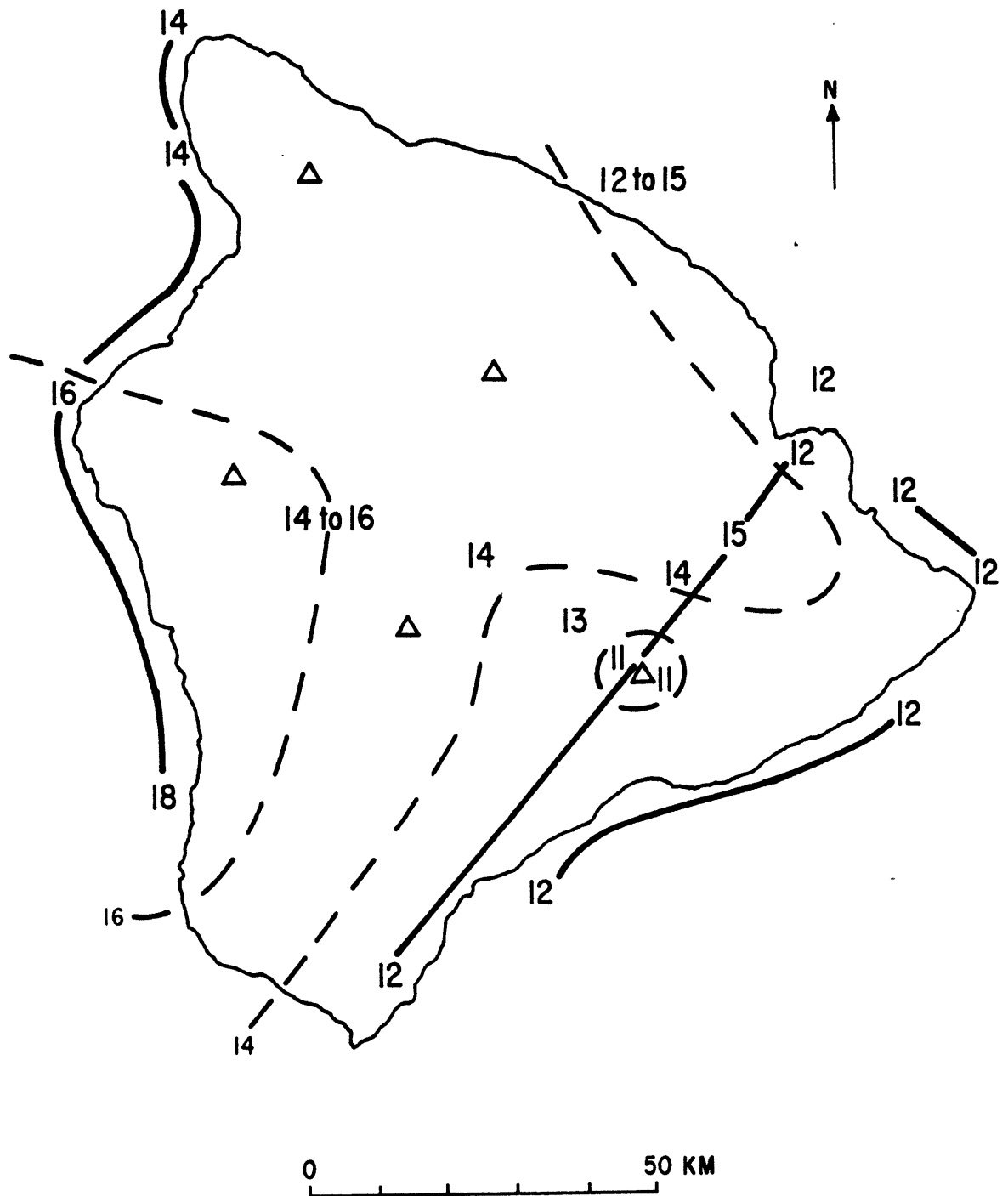


Figure 2.23

Figure 2.24



CHAPTER 3: Determination of Three-Dimensional Velocity Structure Using Distant Sources

Teleseismic P-waves observed by multi-sensor arrays show spatial variations in both phase and amplitude which defy explanation by the classical layered-earth models of seismology. Variations between waveforms recorded at nearby sites (~ 10 km) in apparently uniform geologic settings indicate that inhomogeneities in the crust and upper mantle underlying the receivers are the source of the observed signal fluctuations (Aki, 1973). Distortion of the recorded waveform by this near-receiver scattering limits the usefulness of the signals for the study of distant structure and source processes. Were it possible to remove from the observed signals the effects of local structural heterogeneities, the capability of arrays for studying remote structure and sources would be greatly enhanced. Alternatively, locally generated irregularities in the waveform are potentially useful data for deterministic study of the structure underlying the receiver array.

In this chapter the deterministic modeling method of Aki, Christoffersson and Husebye (1977a), through which three-dimensional estimates of velocity structure are made from body wave travel time data, is studied. Extensions of the basic method are introduced which allow for a self-consistent solution to both the forward, travel

time estimation problem and the inverse, structure estimation problem.

3.1 Inverse Solution for Structure from Travel Time Data

The method for modeling inhomogeneous structure underlying a seismic array introduced by Aki et al. (1977a) is based upon four fundamental assumptions. First, it is assumed that geometric ray theory adequately describes the travel paths and travel times of the waves studied. Secondly, since the method is non-iterative, the initial guess at the structure must be sufficiently close so that a linearized solution is justified. The latter assumption will be relaxed in §3.4, in which a framework for iterative improvement of the model is introduced.

The two final assumptions are related to the limited ability of finite models to describe the earth. Since the region of the earth which can be resolved by the model is restricted to the region underlying the array and to a depth of only 1-2 times the linear dimension of the array, it is necessary to assume an accurate description of the source wave slowness and azimuth outside of the model. In general, errors in describing the source wavefront may be projected into the model, which is undesirable. The final assumption is the converse, namely that fluctuations in velocity within the volume modeled can be described by the limited number of parameters comprising the model. This assumption is non-trivial,

and is discussed in §3.3.

3.1.1 Overview

Development of a system of linear equations through which an estimate of laterally-varying structure may be obtained begins with a description of the associated forward problem, the calculation of the travel time along the ray from source to receiver. From Fermat's Principle, the ray between two points is given by the path S , for which the travel time

$$t = \int v^{-1} ds \quad (3.1)$$

is stationary (a clear statement of Fermat's Principle may be found in Jenkins and White, 1957). Knowing the boundary conditions on the ray, and the medium velocity v , the solution of (3.1) for the travel time can be found. This problem has been studied by many authors (Eliseevnin, 1965; Julian, 1970; Wesson, 1971; Julian and Gubbins, in press).

When the boundary conditions on the ray are known together with the travel time, it is not, in general, possible to solve (3.1) constructively for the v which satisfies the time data. Furthermore, solution to this inverse problem is nonunique for finite data (Backus and Gilbert, 1967). One approach to solving (3.1) for v is to seek linearized perturbations δv to an initial model v_0 which improves the fit between predicted travel times

\hat{t} and the observed times t . This method is described for one-dimensional earth models by Backus and Gilbert (1969) and for three-dimensional models by Wesson (1971). Application of this method to complex structures requires that the velocity distribution be parameterized by a compact set of functions if resolution is to be maintained. Examples of several medium characterizations are presented in §3.2.

To the first order in δv , the change in travel time is

$$\delta t = - \int_{\text{along the ray}} v_0^{-2} \delta v ds \quad (3.2)$$

where the integration path is that used in (3.1). Backus and Gilbert (1969) show that the change in δt due to changes in the ray path are of the order $(\delta v)^2$ and may be neglected. If the medium is specified by a finite set of discrete parameters m_k , it follows that

$$\frac{\delta t}{\delta m_k} = - \int_{\text{along the ray}} v_0^{-2} \frac{\delta v}{\delta m_k} ds. \quad (3.3)$$

The difference between the true travel time and our initial estimate may then be expressed as

$$t - \hat{t} = \sum_k \frac{\delta t}{\delta m_k} \delta m_k + e \quad (3.4)$$

with error, e , of order δm^2 . Defining a travel time

residual for the i th observation of the j th source as

$$r_{ij} = t_{ij} - \hat{t}_{ij}$$

(3.4) becomes

$$r_{ij} = \sum_k - \int_{\text{along the ray}} v_0^{-2} \frac{\delta v}{\delta m_k} ds \delta m_k + e_{ij} \quad (3.5)$$

with the integration following the unperturbed ray from i to j as given by the solution to (3.1) with $v = v_0$. This result is equivalently obtained by expanding (3.1) in a Taylor series in m_j about v_0 where e_{ij} contains all terms of higher order than δm .

3.1.2 Formulation of the Model

Application of (3.5) to the study of structure along a segment of the ray path requires evaluation of kernels for the particular model specified by the m_k 's. For reasons discussed below, it is appropriate to use a layered structure as the framework for a laterally varying model when the volume modeled contains one end of the ray (source or receiver) but not the other. In this case the ray path through the model is specified by components of the slowness vector in the plane of the bottom boundary at the point the ray enters the model. When teleseismic sources ($\Delta \geq 30^\circ$) are used to study structure underlying an array with an aperture of about 1° or less, errors

introduced by treating rays from the source as having constant slowness and azimuth are insignificant. For this geometry, earth curvature is also negligible and the local layered framework is adequately described by plane parallel layers.

Removal of one ray endpoint from the model simplifies the integral in (3.3) by dividing the integration path into two parts, one through the region described by the m_k 's and the other containing no formal parameters. This latter part is common, by assumption, to all rays passing through the model and constitutes one additional unknown corresponding to each source. This unknown represents changes in travel time common to all stations, which will be represented by dO_j . The travel time residual may then be written

$$r_{ij} = dO_j - \sum_k \int_{\text{base}}^{\text{station } i} v_0^{-2} \frac{\delta v}{\delta m_k} ds \delta m_k + e_{ij} \quad (3.6)$$

Changes in the calculated travel times arising from a change in average velocity at any depth within the model will also have an equal effect on all calculated travel times. Consequently, this perturbation is also accounted for by dO_j .

Introducing new notation:

$$a_{ijk} = - \int_{\text{base}}^{\text{station}} v_0^{-2} \frac{\delta v}{\delta m_k} ds$$

$$x_k = \delta m_k \quad (3.7)$$

(3.6) becomes

$$r_{ij} = \sum_k a_{ijk} x_k + d0_j$$

where the equality is approximate since the error term has been dropped. Using matrix notation this becomes

$$r_{ij} = [a_{ij1}, \dots, a_{ijk}, 1] \begin{bmatrix} x_1 \\ \cdot \\ \cdot \\ \cdot \\ x_k \\ d0_j \end{bmatrix}$$

Pre-multiplying by $[a_{ij1}, \dots, a_{ijk}, 1]^T$ and summing over n observations for event j , we have

$$\sum_i \begin{bmatrix} a_{ij1} \\ \cdot \\ \cdot \\ a_{ijk} \\ 1 \end{bmatrix} r_{ij} = \sum_i \begin{bmatrix} a_{ij1} \\ \cdot \\ \cdot \\ a_{ijk} \\ 1 \end{bmatrix} [a_{ij1}, \dots, a_{ijk}, 1] \begin{bmatrix} x_1 \\ \cdot \\ \cdot \\ \cdot \\ x_k \\ d0_j \end{bmatrix} \quad (3.8)$$

The last equation is easily solved to obtain

$$d0_j = \sum_i \frac{r_{ij}}{n} - \sum_i \frac{a_{ijk}}{n} \cdot \bar{m}_k \quad (3.9)$$

Let

$$\sum_i a_{ijk} = \bar{a}_{jk}$$

and

$$\sum_j r_{ij} = \bar{r}_j$$

Using (3.9) the travel time correction $d\theta_j$ can be decoupled from (3.8), so that the k th equation of (3.8) becomes

$$\sum_i a_{ijk} \left(r_{ij} - \frac{\bar{r}_j}{n} \right) = \sum_{i\ell} \left(a_{ijk} a_{ij\ell} - \frac{\bar{a}_{jk} \bar{a}_{j\ell}}{n} \right) x_\ell \quad (3.10)$$

Note that the unknown perturbations x_ℓ do not depend on either changes in the total travel time or the average travel time residual. Consequently the solution contains no information about the average velocity at any depth in the model. All that can be recovered are the velocity fluctuations about an unknown mean.

Collecting terms in (3.10) and summing over all events we obtain the k normal equations for the medium parameters:

$$\sum_{ij\ell} \left(a_{ijk} a_{ij\ell} - \frac{\bar{a}_{jk} \bar{a}_{j\ell}}{n} \right) x_\ell = \sum_{ij} a_{ijk} \left(r_{ij} - \frac{\bar{r}_j}{n} \right)$$

which in matrix notation may be written as

$$Gm = d \quad (3.11)$$

where G is a semi-definite, symmetric matrix, m is a vector containing the yet unknown model perturbations and

d is a vector containing combinations of the observed residuals and model partial derivatives. Solution of (3.11) by classical least squares fails because the integral of the perturbed velocity at a constant depth is known only to within an arbitrary constant (Aki et al., 1977a). This non-uniqueness applies only to perturbations at the same depth, and may be removed by introducing a constraint on the parameters at each depth level such as minimizing the average squared perturbation. Such a constraint will introduce an interdependence of parameters at the same depth with no influence between parameters at different depths. With the solution for parameters at the same depth being unavoidably coupled, it is natural to describe inhomogeneous structures by basis functions which are restricted to a specific depth interval. Inter-layer non-uniqueness due to inadequate observational data is not remedied by this medium description and must be treated by other means.

3.1.3 Computation of the Inverse Solution

The solution of linear systems of equations, such as (3.11) has received much attention in recent years. Since (3.11) does not have a "unique" least squares solution we must choose a particular solution from infinitely many solutions, each of which satisfies the data equally well. The "natural" solution to this problem, as given by Lanczos (1961), has the minimum euclidian length of all possible

multi-dimensional solution vectors. This solution is referred to as the "generalized inverse" or "minimum length" solution.

To obtain this solution, first decompose the symmetric matrix G into its eigenvalues and normalized eigenvectors

$$G = V\Lambda V^T$$

where Λ is a diagonal matrix containing the eigenvalues of G and V contains the corresponding eigenvectors. Let Λ_p and V_p contain only the non-zero eigenvalues and corresponding eigenvectors of G . Then the generalized inverse solution \hat{m} for (3.1) is given by

$$\hat{m} = G^{-g}_d \quad (3.13)$$

where

$$G^{-g} = V_p \Lambda_p^{-1} V_p^T.$$

Aki et al. (1977) discuss this solution in detail and show that the resolution matrix for this system is

$$R = V_p V_p^T.$$

When the observational data are adequate, this solution has the maximum possible resolution, with smoothing of the

solution restricted to between parameters of the same layer. The change in the averaged layer velocity is also zero.

Unfortunately, several factors limit the practical application of the generalized inverse solution. From a purely economic standpoint, decomposition of G into its eigenvalues and eigenvectors is time consuming and very expensive even when using fast, accurate algorithms on modern, high speed computers. As a single set of simplified basis functions which describe the medium cannot model all possible or even reasonable structures, it is necessary to explore a range of model characterizations when applying this method to real data.

A more fundamental objection to the generalized inverse lies in the trade-off between resolution and error. Because the actual number of observations is finite, the solution for infrequently sampled model elements may be dominated by errors. For these elements the high resolution achievable by the generalized inverse is traded for unacceptable uncertainty in the solution. One remedy for this difficulty would be removal of elements with large standard errors from the solution space. This approach is discussed below. Wiggins (1972) suggests stabilization of the solution, at the expense of optimal resolution, by limiting the particular eigenvectors used in (3.12) to those whose eigenvalues exceed a cut-off value. By "winnowing" the eigenvectors the condition number of the

matrix is improved which stabilizes the numerical solution as well. Unfortunately, choice of an appropriate cut-off value is subjective and it requires at least a partial decomposition of G which is expensive.

An alternative method of solving (3.11) which retains many of the benefits of the generalized inverse solution and approximates the "winnowed" solution of Wiggins (1972) is the "damped least squares" solution discussed by Levenberg (1944). In this method, the normal equations (3.10) are modified by adding a positive constant, θ^2 , to the diagonal elements of G .

$$(G + \theta^2 I)m = d \quad (3.13)$$

This system of equations is non-singular because the addition of θ^2 forces the eigenvalues of $(G + \theta^2 I)$ to be non-zero. The solution to (3.13)

$$\hat{m} = (G + \theta^2 I)^{-1} d \quad (3.14)$$

can be calculated efficiently using an elimination algorithm. The damped least squares solution (3.14) can be obtained by minimizing $|d - Gm|^2 + \theta^2 m^T m$ instead of $|d - Gm|^2$.

By a proper choice of θ^2 , (3.14) reduces to a simplified case of the stochastic inverse solution of Franklin (1970). When the covariance matrices for both data errors, Δd , and the model are a constant times the identity matrix

$$\begin{aligned} \langle \Delta d \Delta d \rangle^T &= \sigma_d^2 I \\ \langle m m^T \rangle &= \sigma_m^2 I \end{aligned} \quad (3.15)$$

choice of θ^2 as

$$\theta^2 = \sigma_d^2 / \sigma_m^2$$

in (3.14) gives the stochastic inverse solution. The resolution matrix discussed by Backus and Gilbert (1968) is in this case

$$R = (G + \theta^2 I)^{-1} G. \quad (3.16)$$

Resolution for the damped least squares solution is poorer than that for the generalized inverse, with non-vanishing elements of R in different layers than the diagonal element. However, solution standard errors are greatly reduced.

Using (3.15) the covariance matrix of errors in the model $\Delta \hat{m}$ is

$$C = \langle \hat{m} \Delta \hat{m}^T \rangle = \sigma_d^2 (G + \theta^2 I)^{-1} R$$

The standard error of the solution \hat{m}_i is

$$\Delta \hat{m}_i = C_{ii}^{1/2}.$$

Model parameter errors for the damped least squares solution are bound by

$$\Delta \hat{m}_i \leq \frac{\sigma_d}{\theta} (R_{ii}(1 - R_{ii}))^{1/2} \quad (3.17)$$

where R_{ii} is the corresponding diagonal element of R . The right hand side of (3.17) attains its maximum value when $R_{ii} = 0.5$, so $\Delta \hat{m}_i$ is always bound by

$$\Delta \hat{m} \leq \frac{\sigma_d}{2\theta}$$

Although this bound is less restrictive than (3.17), it is independent of R and is useful in evaluating, a priori, the effect of a particular choice of θ^2 on the inverse solution (see Appendix B).

3.2 Characterization of the Medium

In this section, several methods of parameterizing the earth by a compact set of parameters are introduced. Before considering the details of each model formulation, several features and general requirements which apply to all models are examined.

In each model, the region affected by any given parameter will be restricted to a specific depth interval. This limits unavoidable averaging in the solution to unknowns determinant only to within a constant factor when model resolution is optimal. Undesirable vertical smoothing introduced by use of (3.14) can be limited by adjustment of the ratio of the layer thickness to the horizontal "length" of parameters within the layer.

Selection of a horizontal "length" or distance of influence of each parameter is limited by assumptions allowing evaluation of (3.3) using ray theory. The ray approximation requires that inhomogeneities are smooth within a wavelength. The effect of heterogeneous structure with a correlation distance much smaller than a wavelength will tend to be smoothed out by the wave which responds to the average properties.

Limitation of the domain of influence of each parameter to a single depth interval also assumes that the structure has a vertical smoothness over the layer thickness. This assumption can be tested to a certain degree by generating solutions using a variety of layer boundaries and thicknesses. However, choice of a horizontal parameter length to layer thickness ratio which optimizes resolution implies a vertical correlation length roughly twice the horizontal correlation length for teleseismic ray paths.

3.2.1 Quantized model of Aki, Christoffersson and Husebye

The medium description originally introduced by Aki et al. (1977a) will be called "quantized" in this discussion because of the algorithm by which the partial derivatives of (3.3) are evaluated. In their model, the initial estimate of earth structure consisted of plane parallel layers of constant thickness with fixed average velocity. For this medium, the ray paths reduce to line segments

within each layer. The actual raypaths are easily calculated by tracing the ray from each station to the base of the model since the ray slowness, \vec{u} , is assumed.

Lateral variations in velocity are described by parameters distributed on a rectangular grid. Sampling of the medium is done by assigning the ray path segment in each layer entirely to the domain of influence of the parameter to which it is closest at the mid-layer depth (Figure 3.1). All rays passing through the rectangular region in the mid-layer plane centered on a given parameter will be assigned to this parameter. Aki et al.

call these parameters "blocks" and argue that this sampling places the ray in the rectangular parallelepiped containing most of the unperturbed raypath. As can be seen in Figure 3.1, this will not always happen. In fact, a ray can even be assigned to a "block" not penetrated by the ray. I suggest that this model be called "quantized" to reflect the sampling and to avoid confusion with a model based upon rectangular blocks described in §3.2.2

The kernals for this quantized model, represented by the a_{ijk} 's in (3.10) reduce to

$$a_{ijk} = - \frac{x_{ijk}}{v_{ok}^2}$$

where x_{ij} is the distance traversed by the ray in crossing the layer containing parameter k and v_{ok} is the velocity in that layer. Rather than solve for the new velocity estimate at location k directly, fractional velocity changes

are solved for, so

$$m_k = \left(\frac{\delta v_k}{v_0} \right). \quad (3.18)$$

For this choice of m_k , we have

$$a_{ijk} = -T_{ijk} \quad (3.19)$$

where T_{ijk} is the time spent by the ray crossing the layer containing element k .

The simplified ray tracing and sampling contained within this quantized model has several advantages over the other methods described below. First, construction of the G matrix is computationally very efficient since the location of each ray is calculated but twice in each layer (top and midpoint). Also, the travel time through each layer depends only upon the source wave slowness so the travel time T_{ijk} need be calculated but once for each layer and event pair. More importantly, when compared with other methods described below, the quantized model has the best resolution and smallest standard errors.

The major drawback to this method is interpretation of the derived model, resulting from heavy spatial smoothing introduced by the ray path quantization algorithm. The spatial region affected by each model parameter is well defined only in the mid-layer plane. Above and below it the solution averages the velocity in a poorly defined

data-dependent manner, and the improved velocity model is not explicitly defined. Consequently, the solution cannot be refined by iteration or even verified by recalculation of travel time residuals to the forward problem.

3.2.2 Block Model

A conceptually simple extension of the quantized model is obtained by calculating the model derivatives continuously along the initial ray as it passes through an array of right rectangular prisms. For this model, the unknowns correspond to the fractional change in velocity within each prism. We will call this representation a "block" model.

Computation of the exact path length through each block is approximately achieved by dividing the ray in each layer into many segments. The sampling algorithm used in the quantized model is then applied to the midpoint of each segment (Figure 3.2). As the sampling interval is reduced, the accuracy of the approximation improves.

The principal advantage of the block model over the quantized model is the explicit definition of the region influenced by each model parameter. In principle, the solution could be improved by iteration, or verified by recalculation of time residuals. However, the many velocity discontinuities makes ray tracing through the model cumbersome. The effect of these sharp contrasts, which are too high frequency to be resolved by the data, can

be minimized by smoothing the solution (or solutions). Model parameter resolution for the block model is slightly poorer than that achieved by the quantized model.

3.2.3 Continuous Velocity Models

Characterization of the medium velocity as a continuous function of space by a finite set of parameters combines the conceptual advantage of both the quantized and block models. A suitable choice of basis functions allows control over model smoothness while retaining an explicit definition of velocity everywhere within the model.

3.2.3.1 Hanning basis functions

A node centered medium representation similar to the quantized model, but with explicit smoothing is given by

$$V(x,y) = \sum_{i,j} W_{ij}(x,y) V_{ij}$$

where V_{ij} is the velocity at node located at $x = x_i$ and $y = y_i$ and $w_{ij}(x,y)$ is a weighting function.

The block model of §3.2.2 is a special case of this type of model. A more useful model, with superior spatial wave number characteristics is defined by the weighting function

$$\begin{aligned}
 w_{ij}(x,y) &= \frac{(1 + \cos p)(1 + \cos q)}{4} && \text{for } \begin{cases} |x-x_i| \leq DX \\ |y-y_i| \leq DY \end{cases} \\
 &= 0 && \text{elsewhere}
 \end{aligned} \tag{3.20}$$

where DX and DY are the distance between adjacent nodes and

$$\begin{aligned}
 p &= \frac{\pi}{DX} (x-x_i) \\
 q &= \frac{\pi}{DY} (y-y_i).
 \end{aligned}$$

This weighting function is a bivariate hanning window and the model based upon this choice of weights is called a hanning model (Figure 3.3).

Although many similar weighting functions can be designed, weights given by (3.20) are attractive since they act as a low pass filter on wave numbers represented in the model. Note also that when the velocity at the four nodes enclosing (x,y) are equal, the velocity at (x,y) equals that constant values.

Model parameter partial derivatives for the hanning model to be used in (3.7) are simply the weights $w_{ij}(x,y)$ given in (3.20). Again, rather than solve for v_{ij} directly, it is more convenient to find the fractional change in velocity. Using (3.18) as the definition of the unknown velocity

$$a_{ijk} = \int_{\text{along the way}} \frac{-ds}{v} w_k \left(\frac{v_0}{v} \right) m_k$$

where v_0 is the average velocity in the layer. If the ray path is approximately by discrete segments, the term dS/v is the incremental travel time for each segment.

The principal drawback to this model is significant degradation of resolution, for fixed damping θ , relative to the quantized and block models.

3.2.3.2 Model representation using Fourier Series

At the opposite extreme of possible continuous medium representations to the localized basis functions used in the hanning model is a description employing periodic basis functions. The two-dimensional Fourier transform of $v(x,y)$ in a specific layer is

$$v(x,y) = \sum_{j,\ell} W_{j\ell} e^{2\pi i(k_j x + k_\ell y)}. \quad (3.21)$$

Use of (3.21) in the inverse problem reduces to finding the weight functions $w_{j\ell}$ for a pre-selected, finite set of wave numbers, k_j and k_ℓ . Since it is unlikely that $v(x,y)$ is periodic, the wave numbers selected need not conform with rules for allowable wave numbers of periodic functions.

Model parameter partial derivatives corresponding to (3.21) are

$$a_{ijk} = \text{along the way} \int \frac{-dS}{v} e^{2\pi i(k_j(k)x + k_\ell(k)y)} \left(\frac{v_0}{v}\right) \delta m_k$$

where

$$m_k = \frac{w_{j\ell}}{v_0}$$

Construction of a complex G matrix can be avoided by rewriting (3.21) in terms of real coefficients of a series of sines and cosines instead of the complex $x_{j\ell}$'s. Description of the medium by (3.21) avoids the artificial position of boundaries inherent in space-centered descriptions.

Finally, (3.21) isolates the indeterminate, average layer velocity in a single term, which can be excluded from the model basis. With the D.C. Term of (3.21) excluded from the model basis, the least squares solution to (3.11) is the generalized inverse.

3.3 Strategies for Modeling the Earth

3.3.1 Network Geometry and Source Distribution

Successful three-dimensional modeling requires both suitable network geometry and a proper source event distribution. Neither is a satisfactory substitute for the other. On the one hand, both the detail with which information can be recovered and the depth to which modeling is possible are principally controlled by the number and distribution of sensors. Model resolution, on the other hand, depends principally upon the distribution of source events.

Network characteristics favorable to the method include an equidimensional shape and uniform station density. For optimum performance, the maximum depth of modeling is restricted to the deepest crossing of ray paths along the minimum array diameter. Although acceptable numerical resolution can be obtained locally for deeper regions, layers substantially below the deepest crossing of ray paths generally contain large regions with few samples and poor resolution near the center of the layer. Station spacing within the network controls the horizontal scale length of model elements, especially within the uppermost model layers. The horizontal scale length, in turn, controls layer thickness. For a fixed horizontal sampling, layers which are too "thin" have very poor parameter resolution matrix compared with "thicker" layers. The appropriate choice of height to length ratio is governed by the range of incidence angles of the source rays. By equalizing the horizontal and vertical travel times through model elements resolution is optimized. Resolution for thinner layers is degraded since model elements are linked vertically by most rays. Elements in models with substantially thicker layers are unrealistically elongated with little or no improvement in resolution. When using teleseismic P-waves with a maximum incidence angle of about 30° , a height to width ratio of 1.5:1 is a reasonable compromise between the optimum choice of 2:1 and a more physical

choice of 1:1 (which assumes a constant heterogeneity correlation length in all directions).

In practice, model resolution is effectively controlled by the distribution of source events. Regardless of the network configuration and model geometry, unless the model elements (or basis functions) are sampled by rays from a variety of azimuth and preferably with a range of slowness values the inverse method cannot achieve adequate resolution. Regions on the periphery of the model will generally have poor resolution even when sources are well distributed since rays through these regions come from a limited azimuth range. For these extreme regions, it is sometimes better to hold constant basis functions which describe these inadequately sampled areas.

3.3.2 Effect of Earth Structure Outside the Model

Contributions to observed travel time residuals arising from inadequate description of ray path segments lying outside the modeled volume are a potential source of systematic error in solution. This is because the inverse method fits a finite set of travel time residuals by an optimum adjustment of model basis functions regardless of whether or not the basis functions describe the region in which the travel time residual arises. Particularly troublesome sources of travel time error lying beyond the limits of the model include broad scale inaccuracies in the radial earth model and strong lateral structure near the source or in the lower mantle. Constant errors in

total travel times do not affect the model since relative residuals are used.

Misspecification of the radially symmetric earth model used to predict ray slowness across the array can introduce a systematic bias in the calculated residuals. For example, relative differences between the Jeffreys-Bullen and Herrin P-wave travel times across a 1° array can be as large as 0.1 sec and are several times that figure for arrays with a wider aperture. Assuming that the travel time error between Jeffreys-Bullen and Herrin is representative of the systematic error introduced by imperfect knowledge of the radial velocity structure in the mantle, it is possible to estimate the magnitude of this error upon the inverse solution. Inversion of this systematic error for the same events and stations used in the study of structure underlying Hawaii in §4 (Table 3.1) shows that this source of model error is unimportant for this array. However, a similar study using the USGS central California network (maximum aperture of 3°) leads to solution bias as large as 2%. Clearly, this effect is potentially a significant source of bias and should be investigated especially when using the Jeffreys-Bullen travel time table as the reference earth model.

Strong lateral variations in structure far from the array which distort either ray slowness or azimuth also give rise to time residuals which may distort the solution. Identification of the residual component, if any, arising from these external sources is very difficult. In her

study of four large aperture arrays in the western U.S., Powell (1976) found common systematic biases in apparent azimuth and slowness for selected source regions. Observation of a common error by each of the distinct arrays is strong evidence that the source of the heterogeneous structure responsible for the event mislocation lies at considerable distance from the arrays. Sudden changes in mislocation vector with small changes in incidence angle or azimuth caused by distant structure generate significant changes in observed residuals which cannot be explained by the local model. This is because small changes in the incidence angle produces negligible changes in travel time through the local model. Therefore, deep-seated heterogeneities which give rise to sharp changes in the array diagram are left unexplained by the modeling and presumably remain in the residual of the inversion. Evidence for possible distant heterogeneities within the HVO teleseismic observations and their effect upon inverse solutions is discussed in §2.5.

3.3.3 Non-Modelable Local Structure

The need for a simplistic but flexible description of laterally varying structure guarantees that the local structure cannot be completely described by the basis functions employed. Hopefully, the discrepancies between the earth and our model of it will not result in the introduction of spurious perturbations elsewhere in the model. To a certain extent, the smoothing effect of the

long wavelength (~ 10 km) P-wave helps prevent this from being a serious problem when the variations are small. However, certain types of structures can significantly affect the results, and special precautions need to be taken to eliminate their influence.

The most serious complication which arises in the case of every array personally studied by the author is the presence of rapidly varying structure at very shallow depth. Evidence for shallow structures usually appears as statistically discernable variations in mean travel time residual between nearby sites. Traditionally, seismologists have attempted to account for these site specific structures through station corrections. By fully utilizing a three-dimensional structural model it is possible, in principle, to completely account for these local structures. However, station density is rarely sufficient to allow for the detailed modeling necessary. Even on Kilauea, where the inter-station distance is 5 km or less, site to site variation in mean residual indicates that the correlation length of the medium is of this scale or somewhat smaller. Thus, modeling of near surface heterogeneities when mean residuals at adjacent sites are poorly correlated is a complex matter.

Failure to adequately account for the average residual in the region where it most likely originates -- immediately beneath the station -- may result in spurious solution values elsewhere in the model. Special care must be

taken therefore to ensure that structure underlying stations with measureable different mean residuals are not described by the same first layer model parameters. It should be noted that removal of mean station residual sharply reduces the data variance (by over 50% for the Hawaiian data).

Even when laterally varying structures can be adequately represented by the model, other types of non-modelable structures may influence the inversion results. Non-horizontal boundaries, such as a dipping Moho, are not adequately described by the models described in §3.2. Interpretation of models obtained using a plane parallel layered framework must include the possibility that the obtained velocity contrasts may result from vertical relief on layer boundaries as well as variations in layer properties. Since the Moho is by far the largest "horizontal" boundary encountered beneath the HVO array, the effect of possible relief on the Moho upon both observed residuals and inverse solutions needs to be considered. This question is addressed in §2.5 and §4.5.

The formulation of the three-dimensional modeling presented in §3.1 tacitly assumes that the medium is isotropic. Velocity anisotropy, which is suspected to exist at the base of the oceanic lithosphere, may affect the solution for certain problems. However, if the medium is transversely anisotropic in the horizontal plane, then it will not show up in the residual data at any angle of

incidence. The only effect it will have on the solution is a negligible error in the incidence angle assumed when tracing the ray path through the medium.

3.3.4 Model Resolution - The Big Picture

The primary objective of the three-dimensional modeling is, of course, to yield quantitative information about the size, distribution and intensity of lateral variations in velocity structure. Because the modeling technique arrives at a solution which minimizes travel time residual data by constructing a linear combination of basis functions which cannot completely describe the medium it is useful to inquire into the relationship between the solution so obtained and the earth. The relationship between the calculated solution and "true" solution is given by the parameter resolution matrix R when the problem is linear (Backus and Gilbert, 1968). This matrix R maps the "true" model m into the calculated solution \hat{m} by

$$\hat{m} = Rm.$$

In the problem at hand, the "true" model is itself an approximate description of the earth in the sense that the basis functions that comprise it do not fully describe the earth. Consequently, R tells us how well the basis functions of the solution are resolved but not

(directly, at least) how well the obtained velocity structure resolves the earth. To answer this question we must first determine the relationship between the earth and the "true" model, m .

Ideally, m should be the "best" description of the medium velocity $v(x,y,z)$ attainable through a linear combination of basis functions $m_k(x,y,z)$. This observation naturally leads to an inverse problem in which we seek the minimum of some functional $F(m(x,y,z), v(x,y,z))$. A natural choice for F would be the squared error between m and v integrated over the volume modeled. Since

$$m(x,y,z) = \sum_k a_k m_k(x,y,z)$$

where the a_k 's are unknown coefficients, the desired m is given by the solution to k normal equations

$$0 = \sum_j a_j \int_{Vol} m_k m_j dV - \int_{Vol} m_k v dV. \quad (3.22)$$

For the case when the m_k 's are the block described in §3.2.2 the solution to (3.22) is

$$a_k = \frac{\int_{block} v dV}{\int_{block} dV}. \quad (3.23)$$

This is just the average velocity within the block. Thus, if this intuitive definition of the "true" model is correct,

then for block model basis functions the resolution matrix connects the three-dimensional solution for the "best" constant velocity for each block with the true average velocity within the block.

Three-dimensional model results for test problems using exact residual data obtained by tracing rays through a known three-dimensional structure suggest that the intuitive definition of the "true" model obtained from (3.22) is not entirely correct. Model inaccuracies were discovered for one test case in §B.2.3 which cannot be explained by appeal to the resolution matrix. Criteria for detecting modeling difficulties of this kind are developed in §B.4 which include not only study of the parameter resolution matrix, solution standard errors but also the examination of alternative arrangements of locations and layer boundaries and alternative element dimensions.

3.4 Iterative Refinement of the Three-Dimensional Solution

In formulating the earth modeling discussed above it was necessary to neglect non-linear terms in the expansion of the travel time about an initial earth model. Although the effect of the neglected higher order terms on the solution may be insignificant, and the linear estimate of three-dimensional structure quite satisfactory, there is no guarantee that this is the case. In fact, it would be unusual if the solution to this problem, involving typically

hundreds of unknowns, converged in a single iteration based on a homogeneous initial model. Refinement of the solution through iteration is desirable not only because it allows for model convergence, but also because it allows us to examine, in detail, what data is explained by the model (and what data is not explained).

Iteration of the inverse solution generated using the initially homogeneous layered model requires calculation of both travel times and medium partial derivatives in laterally heterogeneous media. A self-consistent approach using geometric ray theory is developed for calculating travel times and partial derivatives of travel time with respect to model basis functions for a single description of the velocity field. The principal advantage of this approach is the ability to verify the inverse solution under the same assumptions by which it was generated.

3.4.1 Ray Tracing in Heterogeneous Media

Calculation of seismic ray travel times in heterogeneous media requires the solution of a "two point" boundary value problem which cannot be solved, in general, directly. The minimum time path can be found by iteratively refining approximate solutions using a number of distinct strategies. The two strategies most commonly employed are sometimes called "shooting" and "bending" (Julian and Gubbins, in press).

The shooting method reformulates the problem in terms of an initial value problem in which ray slowness at one endpoint is specified. The ray is propagated forward until a termination condition is met, at which time the error between the ray endpoint and the desired coordinates are compared. This shooting error is used to refine the initial conditions and the process is repeated until satisfactory agreement between the desired and actual endpoints are obtained. This method has been studied extensively by Jacob (1970), Julian (1970) and Wesson (1970), among many others.

The bending method, introduced in seismology by Wesson (1970, 1971) connects the desired endpoints of the ray by a line path which is iteratively deformed until Fermat's principle of stationary time is satisfied. This method has recently received considerable attention (Julian and Gubbins, in press; Yang and Lee, 1976; Lee and Pereyra, in prep.; Pereyra and Lee, in prep.) because it rapidly converges to a solution in extremely complex media.

The ray tracing problem to be solved for use in the teleseismic three-dimensional inversion is not the same as the two point boundary value problem solved by the bending method. This is because the entry point of the ray into the base of the model is unknown, while the slowness vector along the bottom boundary is known and is equal to the ray parameter of the teleseismic ray. The

shooting method is easily adapted to the solution of this "mixed" boundary value problem and is used to calculate the desired ray paths.

Equations for the initial value problem are conveniently parameterized by the travel time, t , along the ray, and are

$$\frac{d\vec{r}}{dt} = v^2\vec{L}$$

and

(3.24)

$$\frac{d\vec{L}}{dt} = \frac{\vec{\nabla}v}{v}$$

where \vec{r} is the position vector and \vec{L} is the slowness vector or instantaneous tangent to the curve described by $\vec{r}(t)$ having magnitude

$$|\vec{L}| = 1/v.$$

The six first order differential equations specified by (3.25) may be numerically integrated forward in time to generate the ray path from an initial location \vec{r}_0 with slowness specified by \vec{L}_0 . In practice, a very fast second order Runge Kutta scheme due to Wesson (1970) performs the integration satisfactorily. Extensive comparisons between more elaborate integration techniques, such as the step-size extrapolation method of Bulirsch and Stoer (1966)

(Acton, 1970), show that the Runge Kutta solution is sufficiently accurate (0.01 sec along a 20 sec ray path) for use in this problem. Computation of the ray by the Runge Kutta algorithm is also about one order of magnitude faster than the variable step size method used in the comparisons.

The ray equations (3.24) break down at layer boundaries where the velocity is discontinuous. The ray is advanced across the boundary using the fact that the parallel components of the slowness vector are constant across it (Snell's law). Propagation of the ray terminates when it reaches a predetermined datum, usually at the elevation of the station. When the shooting error or horizontal distance between ray endpoint and target station falls within a pre-selected tolerance (typically 100 m) the ray is considered to have converged. Larger shooting error requires the forward propagation of the ray to be repeated from the base of the model using a revised entry point.

Viewed formally, the coordinates of the required basal entry point (x_b, y_b) are the roots of two non-linear simultaneous equations implicitly defined by (3.24) as

$$\begin{aligned} X(x_b, y_b) &= x_t \\ Y(x_b, y_b) &= y_t \end{aligned} \tag{3.25}$$

where (x_t, y_t) are the surface coordinates (in the horizontal

plane) of the desired endpoint (Julian and Gubbins, in press). The False Position method is well suited for the solution of (3.25) because all of the required information is at hand. Initially x_b and y_b must be estimated independently because the two-dimensional False Position method requires three previous trial values. Given three previous estimates the False Position solution may be written compactly as (Acton, 1970):

$$\begin{vmatrix} x_b - x_b^1 & x_b - x_b^2 & x_b - x_b^3 \\ \Delta x_t^1 & \Delta x_t^2 & \Delta x_t^3 \\ \Delta y_t^1 & \Delta y_t^2 & \Delta y_t^3 \end{vmatrix} = 0$$

and

(3.26)

$$\begin{vmatrix} y_b - y_b^1 & y_b - y_b^2 & y_b - y_b^3 \\ \Delta x_t^1 & \Delta x_t^2 & \Delta x_t^3 \\ \Delta y_t^1 & \Delta y_t^2 & \Delta y_t^3 \end{vmatrix} = 0$$

where Δx_t and Δy_t are components of the shooting error and superscripts denote values from previous trials. In practice the trial values used in (3.26) must be carefully chosen. The algorithm outlined by Acton (p. 377, 1970) is used here and appears to be satisfactory in most circumstances.

3.4.2 Application to the Hanning Model

The layered velocity structure with lateral heterogeneities specified by hanning basis functions is well suited for the calculation of ray paths and travel times since the velocity and its first derivative are continuous everywhere within a layer. Partial derivatives of the travel time with respect to the basis functions for use in the model inversion are calculated at the midpoint of each Runge Kutta step and accumulated along the ray path as described in §3.2.3.1. Convergent solutions for 2000 rays, together with medium partial derivatives calculated for a 100 km thick heterogeneous structure for Hawaii requires about 1 minute of CPU time on a CDC 7600 computer. Iterative solutions for several simple, known structures are examined in Appendix B.

TABLE 3.1. Inversion results for Hawaii stations and teleseismic sources using systematic differences between Jeffreys-Bullen and Herrin tables as data.

<u>Layer</u>	<u>Thickness</u>	<u>Block Length</u>	<u>Maximum Perturbation (%)</u>	<u>Range (%)</u>
1	15.0	7.5	-0.19	0.35
2	30.0	20.0	0.23	0.46
3	30.0	20.0	0.42	0.72
4	30.0	20.0	-0.32	0.61
5	60.0	40.0	0.34	0.62

Chapter 3 - Figure Captions

Figure 3.1 Spatial sampling of model elements used by quantized model. Note that sampled element contains only a small fraction of the total ray path in the layer in this example.

Figure 3.2 Sampling algorithm used by block model. Parts of blocks in a single layer with non-zero travel time partial derivatives are shown.

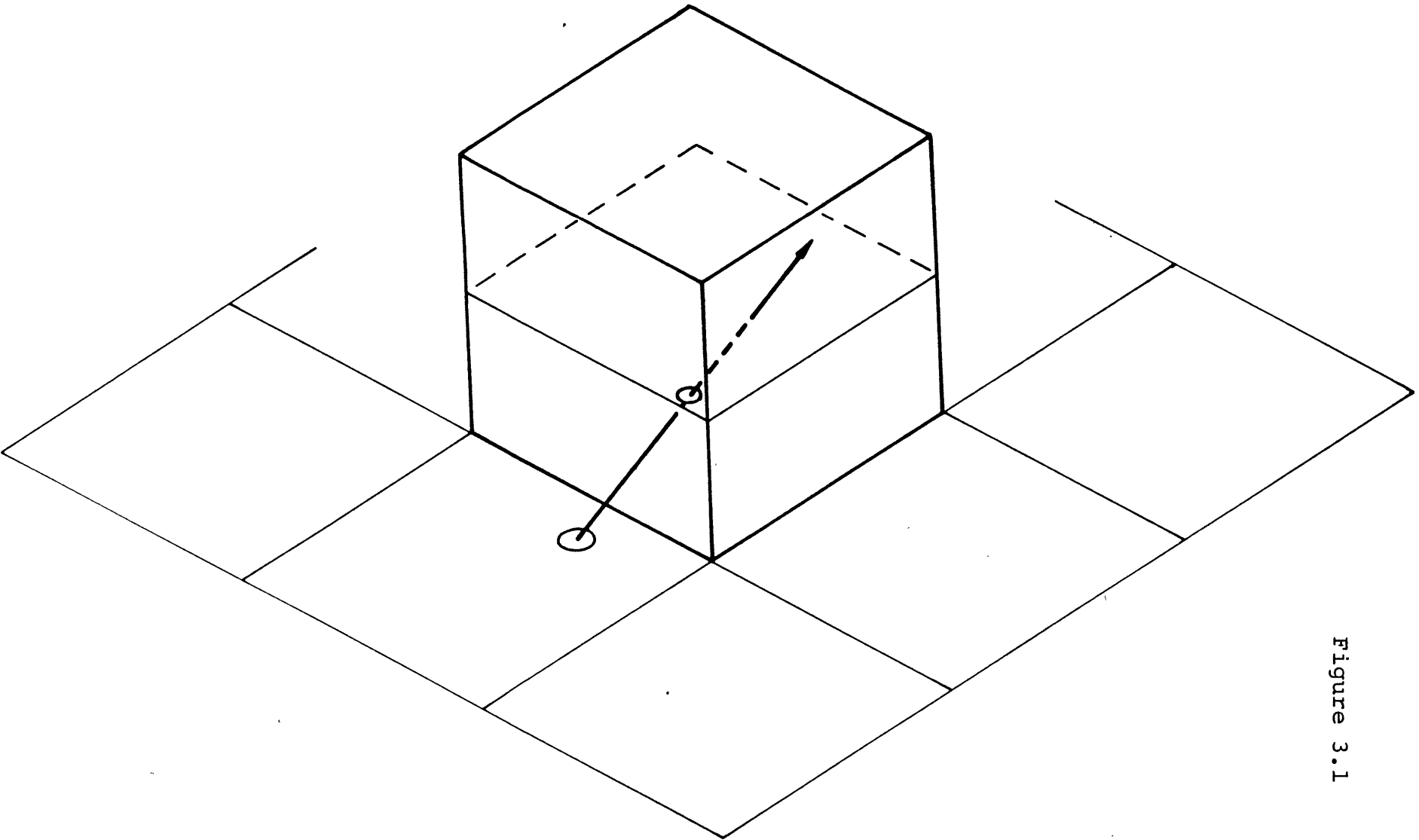


Figure 3.1

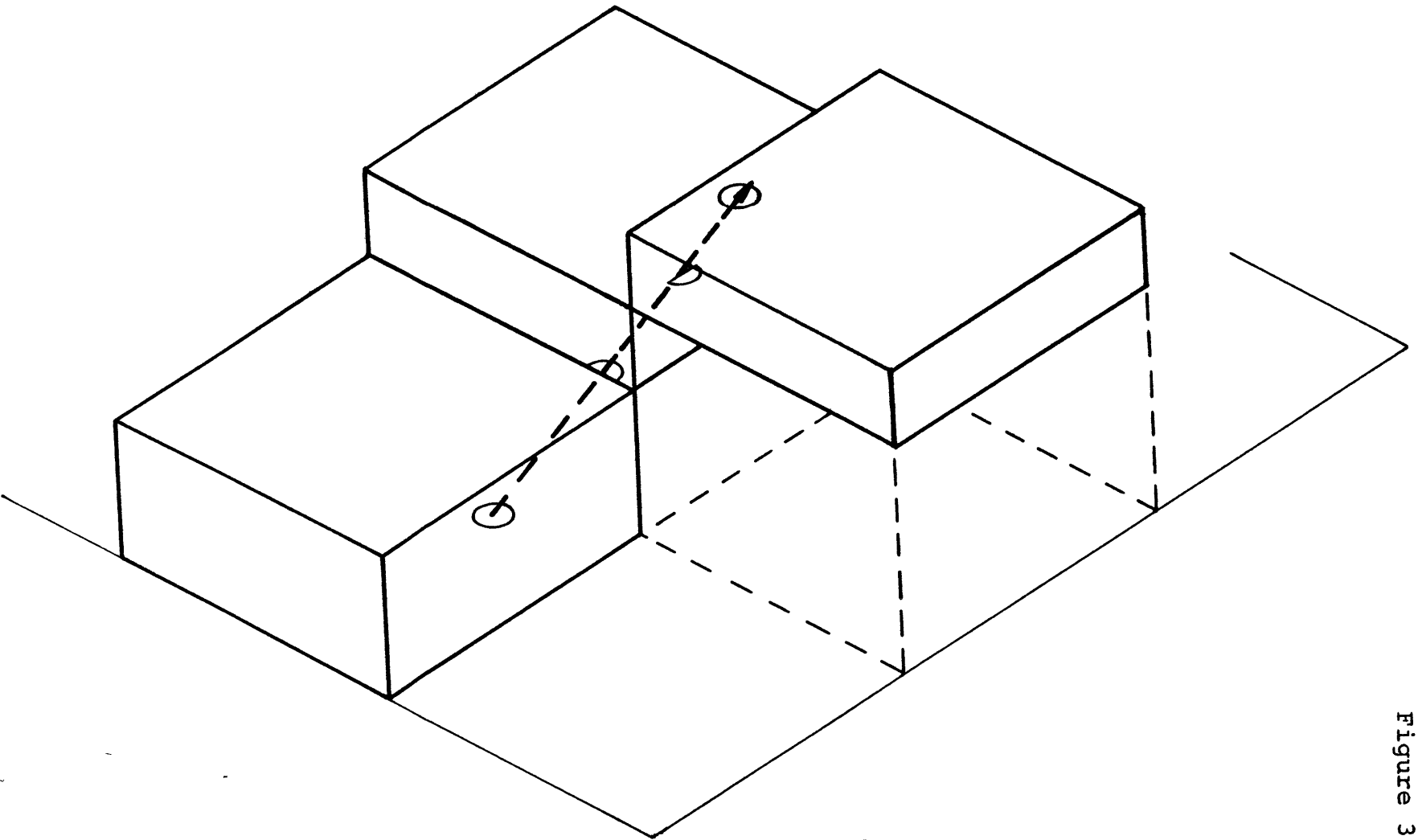


Figure 3.2

CHAPTER 4: Three-Dimensional Crust and Mantle Structure Beneath Hawaii from Teleseismic Waves

Qualitative analysis of teleseismic travel time data recorded on the Island of Hawaii indicates the presence of strong lateral velocity contrasts in the underlying crust and mantle. In this chapter relative teleseismic travel time residual data are analyzed using the method developed in §3 to obtain quantitative estimates of the location and velocity contrasts of three-dimensional heterogeneous structures near the Hawaiian seismograph array.

Because models obtained by the inverse method may possess some dependence on the size and spacing of model elements, solutions for a variety of element configurations need to be compared. Strong lateral variations in crustal structure complicate the modeling and require additional care in their treatment. To this end, several distinct element gridworks are described in the first section, with later sections being devoted to the inversion results.

4.1 Model Framework for Three-Dimensional Inversion Studies

The general problem of selecting a framework suitable for use in inverting a particular set of travel time data requires a balance between element resolution and flexibility of the model to describe heterogeneous structures. In the limit of arbitrary dense sampling by azimuthally

well distributed ray paths, element dimensions are limited only by the condition that ray optics apply.

According to Chernov (1960) ray theory is valid along a path of length L for waves with wave number k when

$$ka \gg 1$$

and

$$ka^2 \gg 2\pi L$$

where a is the scale length (correlation distance) of randomly distributed heterogeneities. Scattering of the waves by small scale heterogeneities ($ka \ll 1$) will be negligible when

$$8 \left(\left\langle \left(\frac{\Delta V}{V} \right)^2 \right\rangle \right) k^4 a^3 L \ll 1$$

(Rayleigh scattering). In this case the wave travel time will be perturbed as if it had traversed an equivalent homogeneous body with average velocity V . In between these bounds on a , scattering of the wave front may be important.

Because both the number of receivers and sources is finite some loss of flexibility in describing the medium must, in general, be exchanged for better resolution

of average properties over larger volumes. Practical factors controlling element dimensions suitable for study of the crust and mantle beneath Hawaii include the station network configuration, the distribution of sources observed, including both distance and azimuth, and the vertical velocity structure underlying the array. Of these factors, the network configuration chiefly influences the horizontal spacing of elements, while the source distribution together with the velocity structure control both the vertical spacing of elements and the depth to which the earth may be modeled.

4.1.1 Initial Vertical Velocity Structure

The average vertical velocity structure determines the geometry of the (assumed) ray paths between source and receiver through the familiar expression

$$p = r \sin i/v(r)$$

where p is the ray parameter and i is the angle the ray makes with the vertical at a fractional radius r where the velocity is $v(r)$. Since we assume p to be known for the teleseismic sources, and a flat earth is a valid approximation for our models, this expression reduces to

$$p = \sin i/v(z)$$

where z is the depth below the surface. With ray parameters

restricted to the interval between about 3.8 sec/deg and 8.5 sec/deg this relation implies that the shallowest rays have $i < 45^\circ$ for any reasonable velocity structure ($v(z) < 9$ km/sec). As adequate model element resolution requires that elements are not vertically linked by most rays, the height to width ratio for elements should not be less than 1:1 for Hawaii (§3.1.1).

Exact knowledge of $v(z)$ is not crucial for the inversion chiefly because changes of up to about 10% in $v(z)$ does not significantly alter the sampling of the model. The adopted initial model (Table 4.1) matches average crustal velocities and thicknesses reported by Hill (1969). The P_n velocity falls within the range of values reported by Eaton (1962), Ryall and Bennett (1968), and Hill (1969). Velocities below this depth are conjectural but generally agree with current ideas of plate structure in the oceanic mantle (Forsyth, 1977). The configuration and velocities of the low velocity zone compensate for the effect of the high velocity lithosphere on the total travel time of teleseismic waves so that the systematic residual of the model is nearly zero between 30° and 95° .

4.1.2 Depth of Modeling

The ensemble of ray paths connecting Hawaiian stations and their respective teleseismic sources diverge from the island into an ever expanding area (Figure 4.1). Above a depth of about 100 km the density of rays per

unit area is fairly constant beneath the island. However, at greater depths the absence of adequate numbers of sources from southeastern azimuths becomes apparent as the density of rays directly beneath the island begins to thin rapidly. Because resolution of lateral velocity structure depends upon a crossfire of ray paths through model elements, the appearance of a void in the center of the ray density map (layer 6, Figure 4.1) indicates that raypaths are no longer crossing beneath the island. For the Hawaiian data this effectively limits the depth of modeling to about 150 km.

4.1.3 Selection and Specification of Model Framework

Maintenance of adequate model resolution with acceptable standard errors for the Hawaiian teleseismic observations requires an average of about 50 rays to penetrate each model element. This requirement limits acceptable horizontal spacing of elements to about 20 km in the mantle at depths shallower than about 100 km and to about 40 km below that depth. Because the teleseismic waves may be sensitive to structures with lateral dimensions as small or smaller than the element grid spacing, we anticipate possible difficulties in faithful recovery of three-dimensional structures (see §3.2). To guard against misinterpretation of inverse solutions three distinct frameworks will be employed. These frameworks are specified in Table 4.1 and will be referred to as the coarse grid model (G), the detailed lithospheric model (L),

and the detailed deep structure model (D).

Rapid variations in crustal structure, so evident in the distribution of average station residuals, stress the need for a careful treatment of the crust in the inverse modeling. With about half of the total data variance attributed to the average station residuals, successful models must be capable of explaining this component of the total residual. Although it is likely that the average residual reflects localized conditions near each site, we prefer not to employ algebraic-type station corrections but rather estimate a local contribution to the travel time simultaneously with deeper structures.

Two distinct approaches to modeling of the crust are used. The first divides the crust into a rectangular grid of elements and uses the same element type as employed in the deeper layers. When using this modeling it is necessary to exclude some stations from the inversion, principally those on the summit and central shield of Kilauea, so that stations with very different mean travel time residuals are not grouped into the same crustal model element. The decimated network appears in Figure 4.2 together with the selected gridwork.

The other modeling assigns each station to a unique crustal layer element, thereby eliminating interaction between the solution for elements corresponding to the crust. This procedure allows the use of all stations

while sacrificing direct modeling of the first model layer. Since ray paths to most stations only cross ray paths to adjacent stations below the crust, direct modeling of the crust can only give very limited information about lateral variations in structure. Thus, the loss of the ability to model heterogeneous crustal structure is not serious.

All models studied have their rectangular gridwork oriented along an axis rotated 45° west of north. This direction roughly coincides with the axis of the Hawaiian Island chain. Other studies (Ellsworth and Koyanagi, in press) have shown that rotation of the element grid does not alter the overall character of the solution.

With three separate model frameworks for the mantle, two separate frameworks for the crust and three distinct types of model elements being studied, a simple method for identifying the type of model is needed to avoid confusion. The code adopted to identify the model types appears in Table 4.3. Following the symbol table, the code 5DH3, for example, denotes the third iteration solution for a five layer deep structure model with hanning type elements. Model codes ending with the letter 'A' use travel time data from all stations (3201 readings) whereas all other models use only readings from the selected subset of stations (2434 readings) identified in Figure 4.2.

4.1.4 Model Performance

Evaluation of the performance of a specific inverse solution is not an easy task. Successful models are identified not only by measures of the overall fit to the data, but also through a parameter by parameter evaluation of uniqueness and reliability. Of the 150-300 unknowns contained in each of the models considered below, some of the parameters are well resolved by the data while others are poorly constrained. Similarly, the standard error of the solution also shows considerable variation.

The full resolution matrix for a solution contains n^2 elements, where n is the number of unknowns and is impractical to display directly. Concrete information on resolution for individual parameters is presented in two ways. Selected rows of the resolution matrix are shown in the same block-layer format used to display the solution to give the reader a feel for model smoothing on a parameter by parameter basis (Table 4.3). Secondly, the diagonal element of the resolution matrix is shown together with solution values for all the models illustrated. This single value acts as an accurate discriminator between well-resolved and poorly-resolved parameters.

Solution standard error, like the resolution matrix, needs to be examined on an element by element basis. Fortunately, a simple relation exists between standard error and the diagonal element of the resolution matrix

(§B.1, Figure B.1). This exact bound on model standard error as a function of the diagonal element of the resolution matrix (3.17) is shown in Figure 4.3 with $\sigma_d = .1$ sec and $\theta^2 = .005$ sec²/°². Rather than clutter the figures showing solutions with both resolution information and standard error, the standard error bound corresponding to any diagonal element of the resolution matrix can be read directly from Figure 4.3.

Two useful gross indicators of solution performance are the variance explained by the model and the trace of the resolution matrix. The former directly measures how successfully the model explains the data while the latter gives a rough idea of the number of model space eigenvectors contributing to the solution (§B.1). These values appear in Table 4.4 for each of the models discussed below.

A more detailed examination of variance improvement can be made for the hanning type models. Since the forward ray tracing problem can be solved for these heterogeneous models, it is a simple matter to isolate the variance explained by each layer. This is done by calculating the residual variance explained by the top layer alone, then the top two layers alone, and so forth. The difference in residual variance between forward models which differ by one layer equals the variance explained by heterogeneous structure in that layer.

Inter-model comparisons between solutions computed under a wide range of assumptions is an essential part of

the model evaluation process. Suites of solutions which undergo radical changes when the element framework is shifted or has its dimension altered, or when element types are changed, are of questionable validity and cannot be interpreted with confidence (see §B.4). A useful statistical measure of the similarity of two solutions is the linear correlation between them. Models are judged to be similar when the linear correlation has appropriate slope (usually positive with a value of about 1.0) and its correlation coefficient exceeds the critical confidence level appropriate for the number of degrees of freedom. Only solution elements with $R_{ii} \geq 0.5$ are compared in this analysis.

4.2 Three-Dimensional Models on a Coarse Grid

The initial suite of models for crust and mantle structure to be considered use the coarse grid framework (G), and a variety of model element types. Presentation of a multifirmity of model solutions based upon a common geometric division of the medium allows us to study the merits of each characterization of lateral heterogeneity. For all models a common damping parameter of $\theta^2 = 0.005 \text{ sec}^2/\%^2$ is used in computation of the damped least squares solution (3.14).

4.2.1 Four Layer Models

The most exhaustive comparison of the effect of the model parameter describing inhomogeneous velocity structures is made for this simple model. From top to bottom, the four layers correspond, approximately, to the crust, upper and lower halves of the lithosphere, and the uppermost part of the asthenosphere.

The initial comparison is made between six models including two single iteration solutions (models 4GQ and 4GB) and for solutions iterated until they converged (4GSB3, 4GH2, 4GSH3, and 4GSH3A). The number of parameters modeled and the variance improvement for each solution appear in Table 4.4. Approximately half of the variance is explained by the crustal model with about 30% being explained by mantle structure. The residual variance of about 0.01 sec^2 agrees with our a priori estimate of σ_d . Although all models reduce the variance of the travel time data to acceptable levels, SH type models (unique first layer elements for each station and hanning type elements in lower layers) exhibit the best performance.

Solutions for the crustal layer based upon three distinct modeling strategies (Figure 4.4) are quite similar in overall character. The coefficient of linear correlation, r , exceeds 0.9 in all cases. In fact, these crustal solution values are essentially the average station residual cast in the format of per cent velocity contrast. The comparison between station residuals and crustal

velocity perturbations for model 4GSH3A gives a correlation value of $r = .96$.

Volcanic summits and rift zones are clearly identified by high velocity material which averages from 10 to 20% faster than the non-rift shield. Note the clear delineation of the high velocity core of the east rift zone of Kilauea along the entire subaerial extent of the rift. The absence of elongate high velocity contours around other principal rift zones is the result of inadequate station coverage. Extrapolated contours in Figure 4.4c indicate crustal velocities for unsampled portions of the crust based upon analogy with Kilauea.

Point by point comparison of crustal velocities shows some variation in the magnitude of the velocity perturbations. These discrepancies arise through at least two distinct mechanisms. First, intrinsic differences between model element types unavoidably result in variations in the numerical values for the fit of model to data (§B.2). For example, solution values for the hanning model generally exceed those of the block model simply because the hanning value is weighted toward the center of the space sampled by the element.

The second reason for differences between solutions is variations in model resolution between model types. In general, solutions for poorly resolved elements ($R_{ii} \ll 0.5$) are heavily damped. Peripheral model elements with small perturbations often reflect this

condition and do not necessarily imply an actual decrease in the level of velocity fluctuations on the edges of the model.

Velocity perturbations for the three mantle layers derived from six separate modelings (Figure 4.5) exhibit broad scale correspondence at all levels. The linear correlation between models exceeds 0.75 for all inter-model comparisons. The chance occurrence of a linear correlation at least as large is less than 0.5%. Below average velocities appear in the central part of the island with higher than average velocities generally occurring on the periphery, especially off the northeast and west coasts in the two deepest layers. Element by element comparisons between solutions show generally close agreement between all model types. Virtually all the comparisons fall within two standard errors of the least squares correlation determined by all mantle perturbations. Different modelings of crustal heterogeneity do not appear to alter mantle results too greatly (Figure 4.5b and c, d and e) except along the west coast of Mauna Loa in model 4GH2 where exceptionally low velocities are indicated. These low velocities are an artifact of improper modeling of the crust in this model caused by inadvertent deletion of poorly resolved parameters describing the crust beneath a single station (KII).

Expansion of the travel time data set by about 25% produces few changes in the solution (Figure 4.5e and f).

The basic trend is toward a modest increase in solution amplitude, especially in the top two mantle layers. This suggests that the overall pattern is not controlled by data errors but by signal. The most marked variations among the set of models occurs for the middle mantle layer, especially between solutions based upon block elements and those based on hanning elements. Solution values for a few elements can be found which differ by more than twice the standard error of the solutions, as is the case for the comparison between models 4GSB3 and 4GSH3A. However, the overall linear correlation at this depth between these models is still significant ($r = .63$) at very high confidence levels ($p < .005$).

The correlations between solutions in the fourth layer is uniformly excellent. For example, the correlation between models 4GSB3 and 4GSH3A is $r = .90$ in this case. This layer shows significantly greater heterogeneity than either of the overlying mantle layers believed to coincide with the lithosphere. Velocity variations at this level explain almost twice as much of the data variance (18%) as the upper two mantle layers combined (11%) (Table 4.5). This marked increase in lateral structure suggests that this layer may extend into the source volume for Hawaiian basalts.

4.2.2 Smoothed Model

Because the coarse grid framework has only limited flexibility to model lateral inhomogeneities with scale lengths comparable to the element spacing (30 km), it is desirable to compare solutions computed using a translated element grid. Here, the station-block model 4GSB3 is compared with a shifted version of the same model, 4GSBT3 (Figure 4.6a). Visually, the models correlate well, especially in layers 2 and 4. An improved estimate of the velocity fluctuation is obtained by superposing the two solutions and then taking four point averages. This procedure effectively trades resolution length for greater stability. Velocity anomalies for the smoothed-block model (Figure 4.6b) are readily identifiable in not only the unsmoothed station-block models but also the other models of Figure 4.5. Absolute values of the perturbations do not agree as favorably, with the smoothed model displaying greatly reduced velocity contrasts.

4.2.3 Five Layer Model

Teleseismic raypath density for the Hawaiian data is sufficient to permit modeling of the mantle to depths in excess of 150 km. Utilization of model elements with enlarged dimensions maintains resolution for a single additional layer which extends the coarse grid model by 60 km to a total depth of 165 km. Velocity perturbations for this model (Figure 4.7) are very similar to those for the corresponding four layer model (Figure 4.5f). Within

the mantle the coefficient of linear correlation is $r = .76$. Discrepancies between solution values in the upper three mantle layers are virtually restricted to peripheral blocks with inadequate resolution. Note that there is measurable loss of resolution in layer four of model 5GSH3A. This reflects the fact that resolution is artificially enhanced in the bottom layer of any model because homogeneous layers are assumed below it.

Lateral velocity contrasts in the fifth layer of model 5GSH3A (Figure 4.7) differ significantly from the pattern in the overlying layers. Nearly normal velocities underly the island which contrasts with the centralized velocity low seen at shallower depths. In fact, the vertically connected low velocity zone appears to have migrated off the northeast coast of the island. Higher than average velocities continue to border the island on west and on the northeast margin of the model.

4.3 Detailed Deep Structure Models

Structure models computed with a fixed element spacing potentially contain "ghost" images of non-existent structures caused by the inability of the model elements to reproduce rapidly varying structure (see §B.2.3). Smoothing of models with transposed elements, as was done in §4.2.2, is not guaranteed to remedy this problem.

The most direct test for "ghost" structures is

numerical experiments performed with modified grid dimensions. This approach is used in this section to test the stability of models computed using the layer spacings adopted for the coarse grid framework. New models are computed on an element grid with the spacing of element centers reduced from 30 to 20 km.

4.3.1 Four Layer model

The first model considered contains four layers and employs elements unique to each station in the crust and hanning elements in the deeper layers. In general, the solution for this framework (Figure 4.8) compares favorably with the coarse grid models. As with internal agreement between coarse grid models (Figures 4.4, 4.5, and 4.6) the more detailed model of Figure 4.8 agrees satisfactorily in all mantle layers. The similarity of velocity perturbations in the deepest layer is particularly striking.

4.3.2 Five Layer Model

Addition of a single 60 km thick layer results in an inverse solution which bears an overall similarity to other models considered thus far (Figure 4.9). Comparing mantle elements from this model, 5DSH3A, with another solution on the same grid, 4DSH2A, we find an overall correlation of $r = .69$. This correlation is measurably poorer than those found earlier. While the anomaly pattern in the second and third layers are

essentially unchanged, variations in the fourth layer solution are more pronounced. The deepest layer is similar to the five layer coarse grid model of Figure 4.7. Both solutions contain a pronounced low velocity region offset to the northeast of the island.

4.4 Detailed Lithosphere Model

The final comparison between solutions for laterally varying structure in the mantle considers models based upon a different choice of layer boundaries. Except for the position of the moho, the layers used thus far were arbitrarily selected. The new layered framework (Table 4.1) divides the lithosphere into three layers instead of the two used previously. Elements are distributed on the same gridwork used for the detailed deep structure models. A wider spacing of elements is impractical since it would make elements broader than they are tall and resolution would suffer markedly. In fact, resolution for hanning-type models is already unacceptable for this framework with the damping selected. Consequently, we shall examine only the station-block model.

Inversion results for the three mantle layers of this model (Figure 4.10) show a velocity anomaly pattern quite similar to the models with thicker layers. The agreement between this model, 4LSB2, and the smoothed version of models 4GSB3 and 4GSBT3 (Figure 4.6b) is particularly striking. Each model clearly indicates the

presence of below average velocities beneath the center of the island at shallow depth in the mantle. Descending deeper into the mantle, the pattern remains centralized beneath the island through the upper two-thirds of the lithosphere, and separates into two distinct low velocity bodies in the basal lithosphere. Well resolved high velocities cluster about South Point, at the southern tip of the island. Less well resolved higher than average velocities generally ring the velocity anomaly pattern.

A linear correlation analysis between the model 4GSB2 (Figure 4.10) and model 4DSH2A (Figure 4.8), which has its elements arranged on the same grid but in thicker layers permits us to examine in greater detail the effect of different layer boundaries upon the solution. Correlation coefficients computed for paired layers (Table 4.6) shows that solution values in the same numbered layer correlate better than solution values in corresponding depth intervals. Although the best correlation occurs between both top mantle layers (layer 2) and these layers have complete overlap, no significant correlation exists between layer 3 of model 4DSH2A and layer 4 of model 4LSB2, which also overlap. In fact, layer 4 from 4LSB2 correlates best with layer 4 from 4DSH2A which completely underlies it. The marginally significant correlation between layers 2 and 4 of the two models is probably coincidental and reflects the fact that the solutions for these two layers are themselves

similar. For model 4DSH2A the correlation between these layers is $r = .57$.

A more critical appraisal of the difference between the models in the depth interval from 55 to 75 km reveals that the major discrepancies are restricted to the mantle underlying Kilauea in the lower right part of the diagram. The correlation between solutions with these values excluded is $r = .72$. Elements excluded from this comparison in model 4LSB2 correlate well with similarly positioned elements of the underlying layer of model 4DSH2A ($r = .77$) which suggests that the bottom layer of the shallower model is contaminated by projection of deeper seated heterogeneities into it from regions which were assumed to be homogeneous. If true, this recommends that modeling should always be extended to the maximum depth allowed by the data.

4.5 Crust and Uppermost Mantle of Kilauea

Inversion studies presented above show that models for three-dimensional anomalies in the mantle underlying Hawaii are not strongly dependent upon either the details of the element framework or the type of elements employed. Because the treatment of crustal structure in all of these studies is exceedingly simplistic, the possibility remains that unmodeled lateral structure with strong velocity contrasts very near the surface contaminate the results. Unfortunately, the distribution of stations does not permit a more detailed analysis of near-surface

structure except within a limited region encompassing the summit of Kilauea (Figure 4.11a). Within this region, station density is marginally sufficient to permit a detailed investigation of small scale heterogeneities at shallow depth.

The modeling of near-surface structure used thus far accounts principally for constant differences in travel time residuals between stations but does not adequately model rapid variations in near-surface structure. Rugged topography on the moho and/or strong lateral variations in lower crustal structure are the most probable alternatives to deep-seated structures for explanation of azimuthal dependencies in the teleseismic residual data (§2.5.3). We will test for the presence of such structures on Kilauea where there is clear evidence for azimuthal variations in relative travel time residuals (Figures 2.16 and 2.17).

The layered framework adopted for this modeling consists of two layers (Table 4.1). The upper layer encompasses the volcanic pile and possibly part of the old sea floor while the lower layer spans the crust-mantle boundary. Because the horizontal divergence of teleseismic rays at opposing azimuths from a single station amounts to only 3 to 6 km at the base of layer one, the effect of laterally varying structures on P wave travel time will be minimal. Consequently, the first layer is safely modeled by elements uniquely

associated with each station. The bottom layer is allowed lateral variations through block elements which are horizontally bisected by the nominally 12 km deep moho (Figure 2.24). The degree of flexibility this model provides should be adequate to determine the magnitude and regularity of structures in the lower crust or uppermost mantle required to fit the residual data.

Inversion results for this modeling indicate that 70% of the total variance of 0.033 sec^2 is explained by first layer parameters and less than 8% is explained by lateral variations in the second layer. Although the variance left unexplained by the model is comparable to the noise level, the total variance reduction exceeds the variance reduction obtained from the simplified crustal layer employed when modeling the entire island by less than 10% (Table 4.4). As heterogeneous structure found deeper in the mantle reduces the variance unexplained by the simplified crustal structure by 50 to 60%, it would appear that detailed modeling of the crust cannot by itself explain the data.

Solution values for the second layer of the Kilauea model are shown in Figure 4.11b as the variations about its mean depth. These depths are obtained from the inversion results (fractional change in layer velocity) by assuming that the velocity contrast in each block originates exclusively from variations in the position of the moho. The standard error of these values is estimated to be 0.7 km. Topography of the moho is quite

gradual within the central part of the figure where resolution is marginally adequate. Unrealistically large vertical relief occurs principally on the model periphery where an inadequate crossfire of ray paths through model elements results in very poor resolution. Because travel time residuals associated with rays traversing these elements are more completely explained by high resolution elements in models of mantle structure, the available data forces us to conclude that exaggerated structure near the crust-mantle interface most probably does not explain the azimuthal variation in relative travel time residuals.

4.6 Synthesis of Mantle Structure Beneath Hawaii

Comparisons between inverse solutions for mantle structure computed using a wide range of medium descriptions show broad structural similarities in the distribution and amplitudes of three-dimensional velocity anomalies. Inter-model comparisons based upon solution values for which $R_{ii} > 0.5$ has shown that the suite of inversion models are linearly related at high confidence levels. Because the existence of a linear relationship demonstrates that the solutions are fundamentally similar, we can reasonably conclude that the average properties of these models are unbiased by the particular choice of model framework or element type. Assessment of the probable error of individual solution values appears to be somewhat more difficult, as point by point comparisons between

models occasionally differ by more than twice their standard error. However, when the basis of comparison is the least squares linear relation between models, the number of discrepant values is reduced to satisfactory levels (<5%). Consequently, standard error bounds given by (3.17) in Figure (4.3) are viewed as acceptable. Based upon these observations, a general statement of solution acceptability is that we may be reasonably confident of the solution value for elements with $R_{ii} \geq 0.5$ and for which $|\Delta V_i/V| \geq 1.4\%$ (based on an intrinsic error variance of 0.01 sec^2). When considering the broad scale features of mantle structure we restrict our attention to features which meet these criteria and disregard weak or poorly resolved features.

Inversion results for representative solutions appear in Figures 4.12 and 4.13. These solutions include the smoothed average of models 4GSB3 and 4GSBT3 (Figure 4.12a), models 4DSH2A and 5GSH3A, which are contoured without smoothing (Figures 4.12b and c), and the detailed lithosphere model 4LSB3 (Figure 4.13). Broad scale features of the solutions are emphasized in these figures by presenting velocity contours at 2% intervals ($\pm 1\%$, $\pm 3\%$, etc.). Details of these solutions may be found in Figures 4.6b, 4.8, 4.7, and 4.10, respectively.

4.6.1 Structure of the Upper Lithosphere

Perhaps the most striking feature in the upper lithosphere is the presence of low velocities directly beneath the island of Hawaii. This low velocity region is especially pronounced within the region bounded approximately by the summits of Mauna Loa, Mauna Kea, and Hualalai where velocities average 2% below normal. Low velocities also appear in an offshore zone south of Kilauea's summit, as was found by Ellsworth and Koyanagi (in press). Curiously, this pronounced velocity low does not encompass summits of either the youngest volcano, Kilauea, or the oldest, Kohala. Average to above average velocities appear beneath these volcanoes.

Higher than average velocities underlie the two largest areas of the island without nearby volcanic summits, the lower eastern flanks of Kilauea and Mauna Loa and the lower south flank of Mauna Loa including South Point. Less well resolved high velocities also appear to bound the island along its northeast coast.

The distribution of velocity anomalies at mid-lithosphere depths (35 to 55 km, Figure 4.13) are basically similar to the overlying pattern. Low velocities occupy the core of the island with higher velocities bounding it on the northeast and southwest coasts. It is noteworthy that velocities average -2.3% below normal beneath the four youngest volcanoes in this depth range (the mantle beneath Kohala was not modeled in this depth interval). One to one correlation

between the position of volcanic summits and low velocities is not found at higher or lower levels in the lithosphere, suggesting that intermediate magma reservoirs may be concentrated at depths of about 40 km.

4.6.2 Structure of the Lower Lithosphere

The depth interval between 45 to 75 km nominally spans the lower half of Pacific lithosphere of the same age as Hawaii (Forsyth, 1977). However, the term "lithosphere" may be misleading because volcanism may have altered the density, temperature, and mechanical properties of the plate to such a degree that the term lithosphere may not strictly apply (Detrick and Crough, 1977, and in press).

Velocity anomalies in this depth interval are the least certain, showing substantial discrepancies between individual solutions (Figures 4.5, 4.12). The most discordant estimates are for the coarse grid models using hanning type elements, with all other solutions, including those using hanning type elements on a different grid, being essentially similar. Features common to the majority of solutions include the continuing presence of low velocities beneath most of the island with higher velocities flanking the lows along the northeast and west coasts. The distribution of the low velocities, which average 2 to 3% below the flanking high velocities is distinctly elongated in the northwest-southeast

direction (top to bottom, Figures 4.12, 4.13). This direction coincides with the lineation of the island chain.

Anomalies for the dissimilar solutions (second mantle layer in Figures 4.6d, e, f and 4.12c) have the same basic pattern in the form of a low enclosed by highs, but the pattern is shifted westward by about 60 km. As the variance explained by this type of model in this depth interval is very small (<5%) and is two to four times smaller than that for the mantle layers immediately above and below, we can disregard these anomalous results without seriously affecting the overall fit of the data.

4.6.3 Structure of the Uppermost Asthenosphere

Excellent correlation between models is found for the strong velocity fluctuations present between 75 and 105 km. Two separate low velocity zones are clearly resolved by the data. One occupies the region beneath the central to northwestern part of the island while the other lies to the east of Cape Kumakahi. Together they form a northwest trending lineation flanked on the northeast and southwest by high velocities.

The magnitude of the velocity contrasts are generally greater in this depth interval than they are at shallower depths, which is reflected in the fact that the model for this layer explains nearly twice as much of the data variance as the two overlying mantle layers.

Locally the contrast between the flanking high velocities and very intense low velocities exceeds 10%.

4.6.4 Deepest Structure Resolvable by the Data

Solutions for lateral variations in velocity between 105 and 165 km from both modelings presented (Figures 4.9 and 4.12c) show a clear northwest to southeast lineation of the velocity field. As with the overlying layers, a central low velocity is flanked by high velocities. The total breadth of the "normal" to low velocity region between the high velocities averages 200 km. The intense low velocity region seaward of the northeast coast of Hawaii coincides with the axis of the Hawaiian island chain extrapolated from the older islands. Its location emphasizes the distinctive step right en echelon offset of the island of Hawaii from the principal direction of island chain growth (Figure 1.1). Maximum low velocities within this elongate anomaly appear to be localized at its southeastern end, ahead of the youngest volcanism. This low velocity anomaly, together with those present at shallower depth, clearly show a broad, connected low velocity region extending upward from the axis of the island chain to the volcanic summits on Hawaii.

Two other distinctive low velocity anomalies appear in the solution for this deepest model layer. An intense, but poorly resolved region appears well ahead of the

island chain, some 100 km southeast of Kilauea. The second region underlies the island of Maui. Although resolution of the latter is somewhat better than for the former, the fact that it also lies on the extreme boundary of the model means that its absolute position is poorly constrained. The data could be equally well explained by a body with similar velocity contrast at either slightly shallower or substantially greater depth along the exiting ray path. Consequently, the correlation of peripheral anomalies in the basal layer with surficial features is highly non-unique and quite possibly coincidental.

4.6.5 Structural Summary

Viewed broadly, lateral variations in velocity at all levels of the mantle beneath Hawaii from 15 km to 165 km depth exhibit a common pattern. Low velocity regions with typical horizontal dimensions of 50 km occupy the central portion at each level. The in-plane shape of the velocity low becomes increasingly elongate, trending northwest to southeast with increasing depth. High velocities characteristically occupy the offshore zone about the island in the lithosphere and bound the tabular low velocity zone in the asthenosphere. The velocity contrast between lows and highs average 3 to 4% in the lithosphere and increases to upwards of 10% in the asthenosphere.

Several facets of the velocity distribution, including

the vertical continuity of low velocities through the lithosphere into the asthenosphere, the increase in heterogeneity below the base of the Pacific plate, and the existence of localized low velocity bodies in the deepest levels strongly support the conclusion that Hawaii overlies a mantle hot spot (Wilson, 1963).

Regardless of the exact nature of the mechanism responsible for the large velocity contrasts, the vertical continuity of the anomalies through the rigid lithosphere into the plastic asthenosphere suggests a common origin for these features. We will examine the implications of these deep-seated features for theories of island chain formation in §6.

4.7 Further Examination of Three-Dimensional Model Performance

The primary features of the relative travel time data from which the three-dimensional models of this chapter are derived include site-to-site variations in mean station residual, azimuthal dependence of the residual at each station, and the array mislocation of the predicted source wavefront (§2.5). By assuming that the theoretical wavefront given by a radially symmetric earth model accurately describes the P-wave incident upon the base of the region modeled, we have shown that the three-dimensional inverse solution is internally consistent and reduces the data variance to our a priori estimate. However, it remains to be

demonstrated that the velocity models actually satisfy the salient features of the relative residual data.

To study this question we need to examine the data left unexplained by the three-dimensional models. These relative travel time residuals are determined by solving the ray equation for the appropriate source-receiver pairs using three-dimensional solutions for hanning type models. They show that these models do, in fact, satisfy the primary components of the data. Mean station residuals are uniformly less than 0.03 sec. The azimuthal variation of residuals at individual stations is reduced to virtually patternless fluctuations, as can be seen in the examples of Figure 4.15. And, finally, the array mislocation diagram computed from the residuals left unaccounted for by the three-dimensional model consists almost entirely of short, randomly oriented vectors (Figure 4.16). The few exceptions are either isolated vectors which also stand out as being anomalous on the original array diagram or belong to clusters of vectors which maintained their orientation but have had their lengths greatly reduced. All in all, it is clear that these three-dimensional models satisfy the primary attributes of the relative teleseismic travel time data.

TABLE 4.1. Element Frameworks for Inversion Studies

COARSE GRID FRAMEWORK (G)			
<u>Depth Interval (km)</u>	<u>Layer Thickness (km)</u>	<u>Velocity (km/sec)</u>	<u>Element Spacing (km)</u>
-4 to 15	19	6.0	7.5
15 to 45	30	8.2	30.0
45 to 75	30	8.3	30.0
75 to 105	30	8.2	30.0
105 to 165	60	8.1	60.0

DETAILED DEEP STRUCTURE FRAMEWORK (D)			
<u>Depth Interval (km)</u>	<u>Layer Thickness (km)</u>	<u>Velocity (km/sec)</u>	<u>Element Spacing (km)</u>
-4 to 15	19	6.0	7.5
15 to 45	30	8.2	20.0
45 to 75	30	8.3	20.0
75 to 105	30	8.2	20.0
105 to 165	60	8.1	40.0

DETAILED LITHOSPHERE FRAMEWORK (L)			
<u>Depth Interval (km)</u>	<u>Layer Thickness (km)</u>	<u>Velocity (km/sec)</u>	<u>Element Spacing (km)</u>
-4 to 15	19	6.0	7.5
15 to 35	20	8.2	20.0
35 to 55	20	8.25	20.0
55 to 75	20	8.3	20.0

KILAUEA CRUST AND UPPERMOST MANTLE FRAMEWORK (K)			
<u>Depth Interval (km)</u>	<u>Layer Thickness (km)</u>	<u>Velocity (km/sec)</u>	<u>Element Spacing (km)</u>
-2 to 8	10	6.0	---
8 to 16	8	7.1	2.5

TABLE 4.2. Symbol Code Key for Inversion Models

Code Format: 1 A B 2 C

Key:

- 1 - Number of layers in model
- A - Element Framework
 - G: Coarse Grid
 - D: Detailed Deep Structure
 - L: Detailed Lithosphere
 - K: Kilauea Crust and Uppermost Mantle
- B - Type of elements describing medium
 - Q: Quantized elements
 - B: Block elements
 - H: Hanning elements
 - SB(SH): Unique block element in top layer for each station and block (hanning) elements in deeper layers
 - SBT: SB-type model with a shifted gridwork
- 2 - Number of iterations. A single iteration is implied when omitted.
- C - Data used in inversion
 - A: Travel time data for all stations used
 - (blank): Travel time data for 30 selected stations used

TABLE 4.4. Data Variance Improvement
and Trace of Resolution Matrix for Three-Dimensional Models.

<u>Model Type</u>	<u>Parameters Modeled</u>	<u>ΣR_{ii}</u>	<u>Variance Improvement*</u>	<u>Residual Variance*</u>
4GQ	149	118	(69.5%)	(.0136 sec ²)
4GB	206	116	(73.8)	(.0117)
4GSB3	140	100	(74.4)	(.0112)
1GSB3	30	23	48.9	.0228
4GH2	230	94	76.2	.0106
4GSH3	146	82	77.6	.0100
4GSH3A	164	99	77.9	.0095
5GSH3A	195	112	79.8	.0087
4DSH2A	248	142	80.0	.0086
5DSH3A	294	168	82.6	.0075
4LSB2	190	94	(72.7)	.0122
2KSB	166	67	(76.9)	(.0076)

* Values in parentheses are estimates, and most probably overestimate the actual improvement by 1-2%.

TABLE 4.5. Variance Improvement Due to Each
Layer of the Solution for Model 4GSH3

<u>Layer</u>	<u>Variance Explained</u>	<u>Percent</u>
1	0.022 sec ²	49%
2	0.003	7
3	0.002	4
4	0.008	18
residual variance	0.009	21

TABLE 4.6 Linear Correlation Coefficients Between
Selected Layers for Models 4LSB2 and 4DSH2A

Model 4LSB2	Model 4DSH2A		
	<u>Layer 2</u> <u>15 to 45 km</u>	<u>Layer 3</u> <u>45 to 75 km</u>	<u>Layer 4</u> <u>75 to 105 km</u>
Layer 2 15 to 35 km	.90	.28	.45
Layer 3 35 to 55 km	.27	.62	.01
Layer 4 55 to 75 km	.52	.11	.61

Chapter 4 - Figure Captions

Figure 4.1 Ray density map at indicated depth below
Island of Hawaii.

Figure 4.2 Seismograph network subset (triangles) used in
inversion studies. Grid outlines boundaries of block
elements in crust.

Figure 4.3 Exact bound on solution standard error as a
function of diagonal element of parameter resolution
matrix.

Figure 4.4 Velocity perturbations (%) in crust of island.
a) Block model 4GB. b) Hanning model 4GH2. Solution
values with $R_{ii} \geq 0.5$ are enclosed by lines c) station-
hanning model 4GSH3A. All solution values have
 $R_{ii} \geq 0.5$. Dashed percent velocity contours are
extrapolated by analogy with Kilauea from crustal geology.

Figure 4.5 Velocity perturbations (%) in mantle for a)
Quantized model, b) Block model, c) station-block
model, d) Hanning model, e) station-hanning model and
f) station-hanning model using all data. Values in
parenthesis are diagonal elements of parameter
resolution matrix.

Figure 4.6 Velocity perturbations (%) in mantle for a)
station-block model 4GSBT3 computed on a translated
grid and b) smoothed superposition of models 4GSB3
and 4GSBT3.

Figure 4.7 Velocity perturbations (%) in mantle for model 5GSH3A. Values in parentheses are diagonal elements of resolution matrix.

Figure 4.8 Velocity perturbations (%) in mantle for model 4DSH2A. Values in parentheses are diagonal elements of resolution matrix.

Figure 4.9 Velocity perturbations (%) in mantle for model 5DSH3A. Values in parentheses are diagonal elements of resolution matrix.

Figure 4.10 Velocity perturbations (%) in mantle for model 4LSB2. Values in parentheses are diagonal elements of resolution matrix.

Figure 4.11 Map of summit region of Kilauea: a) stations used in inverse modeling (triangles). Enclosed regions correspond to second layer blocks with $R_{ij} \geq 0.5$. b) contour map of deviations from mean depth of moho. Some contours are omitted for clarity.

Figure 4.12 Laterally heterogeneous velocity structure in the mantle beneath Hawaii from a) smoothed superposition of models 4G B3 and 4GSBT3, b) model 4DSH2A, and c) model 5GSH3A. Contour interval 2%. Coastline of Island of Hawaii is shown.

Figure 4.13 Laterally heterogeneous velocity structure determined for model 4LSB2. Bold line encloses blocks with $R_{ij} \geq 0.5$. Coastline of Island of Hawaii is shown.

Figure 4.14 Deepest lateral variations in velocity resolvable by available data from model 5GSH3A. Outline of Hawaiian Islands are shown. Percent velocity contour interval 2%.

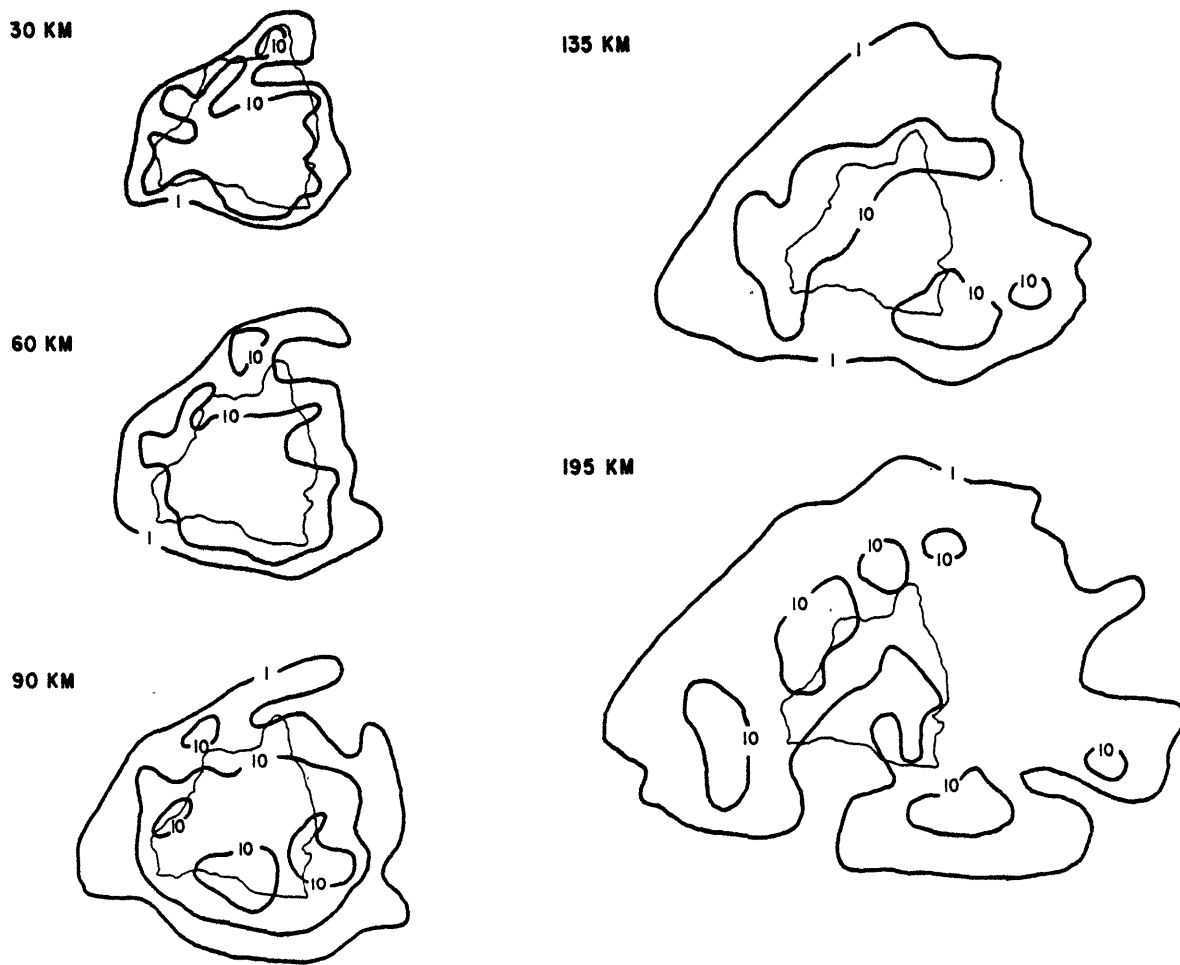
Figure 4.15 Azimuthal plot of relative travel time residuals, not explained by model 5GSH3A.

Figure 4.16 Array mislocation diagrams for Hawaii.

Vector heads locate slowness and azimuth of predicted wavefront. Vector tail locates least squares fit to data. Left diagram has station elevation removed. Right diagram has effect of three-dimensional model 4GSH3A removed.

Figure 4.1

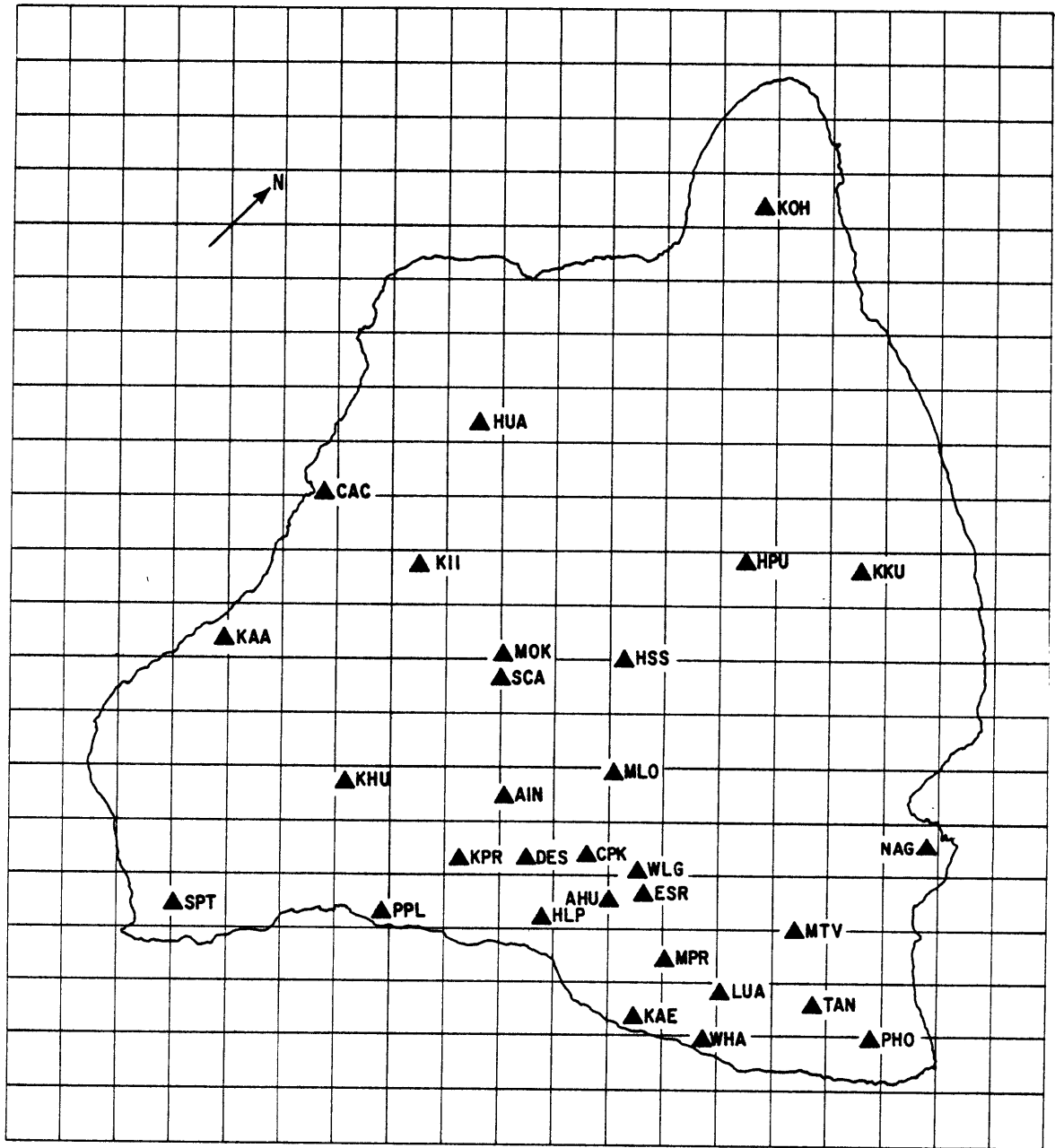
TELESEISMIC RAY DENSITY MAP



0 100 KM

CONTOUR INTERVALS: 1 RAY / 100 KM²
10 RAYS / 100 KM²

Figure 4.2



GRID SIZE 7.5 KM

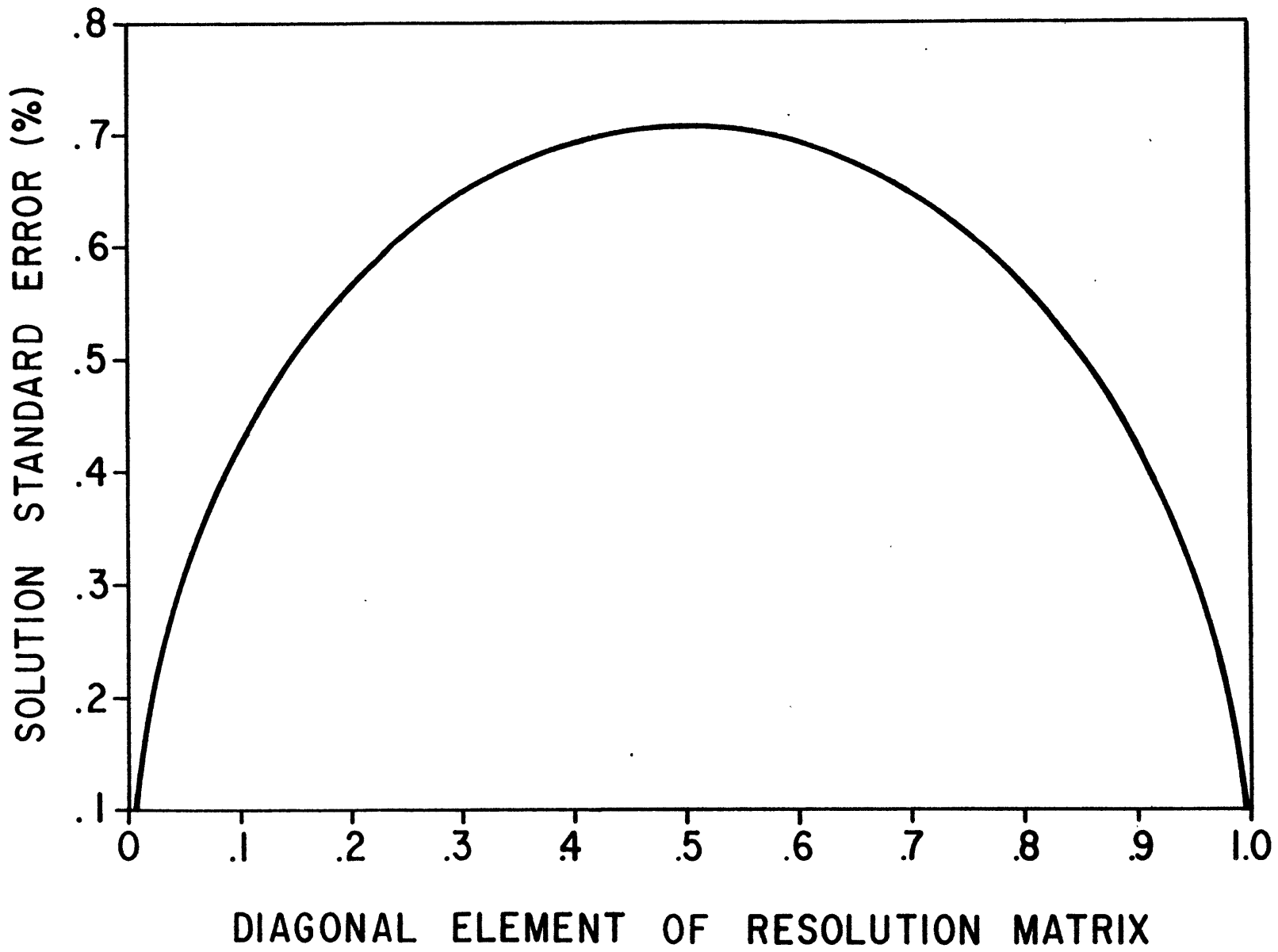


Figure 4.3

Figure 4.4

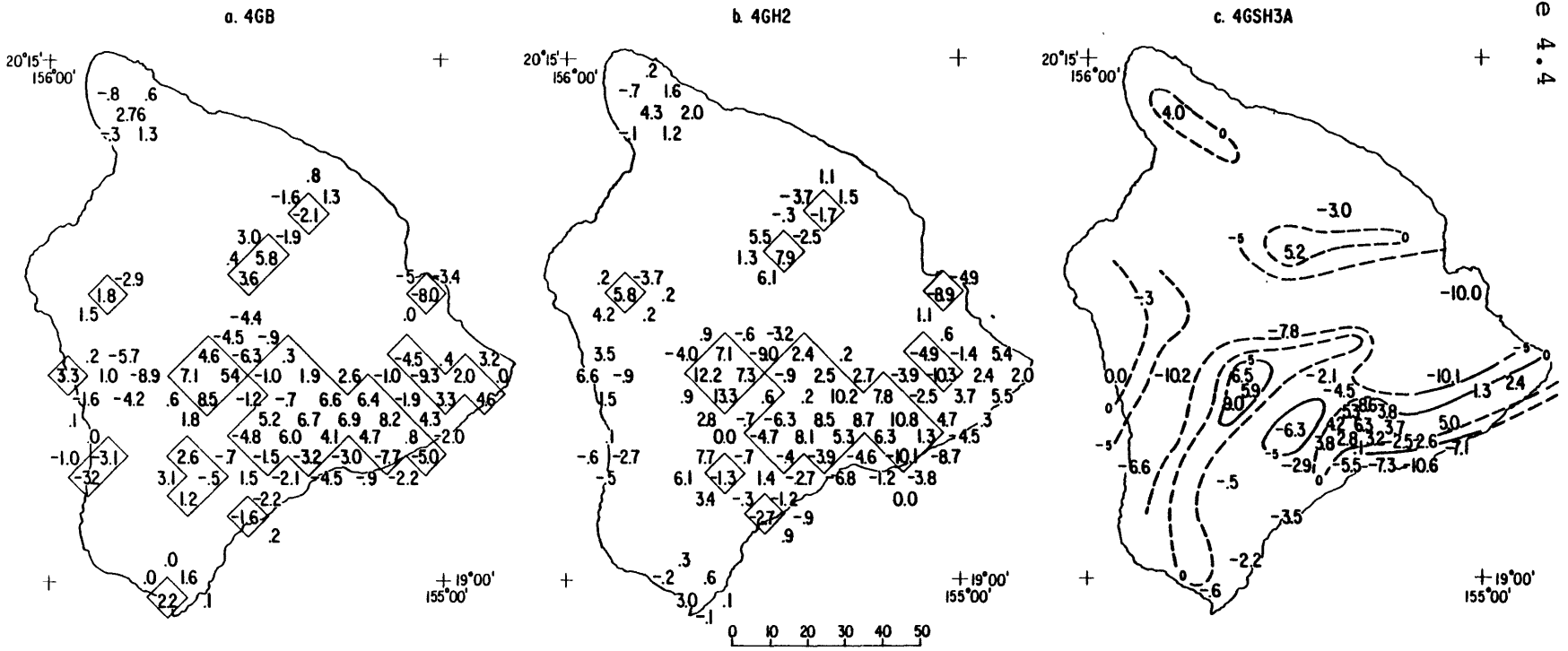


Figure 4.5

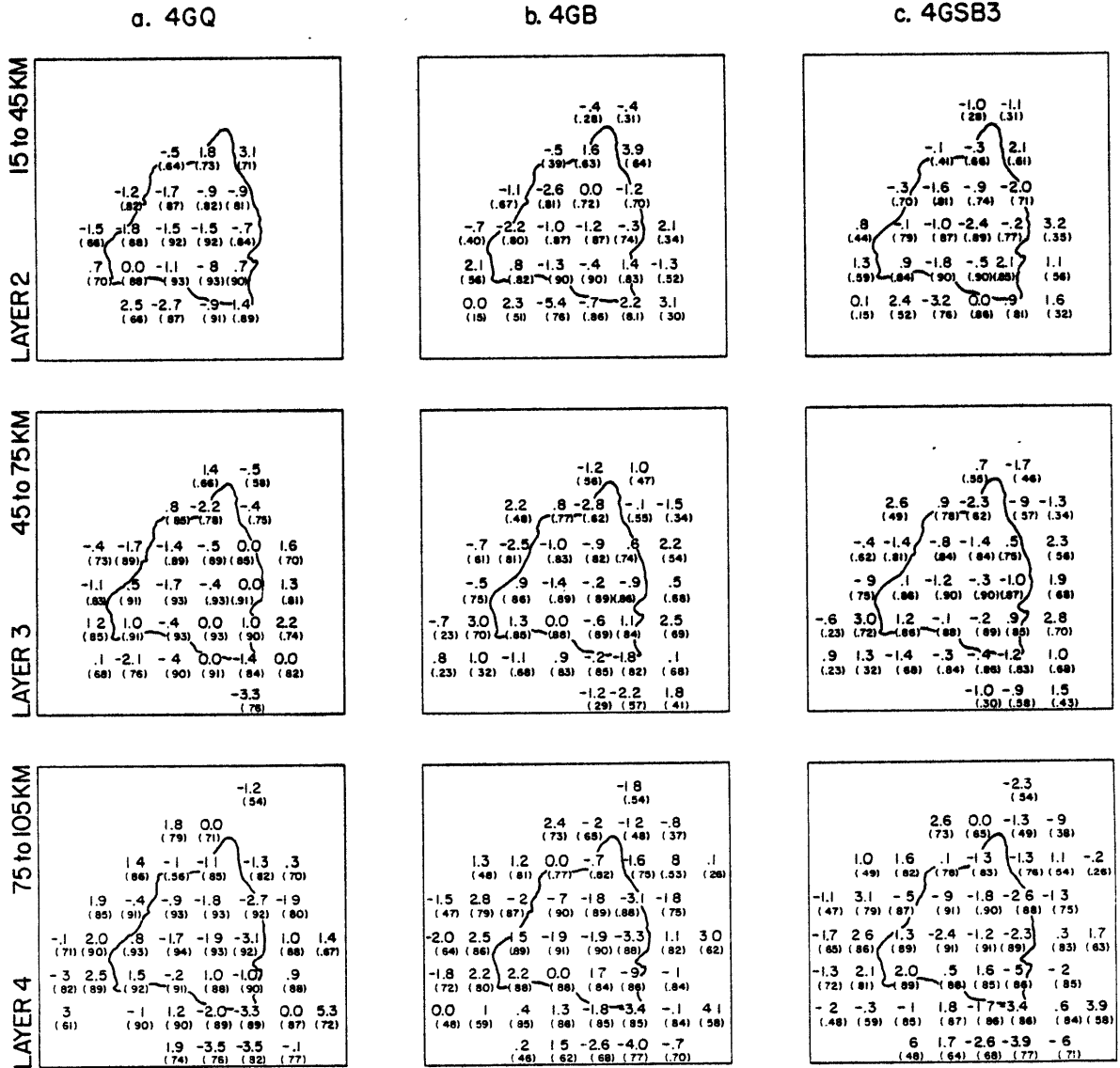


Figure 4.5 (concluded)

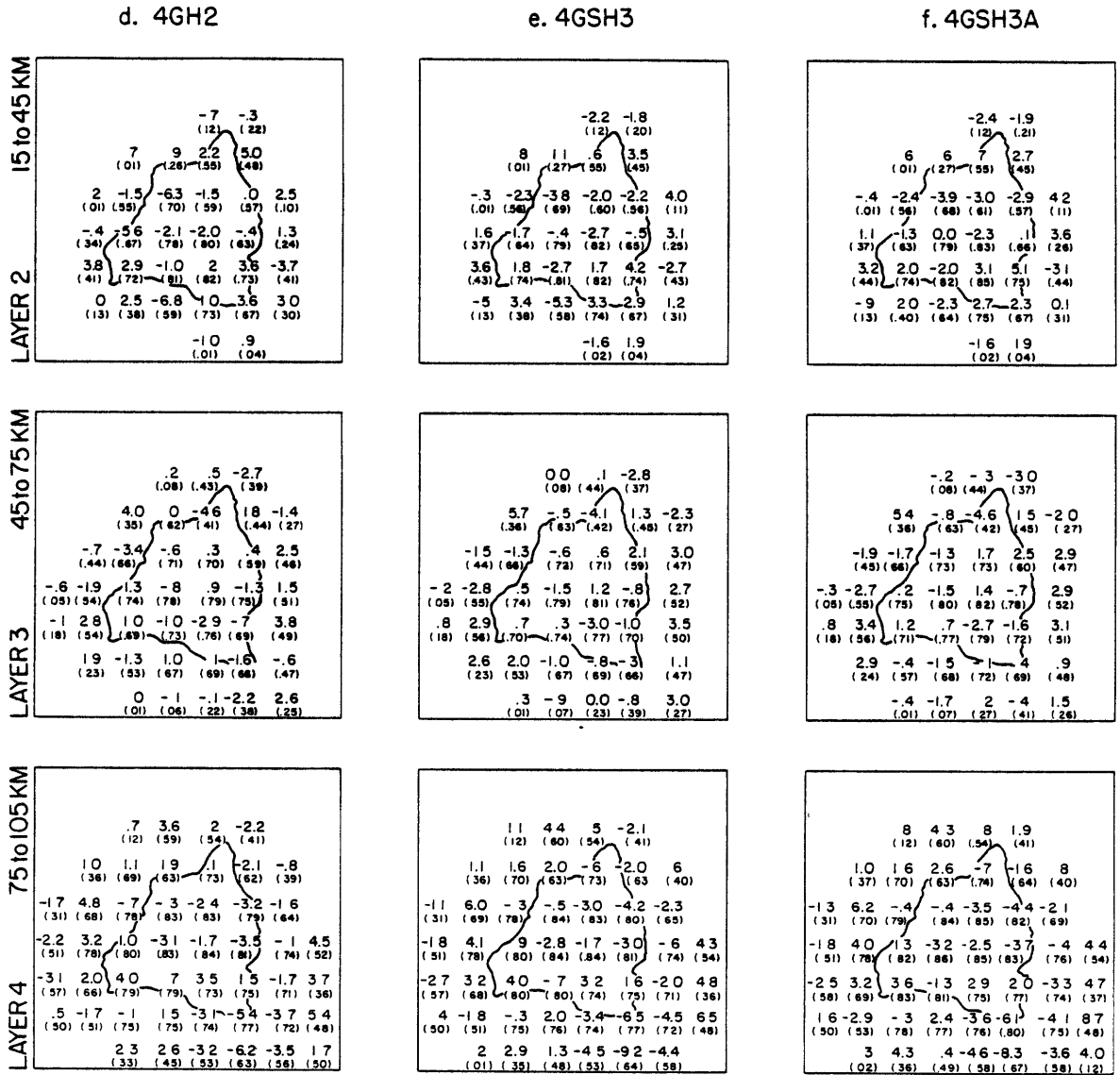


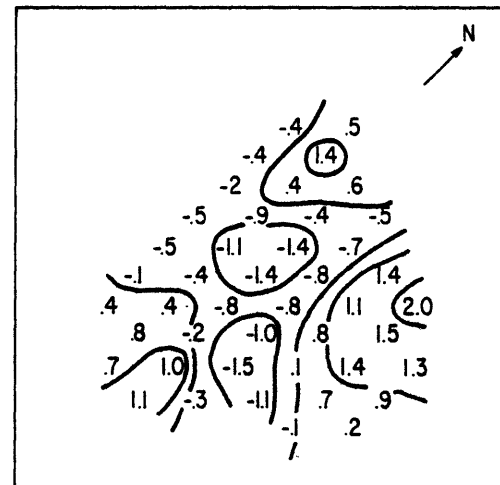
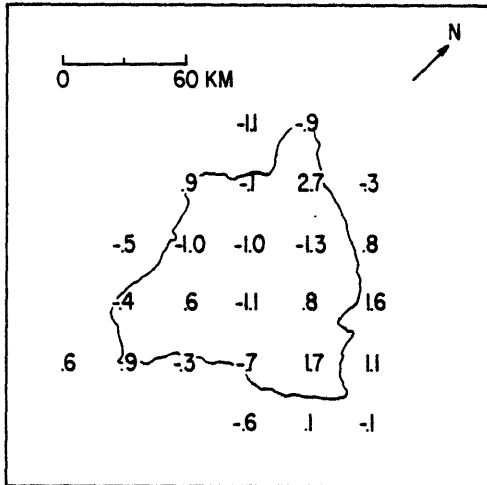
Figure 4.6

a. SHIFTED MODEL

b. SMOOTHED MODEL

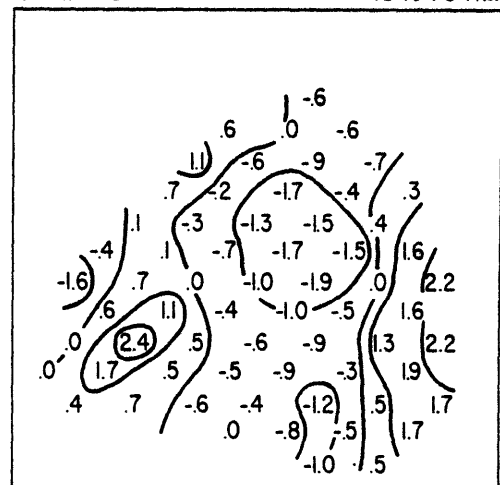
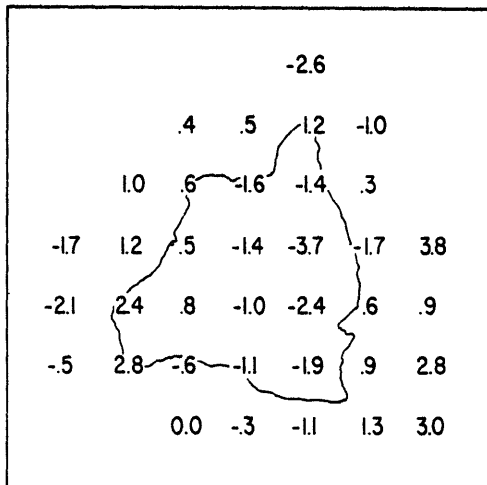
LAYER 2 15 to 45 KM

LAYER 2 15 to 45 KM



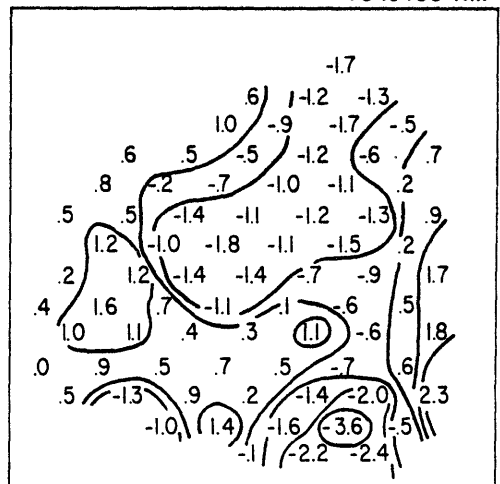
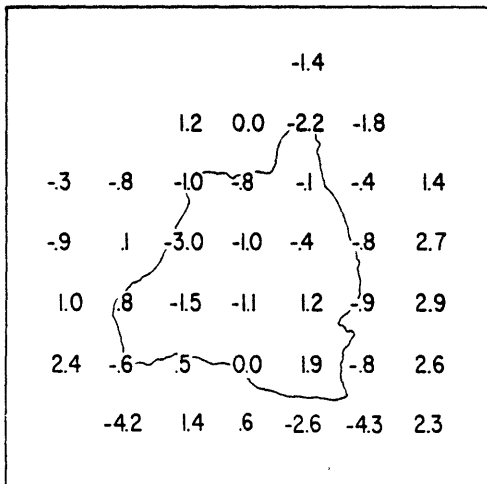
LAYER 3 45 to 75 KM

LAYER 3 45 to 75 KM



LAYER 4 75 to 105 KM

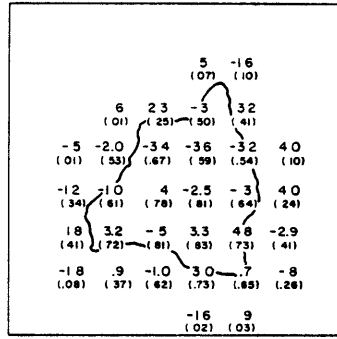
LAYER 4 75 to 105 KM



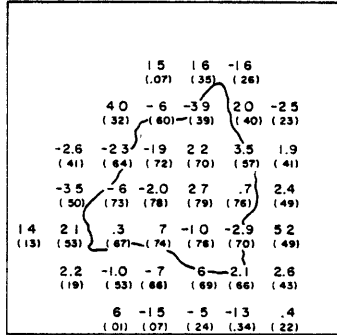
MODEL 5GSH3A

Figure 4.7

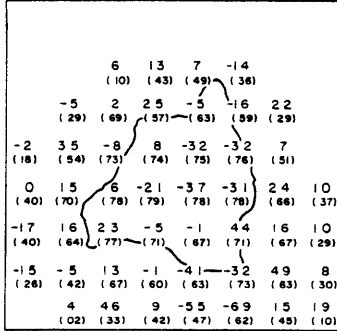
LAYER 2 15 to 45 KM



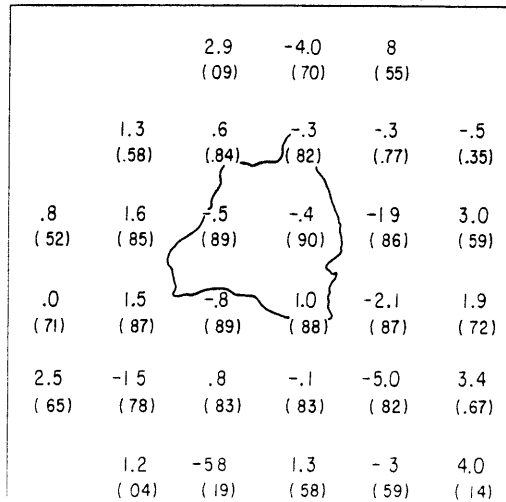
LAYER 3 45 to 75 KM



LAYER 4 75 to 105 KM

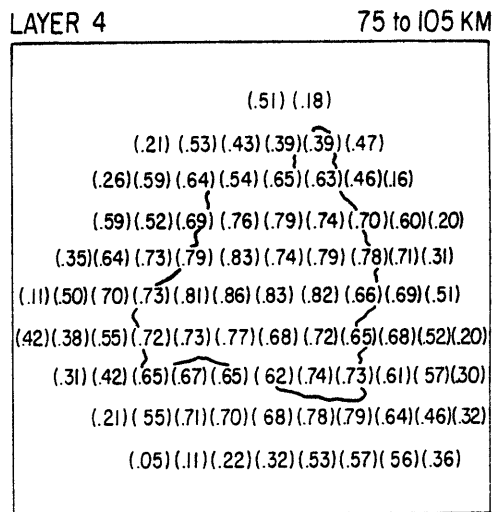
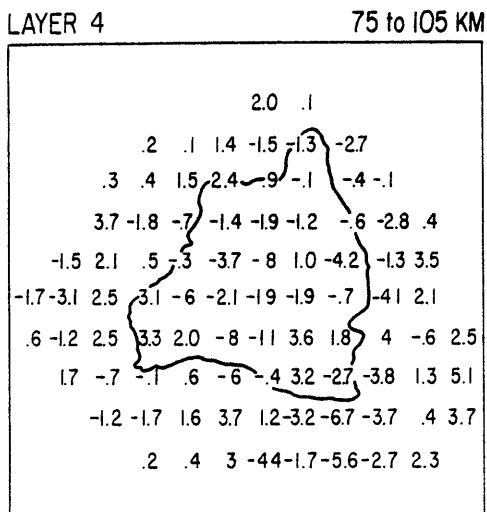
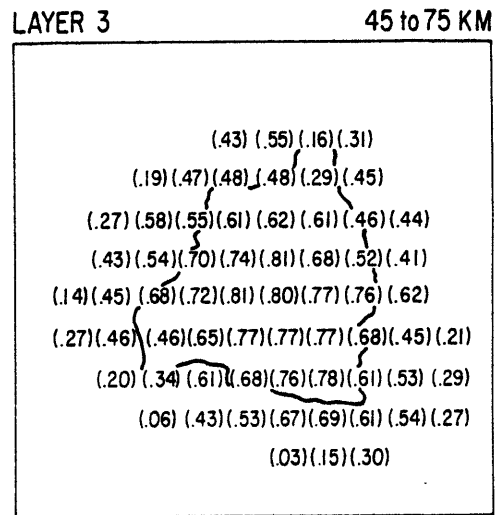
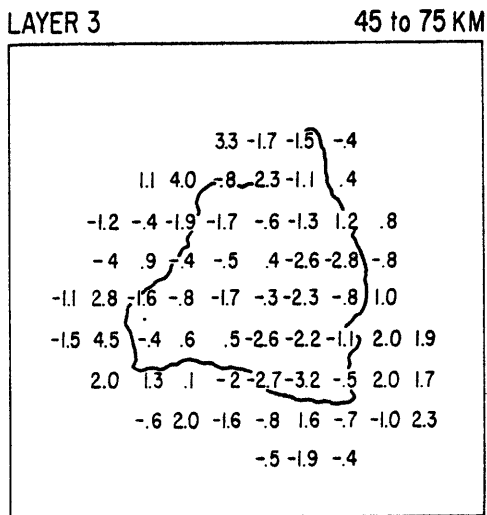
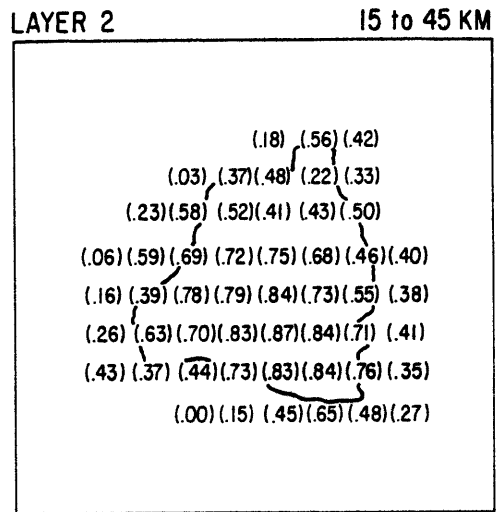
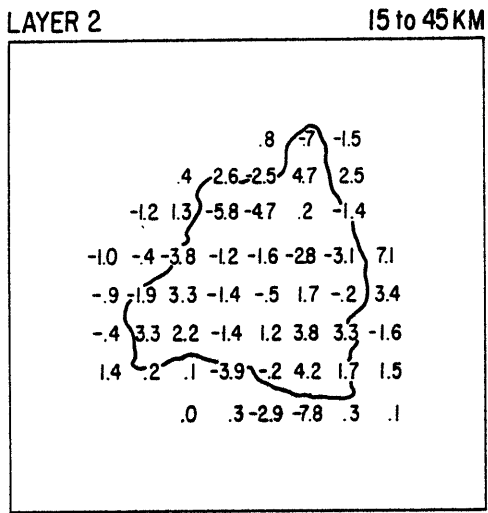


LAYER 5 105 to 165 KM



MODEL 4DSH2A

Figure 4.8



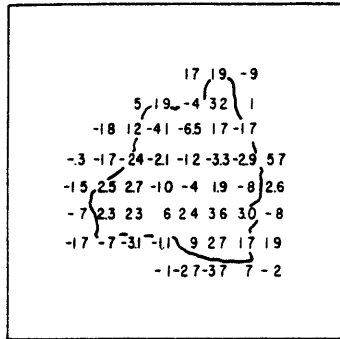
VELOCITY PERTURBATIONS IN %

DIAGONAL ELEMENTS OF RESOLUTION MATRIX

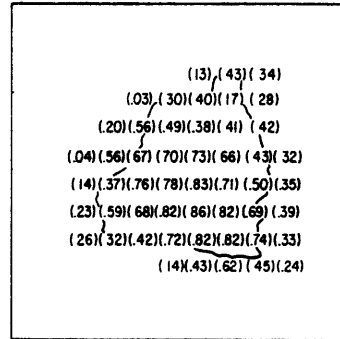
Figure 4.9

MODEL 5DSH3A

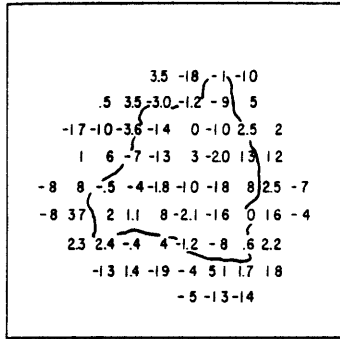
LAYER 2 15 to 45 KM



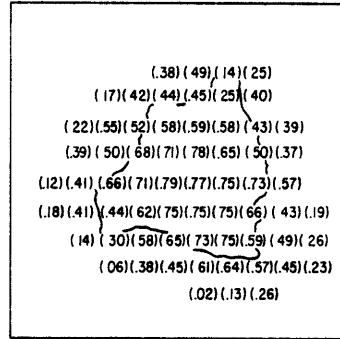
LAYER 2 15 to 45 KM



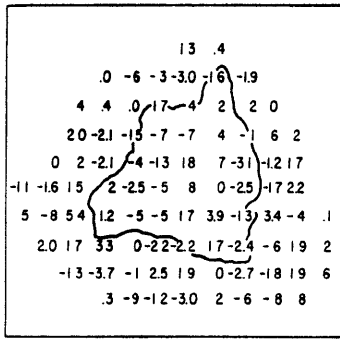
LAYER 3 45 to 75 KM



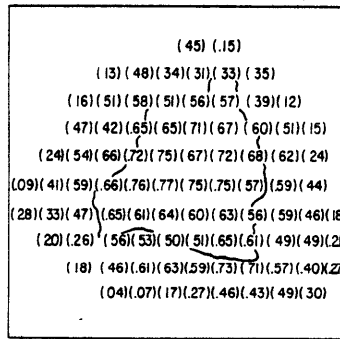
LAYER 3 45 to 75 KM



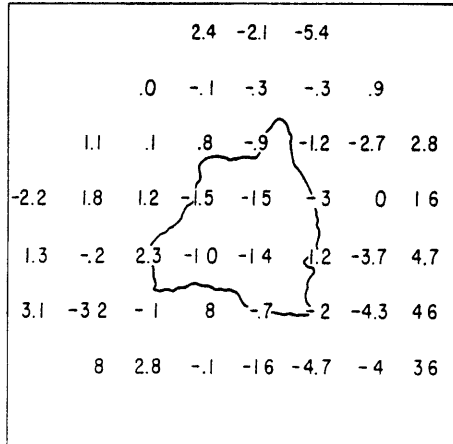
LAYER 4 75 to 105 KM



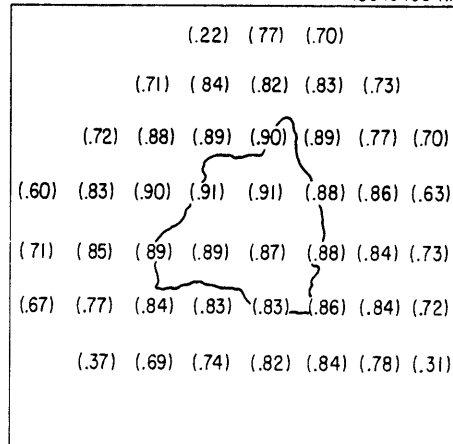
LAYER 4 75 to 105 KM



LAYER 5 105 to 165 KM



LAYER 5 105 to 165 KM



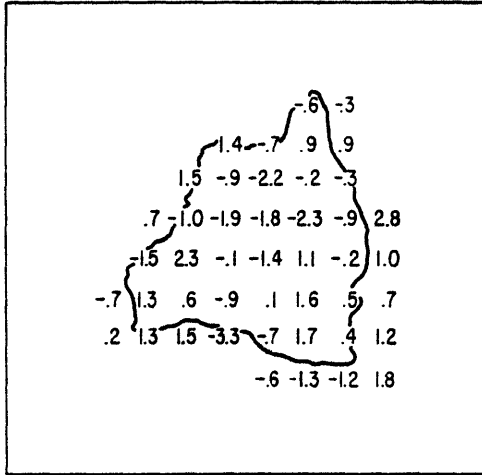
VELOCITY PERTURBATIONS IN %

DIAGONAL ELEMENTS OF RESOLUTION MATRIX

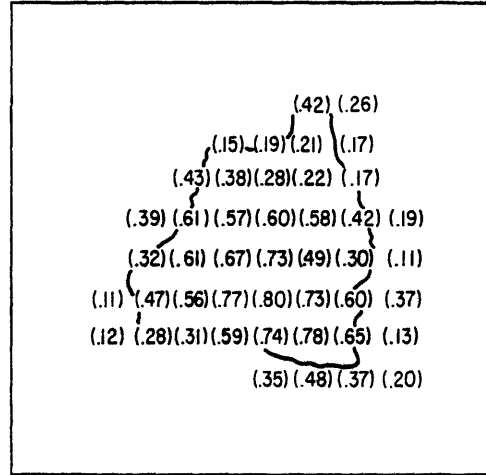
MODEL 4LSB2

Figure 4.10

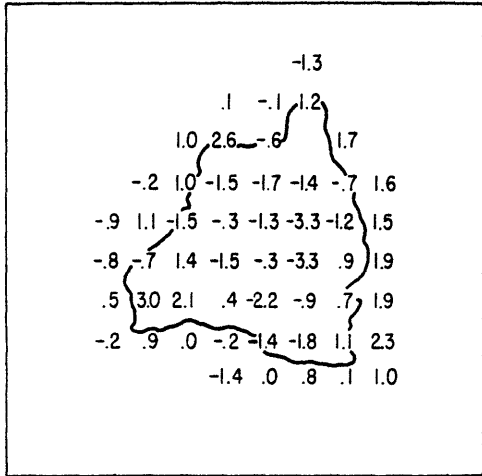
LAYER 2 15 to 35 KM



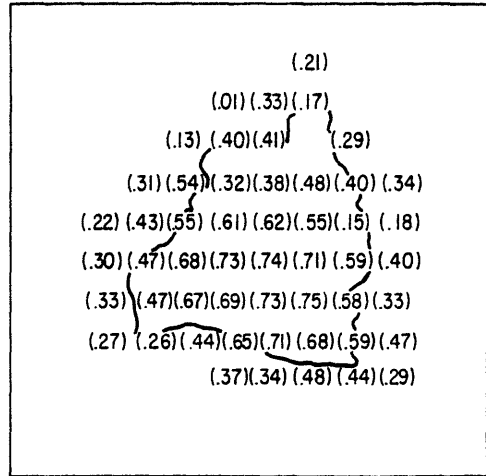
LAYER 2 15 to 35 KM



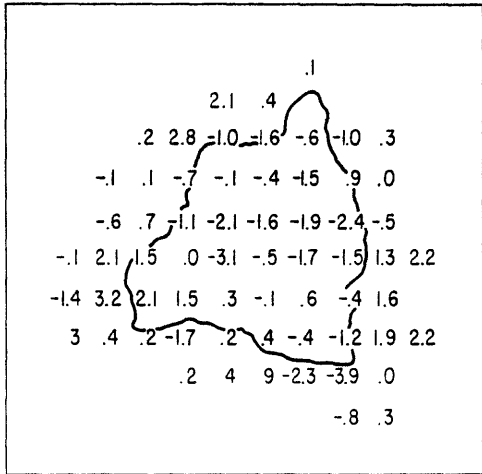
LAYER 3 35 to 55 KM



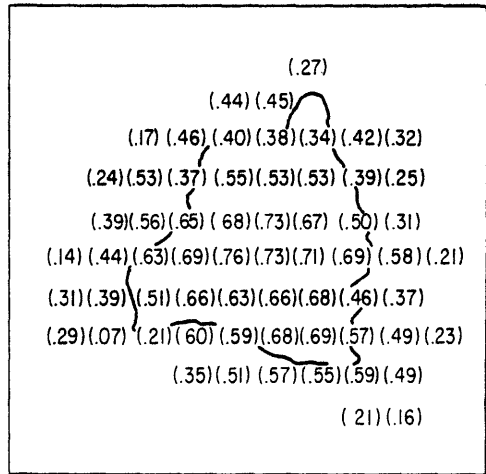
LAYER 3 35 to 55 KM



LAYER 4 55 to 75 KM



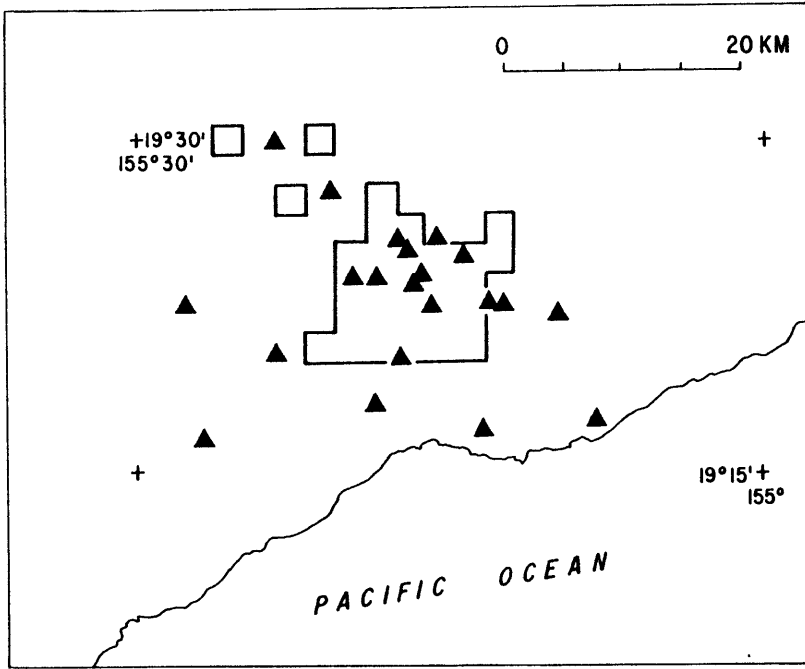
LAYER 4 55 to 75 KM



VELOCITY PERTURBATIONS IN %

DIAGONAL ELEMENTS OF RESOLUTION MATRIX

a.



b.

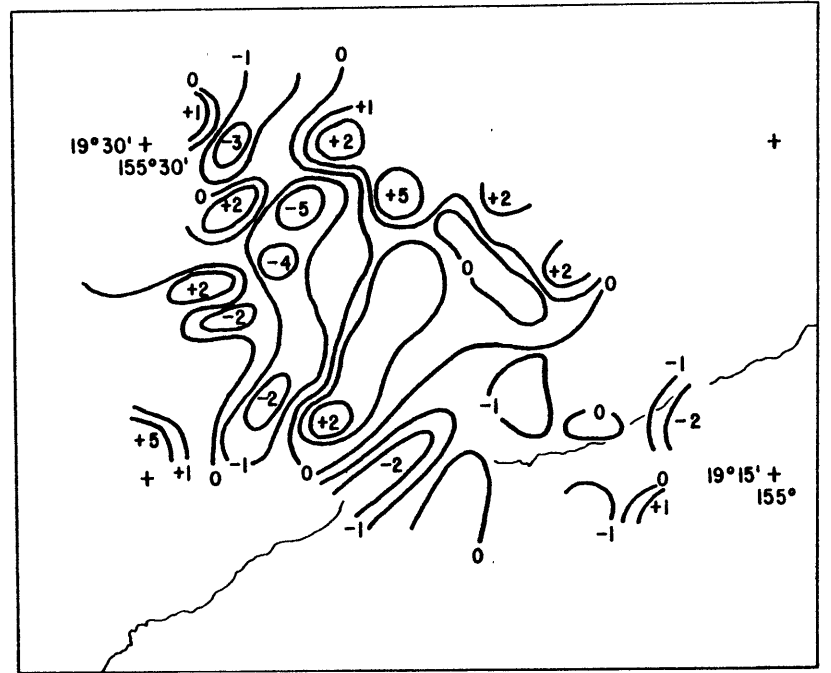


Figure 4.11

Figure 4.12

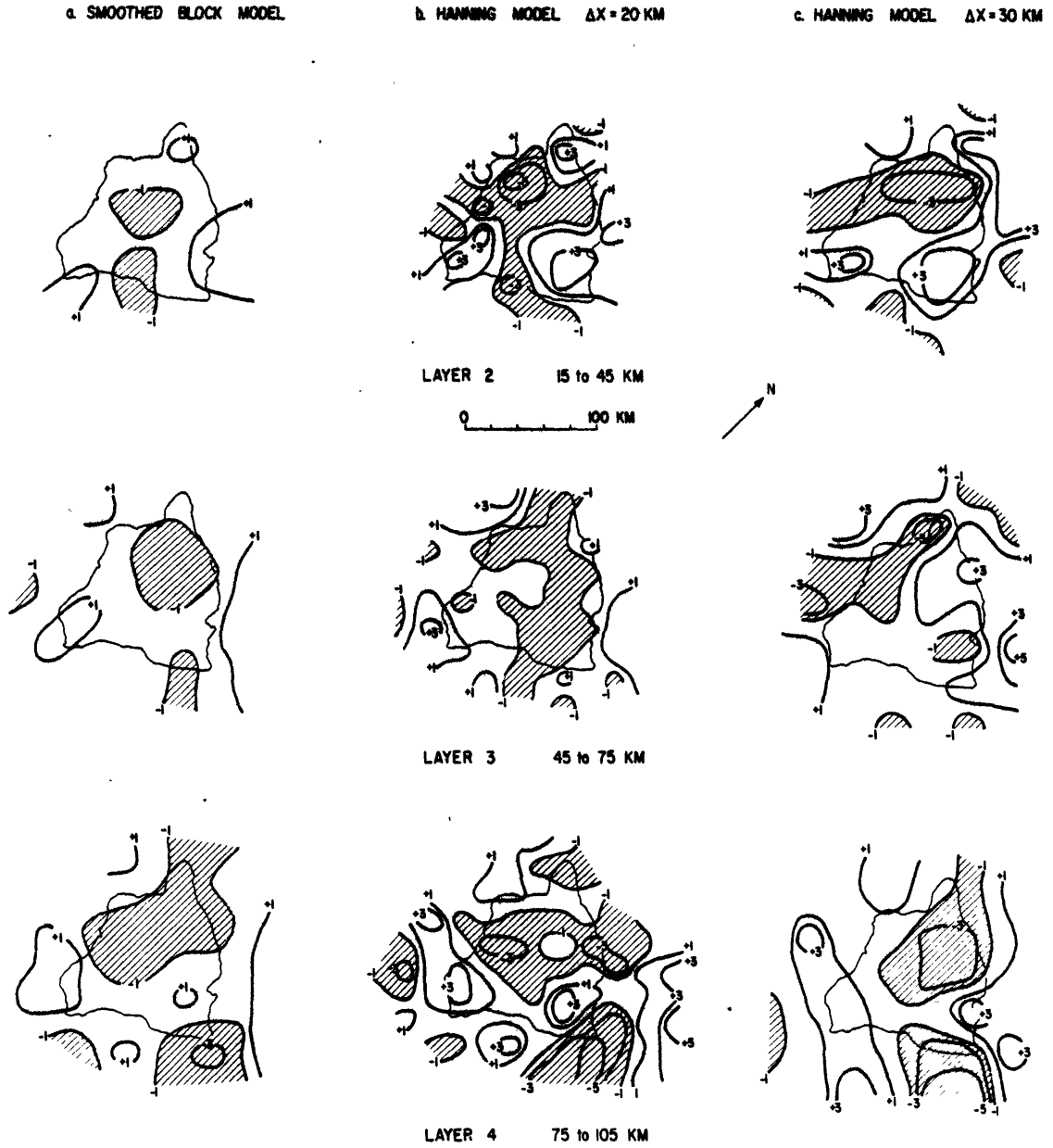
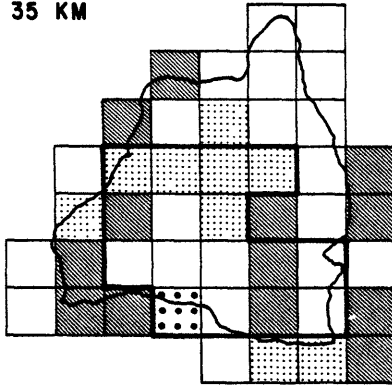


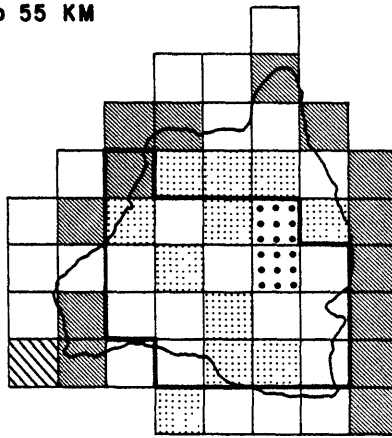
Figure 4.13

MODEL 4LSB2

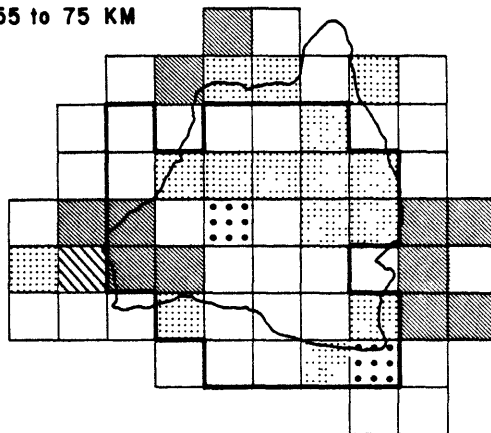
15 to 35 KM



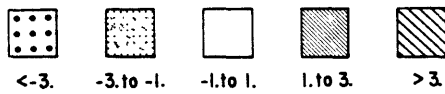
35 to 55 KM



55 to 75 KM



$\Delta V / V$ (%)



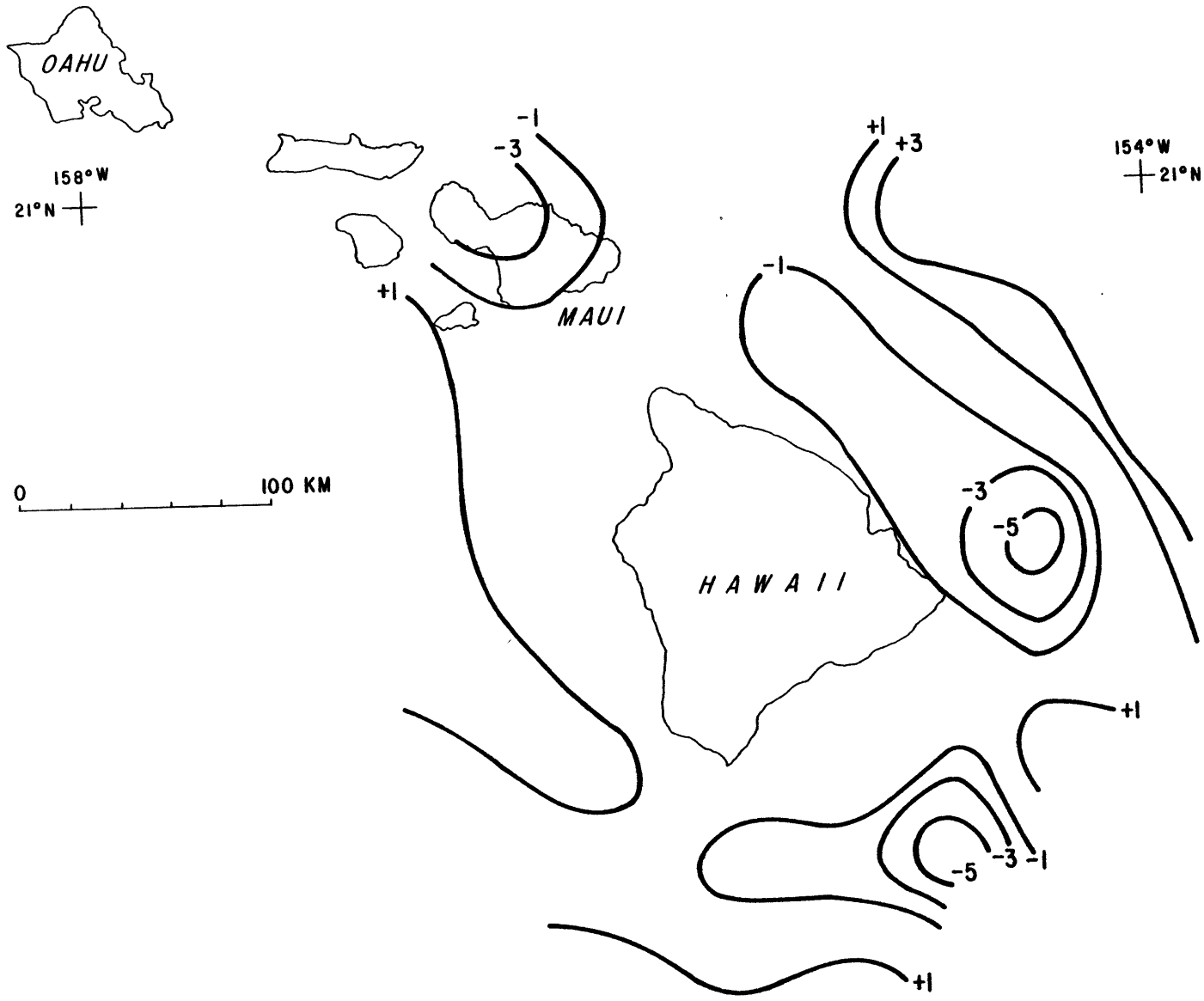
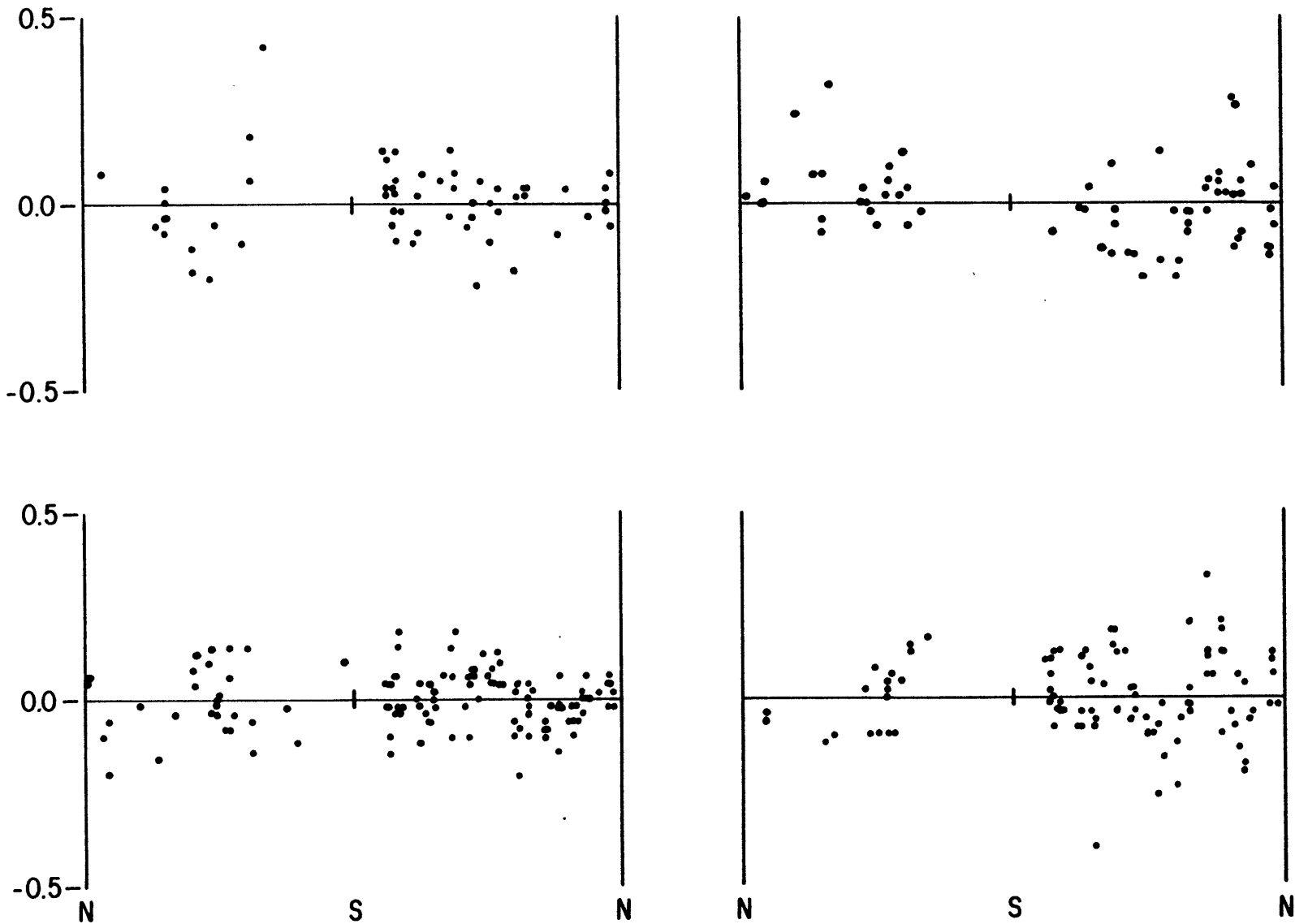


Figure 4.14

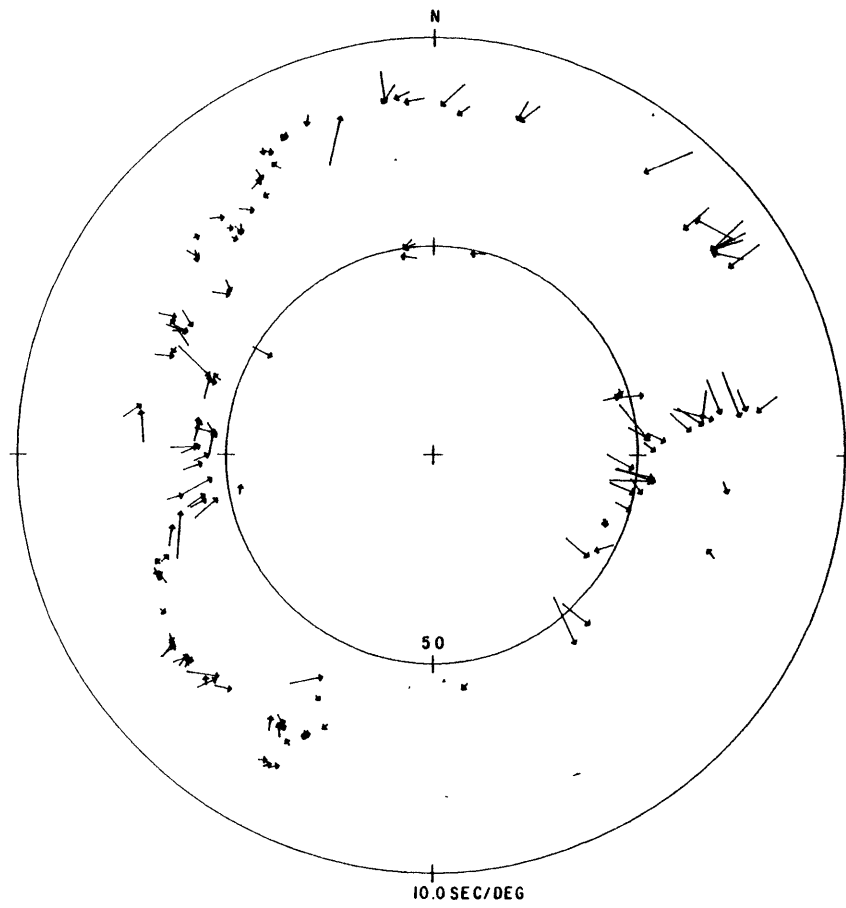
RELATIVE TRAVEL TIME RESIDUALS (SEC.)
AFTER REMOVAL OF THREE-DIMENSIONAL STRUCTURE



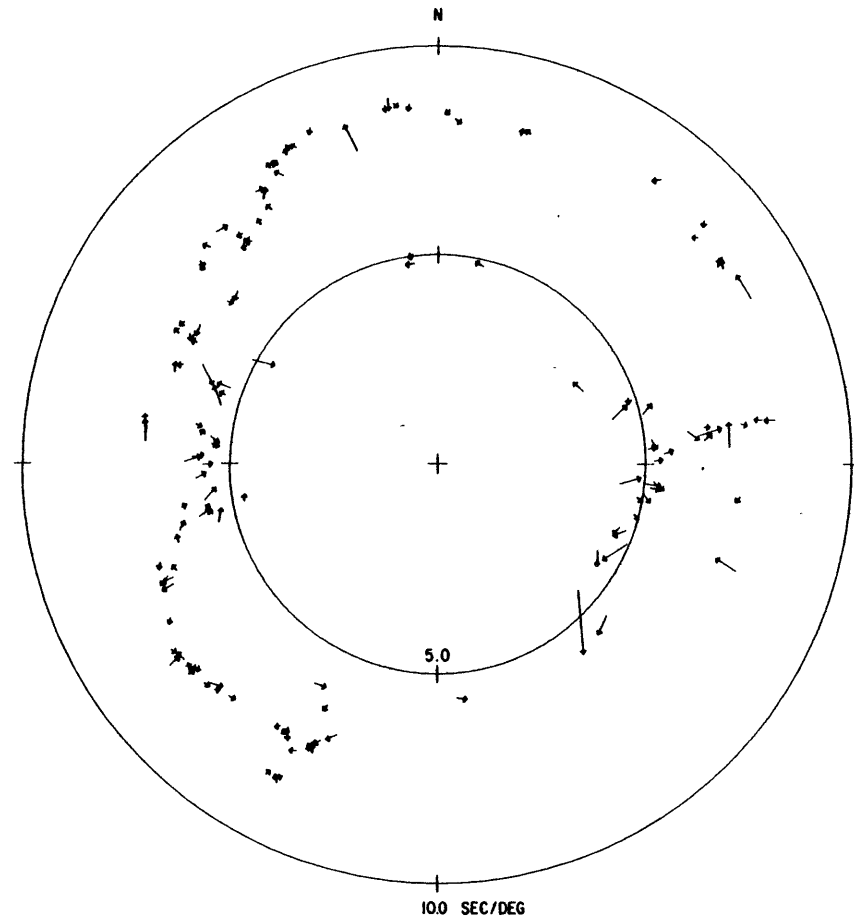
AZIMUTH TO SOURCE

Figure 4.15

ARRAY MISLOCATION DIAGRAM FOR HAWAII



STATION ELEVATION REMOVED



THREE-DIMENSIONAL CRUST AND MANTLE STRUCTURE REMOVED

Figure 4.16

CHAPTER 5: Simultaneous Determination of Velocity
Structure and Local Earthquake Focal Parameters

Three-dimensional velocity models of the crust and mantle beneath Hawaii derived from teleseismic P-wave travel times represent self-consistent, although non-unique, explanations for these data. Alternative models combining lower mantle structures, however improbable, with lateral heterogeneity near the island cannot be conclusively ruled out by these data. Although the teleseismic data favor explanations by upper mantle structures beneath Hawaii (§2.5, §4.5) validation of the models of §4 requires independent evidence.

Fortunately, an independent and unique modeling of crust and mantle velocities to depths in excess of 40 km is possible for Hawaii. The data for this modeling are the travel times of local earthquakes occurring in the crust and upper mantle of the island. Local earthquake travel times are especially powerful data for determining velocity structure because the solution contains information on absolute velocities in addition to relative velocity variations about the mean level. In contrast, velocity structures derived from teleseismic data cannot recover absolute velocities (§3.1). The difference being that when the travel time sources locate within the modeled volume focal parameters, including the origin time, must be allowed to vary together with medium parameters. Consequently, the total travel time from each

source to receiver, and therefore the absolute velocities, can in principle be determined.

Our purpose in this chapter is not to present an exhaustive analysis of three-dimensional structure for Hawaii based upon local data (which is not possible at present for reasons discussed below) but is rather to construct models suitable for direct comparison with velocity structures derived from teleseismic travel times. A comprehensive analysis of travel time data from local sources can, in principle, provide for greater spatial resolution of structure not only because the waves are substantially higher frequency (10 Hz as opposed to 1 Hz) but also because the ray paths sample the medium through a far wider range of incidence angles than do the teleseismic waves. The reasons why this analysis is currently postponed include the need for an efficient ray tracing algorithm for solving the two point boundary value problem, limitations on the number of simultaneous equations which can be handled on available computers (at an affordable price!), and lastly the desire to obtain S-wave, as well as P-wave, data. ←

5.1 Simultaneous Inversion Method for Hypocenters and Velocity Structures

Modeling of arrival time data recorded by an array for both the focal parameters of the sources and the velocity of the medium is accomplished through the union

of Geiger's method for earthquake location (Geiger, 1910; Buland, 1976) with a linearized velocity modeling technique. In each problem the travel time is expanded about a trial solution using appropriate model parameters and Taylor's theorem. Retaining only first order terms, the expansion is used to construct a linear system of equations, the solution of which gives an improved estimate of either source location or medium velocity.

When constructing the Taylor series for either problem, the parameters describing the other are held fixed by assumption. However, there is no fundamental reason why this must be so. Recently several authors have combined the first order series expansions for each of these problems to obtain a single equation relating changes in travel time to variations in both source location and velocity along the ray path (Peters, 1974; Crosson, 1976a; Aki and Lee, 1976). Because the sampling of the medium by the available data is grossly inadequate, all of the above authors have been forced to parameterize the medium in some simple way. Fortunately, the mathematical formalism is independent of the details of the medium description and all possible parameterizations can be described by a single formalism.

5.1.1 Formulation of the Method

Consider the observed travel time of a body wave phase from source j to station i , t_{ij} , and its predicted

value \hat{t}_{ij} given by the stationary solution of

$$\hat{t}_{ij} = \int_{\text{source } j}^{\text{station } i} v^{-1} ds \quad (5.1)$$

along the appropriate ray path with the medium velocity v specified by model parameters m_k . Allowing both the medium parameters m_k , source coordinates $x_{j\ell}$ and origin time O_j to vary from their trial values, the travel time residual $r_{ij} = t_{ij} - \hat{t}_{ij}$ may be expressed as a series in small perturbations to the free parameters:

$$r_{ij} = \delta O_j + \sum_{\ell} \frac{\partial t_{ij}}{\partial x_{j\ell}} \delta x_{j\ell} - \sum_k \int_{\text{source } j}^{\text{station } i} v_0^{-2} \frac{\partial v}{\partial m_k} ds \delta m_k + e_{ij} \quad (5.2)$$

The first two terms come from Geiger's method (1910) and give the change in travel time resulting from changes in the origin time and hypocenter position. The third term represents the change in travel time between the original hypocenter and receiver due to variations in the medium velocity along the ray path. This term was derived in §3.1.1. The final term e_{ij} contains both higher order terms of the Taylor expansion about the initial model and error terms.

Following the procedure used in §3.1.2 and introducing the notation

$$a_{ijk} = - \int_{\text{source } j}^{\text{station } i} v^{-2} \frac{\partial v}{\partial m_k} ds \quad (5.3)$$

$$p_{i\ell}^j = \frac{\partial \hat{t}_{ij}}{\partial x_{j\ell}} \quad (5.4)$$

(5.1) becomes

$$\dot{r}_{ij} = \partial O_j + p_{i\ell}^j \delta x_{j\ell} + a_{ijk} \delta m_k \quad (5.5)$$

where the equality is approximate since the error term has been dropped, and the summation convention is used. Observation of a suite of sources by a common receiver array then gives a linear system of equations relating the travel time residual to changes in focal parameters and velocity structure.

Introducing column vectors

$$r^T = (r_{11}, r_{12}, \dots, r_{21}, r_{22}, \dots)$$

$$m^T = (\delta O_1, \delta x_{11}, \delta x_{12}, \dots, \delta O_2, \delta x_{21}, \dots, \delta m_1, \delta m_2, \dots)$$

the system of equations may be written in matrix notation as

$$Am = r \quad (5.6)$$

where the elements of A are defined by (5.5). This system of equations may be solved for the unknown perturbations

m by a number of standard methods. All of the calculations presented below use the method of damped least squares which is discussed in §B.1.

5.1.2 Application to the Earth

The fundamental difficulty in applying (5.5) is finding medium parameterizations for which the forward travel time problem (5.1) can be solved. Although considerable progress has been made toward solving (5.1) for laterally complex earth models (Wesson, 1971; Engdahl and Lee, 1976; Yang and Lee, 1976; Julian and Gubbins, in press; Lee and Pereyra, in prep.; Pereyra and Lee, in prep.) none of the currently available algorithms are entirely satisfactory. The ray tracing introduced in §3.4 and applied to teleseismically determined velocity structures is also inadequate for the problem at hand. Thus application of (5.5) is currently restricted to simple medium descriptions such as one-dimensional earth models.

Two different approaches have thus far been successful in making use of the method. Crosson (1976a) adopted a one-dimensional earth model composed of constant velocity, plane parallel layers and applied this modeling to the Puget Sound, Washington, region (Crosson, 1976b). This medium parameterization is attractive since the forward problem can be solved, allowing for iterative refinement of the solution. It is also possible to

determine the location and velocity of low velocity layers (if present) when sources are located within or below those layers. The major limitation of a one-dimensional model is that it provides no information on lateral variations in structure, except for station delay times. Steppe and Crosson (in press) argue that this limitation is not too serious as most of the data variance is usually explained by the layered model when combined with station delays.

Aki and Lee (1976) have approached this problem from a somewhat different perspective. They extended the three-dimensional modeling introduced by Aki and others (1977a) for teleseismic data to include source focal parameters, as well as local three-dimensional structure as described by quantized model elements (§3.2.1). As with Crosson's method, Aki and Lee's method treats only first P-wave arrivals. Their solution is, however, freed from the need to include linear station delay times as model parameters as was found necessary by Crosson (1976b) since the three-dimensional element grid can model near surface structural variations directly. The principal drawbacks to this method are its inability to iteratively refine the solution and the need to use an initially homogeneous earth model. The latter limitation is perhaps most serious as differences between the assumed straight ray paths and the actual ray paths can result in significant mis-sampling of the medium when evaluating (5.3).

Roecker (written communication, 1977) significantly improved upon the initial model used in Aki and Lee's method by replacing the homogeneous earth model by a layered model. The benefits derived by this modification are twofold. Most obviously, ray paths given by the layered model are potentially much closer to the actual ray paths than straight rays, especially when refracted arrivals are possible. The second advantage is that the solution given by Crosson's method can be used as the natural starting point for the single iteration solution. Roecker also extended each of the earlier methods to incorporate first S-wave arrival times and an independent S velocity model. Block model elements (§3.2.2) are also used by Roecker in place of the quantized elements used by Aki and Lee. Velocity models for Hawaii based upon arrival times from local sources presented in this chapter are derived using Roecker's formulation.

5.2 Local Sources for Travel Time Inversion Studies

The Island of Hawaii is a particularly good location for studying velocity structure using local sources because natural seismicity occurs in a broad region beneath the island. Apart from a few persistent sources of earthquakes, the epicentral distribution of both crustal and mantle events appears to be randomly distributed without obvious association to surface tectonics (Koyanagi and others, 1976). Earthquake focal depths

are similarly well dispersed throughout the mantle, with the deepest events locating at depths in excess of 60 km.

This widely scattered distribution of hypocenters is ideally suited as data for local travel time inversion studies because it allows an apportionment of sources throughout the model volume. Ray paths from such a distribution tend to optimize the mixing of ray path directions through individual model elements which improves parameter resolution. Two additional criteria that an ideal data set should meet include observation of each event by every station and unambiguous phase identification.

A data set of 2122 arrival times for 40 stations from 73 earthquakes was selected from the earthquake catalogs of the Hawaiian Volcano Observatory (HVO). The selected events (Figure 5.1, Table 5.1) are from the years 1974-1977. All readings were made by the HVO staff from deconvoluted films using procedures identical to those outlined in §2.1. The criteria used to select the data were, in order of importance, hypocentral location and number of P-wave readings. The first criterion insured that the events were not clustered or otherwise biased toward one specific area. The second criterion not only maximized the number of P-wave readings for a fixed number of epicenters but also assured that the P-wave arrival will be strong and unambiguous at most stations.

The intrinsic variance of these arrival time data is estimated to be $\sigma_d^2 = 0.0025 \text{ sec}^2$ which corresponds to a reading standard error of 0.05 sec. Although this is also the accuracy to which the times are reported, the precision with which sharp arrivals can be read is at least this small (Steppe and others, 1977).

Modeling capabilities of the data were tested using one-dimensional velocity models to determine the sensitivity of the data to layered structures and to search for any model instabilities which might exist. It was found that the data allow use of layers as thin as 5 km above about 20 km depth but require layers about twice as thick below that depth. Velocity values for thinner layers tend to oscillate rapidly as a function of depth. The most extremely aberrant values were low velocity zones which had poor parameter resolution ($R_{ii} = .6$) when compared to well-resolved values ($R_{ii} = .99$).

Further tests of the data were made using synthetically generated travel times calculated for a simple layered structure and the same source-receiver pairs available in the real data. Zero mean, normally distributed, pseudo-random numbers with a variance of 0.01 sec^2 were added to the exact travel times to simulate reading errors. The specific layered structure studied was not designed to test the convergence of the method, which Crosson (1976a) has demonstrated, but rather to study the sensitivity of the data to a deep low velocity layer.

Crust and uppermost mantle velocities for the synthetic layered structure correspond, approximately, to average velocities for Hawaii determined by crustal refraction studies (Eaton, 1962; Ryall and Bennett, 1968; Hill, 1969). Below 35 km, the velocity decreases from 8.3 km/sec to 7.4 km/sec, which is the adopted half space velocity. Starting from a trial velocity structure, a convergent solution is found by iteratively solving (5.6) by the method of damped least squares using damping parameters listed in Table 5.2. When inversion model layer boundaries are positioned at exactly the same depths as were used when generating the synthetic data, the inversion method rapidly converges to the correct solution. Figure 5.2a illustrates the convergence history. Diagonal elements of the resolution matrix exceed 0.99 in the upper four layers and 0.95 in the half space. For this solution, the residual variance of 0.009986 sec² agrees well with the variance of the noise.

A second modeling experiment using one less model layer also gives a statistically acceptable solution with a residual variance of 0.010011 sec². Because in this case the position of layer boundaries in the mantle do not agree with the exact model, the velocity structure determined by the data cannot exactly match the true structure. The solution does roughly equal the average value of the true velocity within each layer (Figure 5.2b). The low velocity half space indicated by the results is

statistically discernable since velocity uncertainties are uniformly less than 0.06 km/sec and corresponding resolution matrix diagonal elements exceed 0.99.

A comparison between the two velocity structures derived from the test data based on the solution statistics and without a priori knowledge of the true solution does not immediately identify the former solution (Figure 5.2a) as the better of the two. Because it more closely agrees with the actual velocity distribution than the other, it would appear that very small differences in residual variance ($<.00002 \text{ sec}^2$) are significant when comparing inversion results.

5.3 One Dimensional Velocity Structure for Hawaii

High resolution layered velocity models for Hawaii were constructed using the local structure for use in three-dimensional modeling of those data. Although the details of the average vertical velocity structure are of themselves of considerable interest, our primary purpose is comparison of three-dimensional solutions derived from independent data sets. Consequently, no attempt is made to push this modeling to its ultimate limits. The derived models are, however, entirely adequate for their intended purpose of providing a realistic framework for comparative modeling of heterogeneous structure.

Because we are not primarily interested in the details of shallow structure, a simplified description

of crustal structure was adopted for this modeling. In this model, the crust is described by two layers with the boundary between them fixed at 8 km below sea level. Depth to the moho is also fixed at 14 km below sea level. These layer boundaries generally agree with the average positions of the top of the intermediate crustal layer and mantle as determined by refraction profiling. Although this two layer model only grossly approximates the complex structure of the island evident in Hill's (1969) analysis, the loss of fine scale resolution is probably unimportant since over 90% of the sources studied are in the mantle. Rays from these sources to the surface spend most of their travel time in the mantle and cross the crust but once. Consequently, regional variations in crustal structure can be treated, to a first approximation, as an algebraic station correction (Crosson, 1976b).

Using this simplified crustal structure, a sequence of models was generated. Beginning with a model composed of two crustal layers over a half space with initial velocities assigned from refraction study results, a solution was found for the best three velocity model. This solution was then used as the initial velocity distribution for a new model within which the mantle has been divided into two parts. The original (catalog) estimates of the hypocenters were again used as the initial trial values for the new model. Station delay

times were also reset to zero. This process was repeated until further subdivision of the mantle would result in either model instability or excessive loss of resolution.

Results of this modeling (Figure 5.3, Table 5.3) indicates a crust and upper mantle structure in good agreement with the refraction studies. The most surprising development is the appearance of a pronounced low velocity zone below 35 km when the velocity in this depth interval is allowed to vary independently of the overlying mantle. Although resolution and standard errors are excellent for this model, the variance improvement over the preceding model is only 0.00003 sec^2 . Synthetic model calculations of §5.2 suggest that this small variance improvement is significant. However, other factors including the possibility of a systematic bias inherited from the trial hypocenters leaves the reliability of this interesting result unresolved. Addition of S-wave arrival times would help clarify this question, because when inverted together with P-wave times they place stricter constraints on the focal coordinates and origin time than can be achieved by either data alone.

The variance left unexplained by these models corresponds to a travel time standard error of 0.1 sec, which is twice the intrinsic error estimated earlier. It is, therefore, not unreasonable to seek laterally heterogeneous models which better satisfy these data.

5.4 Three-Dimensional Velocity Structure Determined from Local Travel Time Data

Acceptable representations for a laterally heterogeneous velocity structure for use in modeling local travel time data are considerably more varied than those which are suitable for analysis of teleseismic waves. Gone is the restriction that the vertical velocity structure remain unknown. Consequently, acceptable medium descriptions may include explicit vertical smoothing in addition to horizontal smoothing.

The specific model framework selected for comparison is virtually identical in design to the coarse grid models studied extensively in §4.2. The medium characterization judged most suitable for detailed comparison is the block model with the crust described by blocks uniquely associated with each seismograph station (station-block model).

Three minor changes are made to the initial layered model used in calculating travel time residuals and model partial derivatives. Most importantly, a layered structure indicated by the one-dimensional modeling replaces the simplistic structure of Table 4.1 which was adequate for the teleseismic modeling. Because the locally determined layered structure contains two crustal layers, the single crustal layer used previously is divided into an upper and lower part. This change is not carried over to the three-dimensional solution where

a single perturbation ($\Delta V/V$) for both layers at each station is treated as the unknown parameter. Finally, it was found by trial and error that mantle velocities at or near the moho differ considerably from the underlying mantle. The velocities at such shallow depths in the mantle are controlled almost entirely by rays which refract along the moho. It is a simple matter to decouple this P_n structure from the mantle below by introducing a thin (2 km) layer at the top of the mantle. Removal of this thin " P_n " layer should not affect comparisons with the teleseismically-derived models since it influences only an insignificant fraction of the teleseismic ray travel time.

The single iteration solution obtained using the initial layered structure described above successfully accounts for over 70% of the data variance left unexplained by the one-dimensional models of §5.3. The residual variance of 0.0035 sec^2 compares favorably with the estimated variance of 0.0025 sec^2 . Perturbations to the trial hypocenters are quite small for this solution, averaging less than 0.2 km for the epicentral correction and 0.6 km for the focal depth correction. Maximum corrections were 0.6 km and 1.4 km, respectively.

Velocity perturbations (Table 5.4, Figure 5.4) span a considerable range averaging 6.2% (r.m.s.) in the crust and 1.5% in the mantle. The marked difference between crust and mantle is not an artifact of reduced resolution

in the mantle, as resolution is excellent. However, it may result from choosing blocks substantially larger (30x30x30 km) than the scale length of heterogeneous structures present in the mantle.

5.5 Comparison Between Structures Determined Using Teleseismic and Local Sources

A direct comparison between three-dimensional velocity models computed using an identical element framework and completely distinct data sets should, in principle, provide the most direct test of the uniqueness and reliability of the solutions. There are, however, several critical assumptions which are of central importance, and it is essential that they are satisfied for the results of the comparison to be meaningful. Foremost among these is the supposition that the equivalent heterogeneity modeled does not depend upon the frequency content of the illuminating waves. This is crucial here because the frequency of the teleseismic waves and the waves from local earthquakes differ by about one order of magnitude (1 Hz versus 10 Hz, respectively). Criteria for the validity of ray theory, introduced in §4.1, show that scattering may be neglected for significantly smaller scale heterogeneities than the chosen block size and that ray theory can be applied for such a grossly homogeneous body whose average properties vary smoothly. However, when the

wave length and heterogeneity scale are comparable, scattering may be important. This means that over a wide range of heterogeneity scales which do not scatter teleseismic waves, the locally-generated waves will suffer from scattering which might introduce systematic biases in the solution.

The second serious problem confronting the model derived using local sources is the possible influence of anisotropy upon the result. Recall that it was argued in §3.3.3 that transverse anisotropy in the horizontal plane would not affect teleseismic models. The immunity to even this simplest form of anisotropy does not carry over to the local models because the ray take-off angles from a single source may fill the focal sphere.

Despite these potential pitfalls, the first-order comparison between the local solution and the most similar teleseismic solution (4GSB3) is quite favorable (Figure 5.5). Both models show substantially greater velocity perturbations in the crust than in the mantle. The overall correlation on an element-by-element basis is also satisfactory, with a correlation coefficient of $r = 0.79$. For the forty-three compared values, a correlation coefficient this large has less than a 0.5% chance of occurrence from a random sample.

Although the overall correlation is favorable, many solution values disagree by substantially larger

amounts than can be reasonably accounted for by their errors. As we shall see below, these discrepant values contain considerable information about the structure of the crust and upper mantle. We now examine, in turn, the details of the comparisons between these two distinct solutions; first for the crust and then for the mantle.

5.5.1 Comparison between solutions for crustal parameters

Crustal solution values for station terms from the local three-dimensional solution and from model 4GSB3 appear in Table 5.4, together with the solution for the iteratively converged model 4GSH3A. Diagonal elements of the parameter resolution matrix exceeds 0.5 for all of these values, which is considered to be the minimum standard for inter-model comparisons as outlined in §B.4. The resolution diagonal element averages 0.8 for these models which means that the standard error averages less than 0.3%, with the data variance generously estimated to be 0.01 sec^2 .

The linear correlation between each of these solutions is excellent with the correlation coefficient exceeding 0.8 for comparisons between the teleseismic and local solutions and equalling 0.98 for the two teleseismic solutions. The least squares fit which takes the local solution as the independent parameter has a slope of 0.82 for model 4GSB3 and 0.85 for model

4GSH3A. These values clearly demonstrate the strong positive correlation between crustal models appropriate for these two distinct data sets. However, the coherence between these models is far from complete as solution values for specific stations disagree by almost half of the total range of $\Delta V/V$.

Considered in detail, the differences between the crustal velocity structure implied by the local and teleseismic data strongly point toward a breakdown in the critical modeling assumptions which must be satisfied for the models to be truly comparable. These solution differences reflect travel time differences which are independent of the modeling analysis, and which can be seen in the comparison between average teleseismic travel time residuals and average local earthquake travel time residuals (Table 5.4). When viewed as a function of the distance to the nearest intrusive complex, either summit or rift zone, per cent velocity variations appropriate for the teleseismic data show considerably greater regularity than those appropriate for the local data (Figure 5.6). In fact, the only teleseismic value which deviates significantly from a nearly linear, monotonic decrease in velocity with increasing separation between station and intrusive complex is CAC (see also Figure 2.10). It is interesting to note that the Bouguer gravity map of Hawaii suggests the presence of a buried rift zone extending south from the summit of Hualalai (Kinoshita and others, 1963). Station CAC is located

about 5 km to the west of this feature. If the gravity high marks the position of a major intrusive feature, then the $\Delta V/V$ value for CAC agrees completely with the overall trend.

The visible degradation of the simple relationship between station location and average crustal velocity, so evident for the teleseismic solution, when the model for local travel time data is considered suggests that the first-order model of constant velocity crustal layers underlying each station is too simplistic. It is likely that both small scale heterogeneities and anisotropy contribute to the disagreement.

The evidence for anisotropy can be seen when the differences between teleseismic and local solution values are displayed on a map of the island (Figure 5.7). Positive values, which mean that the teleseismic waves traverse the crust relatively faster than waves from local earthquakes, are grouped in the northern half of the island and along the east rift of Kilauea. With the exception of KKU, all of these stations locate within 2 km of a major intrusive feature. Because the teleseismic waves cross the crust at steeper incidence angles, on the average, than waves from local earthquakes, the sense of the disagreement is consistent with the vertical velocity exceeding the horizontal velocity by as much as 10%. Erosionally exposed cores of rifts on Oahu show that the rift zones are a complex of dense diabase dikes which intrude subhorizontal flow basalts

(Wentworth and Jones, 1940). Thus the rift zones are approximately transversely isotropic with a vertical symmetry plane aligned along the rift. As Wentworth and Jones (1940) also observed a characteristic reduction of the concentration of dikes and sills with increasing distance from the rift axis, this would explain why the average teleseismic velocities decrease with increasing separation from the rift zone.

Resolution of the differences between the local and teleseismic solutions will require significantly more detailed modeling of the crust. The east rift zone of Kilauea appears to be an ideal location of such a comparison because of its accessibility and the high level of local seismicity. A carefully designed experiment, employing a substantially denser seismograph network would provide the needed data and could greatly extend our understanding of the nature of rift zones.

5.5.2 Comparison Between Solutions in the Upper Mantle

The three-dimensional solution for mantle blocks from layer 3 of the local travel time model and from layer 2 of teleseismic model 4GSB3, repeated in Figure 5.8, agree as to the mean level of velocity perturbations present within the upper mantle. However, the details of these models disagree substantially. On the one hand, the teleseismic model has a relatively low velocity

core beneath the interior of the island with generally higher values bounding it on the left and right as seen in Figure 5.8b. On the other hand, the local model (Figure 5.8a) has its most negative velocities beneath the eastern end of the island with average or slightly negative velocities appearing beneath the central regions of the island.

Given these obvious discrepancies, it is not surprising that the coefficient of linear correlation is only 0.17 for the 13 blocks with $R_{ii} \geq 0.5$, which is not measurably different from zero. Thus it would appear that the teleseismically-determined solution is unrelated to the local solution. However, before rejecting the hypothesis that these two solutions are related, let us examine them in greater detail.

If the models are intrinsically similar, subtraction of the two solution values for the same block leaves a random residual with a variance equal to the sum of the two variances. The mean level of the subtracted values can, of course, differ from zero since the teleseismic solution should average to zero while the local solution may contain a base line shift. This subtraction has been performed for blocks with $R_{ii} \geq 0.5$, and appears in Figure 5.9 with a base line value of 0.9% removed. For these residuals, the standard deviation indicated by the summed variances, estimated conservatively using (B.15), is 0.8%. It is evident from Figure 5.9 that the

only solution values which violate the similarity assumption at the 95% confidence level are for two blocks on the northeast coast of the island. Omitting these two blocks from the correlation analysis, we find that the remaining eleven blocks are related with a positive slope of 0.7. The correlation coefficient for this case is 0.56, which is equaled or exceeded by only one sample in 15 from a random population. Consequently, if an independent criteria would allow us to reject these most discrepant blocks, we could conclude that the two solutions are essentially similar.

To be successful, a discriminant must utilize information from only one solution, since we generally do not have the luxury of comparing two distinct solutions. Within the confines of this constraint, the row of the parameter resolution matrix appear to be most successful for this purpose. As might be expected, either positive or negative side lobes indicate a serious problem even when they are no larger than about 5% of the corresponding diagonal element. The most damaging coupling apparently occurs between the block velocities and poorly constrained hypocenters in the case of the local model. The solution values which are most discrepant are characterized by resolution side lobes linking the block velocity with hypocenters which lie on the periphery of the station network. Solution values in agreement with the tele-seismic inverse do not possess this type of coupling to nearly the same degree.

In effect, this discriminant implies that the solution for blocks on the periphery of the network are unreliable whenever the locations of nearby hypocenters are not well constrained by the station network. Addition of S-wave travel time data should alleviate this problem since it would sharply limit the trade-off between hypocenter, velocity, and origin time. Because this criteria cannot be tested directly and because the number of blocks we are comparing is quite small, a firm conclusion about the correlation between these two distinct models cannot be made. It is considered preferable to leave this question open at this time, as the difference between solutions may, in fact, be related to other factors including a breakdown of the assumptions used to construct the local solution.

5.5.3 Teleseismic Models Which Use the Structure Determined from Local Sources as a Starting Model

The comparison between crust and upper mantle solutions in the preceding section showed that while the overall correlation between the structures indicated by the two data sets was acceptable, significant differences between solutions were present in both crust and mantle. Because a laterally homogeneous model was used as the initial model for both solutions, which is clearly an inadequate description of the medium, it is possible that one model or the other is biased by this overly

simplistic starting model.

This possibility is examined in this section by using the three-dimensional model derived from local travel time data (Figure 5.4) as the starting model for solutions based exclusively on teleseismic data. Two single iteration, four layer solutions are considered (Figure 5.10a and b). Each uses an element framework identical to that used for the teleseismic solution 4GSH3A (repeated in Figure 5.10c). The difference between these two new solutions is that one holds the initial velocities in the upper two layers fixed while the other treats all velocities as free parameters.

The initial, laterally homogeneous model given by the local data explains 28% of the total data variance of 0.043 sec^2 , which slightly less than half of the variance reduction achieved by the upper two layers of teleseismic model 4GSH3A. Holding this initial model for the crust and uppermost mantle fixed gives a solution (Figure 5.10a) which explains a significantly smaller fraction of the total variance (64%) than either its companion model in which all parameters are free (75%, Figure 5.10b) or the solution based upon an initially homogeneous model (79%, Figure 5.10c). The difference in variance reduction between the two free solutions is not significant since the former is a single iteration solution and the latter has been iteratively refined. In fact, differences between the solution values for

these two models (Figure 5.10b and c) are so small and their overall correlation is so high ($r = .85$) that it is safe to conclude that the inverse solution is essentially independent of the starting model when all parameters are allowed to vary. Can a similar statement be made in the case of the solution in Figure 5.10a for which the upper two layers were stripped?

Visual comparisons between the velocity anomalies in the lower two layers of this model and the other two solutions indicate that the overall velocity pattern of the stripped and free models are similar. The third layer contains the greatest distortion, which is primarily a strong velocity gradient from northeast to southwest (right to left) in the stripped model. This gradient apparently compensates for differences between the local model used to remove the upper layers and the solution preferred by the teleseismic residual data. Even with this strong gradient present, the linear correlation coefficient between this model and the original teleseismic solution (Figure 5.10c) is $r = .63$. The correlation in the bottom layer between solutions is better still, with $r = .72$. In fact, differences between solutions within this bottom layer are essentially random which means that the solution at this depth is free from systematic influence of the assumed upper layer velocities. Stated another way, this means that the solution for the deepest layers depends principally upon the slowness, azimuth, and

and curvature of the wavefront assumed at the base of the model and not the details of overlying structure.

5.5.4 Summary of Model Comparisons

The principal conclusions drawn from the comparison of three-dimensional models derived from teleseismic and local travel time data are as follows: (1) a broad and statistically significant correlation exists between these velocity models. (2) Crustal structure is dominated by large, rapid lateral variations in velocity which are directly related to the presence (or absence) of volcanic intrusives. (3) Upper mantle structure is substantially more homogeneous than crustal structure when viewed on a scale of 30 km. (4) Significant differences between the two solution types are present in both the crust and mantle. They reflect, in part, a breakdown of necessary modeling assumptions for the local data and suggest that velocity anisotropy may exert an important influence on these data. (5) Finally, the model solution for the deepest layers of the teleseismic solution are insensitive to the details of crust and upper mantle structure.

TABLE 5.1. Local Earthquake Hypocenters and
Number of Arrival Time Readings

DATE	ORIGIN	LAT N	LONG W	DEPTH	NO
76 115	1241 45.46	19-24.43	155-17.59	14.18	35
76 118	2357 46.58	19-22.36	155- 5.66	6.84	33
76 3 3	6 0 57.84	19-25.09	155-27.98	7.89	33
76 422	554 5.19	19-31.41	155-18.67	11.77	32
76 531	1036 54.79	20- 1.54	155-46.04	9.82	30
76 712	734 39.59	19-20.93	155-18.53	12.42	34
76 824	1937 2.05	19-17.39	155-21.39	5.19	33
76 9 7	22 1 16.39	19-21.90	155- 4.52	6.92	33
770105	22 7 35.21	18-58.98	155-38.53	46.38	27
770112	3 5 59.48	19-23.93	155-17.68	15.71	33
770301	539 20.50	19-59.12	155-48.11	27.58	35
770309	029 16.50	19-23.22	155-30.50	51.72	28
770317	7 4 34.38	19- 9.66	155-33.51	31.75	34
770320	14 7 39.92	19-49.83	155-34.15	24.68	35
770501	13 7 21.79	19-56.46	155-15.20	38.67	27
770521	1657 33.72	19-38.34	155-57.35	42.56	26
74 131	2116 50.64	19-14.44	156- 4.23	49.21	30
74 318	2258 35.15	19-15.93	154-54.81	37.88	32
74 5 5	1218 32.60	19-53.61	155-18.39	25.54	27
74 522	235 59.09	20-29.68	155-42.23	46.31	29
74 525	1338 32.72	20- 9.35	155-49.46	32.74	27
74 610	2359 41.59	19-55.21	155-46.62	32.42	32
74 8 4	1235 56.51	19-27.34	156- 1.10	32.67	31
74 811	21 4 38.65	19-23.32	155- 6.63	36.50	31
74 825	226 43.11	19-26.18	155-29.28	43.69	20
74 914	2119 33.81	20- .05	155-34.04	46.31	30
74 924	2026 34.18	19-28.09	155-35.65	58.70	22
74 925	2018 50.22	20- 9.77	155-32.52	31.36	35
74 930	035 41.80	19-29.80	155-40.25	27.11	19
741130	20 5 56.82	19-32.56	155- 5.28	50.28	26
741228	19 4 6.32	20- 6.53	155-23.44	54.53	34
75 112	1641 42.52	19- 2.87	155-34.17	41.24	31
75 117	516 4.62	19-14.53	155-20.08	41.29	33
75 216	139 42.88	19-45.44	155- 5.92	37.71	27
75 4 9	353 21.98	19-12.24	155-26.35	37.48	31
75 514	316 51.88	19-53.37	155-35.67	24.15	33
75 526	1911 10.97	19-31.12	155- 5.54	39.86	18
75 528	2042 54.80	19-22.33	155-12.97	31.15	33
75 6 3	1557 12.86	19-51.48	155-41.60	34.24	25
75 613	754 1.78	19- 8.43	155- 6.16	58.15	32
75 619	041 46.40	19-10.62	155-49.01	39.66	27
75 626	20 1 14.31	19-35.61	155-26.79	28.89	17
75 7 3	426 31.79	19-13.25	155-28.87	49.92	19
75 7 6	554 33.42	19-31.85	155-36.90	25.91	15
75 713	525 29.92	19-51.61	155-53.90	49.50	25
75 824	1641 15.61	19-52.74	155-30.66	24.01	24
75 829	22 8 20.55	19-45.40	156- 1.55	37.71	29
75 9 7	450 .64	19-25.42	155- .99	45.91	21
75 916	1938 4.97	19-15.90	155-29.87	42.55	31
751014	1910 10.47	19-27.99	155-36.06	59.08	17
751022	1239 14.14	19-45.61	155-23.50	18.06	31
7511 6	4 2 56.56	19-19.83	155-18.75	28.07	34
7511 8	22 1 11.89	19-45.17	155-18.04	25.62	22
751127	2055 54.83	19-28.73	155-33.83	38.52	14
751129	1138 17.23	19-26.18	155-26.89	23.97	20
76 5 5	2317 51.04	19-56.93	155-20.29	34.44	35
76 516	4 7 9.62	19-27.03	155-14.79	30.47	35
76 531	853 53.56	20- 6.06	155-48.79	22.77	27
76 6 4	1427 47.11	19-15.63	155-25.08	33.19	35
76 6 7	1039 37.81	19-19.07	155-15.70	29.91	36
76 611	3 5 35.88	19-46.72	155-25.20	16.96	33
76 830	22 4 23.63	19-12.54	155-32.34	43.99	32
76 9 4	2333 26.79	19-25.10	156- 9.20	53.64	29
76 917	1930 18.75	19-24.38	155-15.26	40.35	23
7610 7	2152 57.79	18-59.71	155-28.54	40.27	36
7610 8	1629 30.14	19-32.81	155-50.50	24.75	36
761012	23 4 47.52	19-55.95	155- 6.21	41.18	29
761014	950 49.06	19-15.53	155-19.08	49.45	31
761029	355 23.49	19-58.31	155-29.86	40.20	35
761111	437 56.22	19-45.76	154-55.19	43.55	33
761117	551 48.71	19-32.00	155-14.32	24.77	32
7612 8	1149 17.02	19-19.29	155-26.79	26.37	33
761216	5 4 16.00	19-32.45	155-26.80	23.28	31

TABLE 5.2. Damping Parameters Used in
Damped Least Squares Modeling
of Local Travel Time Data

<u>Parameter</u>	<u>Damping Applied (θ^2)</u>
Origin time	.01
Epicenter	.04 sec ² /km ²
Focal Depth	.01 sec ² /km ²
Station Delay	.01
Layer Velocity (1-D only)	.04 sec ⁴ /km ²
Block Velocity (3-D only)	.005 sec ² /° ²

TABLE 5.3. Layered Velocity Model
Solutions for Hawaii

<u>Depth Interval</u>	<u>V_p</u>	<u>ΔV_p</u>	<u>R_{ii}</u>
0 - 8	5.66	.06	.986
8 - 14	6.78	.05	.990
14 -	8.07	.01	.999
residual variance .010900 sec ²			
0 - 8	5.96	.05	.994
8 - 14	6.95	.05	.994
14 - 25	8.17	.02	.999
25 -	8.27	.03	.996
residual variance .010431 sec ²			
0 - 8	5.91	.05	.996
8 - 14	6.90	.05	.994
14 - 25	8.13	.03	.998
25 - 35	8.52	.03	.997
35 -	7.30	.11	.941
residual variance .010398 sec ²			
0 - 8	5.91	.05	.998
8 - 14	6.83	.05	.998
14 - 20	7.86	.03	.999
20 - 30	8.07	.04	.998
30 - 40	7.92	.09	.987
40 -	7.39	.22	.912
residual variance 0.1137 sec ²			

TABLE 5.4. Station Residuals and Crustal Layer Solutions
from Three-Dimensional Models

Station	Average Residuals		First Layer Solution (%)		
	Local Earthquakes	Teleseismic Sources	Local 3-D Solution	Teleseismic Solutions 4GSB3	4GSH3A
AHU	-.11	-.08	- 4.0	- 6.0	- 3.2
AIN	.13	.20	- 6.7	- 5.3	- 6.3
CAC	-.07	.05	- .4	- .5	1.0
CPK	-.10	-.10	3.4	7.0	4.2
DAN	-.34	-.30	8.9		
DES	-.11	-.05	4.1	5.0	3.8
ESR	-.16	-.13	6.3	7.0	3.8
HLP	.06	.21	- 2.7	- 4.0	- 5.6
HPU	.01	-.13	- .5	5.9	5.2
HSS	.21	.24	- 6.6	- 6.9	- 7.8
HUA	.26	.01	-10.5	- 1.3	- .3
KAA	-.02	.22	- .3	- 7.0	- 6.6
KAE	.25	.33	-9.7	- 8.5	-10.6
KHU	-.14	-.04	3.9	- .1	- .5
KII	.18	.36	- 6.2	-11.3	-10.2
KKU	.37	.10	-12.2	- 1.4	- 3.0
KOH	-.05	-.12	1.9	4.3	4.0
KPN	-.09	.02	3.3		.1
KPR	.01	.14	- 1.6	- 2.2	- 2.9
LUA	-.12	-.22	4.0	7.7	5.0
MLO	.00 (fixed)	.05	- .4	.6	- 2.1
MLX	.14	.13	- 5.7		- 4.5
MOK	-.24	-.28	6.8	7.7	6.5
MPR	-.08	-.09	3.4	5.6	2.6
MTV	.27	.23	- 8.8	- 8.0	-10.1
NAG	.40	.23	- 9.1	- 9.6	-10.0
NPT	-.24	-.23	9.3		8.6
OTL	-.19	-.17	7.3		6.3
PAU	-.18	-.12	7.4		3.7
PHO	-.01	-.15	1.3	3.3	2.4
POL	.21	.24	- 8.7		- 7.3
PPL	.04	.11	- 3.0	- 2.3	- 3.5
RIM	-.18	-.10	5.6		3.0
SCA	-.23	-.28	5.7	6.8	5.9
SPT	-.12	-.14	1.4	1.9	- .6
SWR	-.42	-.34	12.2		9.0
TAN	.04	-.11	.0	2.1	1.3
UWE	-.11	-.16	2.9		5.3
WHA	.11	.22	- 3.8	- 5.2	- 7.1
WLG	-.18	-.11	5.9	6.6	3.3

Chapter 5 - Figure Captions

Figure 5.1 Epicenters of local earthquakes studied coded by focal depth.

Figure 5.2 Inversion results for hypothetical layered velocity structure: a) model layers positioned correctly, b) model layers incorrectly positioned.

Figure 5.3 Layered velocity structure for Hawaii determined by inversion of local travel time data.

Figure 5.4 Three-dimensional velocity model for mantle beneath Hawaii shown as relative perturbation (%). Bold line encloses blocks with $R_{ij} \geq 0.5$.

Figure 5.5 Correlation diagram for three dimensional velocity structure determined from local sources and from teleseismic solution 4GSB3.

Figure 5.6 Crustal velocity perturbations (%) for each seismograph station versus distance to nearest intrusive complex.

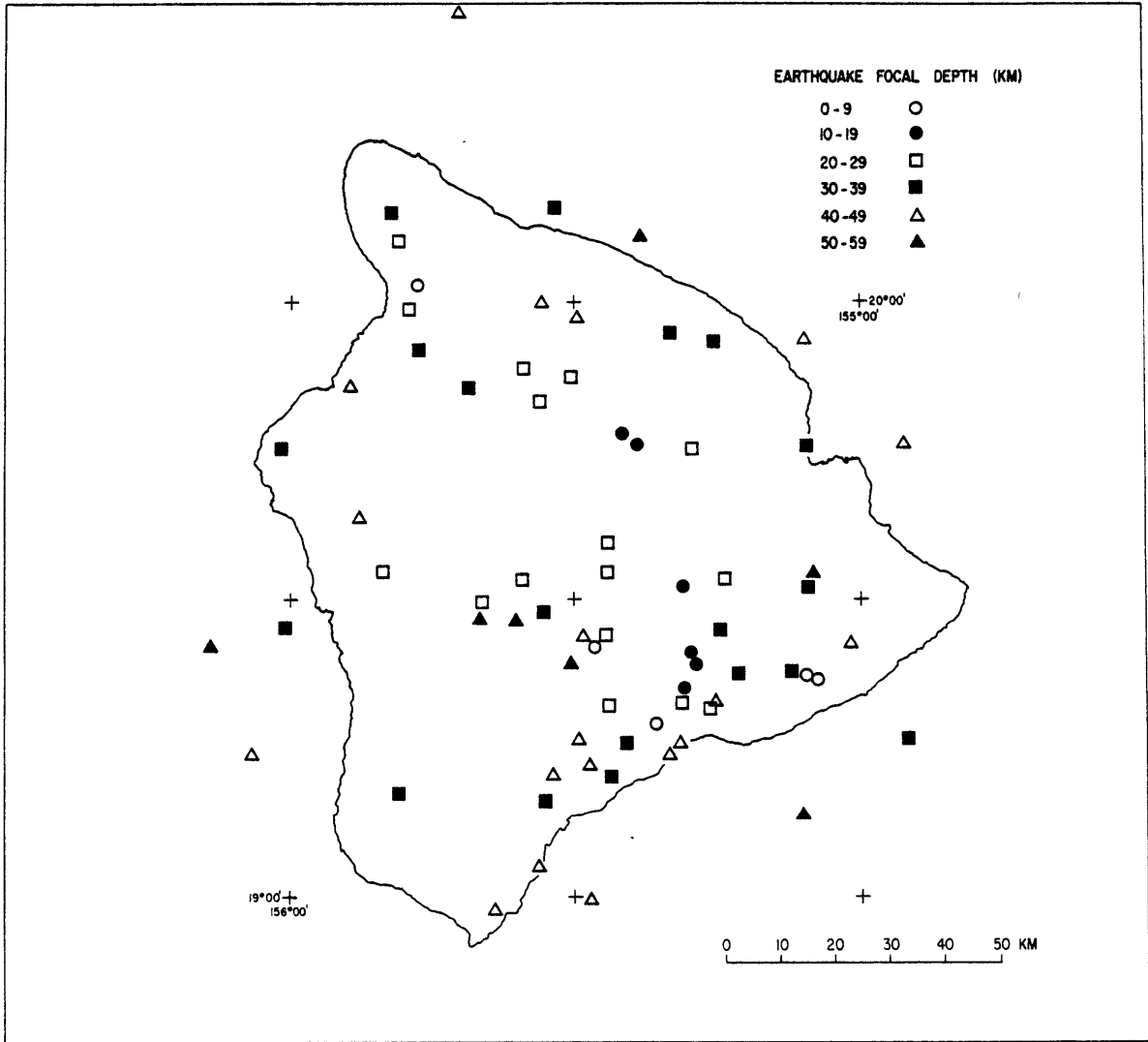
Figure 5.7 Difference between teleseismic and local solutions for crustal velocities (%) plotted on map of Hawaii. Bold dashed lines locate major rift zones. Light dotted lines separate positive and negative values.

Figure 5.8 Block model solution for relative velocity perturbations (%) derived from a) local travel time data and b) teleseismic travel time data (model 4GSB3). Bold line encloses blocks with $R_{ij} \geq 0.5$.

Figure 5.9 Residual difference between local and teleseismic solutions shown in Figure 5.9. A base line correction of 0.9% has been applied.

Figure 5.10 Percent velocity perturbations in mantle derived from teleseismic residuals. Three-dimensional crust and upper mantle solution derived from local travel time data used as the initial model in solutions a) and b). Initial model held fixed in solution a) and allowed to vary in b). Solution c) uses a laterally homogeneous initial model.

Figure 5.1



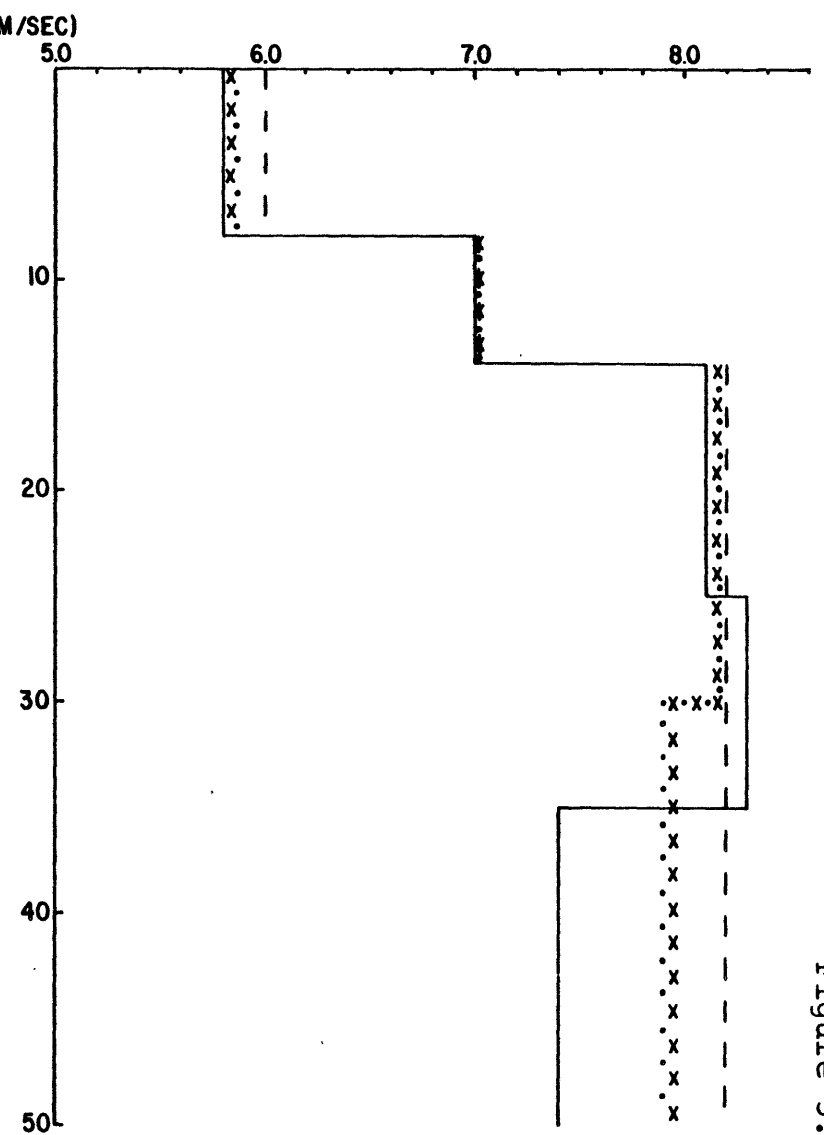
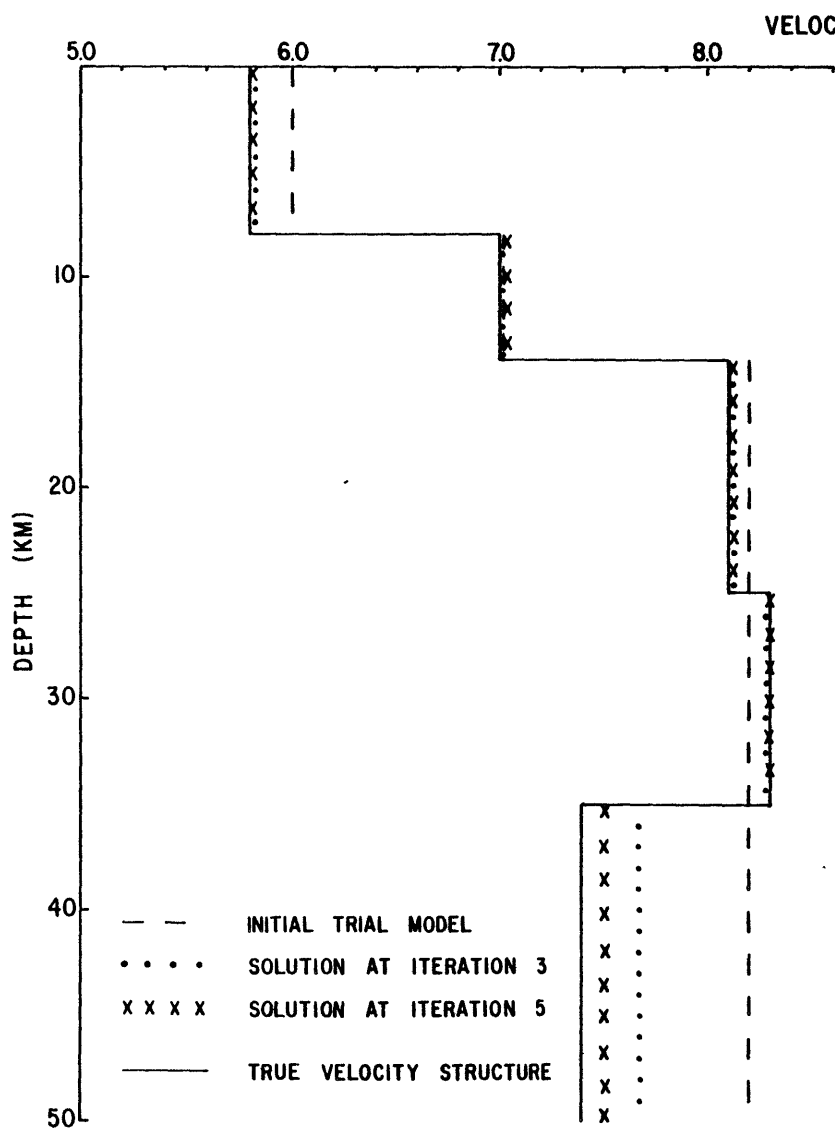


Figure 5.2

Figure 5.3

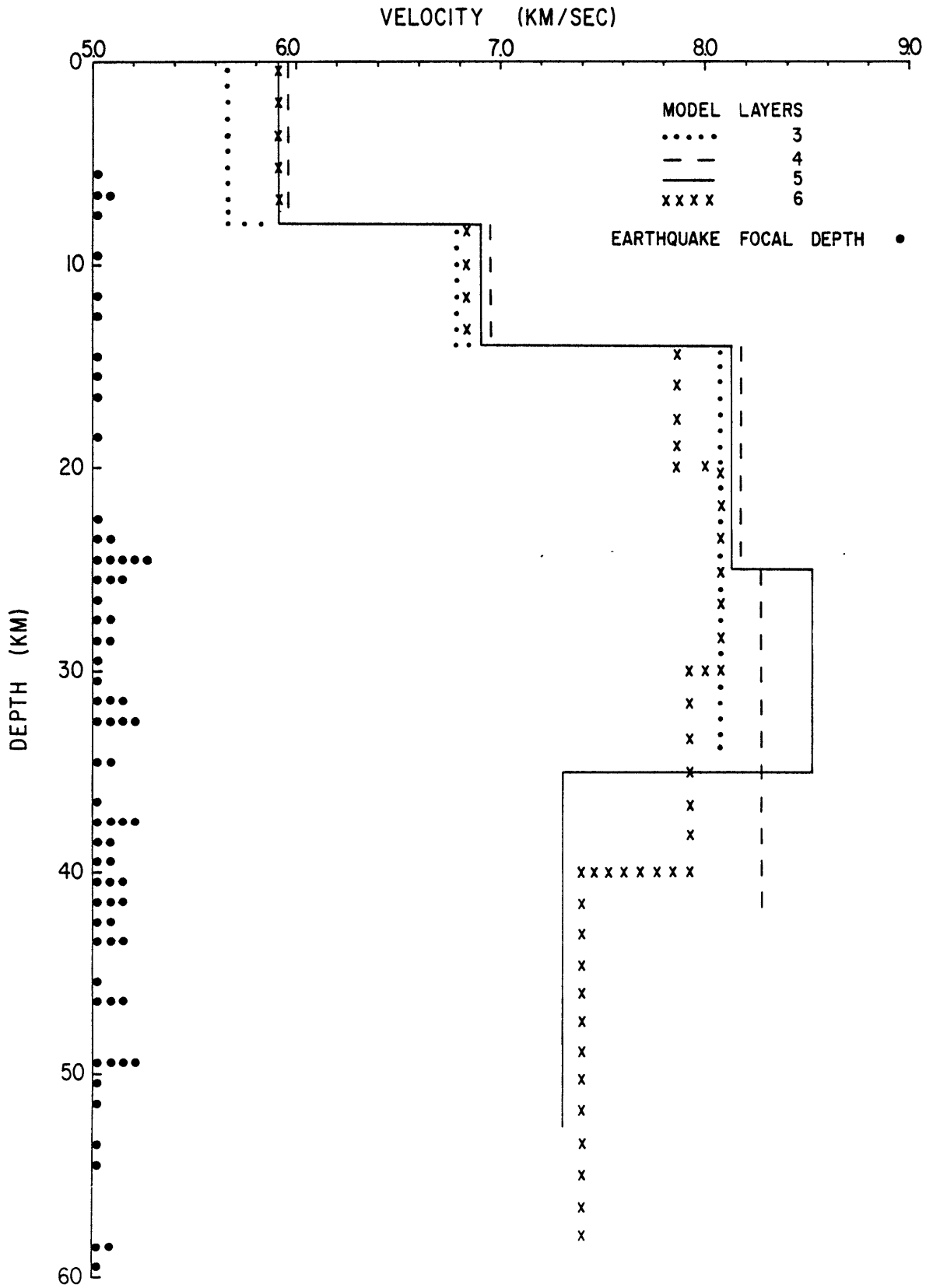


Figure 5.4

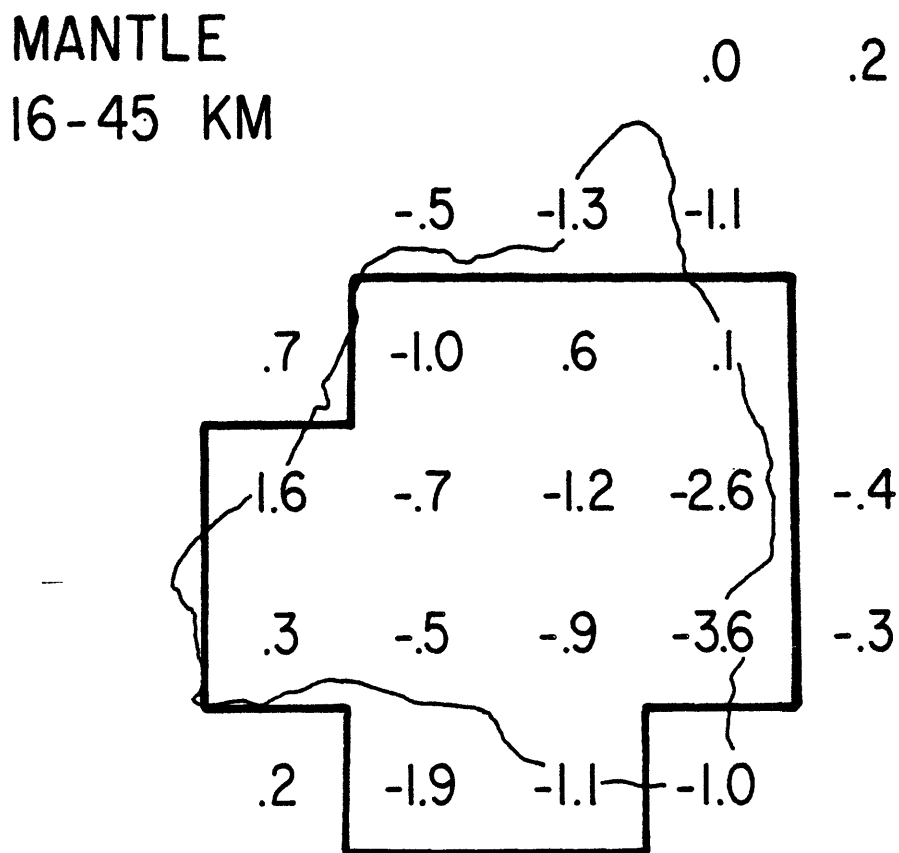
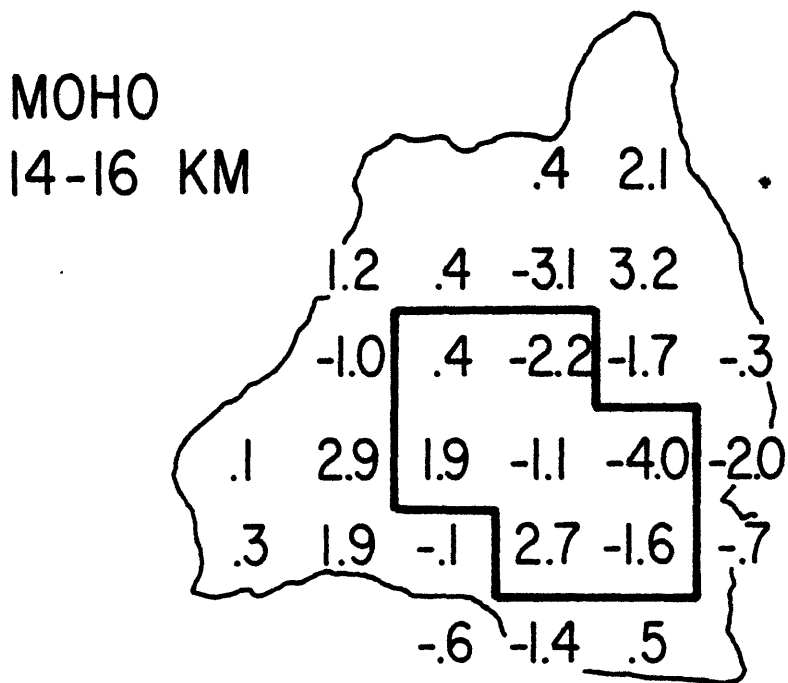


Figure 5.5

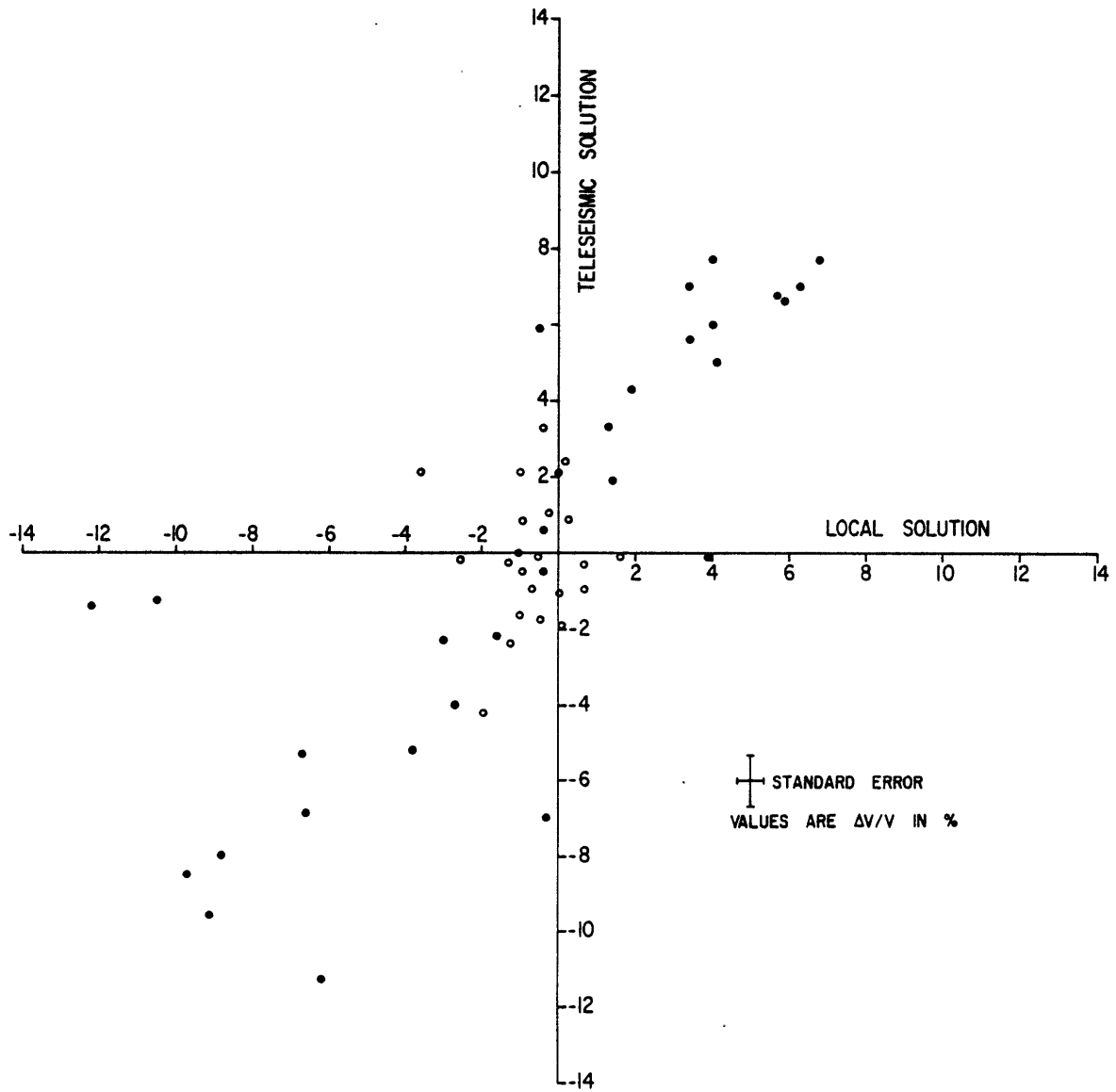


Figure 5.6

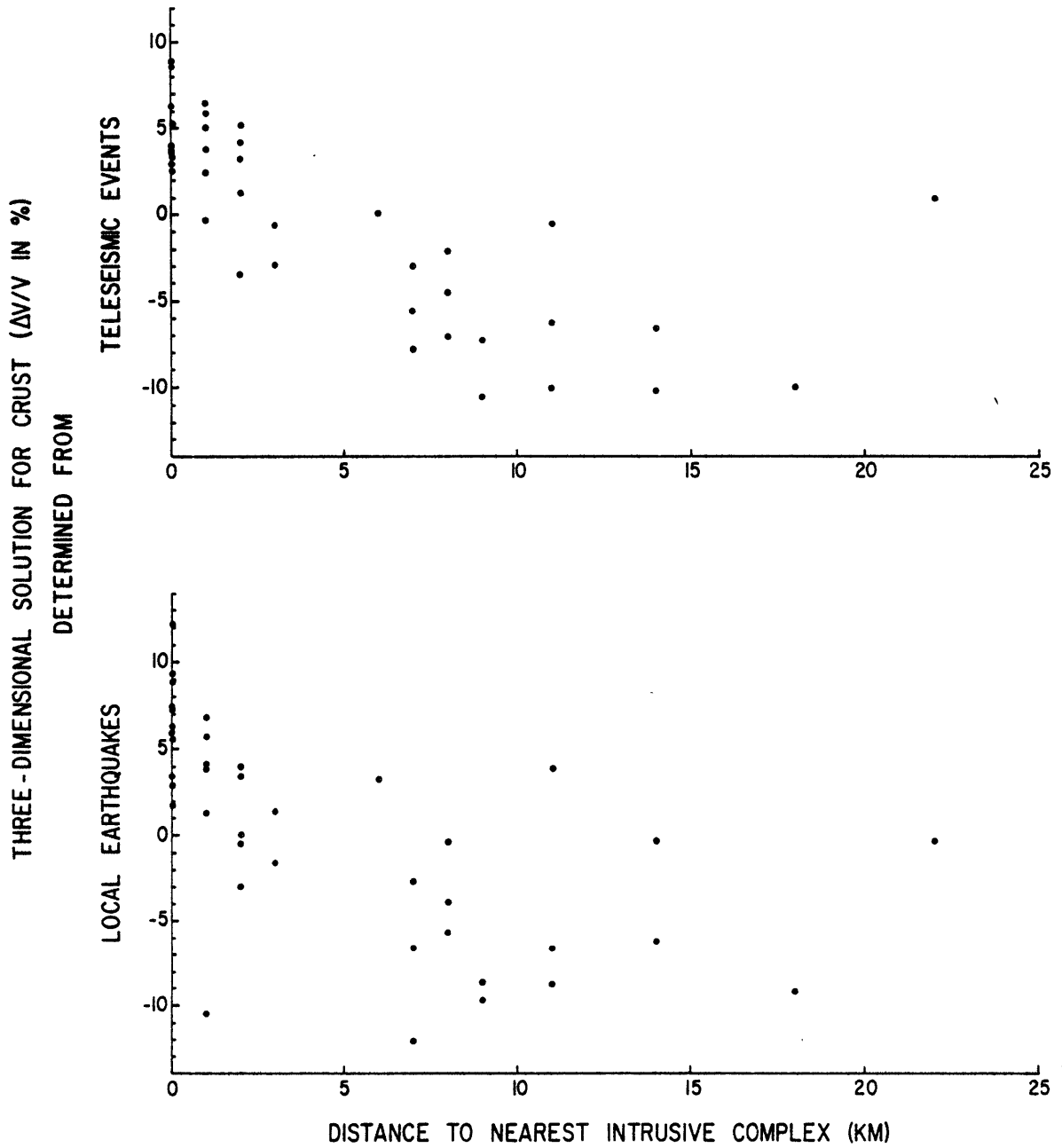


Figure 5.7

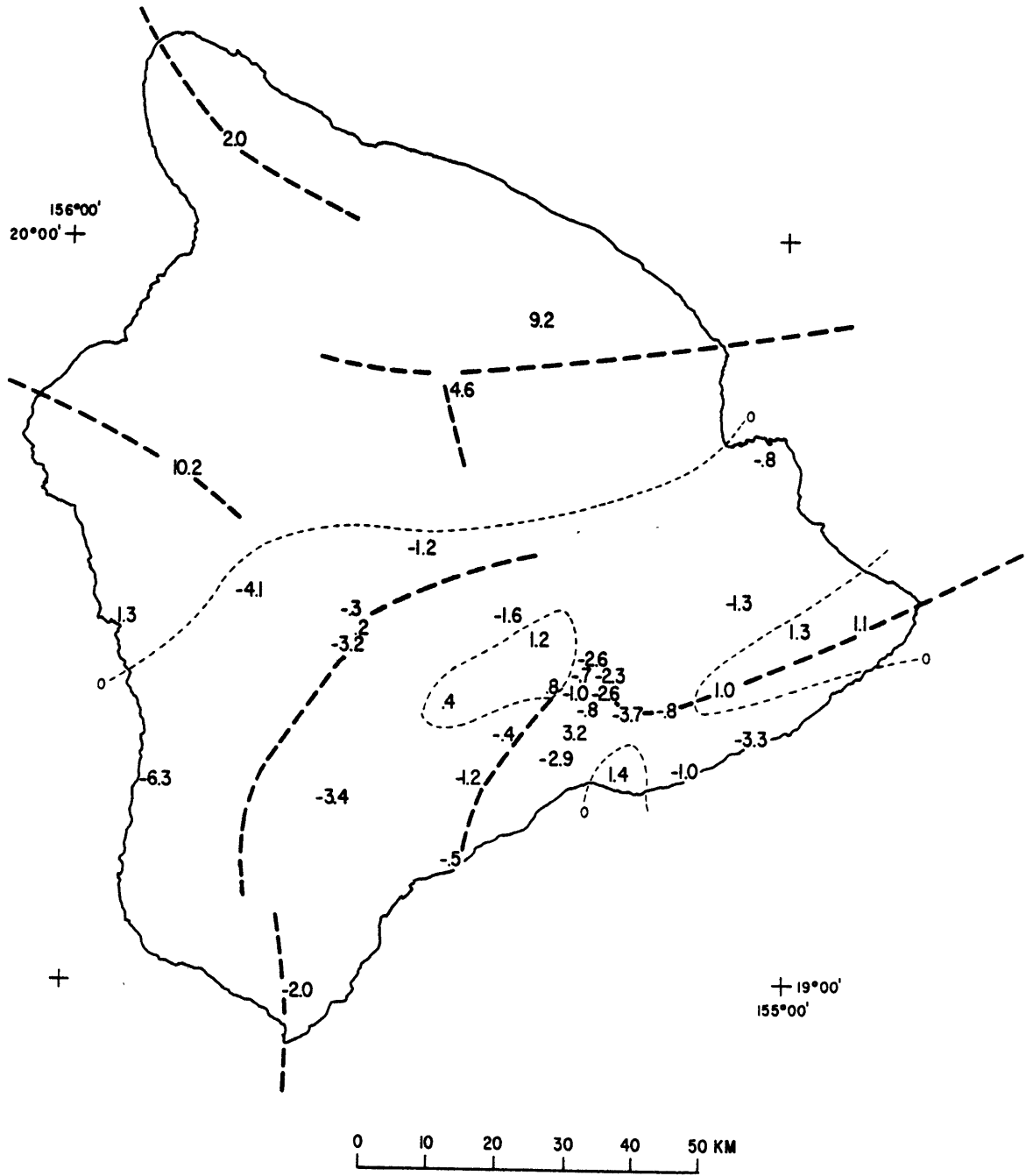


Figure 5.9

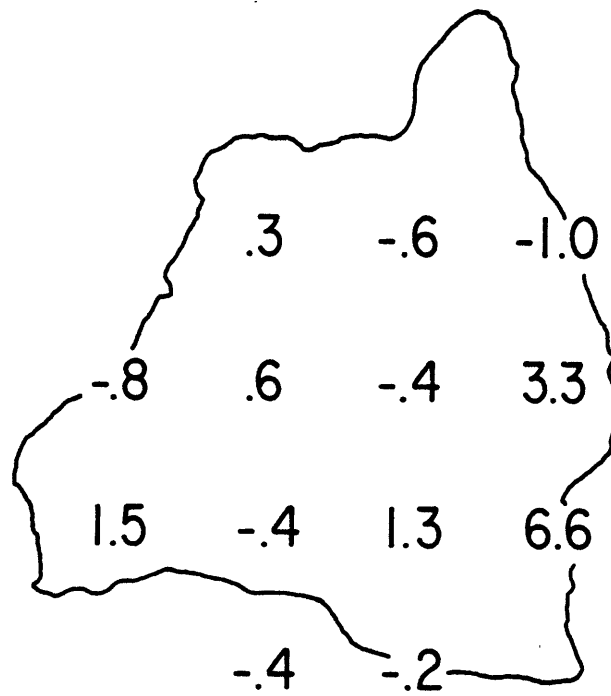
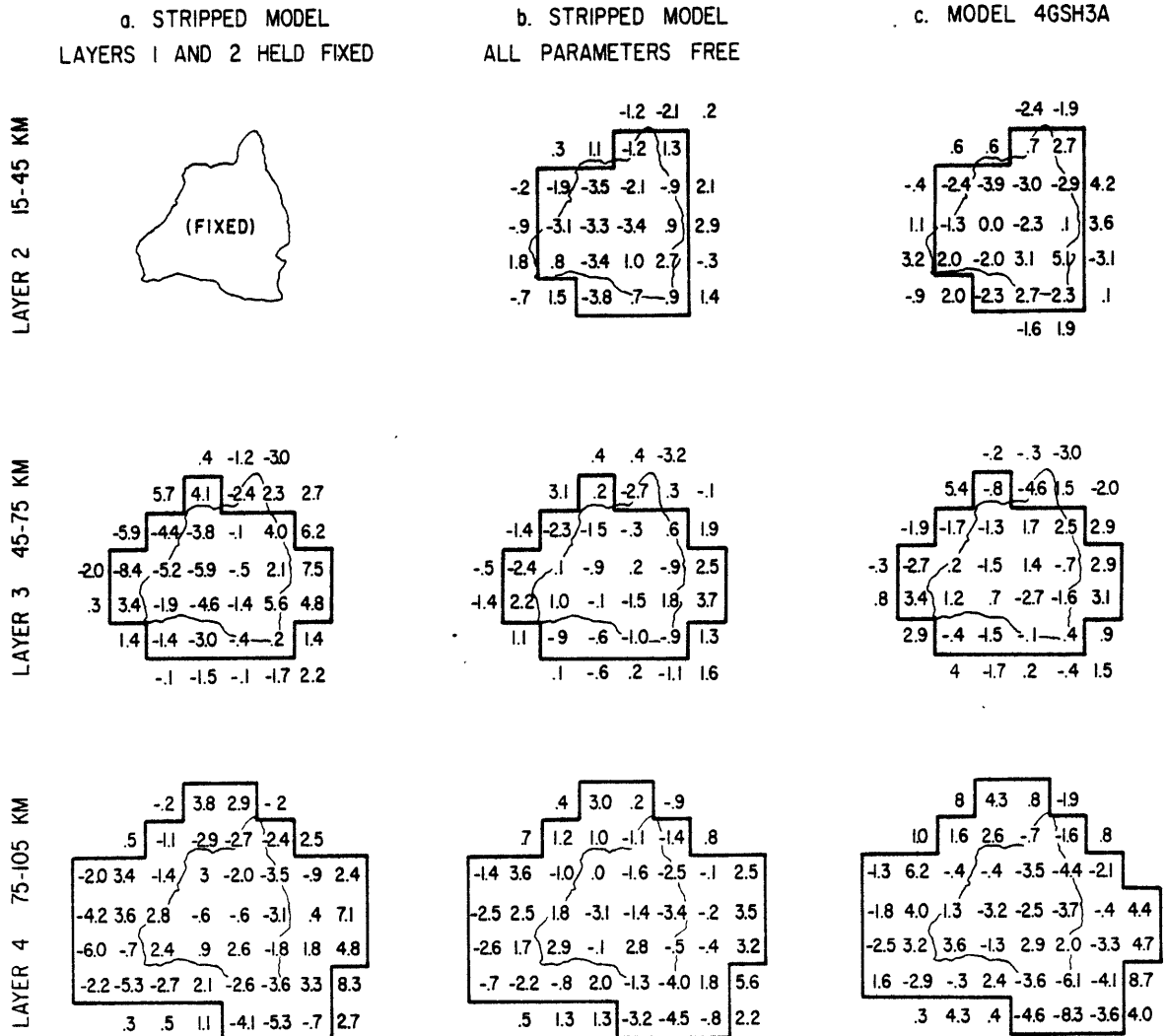


Figure 5.10



CHAPTER 6: Summary and Conclusions

High resolution, three-dimensional velocity models determined by inversion of P-wave travel time data demonstrates the existence of significant lateral heterogeneity within the crust and mantle beneath the Island of Hawaii. Structural variations within the crust are the most pronounced and have an rms fluctuation exceeding 5% on a scale length of about 10 km. These crustal heterogeneities explain about half of the observed variance of relative teleseismic travel time residuals. Heterogeneities within the mantle, measured over longer scale length of 20 to 40 km, are significantly weaker, averaging about 2% rms at depths between 15 and 165 km. These broader scale features do, however, exert a measurable influence upon travel times and explain about 30% of the variance of teleseismic residuals. The variance left unexplained by these structures is at the same level as the intrinsic noise level of the arrival time readings which means that neither deeper structures nor smaller scale heterogeneities are required by the data.

Absolute travel time residuals for both P and PKP indicate that velocities within the mantle underlying Hawaii do not differ greatly from the mean earth. Travel times to Hawaii average only 0.4 sec late for P and 1.2 sec late for PKP (DF branch). Even the questionable evidence that the most vertical rays are

systematically delayed by up to 1.5 sec limits the average velocity deviation in the upper 300 km of the mantle to 4% or less.

Lateral variations in crustal velocity are clearly related to the presence of intrusive dikes and sills within the effusive basalts of the volcanic shield. Velocities of crustal rocks within summit complexes and volcanic rift zones typically exceed those within the non-rift flank by 10% or more. Because magma is undeniably present at shallow depth within the summits and rift zones of Kilauea and Mauna Loa, it is possible that a thermal mechanism such as a high temperature healing of microcracks may contribute to the increase in average velocity. However, inversion results demonstrate that the same velocity relations also apply to Mauna Kea and Kohala, which have passed through the shield building stage in their life-cycles. As it is doubtful that temperatures are greatly elevated within their long abandoned rift zones, the high velocities must result from the dikes and sills, which form the intrusive complexes, having substantially higher P velocity than the effusive basalts. This conclusion is supported by laboratory measurements of velocity of intrusive basaltic rocks (Feves and others, in press). Simple physical models relating laboratory velocity and density data to the three-dimensional inversion results also correctly predict the shape and amplitude of positive Bouguer gravity anomalies over

the volcanic summits and rift zones (Ellsworth and Koyanagi, in press).

The dominant feature of the three-dimensional velocity solution in the lithosphere, between 15 and 75 km depth, is a broad, vertically continuous low velocity zone beneath the central region of the island. Velocities within this zone average 2 to 4% below the relatively high velocities which enclose it on the northeast and to the west. Locally, the velocity contrast between the centralized low velocities and the flanking offshore high velocities exceeds 6%. The lower half of the lithosphere appears to be somewhat more homogeneous than the upper half, as the rms fluctuation there is 1.7%, compared to 2.5% in the overlying mantle.

Structural details, including the configuration and location of individual magmatic passages and magma chambers, escape detection by teleseismic P waves because of the limited resolving power of 1 Hz waves. Although individual heterogeneities cannot be readily associated with specific volcanoes, several broader scale features of the anomaly pattern appear to be significant.

The most pronounced low velocity zone is approximately bounded by the summits of Mauna Kea, Hualalai, and Mauna Loa, but fails to encompass the youngest volcano, Kilauea. Velocities are also systematically lower beneath Mauna Kea than they are beneath its younger neighbors. If we assume that low velocities reflect the presence of magma and/or elevated temperatures,

these relations suggest a simple model for the development of the observed lithospheric velocity structures.

During the first stage of the volcanic life cycle, tholeiite rises rapidly through the lithosphere in comparatively small conduits which connect a deep reservoir to the summit. The narrow (10 km), cylindrical zone of earthquakes which extends from 60 km depth to the summit of Kilauea probably outlines the main passageway of magma to the summit of this youngest volcano (Eaton, 1962; Koyanagi and others, 1976; Figure 6.1). At this stage in its evolution, velocities at distances of 5 to 10 km of the passageway are affected, at least to depths of about 40 km (Ellsworth and Koyanagi, in press).

As the volcano ages, several mechanisms would contribute to a broadening of the low velocity region about the main conduits. Temperature elevation by diffusion of heat could lead to a loss of rigidity and an accompanying decrease in velocity. The volume penetrated by rising magmas could also enlarge with age, especially as eruptions become less frequent and passages close or become obstructed. Mobilization of the more alkaline basalts during the waning stages of tholeiitic volcanism or after its cessation could also account for an increase in the low velocity volume. These basalts erupt from apparently unrelated events scattered on the upper flanks of the shield, which

implies that they do not follow the same pathways used by the tholeiite.

Although speculative, these hypotheses are consistent with current geophysical evidence, including the scattered distribution of mantle earthquakes beneath Mauna Kea, Kohala, and Hualalai, which are absent from either Kilauea or Mauna Loa (Koyanagi and others, 1976; Figure 6.1). Higher resolution modeling of three-dimensional structures attainable by using local earthquakes could provide a critical test of these ideas.

This model for the evolution of the subcrustal roots of Hawaiian-type shield volcanoes outlined above implicitly assumes that the ultimate source of the magmas lies at a greater depth than the deepest earthquakes. At least two independent lines of evidence support this conclusion.

Isotopic compositions of basalts from oceanic islands, including Hawaii, differ significantly from basalts emplaced at mid-ocean ridges (Hedge and Peterman, 1970; Hoffman and Hart, 1975). Unless disequilibrium melting occurs on a broad scale (O'Nions and Pankhurst, 1974), these isotopic differences require chemically distinct mantle sources for ridges and ocean islands (Hoffman and Hart, 1975). This means that remelting of the lithosphere without the addition of deeper-seated material cannot satisfy these data.

Three-dimensional velocity models also support

the conclusion that the source of Hawaiian tholeiites lies below the lithosphere. Although the depth to the base of the lithosphere is not known with certainty, the transition between elastic and plastic behavior probably occurs between the limits given by the deepest earthquakes at 60 km and the lid of the low velocity zone for S waves at about 80 km (Yoshii, 1975; Leeds, 1975; Forsyth, 1977). For the purpose of discussion, we will adopt 75 km as the depth of this transition, and consider deeper structures to lie in the asthenosphere.

Lateral variations in velocity below this depth show two intense, well resolved, low velocity regions in the uppermost asthenosphere. Velocities within these zones average 4 to 6% below their flanking highs (Figure 4.12). Because the asthenosphere is widely regarded to be a zone of incipient melting, or partial melting (Press, 1959; Solomon, 1976), these strong heterogeneities probably result from a lowering of the P velocity by an increased concentration of partial melt. The northeastern of these two zones underlies most of the Island of Hawaii, and is vertically continuous with the low velocity zone in the lower lithosphere, from which it is well resolved (Table 4.3). The southeastern zone is centered south and east of Cape Kumukahi and is not as clearly associated with overlying anomalies, although it could connect with low velocities generally

to the southeast of Kilauea's summit through inclined passages.

The vertical association of the northeastern zone with shallower low velocity regions, coupled with the likelihood that these zones contain a more abundant melt fraction than the surrounding lithosphere, supports the hypothesis that tholeiitic magma is in transit through these zones from a deeper source or that these zones are, in fact, the source volume for the erupted basalts.

Deeper-seated lateral heterogeneities, between 105 and 165 km depth, define several trends which are broadly aligned along the island chain (Figure 6.2). The pattern of a central low sandwiched between flanking highs is again repeated at this level, with the variation that the maximum low velocities lie along the axis of the Hawaiian islands as extrapolated from the older volcanoes rather than beneath the Island of Hawaii. In fact, the low velocity zone beneath the island is only marginally significant by the statistical criteria outlined in §4.6, which suggests that the vertically continuous column of relative low velocities observed at shallower depths bottoms out within the depth interval. In addition to this closed low velocity zone below the island, several isolated low velocity zones can be identified (Figure 6.2).

The intense low velocity zone east of Cape Kumukahi appears to be the downward extension of the low velocity

region which overlies it in the uppermost asthenosphere. Because this zone lies about 100 km east of the summit of the nearest volcano, Kilauea, it probably is not related to existing volcanoes. Its position does, however, coincide with the locus of the "melting spot" predicted by Jackson and others (1972) and Dalrymple and others (1973). Other, less well resolved features loosely align within a zone of about 200 km width which extends from the Island of Maui well to the southeast of Hawaii.

The nature of lateral heterogeneities which exists at even greater depths is conjectured, as the data analyzed here cannot resolve them. However, the persistence of strong (>5%) heterogeneities to the base of the models suggest that they probably continue to greater depths as well. Although these models extend to over 160 km depth, they penetrate only about half of the asthenosphere which terminates between 250 and 300 km (Press, 1970; Kanamori, 1970; Dziewonski and others, 1975; Forsyth, 1977). Consequently, these models cannot by themselves settle the question of the source depth of Hawaiian basalts. They do indicate that the volcanoes are rooted at depths well in excess of 100 km and that the source volume lies within or below the asthenosphere.

The implications of the three-dimensional velocity structure for the origin of linear island chains is, I believe, more straightforward. The critical observations include the vertical continuity of the cylindrical low velocity zone, which underlies the island, from the

asthenosphere into the lithosphere; the absence of strong velocity contrasts directly southeast of Kilauea and Mauna Loa; and the existence of a pronounced low velocity zone well removed from the young volcanoes which aligns along the island chain axis. Each of these pieces of evidence supports the hypothesis that the Hawaiian chain traces the movements of the Pacific plate over a concentrated, convective upwelling (Dietz and Menard, 1953; Wilson, 1963; Morgan, 1971). They do not support the existence of a dense, high velocity residuum as proposed by Shaw and Jackson (1973), and are difficult to reconcile with fracture propagation in the lithosphere.

The most damaging aspect of the lateral velocity structure for any model which confines causal processes to the lithosphere, or to the shear zone between lithosphere and asthenosphere, is the vertical continuity of intense, low velocity zones in the asthenosphere which do not underly the volcanoes. Unless these zones represent typical heterogeneities present within the asthenosphere they require an external source for their formation and maintainance.

The geometrical configuration of the broader asthenospheric zone of below average velocities, including its width of about 200 km, its elongation along a small circle of Pacific plate motion, and its extension well to the southeast of the youngest volcanoes, clearly supports the hypothesis of a lower mantle convective

source for both this zone and, ultimately, for the island chain itself. Taken together with the assembled evidence from many other sources, these data favor the fundamental aspects of the plume model as proposed by Morgan (1971) including the concentrated upwelling of hot, comparatively primitive material in a narrow zone which broadly elevates the sea floor and produces an age-ordered progression of shield volcanoes which trace the movement of the mobile lithosphere over the hot spot.

The primary contribution of this thesis to the resolution of this question is a three-dimensional geometric description of the hot spot within both the lithosphere and upper asthenosphere. A more detailed description of these features, which extends the modeling to substantially greater depths, is, I believe, practical and requires either enlargement of the Hawaiian array through deployment of offshore instruments or collection of a large suite of PKP travel times on the existing array. A better understanding of small scale structures within the crust and upper lithosphere through more intensive analysis of available P and S travel time data would also greatly extend our understanding of lithospheric structure.

Chapter 6 - Figure Captions

Figure 6.1 Map of the Island of Hawaii showing mantle earthquakes occurring between 1970 and 1973, $m_b \geq 3.0$. Average percent velocity contours from smoothed block model in the depth interval from 15 to 45 km are shown. Triangles mark volcanic summits.

Figure 6.2 Percent velocity contours from average of models 5GSH3A and 4DSH3A in the depth interval from 105 to 165 km on a oblique mercator map of the Hawaiian chain. Projection pole is at 69°N , 68°W . Island coastlines indicated by solid lines. Dashed line is the 1000 fathom contour on submarine volcanoes.

Figure 6.1



KEY

△ VOLCANIC SUMMIT

• MANTLE EARTHQUAKE

CONTOUR INTERVAL 2% $\Delta V/V$

0 100 KM

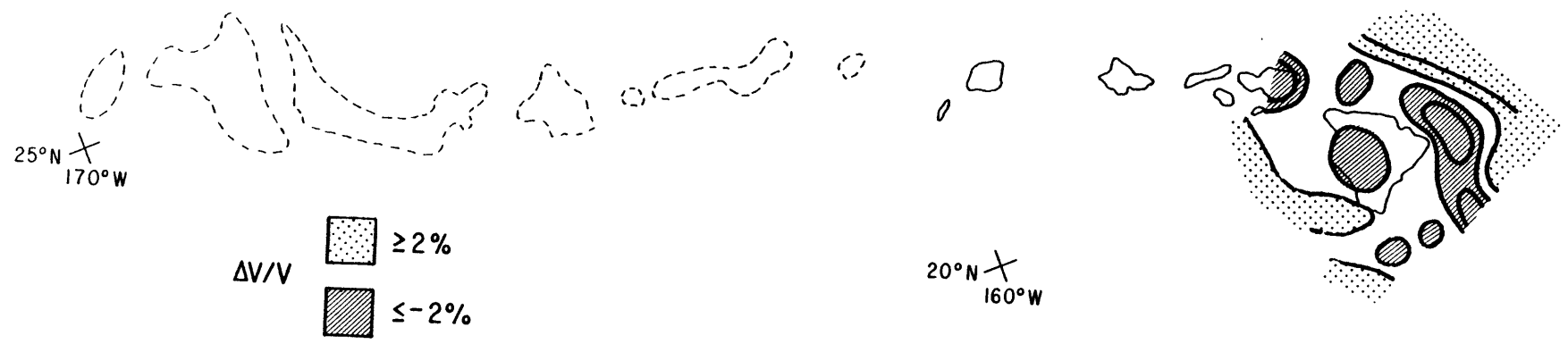


Figure 6.2

REFERENCES

- Acton, F., Numerical Methods That Work, Harper and Row, New York, 541 pp., 1970.
- Aki, K., Scattering of P waves under the Montana LASA, Jour. Geophys. Res., 78, 1334-1346, 1973.
- Aki, K. and W.H.K. Lee, Determination of three-dimensional velocity anomalies under a seismic array using first P arrival times from local earthquakes. 1. A homogeneous initial model, Jour. Geophys. Res., 81, 4381-4399, 1976.
- Aki, K., A. Christoffersson and E.S. Husebye, Determination of the three-dimensional structure of the lithosphere, Jour. Geophys. Res., 82, 277-296, 1977a.
- Aki, K., M. Fehler and S. Das, Source mechanism of volcanic tremor: fluid-driven crack models and their application to the 1963 Kilauea eruption, Volcanol. and Geotherm. Res., 2, 259-287, 1977b.
- Asada, T. and H. Shimamura, Observation of earthquakes and explosions at the bottom of the western Pacific: structure of the oceanic lithosphere revealed by longshot experiment, in The Geophysics of the Pacific Ocean Basin and Its Margins, Am. Geophys. Un. Mon. 19, 135-153, 1976.
- Backus, G. and J.F. Gilbert, Numerical applications of a formalism for geophysical inverse problems, Geophys. Jour. Roy. Astron. Soc., 13, 247-276, 1967.

- Backus, G.E. and J.F. Gilbert, The resolving power of gross earth data, Geophys. Jour. Roy. Astron. Soc., 16, 169-205, 1968.
- Backus, G.E. and J.F. Gilbert, Constructing P-velocity models to fit restricted sets of travel-time data, Bull. Seis. Soc. Am., 59, 1407-1414, 1969.
- Berteussen, K.A., Array analysis of lateral inhomogeneities in the deep mantle, Earth Planet. Sci. Lett., 28, 212-216, 1975.
- Bessonova, N.E., V.M. Fishman, M.G. Shnirman, G.A. Sitnikova and L.R. Johnson, The tau method for inversion of travel times. II. Earthquake data, Geophys. Jour. Roy. Astron. Soc., 46, 87-108, 1976.
- Betz, F., Jr. and H.H. Hess, The floor of the north Pacific Ocean, Geograph. Rev., 32, 99-116, 1942.
- Bolt, B.A., Travel time tables for the seismic wave PKP, Nature, 207, 967-969, 1965.
- Bolt, B.A., Estimation of PKP travel times, Bull. Seis. Soc. Am., 58, 1305-1324, 1968.
- Buland, R., The mechanics of locating earthquakes, Bull. Seis. Soc. Am., 66, 173-187, 1976.
- Bulirsch, R. and J. Stoer, Numerical treatment of ordinary differential equations by extrapolation methods, Numerische Mathematik, 8, 1-13, 1966.
- Bulter, R. and C. Langston, The Hawaiian earthquake of April 26, 1973: a double event, EOS, Trans. Am. Geophys. Un., 47, 954, 1976.

- Carder, D.S., D.W. Gordon and J.N. Jordan, Analysis of surface foci travel times, Bull. Seis. Soc. Am., 56, 815-840, 1966.
- Chase, T.E., H.W. Menard, and J. Mammerickx, Topography of the North Pacific, Chart TR-17, Inst. of Mar. Res., Univ. of Calif., San Diego, 1971.
- Chernov. L.A., Wave Propagation in a Random Medium, McGraw-Hill, New York, 168 pp., 1960.
- Clague, D.A., G.B. Dalrymple and R. Moberly, Petrography and K-Ar ages of dredged volcanic rocks from the western Hawaiian ridge and southern Emperor seamount chain, Geol. Soc. Am. Bull., 86, 991-998, 1975.
- Cleary, J.R. and A.L. Hales, An analysis of the travel times of P waves to North American stations in the distance range of 32° to 100°, Bull. Seis. Soc. Am., 56, 467-489, 1966.
- Cross, W., Lavas of Hawaii and their relations, U.S. Geol. Surv. Prof. Paper 88, 97 pp., 1915.
- Crosson, R.S., Crustal structure modeling of earthquake data. 1. Simultaneous least squares estimation of hypocenter and velocity parameters, Jour. Geophys. Res., 81, 3036-3046, 1976a.
- Crosson, R.S., Crustal structure modeling of earthquake data. 2. Velocity structure of the Puget Sound region, Washington, Jour. Geophys. Res., 81, 3047-3054, 1976b.
- Dalrymple, G.B., E.A. Silver and E.D. Jackson, Origin of the Hawaiian Islands, American Scientist, 61, 294-303, 1973.

- Dana, J.D., Geology, U.S. Exploring Expedition 1838-1842,
10, 756 pp., 1849.
- Dana, James D., Manual of Geology, Ivison, Blakeman,
Taylor and Co., New York, 30-35, 701-702, 1871.
- Dana, James D., History of changes in Mt. Loa crater,
Am. Jour. Sci., 36, 170-171, 1888.
- Dana, James D., On the origin of the deep troughs of the
oceanic depression: are any of volcanic origin?,
Am. Jour. Sci., 37, 192-202, 1889.
- Darwin, Charles, Geologic Observations on Coral Reefs,
Volcanic Islands and on South America: Being the
Geology of the Voyage of the Beagle, under the
Command of Captain Fitzroy, R.N., during the Years
1832 to 1836, Smith, Elden and Co., London, Part II,
124-129, 1851.
- Davies, D. and R.M. Sheppard, Lateral heterogeneity in
the Earth's mantle, Nature, 239, 318-323, 1972.
- Detrick, R.S. and S.T. Crough, Implications of the subsi-
dence history of mid-plate island chains on the
thermo-elastic response of the lithosphere to hot
spot-related mantle plumes, EOS, Trans. Am. Geophys. Un.,
58, 497, 1977.
- Detrick, R.S. and S.T. Crough, Island subsidence, hot
spots and lithospheric thinning, Jour. Geophys. Res.,
submitted 1977.
- Dietz, R.S. and H.W. Menard, Hawaiian swell, deep and
arch, and subsidence of the Hawaiian Islands, J. Geol.
61, 99-113, 1953.

- Duncan, R.A. and I. McDougall, Linear volcanism in French Polynesia, Volcanol. Geotherm. Res., 1, 197-227, 1976.
- Dziewonski, A. and F. Gilbert, The effect of small aspherical perturbations on travel times and a re-examination of the corrections for ellipticity, Geophys. Jour. Roy. Astron. Soc., 44, 7-17, 1976.
- Dziewonski, A., A.L. Hales and E.R. Lapwood, Parametrically simple earth models consistent with geophysical data, Phys. Earth Planet. Int., 10, 12-48, 1975.
- Dziewonski, A., B. Hager, and R. O'Connell, Large-scale heterogeneities in the lower mantle, Jour. Geophys. Res., 82, 239-255, 1977.
- Eaton, J.P., Crustal structure and volcanism in Hawaii, The crust of the Pacific basin, Am. Geophys. Un. Mon. 6, 13-29, 1962.
- Eaton, J.P. and K.J. Murata, How volcanoes grow, Science, 132, 925-938, 1960.
- Ellsworth, W.L. and R.Y. Koyanagi, Three-dimensional crust and upper mantle structure of Kilauea Volcano, Hawaii, Jour. Geophys. Res., in press, 1977.
- Eliseevnin, V.A., Analysis of waves propagating in an inhomogeneous medium, Soviet Physics-Acoustics, 10, 242-245, 1965.
- Engdahl, E.R. and C.P. Felix, Nature of travel time anomalies at LASA, Jour. Geophys. Res., 76, 2706-2715, 1971.

- Engdahl, E.R. and W.H.K. Lee, Relocation of local earthquakes by seismic ray tracing, Jour. Geophys. Res., 81, 4400-4406, 1976.
- Feves, M., G. Simmons and R.W. Siegfried, Microcracks in crustal igneous rocks: physical properties, in The Earth's Crust: Its Nature and Physical Properties, Geophys. Mono. Ser. 20, J.G. Heacock (ed.), Am. Geophys. Un., Washington, D.C., in press, 1977.
- Forsyth, D.W., The evolution of the upper mantle beneath mid-ocean ridges, Tectonophysics, 38, 89-118, 1977.
- Franklin, J., Well-posed stochastic extensions of ill-posed linear problems, J. Math. Anal. Appl., 21, 682-716, 1970.
- Furumoto, A.S., G.P. Woollard, J.F. Campbell and D.M. Hussong, Variations in the thickness of the crust in the Hawaiian Archipelago, in The Crust and Upper Mantle of the Pacific Area, ed. by. L. Knopoff, C.L. Drake and P.J. Hart, Am. Geophys. Mon. 12, 94-111, 1968.
- Geiger, L., Herdbestimmung bie erdbeben aus den ankunftszeiten, K. Gessell. Wiss. Goett, 4, 331-349, 1910.
- Gerver, M., and V. Markushevich, Determination of a seismic wave velocity from the travel time curve, Geophys. Jour. Roy. Astron. Soc., 11, 165-173, 1966.
- Golub, G.H. and P.A. Businger, Linear least squares solutions by Householder transformations, Numer. Math., 7, H.B. Series Linear Algebra, 269-276, 1965.

- Green, D.H., Composition of basaltic magmas as indicators on conditions of origin: application to oceanic volcanism, Phil. Trans. Roy. Soc., London A, 268, 707-725, 1971.
- Hedge, C.E. and A.E. Peterman, The strontium isotopic composition of basalts from the Gordo and Juan de Fuca Rise, northeastern Pacific Ocean, Contrib. Mineral. Petrol., 27, 114-120, 1970.
- Herrin, E., W. Tucker, J.N. Taggart, D.W. Gordon, and J.L. Lobdell, Estimation of surface focus P travel times, Bull. Seis. Soc. Am., 58, 1273-1291, 1968.
- Hill, D.P., Crustal structure of the Island of Hawaii from seismic-refraction measurements, Bull. Seis. Soc. Am., 59, 101-130, 1969.
- Hofmann, A.W. and S.R. Hart, An assessment of local and regional isotopic equilibrium in the mantle, Carnegie Inst. Washington Yearbook, 74, 195-210, 1975.
- Jackson, E.D. and T.L. Wright, Xenoliths in the Honolulu Volcanic Series, Hawaii, Jour. Petrol., 11, 405-430, 1970.
- Jackson, E.D., E.A. Silver and G.B. Dalrymple, Hawaiian-Emperor chain and its relation to Cenozoic circum-Pacific tectonics, Geol. Soc. Am. Bull., 83, 601-618, 1972.
- Jacob, K.H., Three-dimensional seismic ray tracing in a laterally heterogeneous spherical earth, J. Geophys. Res., 75, 6675-6689, 1970.

- Jaggar, T.A., Seismometric investigation of the Hawaiian lava column, Seismol. Soc. Am. Bull., 10, 155-275, 1920.
- Jarrard, R.D. and D.A. Clague, Implications of Pacific Island and seamount ages for the origin of volcanic chains, Rev. Geophys. Space Phys., 15, 57-76, 1977.
- Jeffreys, H. and K.E. Bullen, Seismological Tables, Brit. Assn. Gray-Milne Trust, 50 pp., 1958.
- Jenkins, F.A. and H.E. White, Fundamentals of Optics, McGraw-Hill Book Co., New York, 7, 1957.
- Johnson, L.R., Array measurements of P velocities in the upper mantle, J. Geophys. Res., 72, 6309-6325, 1967.
- Johnson, L.R., Array measurements of P velocities in the lower mantle, Bull. Seis. Soc. Am., 59, 973-1008, 1969.
- Julian, B.R., Ray tracing in arbitrarily heterogeneous media, Technical Note 1970-45, Lincoln Laboratory, Mass. Inst. of Techn., Lexington, 1970.
- Julian, B.R. and D. Gubbins, Three-dimensional seismic ray tracing, Geophys. Jour., submitted 1977.
- Kanamori, H., Velocity and Q of mantle waves, Phys. Earth Planet. Int., 2, 259-275, 1970.
- Koyanagi, R.Y., Earthquakes from common sources beneath Kilauea and Mauna Loa volcanoes in Hawaii from 1962 to 1965, U.S. Geol. Surv., Prof. Paper 600-C, C120-C125, 1968.
- Koyanagi, R.Y., A.T. Okamura, and G. Kojima, Hawaiian Volcano Observatory Summary 63, U.S. Geol. Surv., 99 pp., 1974.

- Koyanagi, R.Y., E.T. Endo and J.E. Ebinu, Reawakening of Mauna Loa volcano, Hawaii: a preliminary evaluation of seismic evidence, Geophys. Res. Lett., 2, 405-408, 1975.
- Koyanagi, R.Y., E.T. Endo and P.L. Ward, Seismic activity on the Island of Hawaii, 1970 to 1973, in The Geophysics of the Pacific Ocean Basin and Its Margins, Am. Geophys. Un. Mon. 19, 169-172, 1976.
- Lanczos, C., Linear Differential Operators, Chapter 3, Van Nostrand, London, 564 pp., 1961.
- Lawson, C.L. and R.J. Hanson, Solving Least Squares Problems, Prentice-Hall, Englewood Cliffs, 340 pp., 1974.
- Lee, W.H.K. and V. Pereyra, Solving two-point seismic ray tracing problems in a heterogeneous medium, Part 2. Numerical solutions of two-dimensional velocity models, in prep., 1977.
- Leeds, A.R., Lithospheric thickness in the western Pacific, Phys. Earth Planet. Int., 11, 61-64, 1975.
- Levenberg, K., A method for the solution to certian non-linear problems in least squares, Quart. Appl. Math., 2, 164-168, 1944.
- Lilwall, R.C. and A. Douglas, Estimation of P-wave travel times using the joint epicenter method, Geophys. Jour. Roy. Astron. Soc., 19, 165-181, 1970.
- Macdonald, G.A. and T. Katsura, Chemical composition of Hawaiian lavas, J. Petrol., 5, 82-133, 1964.

- Marquardt, D.W., An algorithm for least-squares estimation of nonlinear parameters, J. Soc. Indust. Appl. Math., 11, 431-441, 1963.
- Marsh, B.D. and J.G. Marsh, On global gravity anomalies and two-scale mantle convection, J. Geophys. Res., 81, 5267-5280, 1976.
- McDougall, I., Potassium-argon ages from lavas of the Hawaiian Islands, Geol. Soc. Am. Bull., 75, 107-128, 1964.
- McDougall, I., Volcanic island chains and sea-floor spreading, Nat. Phys. Sci., 231, 141-144, 1971.
- Mercier, J.-C. and N.L. Carter, Pyroxene geotherms, J. Geophys. Res., 80, 3349-3362, 1975.
- Mogi, K., Relations between the eruptions of various volcanoes and the deformations of the ground surface around them, Bull. Earthq. Res. Inst., 36, 99-134, 1958.
- Moore, J.G., Relationship between subsidence and volcanic load, Hawaii, Bull. Volcanol., 34, 562-576, 1970.
- Morgan, W.J., Convection plumes in the lower mantle, Nature, 230, 42-43, 1971.
- Morgan, W.J., Plate motions and deep mantle convection, Geol. Soc. Am. Mem. 132, 7-22, 1972a.
- Morgan, J.W., Deep mantle convection plumes and plate motion, Am. Assoc. Petro. Geol. Bull., 56, 203-213, 1972b.

- Niazi, M. and D.L. Anderson, Upper mantle structure of western North America from apparent velocities of P waves, J. Geophys. Res., 70, 4633-4640, 1965.
- Okal, E. and G. Kuster, A teleseismic study in French Polynesia: implications for distant and local structure, Geophys. Res. Lett., 2, 5-8, 1975.
- O'Nions, R.K. and R.J. Pankhurst, Petrogenic significance of isotope and trace element variations in volcanic rocks from the mid-Atlantic, J. Petrol., 15, 603-634, 1974.
- Otsuka, M., Azimuth and slowness anomalies of seismic waves measured on the central California seismographic array, Part II. Interpretation, Bull. Seis. Soc. Am., 56, 655-675, 1966.
- Pereyra, V. and W.H.K. Lee, Solving two-point seismic ray tracing problems in a heterogeneous medium, Part I. A general numerical method based on adaptive finite differences, in prep. 1977.
- Peters, D.C., Hypocenter locations and crustal structure: inversion of seismic array travel times (abs.), Diss. Abstr. Int., 35, 332B-333B, 1974.
- Pollard, D.D. and J.P. Eaton, Crustal structure of the Island of Hawaii (abs.), Geol. Soc. Am., Special Paper 76, 218-219, 1964.
- Powell, C.A., Mantle heterogeneity: evidence from large seismic arrays, unpubl. Ph.D. thesis, Princeton Univ., 326 pp., 1976.

- Powers, H.A., Differentiation in Hawaiian lavas, Am. Jour. Sci., 30, 57-71, 1935.
- Powers, H.A., Composition and origin of basaltic magmas of the Hawaiian Islands, Geochem. Cosmochim. Acta, 7, 77-107, 1955.
- Powers, S., Tectonic lines in the Hawaiian Islands, Geol. Soc. Am. Bull., 28, 501-514, 1917.
- Press, F., Some implications on mantle and crustal structure from G waves and Love waves, J. Geophys. Res., 64, 565-568, 1959.
- Press, F., Earth models consistent with geophysical data, Phys. Earth Planet. Int., 3, 3-22, 1970.
- Roecker, S., Preliminary crustal velocity modeling under Oroville, California, unpubl. manuscript, 56 pp., 1977.
- Ryall, A. and D.L. Bennett, Crustal structure of southern Hawaii related to volcanic processes in the upper mantle, J. Geophys. Res., 73, 4561-4582, 1968.
- Sengupta, M., The structure of the Earth's mantle from body wave observations, unpubl. Ph.D. Thesis, Mass. Inst. of Techn., 579 pp., 1975.
- Sengupta, M.K. and B.R. Julian, P-wave travel times for deep focus earthquakes, Bull. Seis. Soc. Am., 66, 1555-1579, 1976.
- Sengupta, M. and M.N. Toksöz, Three-dimensional model of seismic velocity variations in the Earth's mantle, Geophys. Res. Lett., 3, 84-86, 1976.

- Shaw, H.R., Mantle convection and volcanic periodicity in the Pacific: evidence from Hawaii, Geol. Soc. Am. Bull., 84, 1505-1526, 1973.
- Shaw, H.R. and E.D. Jackson, Linear island chains in the Pacific: results of thermal plumes or gravitational anchors?, J. Geophys. Res., 78, 8634-8652, 1973.
- Shimozuru, D., K. Kamo and W.T. Kinoshita, Volcanic tremor of Kilauea volcano, Hawaii, during July-December, 1963, Bull. Earthq. Res. Inst., 44, 1093-1133, 1966.
- Solomon, S.C., Geophysical constraints on radial and lateral temperature variations in the upper mantle, Amer. Mineral., 61, 788-803, 1976.
- Steppe, J.A., W.H. Bakun, and C.G. Bufe, Temporal stability of P-velocity anisotropy before earthquakes in central California, Bull. Seis. Soc. Am., 67, 1075-1090, 1977.
- Steppe, J.A. and R.S. Crosson, P-velocity models of the southern Diablo Range, California, from inversion of earthquake and explosion arrival times, Bull. Seis. Soc. Am., in press 1977.
- Swanson, D.A., Magma supply rate at Kilauea volcano, 1952-1971, Science, 175, 169-170, 1972.
- Swanson, D.A., W.A. Duffield and R.S. Fiske, Displacement of the south flank of Kilauea Volcano: the result of forceful intrusion of magma into the rift zones, U.S. Geol Surv., Prof. Paper 963, 39 pp., 1976.
- Toksöz, M.N, M.A. Chinnery, and D.L. Anderson, Inhomogeneities in the Earth's mantle, Geophys. Jour. Roy. Astron. Soc., 13, 31-59, 1967.

- Turcotte, D.L. and E.R. Oxburgh, Stress accumulation in the lithosphere, Tectonophysics, 35, 183-199, 1976.
- Walcott, R.I., Flexure of the lithosphere at Hawaii, Tectonophysics, 9, 435-446, 1970.
- Walcott, R.I., Lithospheric flexure, analysis of gravity anomalies and propagation of seamount chains, Geophysics of the Pacific Basin and Its Margin, ed. by G.H. Sutton, M.H. Manghani and R. Moberly, Am. Geophys. Un., Mon. 19, 431-438, 1976.
- Wentworth, C.K. and A.E. Jones, Intrusive rocks of the leeward slope of the Koolau Range, Oahu, J. Geol., 48, 975-1006, 1940.
- Wesson, R.L., Seismic ray computations in laterally inhomogeneous crustal models, unpubl. Ph.D. thesis, Stanford Univ., 1970.
- Wesson, R.L., Travel time inversion for laterally inhomogeneous crustal velocity models, Bull. Seis. Soc. Am., 61, 729-746, 1971.
- Wiggins, R.W., The general linear inverse problem: implications of surface waves and free oscillations for earth structure, Rev. Geophys. Space Phys., 10, 251-285, 1972.
- Wilson, J.T., A possible origin of the Hawaiian Island, Canad. Jour. Phys., 41, 863-870, 1963.
- Wilson, J.T., Evidence from ocean islands suggesting movement in the earth, in A Symposium on Continental Drift, ed. by P.M.S. Blockett, E. Bullard, and S.K. Runcorn, Phil. Trans. Roy. Soc. London A, 258, 145-167, 1965.

- Wood, H.O., The Hawaiian Volcano Observatory, Seis. Soc. Am. Bull., 3, 14-19, 1913.
- Woolworth, J.B., On the fracture system of joints, with remarks on certain great fractures, Proc. Boston Soc. Nat. Hist., 27, 163-183, 1896.
- Wright, T.L., Chemistry of Kilauea and Mauna Loa lava in space and time, U.S. Geol. Surv. Prof. Paper 735, 40 pp., 1971.
- Yang, J.P, and W.H.K. Lee, Preliminary investigation on computational methods for solving two-point seismic ray tracing problems in a heterogeneous and isotropic medium, U.S. Geol. Surv. open file report 76-707, 66 pp., 1976.
- Yoshii, T., Y. Kono and K. Ito, Thickness of the oceanic lithosphere, in The Geophysics of the Pacific Ocean Basin and Its Margin, Am. Geophys. Un. Mon. 19, 423-430, 1976.

APPENDIX A. Estimation of the average form of a function from multiple observations in the presence of noise.

In many geophysical studies it is often useful to have information about the average behavior of a function, be it a seismic waveform, a travel time curve or some other observed or inferred property of the earth. A flexible but straightforward method for estimating the average shape of a sampled function of one independent variable and the relative offset between independent observations is developed using the generalized inverse of Lanczos (1961). This method is applied in §2.3.1 to estimate the mean teleseismic P-wave travel time curve for epicentral distances between 31° and 79° from several published travel time studies. Other applications for which the method might be of use include estimation of the decay rate of coda waves and stacking marine magnetic anomaly profiles.

Consider n independent, but not necessarily complete measurements $c_i(x)$, $i = 1, n$ where x is the independent variable. If in the absence of measurement error all curves, $c_i(x)$, are identical to within a constant offset, the average curve, $\bar{c}(x)$, is given by

$$\bar{c}(x) = \sum_i \frac{(c_i(x) + d_i)}{n} \quad (\text{A.1})$$

where d_i is the displacement of the i th curve from the mean curve. When our knowledge of the i th curve is imperfect we may estimate \bar{c} by

$$\bar{c}(x) = \frac{\sum_i (c_i(x) + d_i)w_i(x)}{\sum_i w_i(x)} \quad (\text{A.2})$$

where $w_i(x)$ is the weight at x for the i th curve, and is inversely proportional to the variance of $c_i(x)$.

Our problem is to find d_i and $\bar{c}(x)$ given $c_i(x)$. The error between $c_i(x)$ and $\bar{c}(x)$ is

$$e_i(x) = c_i(x) + d_i - \bar{c}(x) \quad (\text{A.3})$$

Replacing $\bar{c}(x)$ in (A.3) by (A.2) we find

$$e_i(x) = \frac{c_i(x) + d_i - \sum_j (c_j(x) + d_j)w_j(x)}{\sum_j w_j(x)} \quad (\text{A.4})$$

Let $\sum_j w_j(x) = W(x)$

and
$$\frac{\sum_j c_j(x)W_j(x)}{W} = S(x)$$

Then (A.4) becomes

$$d_i - \frac{1}{W(x)} \sum_j d_j W_j(x) = S(x) - c_i(x) \quad (\text{A.5})$$

where the error term has been dropped. Equation (A.5) represents one equation in a linear system for the unknown d_i 's. Representing the system specified by (A.5) and all observations by

$$Ad = b$$

we solve for the d_i 's without resort to normal equations by using the natural inverse of Lanczos (1961).

$$d = V_p \Lambda_p^{-1} U_p^T \quad (\text{A.6})$$

where Λ_p is a diagonal matrix containing the non-zero eigenvalues of A and V_p and U_p are the corresponding matrices of model and data space eigenvectors, respectively. By our definition of c, there will be at least one zero eigenvalue in A since changing all d_i 's by a constant does not change (A.4). In practice, the solution (A.6) is efficiently constructed using the Singular Values Decomposition algorithm of Golub (Golub and Businger, 1965).

Several general features of the solution are worth noting. First, when all $c_i(x)$ are known and all weights are equal, the average curve $\bar{c}(x)$ is simply the arithmetic mean of the c_i 's

$$\bar{c}(x) = \sum_i c_i(x) \quad (\text{A.7})$$

and d_i is the average error between c_i and \bar{c}

$$d_i = \frac{1}{m} \sum_x (c_i = \bar{c}) \quad (\text{A.8})$$

where m is the number of x values. When the weights are unequal, but independent of x , it is easy to show that

$$\bar{c}(x) = \frac{\sum_i c_i(x) W_i}{W}$$

and d_i is given by (A.8). Only when the weights depend upon the independent variable or the observed c_i 's are incomplete must (A.6) be used to solve the problem.

APPENDIX B: Test Problems for Three-Dimensional Modeling Using Teleseismic Sources

The three-dimensional modeling technique introduced by Aki and others (1977a) and described in §3 is validated in this appendix through the study of inverse solutions for artificial velocity structures. By examining inversion results for simple structures much can be learned about the relative merits of the different medium characterizations presented in §3.2. Limitations of the technique can also be evaluated, thereby identifying potential pitfalls to be avoided when applying the technique to real data and attempting to infer information about the earth from the solution.

Because all solutions calculated in both this appendix and in the body of the thesis employ the damped least squares method (3.14), it is worthwhile first examining the nature of this method before considering its application.

B.1 Damped Least Squares Solution for Linear Algebraic Systems

The method of solution developed in §3.1 for three-dimensional structure begins with reduction of non-linear expression for the travel time residual into a linear form (equation 3.5). Writing the system of equations in standard matrix notation

$$A_m = r \quad (B.1)$$

the desired model is seen to be the incremental solution for the linear system (B.1). Recently, considerable attention has been given to the computation of the solution to (B.1) using the generalized inverse or "natural" inverse of Lanczos (1961) by the Singular Valued Decomposition algorithm (see Lawson and Hanson, 1974 for a discussion of SVD). This solution employs a truncated set of eigenvalues and corresponding eigenvectors of matrix A (3.12). Because the dimensions of A are quite large, typically 300 rows by 2500 columns, it is computationally more efficient for this particular problem to abandon this elegant solution and solve the linear system given by the normal equations

$$A^T A^M = A^T r. \quad (B.2)$$

Since $A^T A$ is symmetric, only an upper triangular matrix need be stored which greatly reduces computer storage requirements over that required by A. In §3.1.2, the dimension of the semi-definite matrix $A^T A$ is further reduced by removing equations corresponding to changes in total travel time. This reduced system has typically 150 to 250 equations to be solved. As noted in §3 least squares solution of (B.2) fails because $A^T A$ has at least one zero eigenvalue per model layer. Rather than remove the zero or insignificant eigenvalues and associated eigenvectors from the solution using SVD or some other decomposition algorithm the method of damped least squares

is used to stabilize the solution to (B.2). This method, also called ridge regression was discussed by Levenberg (1944) and was popularized by Marquardt (1963).

In this method, equation (B.2) is modified by adding a diagonal matrix \textcircled{H} with positive elements to $A^T A$ given

$$(A^T A + \textcircled{H}) M = A^T r. \quad (\text{B.3})$$

This system may be solved directly using an elimination algorithm because the "damping" matrix \textcircled{H} eliminates solution singularities caused by zero eigenvalues of $A^T A$. The damped least squares solution (3.14) is written in terms of A and \textcircled{H} as

$$\hat{m} = (A^T A + \textcircled{H})^{-1} A^T r \quad (\text{B.4})$$

Aki and others (1977a) motivate selection of \textcircled{H} by noting that (B.4) is a special case of the stochastic inverse (Franklin, 1970) in which both the data and solution are considered stochastic processes. If the data has uniform (or normalized) variance σ_d^2 and the expected variance of the j^{th} component of x is σ_j^2 , the stochastic inverse solution is given by (4.3) with

$$\textcircled{H}_{jj} = \sigma_d^2 / \sigma_j^2. \quad (\text{B.5})$$

Because σ_j^2 is usually unknown, some experimentation

may be necessary to select \textcircled{H} . As we shall see below, other criteria may also suggest reasonable values for \textcircled{H} .

Resolution in the model space for the damped least squares solution is obtained from (B.4) by replacing r with (B.1). The resolution matrix may be written

$$R = (A^T A + \textcircled{H})^{-1} A^T A. \quad (\text{B.6})$$

The covariance matrix of model errors is expressible in terms of R and G as

$$C = \sigma_d^2 (A^T A + \textcircled{H})^{-1} R^T. \quad (\text{B.7})$$

Computation of the model covariance is greatly simplified when $\textcircled{H} = \theta^2 I$ where θ^2 is a positive constant. In this case $R = R^T$ and a column of C is readily obtained from (B.7) when the corresponding column of R is known. In fact, we can always normalize (B.5) into this form by scaling the columns of A .

Scaling of (B.1) into the required form in the general case when neither σ_{di}^2 nor σ_j^2 are uniform is accomplished through the following steps. First, construct weights equalizing the data variances σ_{di}^2 by

$$w_i \propto \sigma_d^2 / \sigma_{di}^2.$$

Next transform A and r by

$$A_{ij}' = w_i^{1/2} \sigma_j / \sigma_o A_{ij}$$

and $r_i = w_i^{1/2} r_i$. The proper choice of \textcircled{H} in (B.3) is now given by

$$\textcircled{H} = \theta^2 I$$

with $\theta^2 = \sigma_d^2 / \sigma_o$. The solution \hat{m} is recovered from the scaled equations (B.3) by

$$\hat{m}_j = \sigma_j / \sigma_o \hat{m}_j'$$

Similarly, the covariance matrix is recovered by

$$C_{ij} = \sigma_i \sigma_j / \sigma_o^2 C_{ij}' \quad (\text{B.6})$$

Having shown that (B.3) may always be normalized into the form $(A^T A + \theta^2 I)m = A^T r$ we are in the position to prove the following theorems relating R and C.

Theorem 1. Resolution and covariance matrices for the normalized damped least squares inverse solution are related by

$$C = \frac{\sigma_d^2}{\theta^2} R(I - R) \quad (\text{B.9})$$

when data errors are uncorrelated.

Proof: Using the fundamental decomposition theorem (Lanczos, 1961) the matrix A may be decomposed into two orthogonal matrices U and V and a diagonal matrix Λ as

$$A = U\Lambda V^T. \quad (\text{B.10})$$

With $\mathbb{H} = \theta^2 I$, equations (B.6) and (B.7) may be rewritten as

$$R = V\Lambda^2 (\Lambda^2 + \theta^2 I)^{-1} V^T \quad (\text{B.11})$$

and

$$C = \sigma_d^2 V\Lambda^2 (\Lambda^2 + \theta^2 I)^{-2} V^T \quad (\text{B.12})$$

respectively. Defining

$$R' = \Lambda^2 (\Lambda^2 + \theta^2 I)^{-1}, \quad (\text{B.13})$$

which is R transformed into the diagonal basis of $A^T A$, (B.12) may be rewritten as

$$\begin{aligned} C &= \frac{\sigma_d^2}{\theta^2} VR' (I - R') V^T \\ &= \frac{\sigma_d^2}{\theta^2} (VR' V^T - VR' R' V^T) \\ &= \frac{\sigma_d^2}{\theta^2} (R' - VR' R' V^T) \end{aligned}$$

The term $VR' R' V^T$ is the square of R as can be seen from

$$\begin{aligned} R^2 &= VR'V^T VR'V^T \\ &= VR'R'V^T \end{aligned}$$

since $V^T V = I$.

$$\text{Therefore, } C = \frac{\sigma_d^2}{\theta^2} R(I-R) \text{ q.e.d.}$$

This theorem is useful for computing the standard errors $\hat{\Delta m}_i = C_{ii}^{1/2}$ directly from R without the need to solve (B.7). From (B.9) we see that

$$C_{ii} = \frac{\sigma_d^2}{\theta^2} (R_{ii} - \sum_j R_{ij}^2).$$

If A and \textcircled{H} have been scaled, C_{ii} must, of course, be restored to its original units using (B.8). The theorem is also useful because it leads directly to the proof of the following theorem on $\hat{\Delta m}$.

Theorem 2. Standard errors for the damped least squares solution are bound by

$$\hat{\Delta m}_i \leq \frac{\sigma_d}{\theta} [R_{ii}(1-R_{ii})]^{1/2} \quad (\text{B.14})$$

Proof: From theorem 1 we know that

$$C_{ii} = \frac{\sigma_d^2}{\theta^2} (R_{ii} - (R^2)_{ii}).$$

The diagonal element of R^2 satisfies the inequality

$$(R^2)_{ii} = \sum_j (R_{ij})^2 \geq (R_{ii})^2$$

Therefore

$$C_{ii} \leq \frac{\sigma_d^2}{\theta^2} (R_{ii}(1-R_{ii})) \quad \text{q.e.d.}$$

This result is particularly useful for several reasons. Noting that $R_{ii}(1-R_{ii}) \leq 0.5$ for all i , it follows from (B.14) that

$$\Delta \hat{m}_i \leq \sigma_d / 2\theta. \quad (\text{B.15})$$

This means that parameter uncertainties obtained from (B.7) are absolutely bounded from above. Stated another way, selection of a value for θ puts an a priori bound on $\Delta \hat{m}$. Replacing θ in (B.15) by σ_d^2 / σ_o^2 and scaling the result by (B.8) we find that parameter standard errors are bounded by the variance of the model, when it is viewed as a stochastic process, by

$$\Delta \hat{m} \leq \sigma_i / 2.$$

Recall that in classical least squares ($\theta = 0$) the errors tend to infinity as the smallest eigenvalue goes to zero. One may inquire into the meaning of the errors derived from C for the damped least squares solution.

I believe that inspection of (B.14) answers this question and gives a natural criteria for a minimum standard that must be met by model parameters before their solution values can be considered reliable. The curve which forms

the upper bound on $\Delta\hat{m}$ (Figure B.1) attains its maximum value for $R_{ii} = 0.5$ and decreases to zero as R_{ii} goes to 0 or 1. Since a value for $R_{ii} < 0.5$ means that less than half of the calculated solution for that parameter comes from the true solution, stability of the solution must be achieved in this case by damping the model adjustment m_i . Small standard errors for such parameters do not imply accurate knowledge of their true values. Rather, they simply reflect the fact that resolution for these parameters is poor. Consequently, it is natural to consider parameters for which $R_{ii} < 0.5$ so poorly resolved that they individually contain little useful information and should not be considered when interpreting the solution.

Parameters with $R_{ii} \geq 0.5$ are, of course, not guaranteed to be meaningful, and other measures of the solution need to be employed to validate the solution for specific model elements. Large, off diagonal elements of R are one indicator of difficulty as are standard errors which exceed the solution value. Because the trade off between resolution and standard error depend upon the choice of θ^2 , it is worthwhile illustrating the effect of θ^2 on the solution.

The relationship between R and C given by (B.9) does not correspond to the classical trade-off curve since it refers to a single solution. By varying θ^2 and studying how R and Δm change for individual parameters, the nature of the trade-off between these two quantities

can be discovered. This is illustrated in Figure B.1 for a solution with θ^2 doubled (open circles). When resolution is poor, relaxation of the damping greatly magnifies the error with little improvement in resolution. Conversely, when resolution is good, decreased damping results in substantially improved resolution with only a modest increase in the error.

Two additional measures of solution quality are the trace of the resolution matrix and the estimated variance improvement. The trace, of $\sum_i R_{ii}$ is equal to the number of eigenvectors effectively contributing to the solution and measures the impact of the damping on the eigenvalue spectrum. The variance improvement estimated with the linear modeling can be derived from the derivation of the damped least squares equations which follow from minimization of

$$|e^2| = |r - Am|^2 + m^T \textcircled{H} m$$

with the result that the estimated variance improvement is

$$|r - Am|^2 = |r|^2 - \hat{m}^T A^T r - \hat{m}^T \textcircled{H} \hat{m}. \quad (\text{B.16})$$

Comparison of this estimate with the variance computed using ray tracing for the complex models of §4 suggest

that (B.16) is a very good approximation, overestimating the actual improvement by less than 5%. Thus the residual variance $|r|^2 - |r-Am|^2$ estimated using (B.16) gives an accurate assessment of model performance when the data variance σ_d^2 is known.

Although the generalized inverse (3.12) is not used in constructing the velocity models presented in this thesis, one final theorem relating standard errors and parameter resolution is worth recording.

Theorem 3. Standard errors for the generalized inverse solution of

$$Am = r$$

are bound by

$$\Delta \hat{m}_i \leq \frac{\sigma_d^2}{\lambda_{\min}^2} R_{ii} \quad (\text{B.17})$$

where λ_{\min} is the smallest eigenvalue retained in the construction of the inverse.

Proof: Recall that the generalized inverse or "natural" solution to (B.1) is

$$\hat{m} = V_p \Lambda_p U_p^T$$

where the subscript p denotes that an incomplete subset of (nonzero) eigenvalues and corresponding eigenvectors.

For this solution, the resolution and covariance matrices are given by

$$R = V_p V_p^T$$

and

$$C = \sigma_d^2 V_p \Lambda_p^{-2} V_p^T$$

respectively. The diagonal element of C for m_i is

$$C_{ii} = \sigma_d^2 \sum_j V_{pij}^2 \lambda_{pj}^{-2}.$$

Every term of the sum satisfies

$$V_{pij}^2 \lambda_{pj}^{-2} \leq V_{pji}^2 \lambda_{\min}^{-2}$$

so

$$C_{ii} \leq \sigma_d^2 \lambda_{\min}^{-2} \sum_j V_{pij}^2.$$

Since $\sum_j V_{pij}^2 = R_{ii}$, it follows that

$$C_{ii} \leq \sigma_d^2 \lambda_{\min}^{-2} R_{ii} \quad \text{q.e.d.}$$

This theorem is useful because it allows one to set a priori limits on $\Delta \hat{m}$ simply by inspecting the eigenvalues of A. Since $R_{ii} \leq 1$, it follows that

$$\Delta \hat{m}_i \leq \sigma_d / \lambda_{\text{small}}.$$

This is a very useful criteria for establishing the cut-off eigenvalue, as advocated by Wiggins (1972) when σ_d is known and other considerations place acceptable bounds on $\Delta\hat{m}_1$.

B.2 Recovery of a Simple Inhomogeneity Using an Idealized Array

A very simplistic test problem is presented in this section to demonstrate the ability of the modeling technique to recover heterogeneous structure under favorable circumstances. Because inappropriate specification of model elements can lead to spurious solutions, the same test problem provides an opportunity to study model dependent bias in a case where the origin of erroneous solution values remain tractable.

The heterogeneous model to be studied consists of a single low velocity body embedded in the second layer of a three layer model (Table B.1). The body is described by the bivariate hanning window (3.20) with $DX = DY = 20$ km. The anomalous region is 10% lower velocity than the average of layer 2 at its center which lies directly beneath the central receiver of the hypothetical array of Figure B.2. Relative travel time residuals to the 25 element array are constructed using geometric ray theory to trace rays through the model. Sixty source waves are assumed, distributed evenly about the circle at a spacing of 30° and with slowness values of 8.5, 7.5, 6.5, 5.5, and 4.5 sec/deg.

Three numerical experiments will be considered in turn. The first compares single iteration solutions obtained with model elements spacing adjusted to match the heterogeneity. The second considers iterative refinement of the solution. The final experiment explores the effect of a misaligned model grid on the inverse solution.

B.2.1 Single Iteration Solutions

The model element grid selected for this experiment has the same element spacing as the anomalous body and is centered on the body. Thus most of the low velocity region falls within the central model element in layer 2, with a minor overlap into the surrounding nine blocks (Figure B.3a). Layer boundaries also coincide with those of the structure. Thus this test would appear to be optimally tuned to the unknown structure, and any misfit between model and inverse solution should indicate inherent pitfalls in the method.

Inversion of error free data using models described by quantized elements, blocks, and hanning functions with a constant damping of $\theta^2 = 50$ are compared in Figure B.4 in a north-south cross-section through the model center. All three models recover a low velocity body in the proper location (middle element of layer 2), and indicate some vertical leakage of the solution into layers 1 and 3. Leakage is smallest for the block model while recovery of the anomalous body is best for the hanning model. The quantized model has the best resolution, but overall the

worst solution leakage and poorest estimate of the velocity within the central element, which averages -6.7% for the exact answer. As the configuration of the hanning model chosen can exactly replicate the artificial structure, it is clear that this model has not converged in a single iteration with the damping used.

Leakage of the solution between layers poses a serious difficulty for the method since it not only distorts the solution but also is strictly forbidden in the "natural" solution or generalized inverse (3.12) when the data are complete. Recall from §3.3.4 that the optimum solution, in a least squares sense, for block model elements and any heterogeneous structure is the average velocity within each block element. This "best fitting" solution, m , is related to the inverse solution, \hat{m} , by the resolution matrix

$$\hat{m} = Rm \quad (B.18)$$

and so it is an easy matter to compare the inverse solution \hat{m} with that predicted by (B.18). Using the row of the resolution matrix for the central block in layer 1 (Figure B.4b) shown in Figure B.5 and m values calculated using (3.23) an estimate for \hat{m} of -0.4% is obtained. This value is half of the inverse solution value of -0.8%. Given that (B.18) is based upon a linearized model, the agreement between the calculated and predicted leakage is considered adequate.

Addition of zero mean, normally distributed pseudo random errors to the data with $\sigma_d = 0.1$ sec improves the problem of solution leakage between layers, especially in the bottom layer (Figure B.6). For this choice of σ_d and θ , from (B.15) it is seen that solution errors are bounded by $\Delta\hat{m} \leq 0.7\%$. So, at the 95% confidence level none of the spurious values are significant. Note, however, that the magnitude of solution leakage into the central element of layer 1 has not changed. Residual variance for each of these models estimated using (B.16) range from 0.0098 sec^2 for the quantized model to 0.0095 sec^2 for the hanning model. With the variance of data errors known to be 0.01 sec^2 this gives an SSWR value of between 1470 and 1425 for the 1500 readings compared with the number of degrees of freedom ranging from 1359 to 1340, respectively. Thus the technique is not overmodeling the data.

B.2.2 Convergent Iterative Solution

A single solution for the synthetic structure using the hanning model (Figure B.6c) falls some 35% short of the correct solution, indicating that iterative improvement of the solution is desirable. To this end, refined solution estimates are calculated by the method described in §3.4 for the data with random errors added. A single additional iteration reduces the solution error for the heterogeneity by 18% and the total residual variance by 1%.

With one additional incremental solution (Figure B.7) the inverse agrees to within 10% of the exact answer, and is within two standard errors of that solution.

B.2.3 Solutions Using a Mis-Aligned Grid

When modeling an unknown structure, the selection of the model element size and grid position is somewhat arbitrary. Solutions for the idealized model discussed above are artificially enhanced in the sense that the model grid used in the inversions is optimally positioned for the heterogeneous structure. We now relax this forced agreement and study a maximally mis-aligned grid (Figure B.3b). In the case of hanning basis functions, this grid effectively forces the inverse solution to match a structure described by cosines with sines.

Inverse solutions for several cases (Figure B.8) show that this particular element framework and the structure to be recovered are essentially orthogonal in layer 2. This is somewhat surprising at least in the case of the block model where the "true" model predicted by (3.23) should average -2.5% in the middle blocks of layer 2. Statistically significant leakage of the anomalous body into layers 1 and 3 is also evident in all of the models. Appeal to the resolution matrix cannot explain the contamination of the solution in these layers by a body restricted to the middle layer. However, comparisons between solutions using aligned and mis-aligned element gridworks clearly

indicates the existence of a serious modeling problem. The dissimilarities between paired solutions of Figures B.6 and B.8 are so strong that they alert the modeler of grave difficulties with one or both of the solutions, without the need of a priori knowledge of the actual velocity distribution. If we use the variance improvement as a measure of solution performance, it favors the original grid alignment, although the difference between the residual variances $.0096 \text{ sec}^2$ versus $.0102 \text{ sec}^2$ is small.

Unexplained distortion of the inverse solution for heterogeneous structure otherwise recoverable with a favorably positioned element framework represents the principal difficulty with the technique. Spatial averaging of the shifted solution with the original solution (Figure B.9) as suggested by Aki and others (1977a) fails to improve the agreement. This problem will be most acute when the scale length of the heterogeneity is slightly smaller than the linear dimensions of the model elements. Numerical experiments show that when the medium remains smooth over distances spanned by several elements, heterogeneous structures are readily recovered regardless of the specific model element orientation, size, or position. Therefore, one must be cautious in interpreting anomaly patterns that undergo marked changes when either element grid is re-positioned or its horizontal scale changed.

B.3 Volcanic Pipe Model for Mauna Loa

Recovery of a simple model using an idealized array and data set demonstrates the viability of the inverse technique, but does not guarantee its success when applied to real data or an existing array. A test of the travel time observations collected from Hawaiian network stations is therefore needed to demonstrate the suitability of the technique to the data described in §2. To this end, travel time residuals for the same source-receiver pairs available for the modeling of §4 are used to construct a synthetic relative residual data set for a simple model.

The model studied corresponds to a vertically regular, low velocity pipe located beneath the summit of Mauna Loa in the depth interval of 15 to 85 km (Figure B.10). Within the 40 km diameter pipe the velocity decreased linearly toward the center from a nominal half space velocity of 8.2 km/sec. The travel time delay shadow cast by the structure is illustrated in Figure B.11 for several slowness values. Representative relative residual values appear in Figure B.12. Note the similarity in form between the residuals at some stations, notably MLO, and the residual pattern shown in the actual observations (Figure 2.16).

As with the idealized model studied above, two grid configurations will be considered: one centered on the pipe and the other shifted diagonally one-half the grid spacing. Initial velocities, layer boundaries and grid dimensions for both models appear in Table B.2. Note

that the pipe structure extends 10 km into the deepest layer.

For these studies, the seismograph network has been thinned through deletion of stations on Kilauea to roughly equalize station density. Selected stations appear in Figure B.13, together with percent velocity contours of the volcanic pipe. All of the models considered in this section use a damping factor of $\theta^2 = 50 \text{ sec}^2$. Normally distributed pseudo-random errors with $\sigma_d = 0.1$ are also used to simulate reading errors.

In this study a new type of model has been added. This model is identical to the block model except in the first (crustal) layer of the model, where crustal structure sampled by each station is isolated in a unique model element. The principal advantage to this model is its ability to isolate the rapid geographic variations in average station residual in a single element. Iterative improvement for this model is also possible through feedback of the station term solutions for the first layer of the forward model while retaining initially homogeneous layers for the deeper layers. This new class of model will be called the "station-block" model.

B.3.1 Single Iteration Solutions

First estimates of three-dimensional structure produced using an element grid centered on the pipe structure (Figure B.14) show that all four parameterizations recover the basic features of the volcanic pipe. As before, the

quantized model has the best resolution but also has the poorest fit and worst leakage into the first layer (Figure B.14a). The block model and station-block model are virtually identical in the lower three layers and agree favorably in the first layer (Figure B.14b and B.14c). The strongest solution leakage into the first layer is clearly associated with rays to station HSS, which is not too surprising since this station has the fewest readings (26) of all stations used. Most of the ray paths to this station are also delayed by the hypothetical pipe structure. Hanning basis functions describe the structure quite well and show less leakage into the first layer than the other solutions (Figure B.14d).

B.3.2 Convergent Iterative Solutions

Iterative refinement of the hanning model and the station-block model (Figure B.15) yields mixed results. The former, computed using full geometric ray tracing, shows a significant improvement in the fit to the pipe structure, especially in the third layer. The new model reduces the residual variance by 4% over the initial solution. In contrast, little improvement can be seen in the fit for the station-block model. However, the fit is not measurably worse either, indicating that the solution for elements in the lower layers are not strongly influenced by the specific set of station terms used.

B.3.3 Solutions Using a Mis-aligned Grid

For this test the element grid is shifted diagonally one-half the grid dimension in the lower three layers. Solutions for the quantized model, block model, and hanning model (Figure B.16) show considerable leakage into the first layer. Spurious solution values in this layer exceed twice the maximum standard error. Statistically discernable values in the region generally underlying Mauna Loa in layer 4 which are absent in Figure B.14 may be interpreted either as spurious values or an attempt to model the part of the pipe which extends into this layer.

Although there is measureable distortion of the inhomogeneous structure in these solutions, there is considerable evidence for its presence in the middle two layers. For these models, smoothing of the shifted and unshifted solutions yields a model with the volcanic pipe restricted to its proper position but with an underestimated velocity contrast. Thus it would appear that the smoothed solution produces a more stable image of heterogeneous structures while sacrificing recovery of absolute velocity contrasts.

B.4 Guidelines for Evaluating Inverse Solutions

The difficulties with the three-dimensional inversion exposed by solutions using a mis-aligned grid illustrate the shortcomings of the resolution (B.6) and covariance matrices (B.7) for evaluating the solutions under certain

conditions. These two measures of the solution are useful and valid indicators provided that they are used in conjunction with comparisons between solutions computed using different element configurations.

When evaluating solutions computed using a repositioned model framework comparisons should only be made between elements which meet minimum standards for both resolution and parameter uncertainty. Foremost is the requirement that the diagonal element of the resolution matrix equal or exceed 0.5. The rationale for this cut-off value is discussed in §B.1.

The minimum statistical requirement that comparisons between solution values meet is that each value fall within the 95% confidence interval of the other (twice the standard error). Satisfaction of these criteria for resolution and error by solution values covering specific locations when the element gridwork is shifted or has its dimensions changed, or when layer boundaries are moved, constitutes strong evidence that the velocities determined at those locations are valid. In practice, alternative models used for comparison should include at least one with a translated grid and one with different element dimensions.

Illustrative examples of solution values which undergo substantial changes when the model framework is modified are evident in the comparisons made in §B.2.3 and §B.3.3. In the former case, the solution in the second layer changes abruptly when the element grid is

shifted diagonally. The overall anomaly pattern for this grossly incorrect result shows strong vertical continuity. Vertical smoothing is also indicated by the resolution matrix, although it underestimates the degree of smoothing. This suggests that the combination of vertical smoothing of the solution (positive side lobes) and vertical continuity of the solution are warnings of model inaccuracies. In this case, the shifted solution could be greatly improved by using substantially smaller elements. However, in practice, the element dimensions are effectively limited by the number and distribution of the observations.

Inverse solutions for the Mauna Loa volcanic pipe model as computed on a mis-aligned grid (B.3.3) show essentially the same undesirable traits as the other synthetic example. However, in this case, the mis-aligned grid gives a far more acceptable solution. This is because, in part, the horizontal element spacing is $1/3$ smaller than the vertical spacing. These taller elements have improved vertical resolution when compared to cubic elements with the same cross-sectional area.

Spatial smoothing of distinct solutions as used by Aki and others (1977a) should succeed in stabilizing broad scale features of the velocity distribution at the expense of small scale details when the distinct solutions meet the criteria outlined above. However, smoothing of solutions, as was done in Figure B.9 show that enhancement

techniques will not produce acceptable results from unacceptable solutions.

TABLE B.1: Initial Layered Model Used in
Study of Idealized Structure

<u>Layer</u>	<u>Velocity</u>	<u>Thickness</u>	<u>Element Spacing</u>
1	6.0 km/sec	15 km	15 km
2	8.2	20	20
3	8.2	20	20

TABLE B.2: Initial Layered Model Used in Study
of Mauna Loa Volcanic Pipe Model

<u>Layer</u>	<u>Velocity</u>	<u>Thickness</u>	<u>Element Spacing</u>
1	6.0 km/sec	15 km	15 km
2	8.2	30	20
3	8.2	30	20
4	8.2	30	20

Appendix B - Figure Captions

Figure B.1 Relationship between solution standard error and diagonal element of resolution matrix. Solid curve is exact bound on standard error. Dashed curve is bound with damping doubled. Lines connecting points and open circles illustrate trade-off between resolution and standard error as the damping is varied.

Figure B.2 Idealized seismograph array. Dashed line entirely encloses heterogeneous zone.

Figure B.3 Element frameworks studied. Dashed lines are percent velocity contours in model layer 2.

Figure B.4 Cross section through single iteration solutions computed using error free data. Percent velocity perturbation is shown. Values in parentheses are diagonal elements of resolution matrix.

Figure B.5 Row of resolution matrix for block model corresponding to first layer element overlying heterogeneity.

Figure B.6 Cross section through single iteration solutions computed using data with normally distributed pseudo random errors added. Resolution is the same as for models in Figure B.4.

Figure B.7 Cross section through iteratively refined solution for hanning model. Values in parentheses are steps taken after third iterative refinement.

Figure B.8 Cross section through solutions with displaced elements.

Figure B.9 Smoothed superposition of block model solutions computed on the two element frameworks shown in Figure B.3. Contour interval 1%.

Figure B.10 Cut-away illustration of low velocity volcanic pipe model. Inclined plane represents wavefront with a slowness of 9 sec/deg. Surface contours are the relative residual shadow cast by low velocity pipe.

Figure B.11 Travel time delays along radius of pipe model for several slowness values.

Figure B.12 Azimuthal plot of relative travel time residuals at selected stations.

Figure B.13 Map of Island of Hawaii showing stations (triangles) used in inversion study and percent velocity contours of volcanic pipe model. Contour interval 2.5%.

Figure B.14 Comparison of inverse solutions for volcanic pipe model. Values are relative perturbations in percent.

Figure B.15 Second iteration solutions for volcanic pipe model.

Figure B.16 Comparison of inverse solutions for volcanic pipe model computed on a misaligned model framework.

Figure B.1

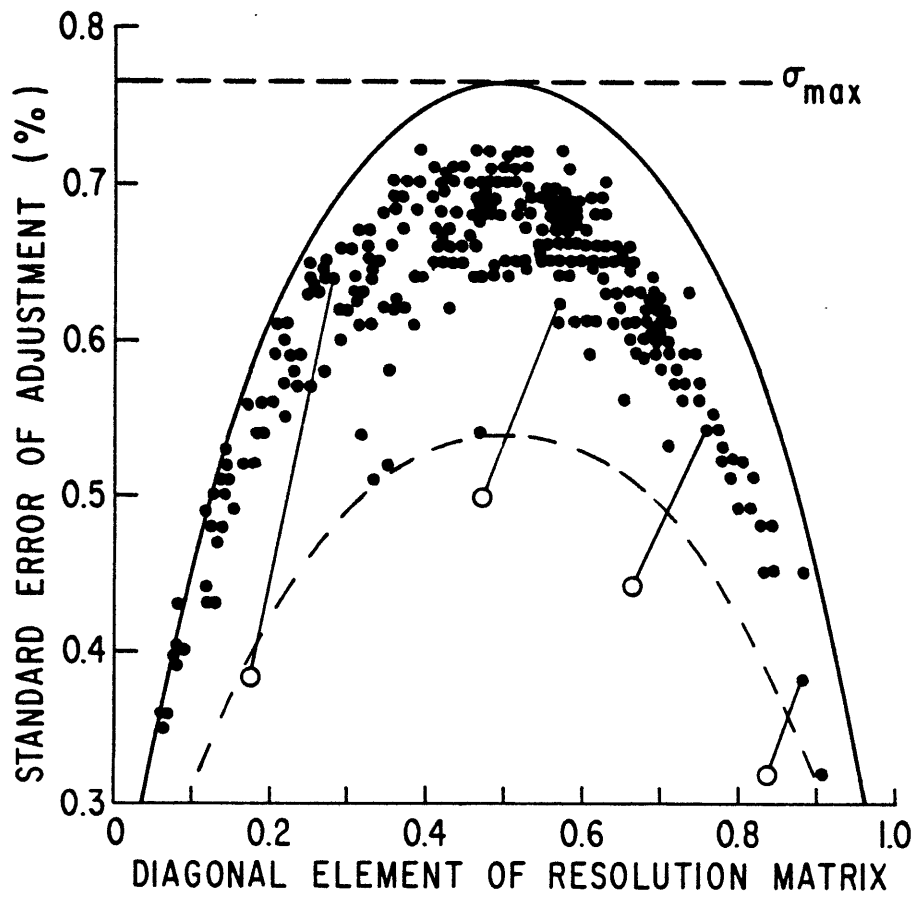


Figure B.2

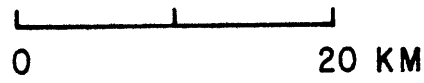
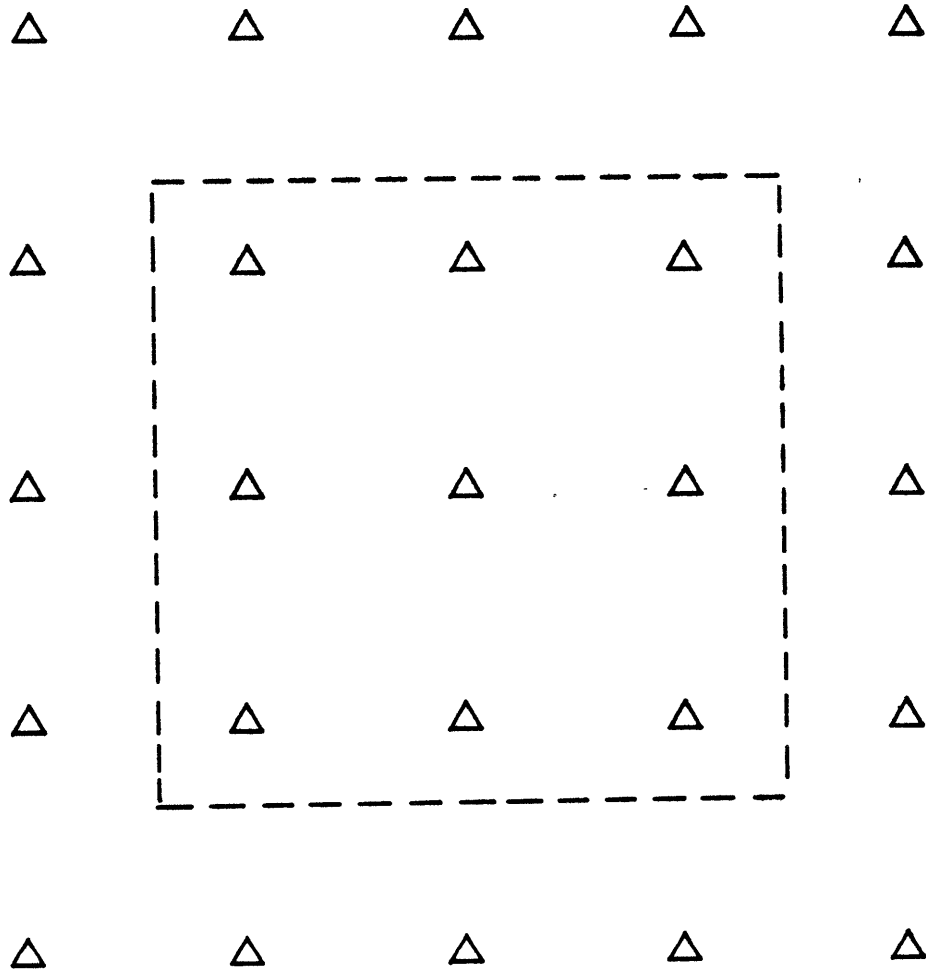
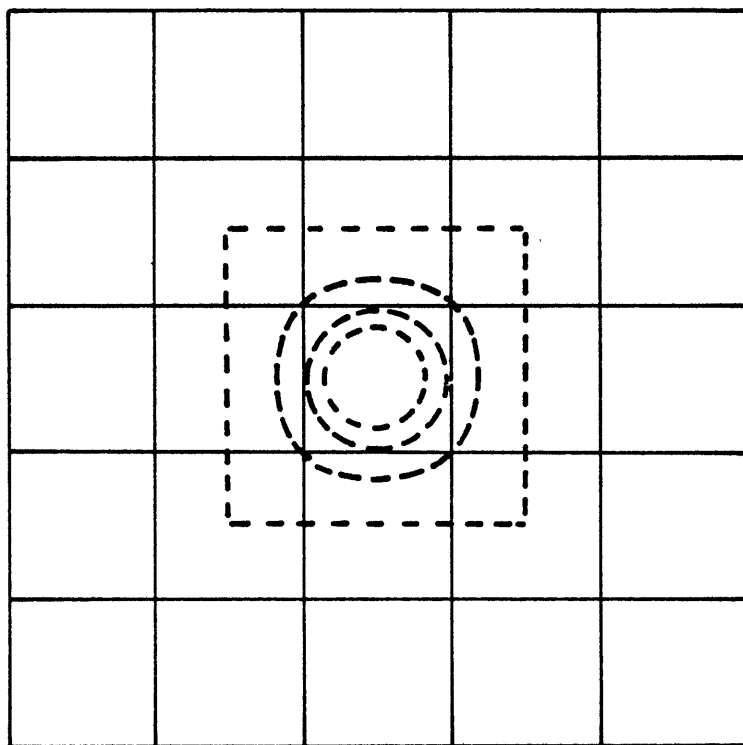
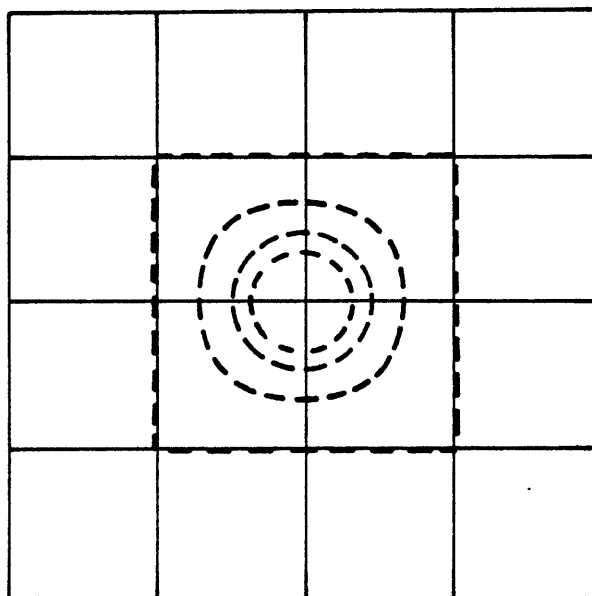


Figure B.3

CENTERED MODEL



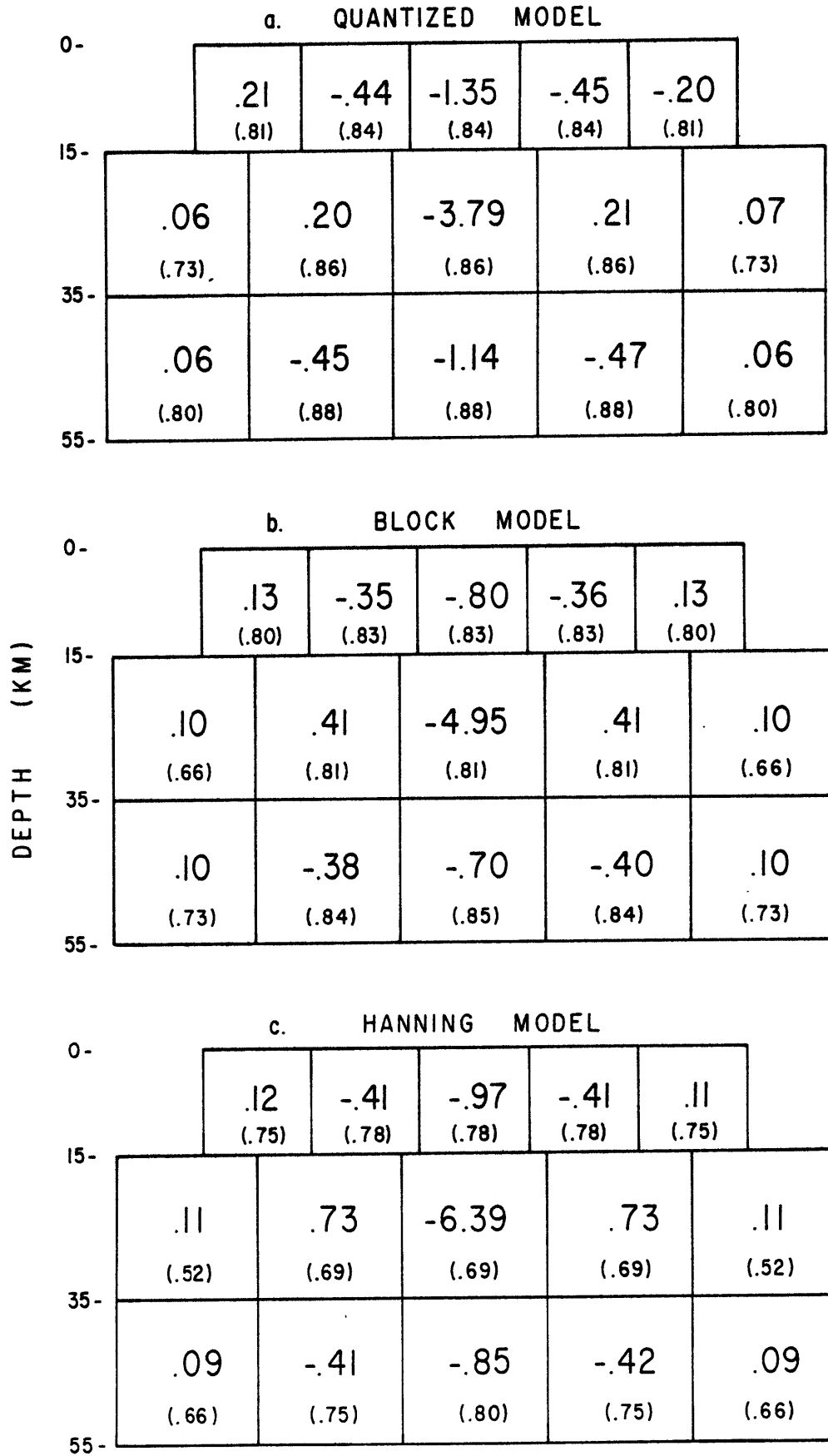
SHIFTED MODEL

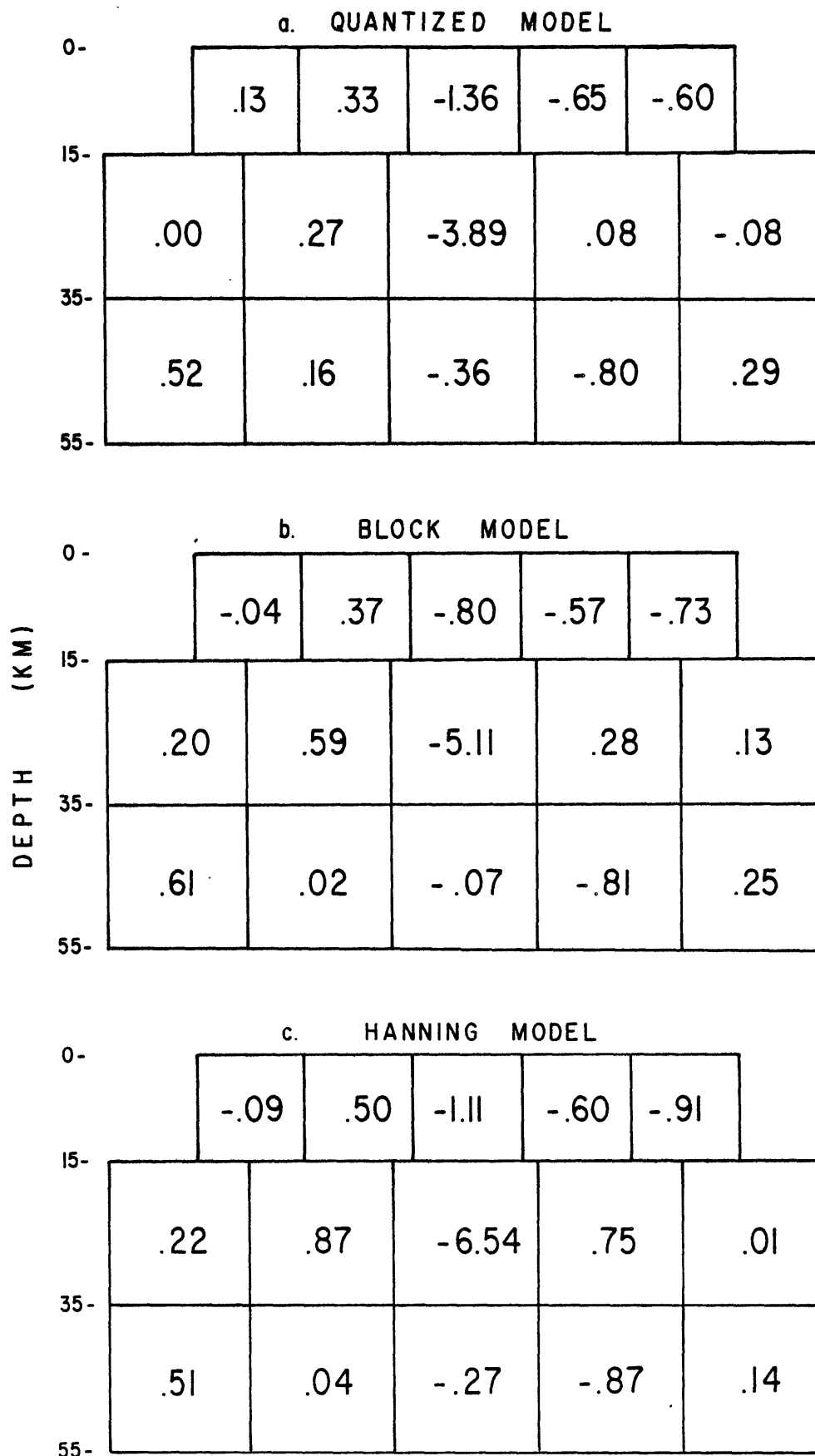


0 20 40 KM

CONTOUR INTERVAL 2.5%

Figure B.4





HANNING MODEL

0-	-.19 (-.05)	.74 (.08)	-.63 (.23)	-.54 (.04)	-1.24 (-.10)
15-	.32 (.03)	.78 (-.07)	-9.01 (-.67)	1.06 (.04)	.06 (.04)
35-	.54 (-.03)	.06 (.02)	.21 (.17)	-1.27 (-.10)	.05 (-.07)
55-					

Figure B.7

Figure B.8

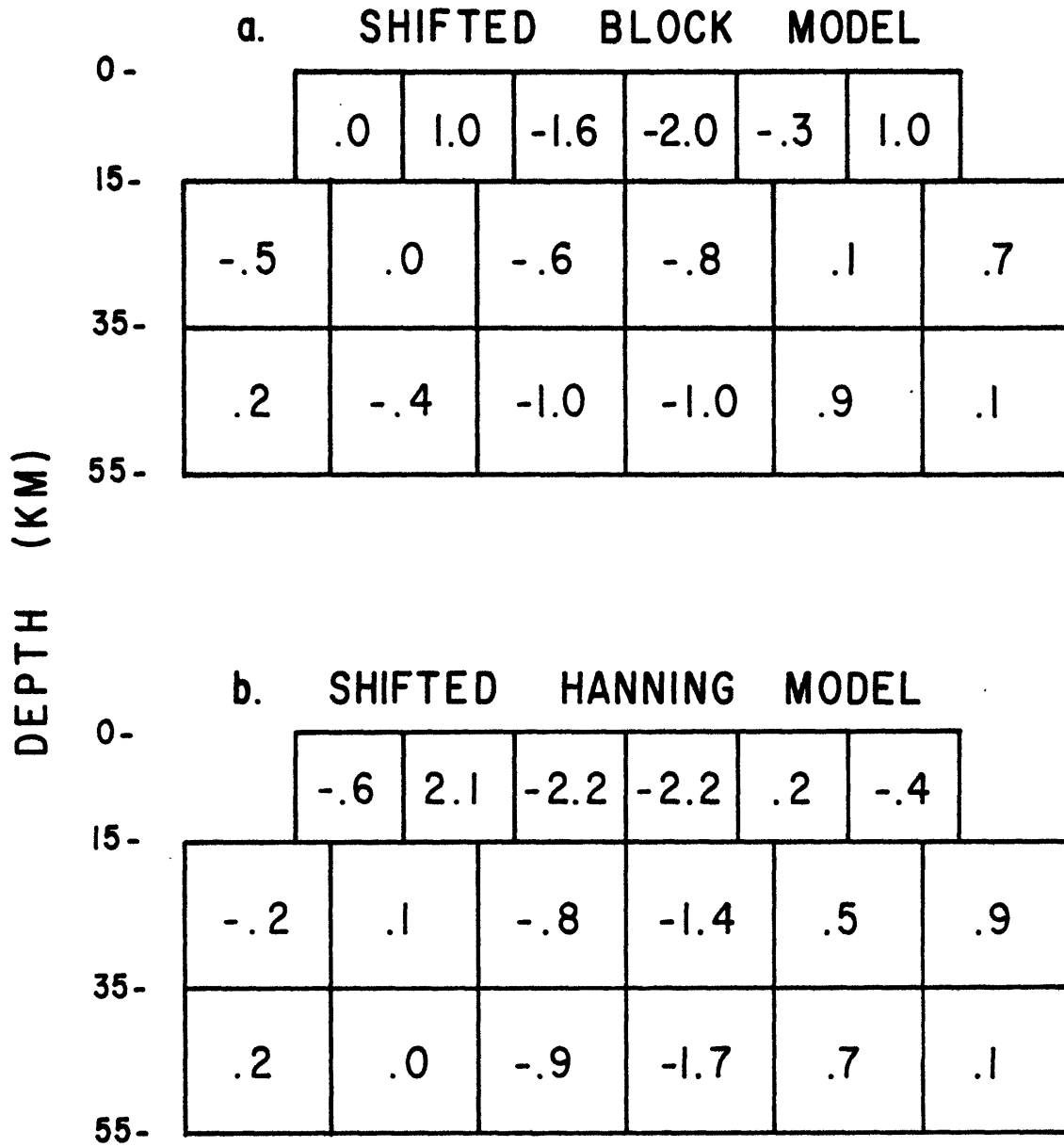
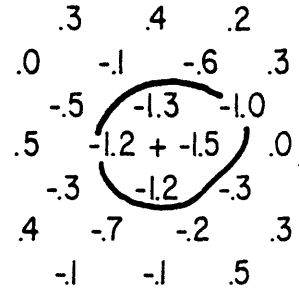
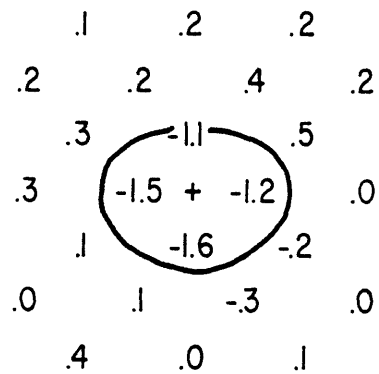


Figure B.9

LAYER 1



LAYER 2



LAYER 3

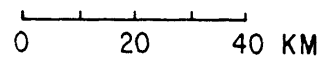
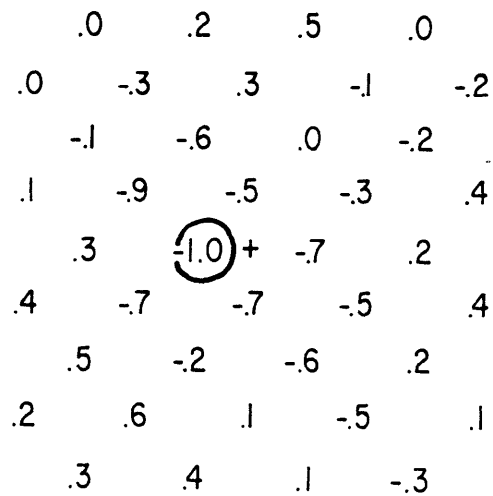
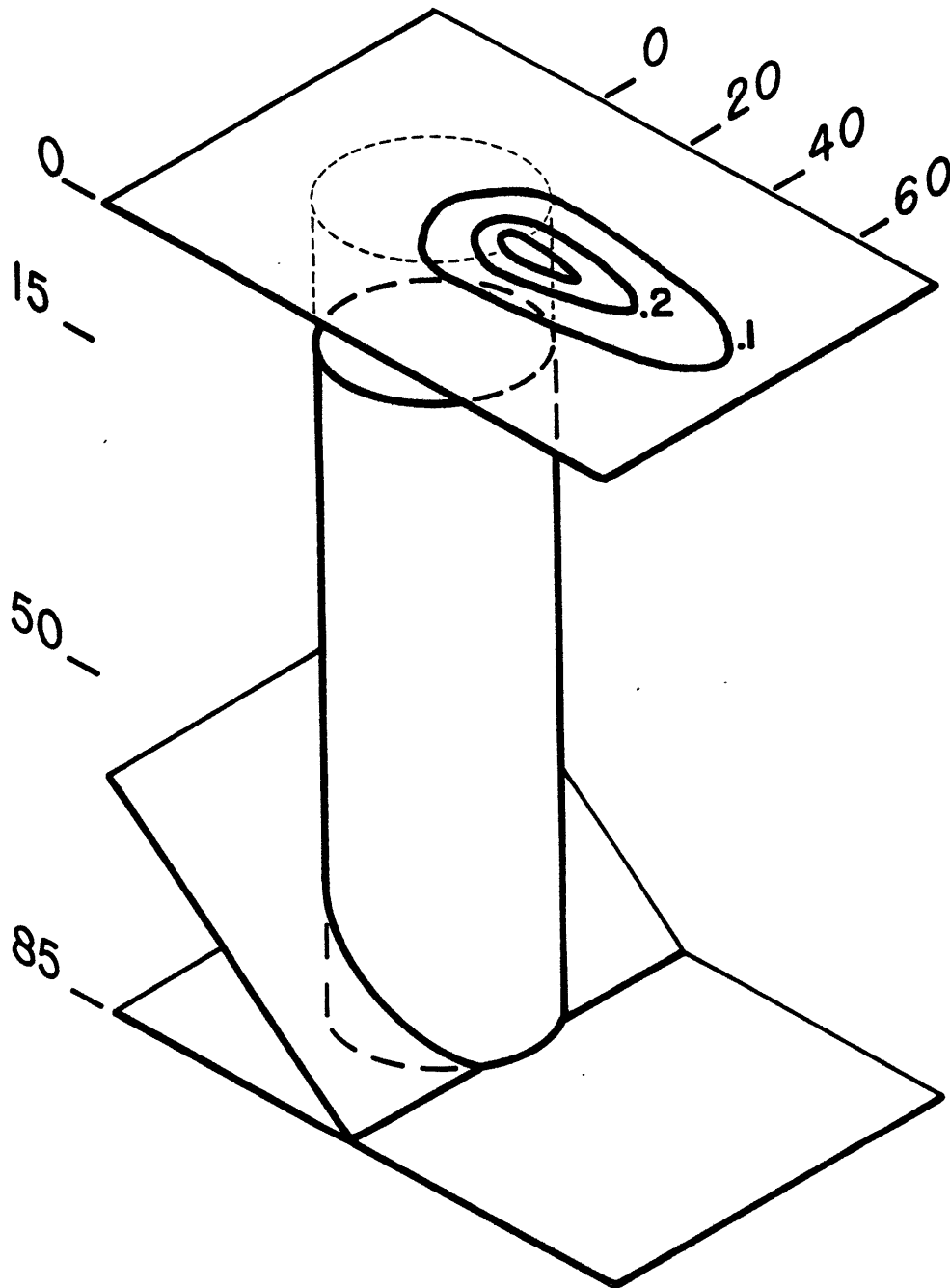


Figure B.10

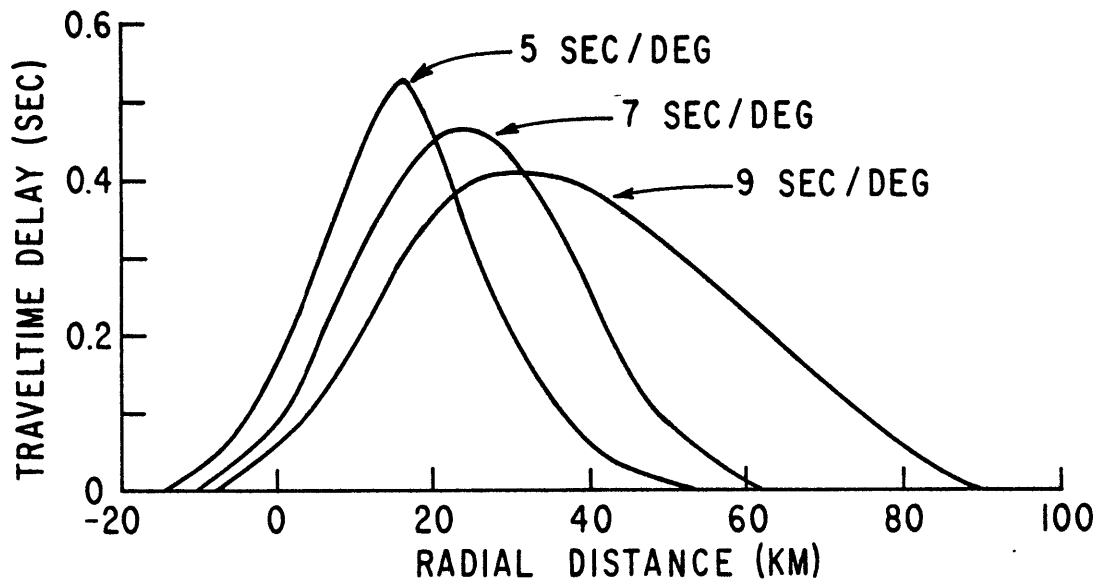


$$dT/d\Delta = 9 \text{ sec/deg.}$$

Distances in km

Delay in sec

Figure B.11



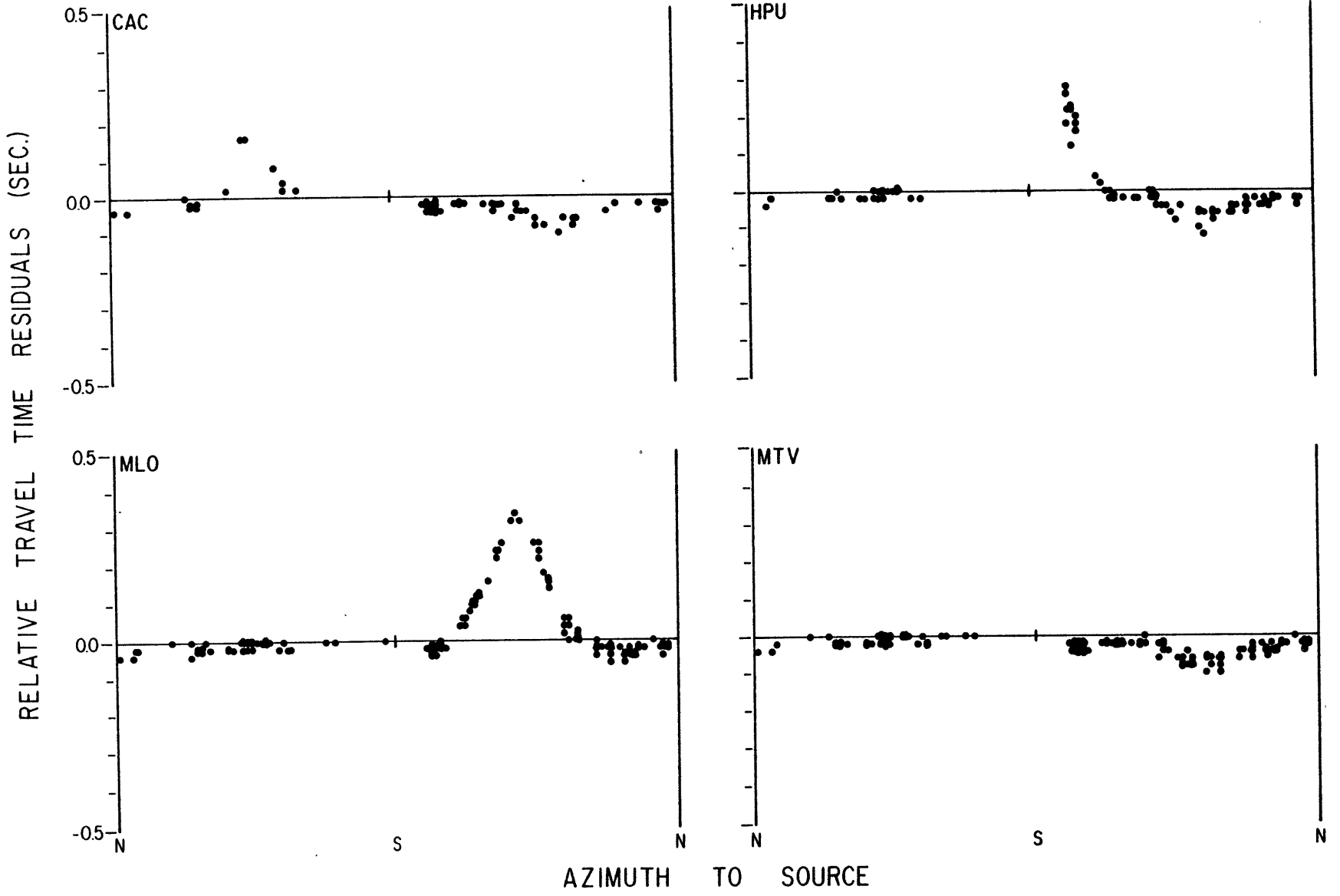


Figure B.12

Figure B.13

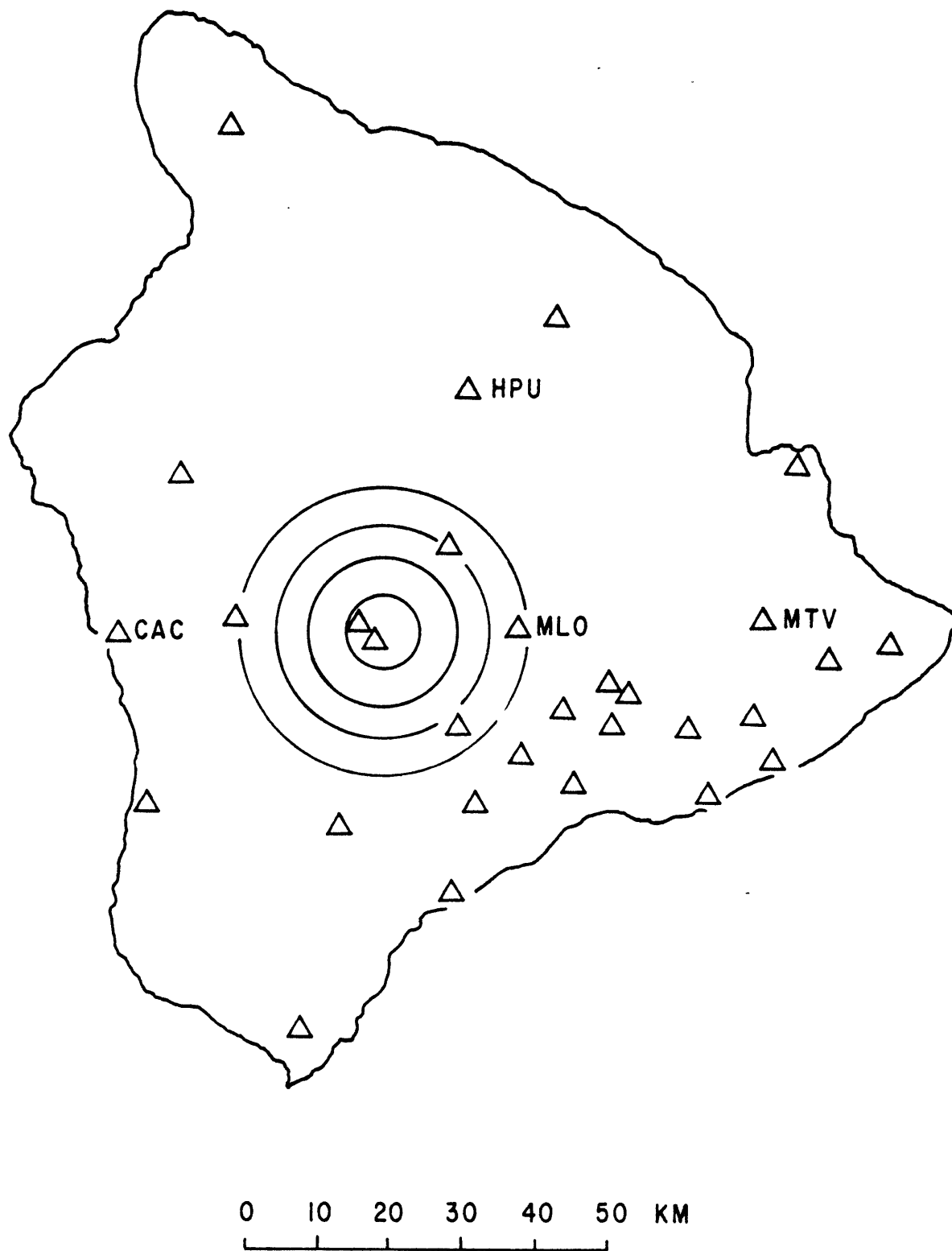


Figure B.14

SOLUTION FOR VOLCANIC PIPE MODEL

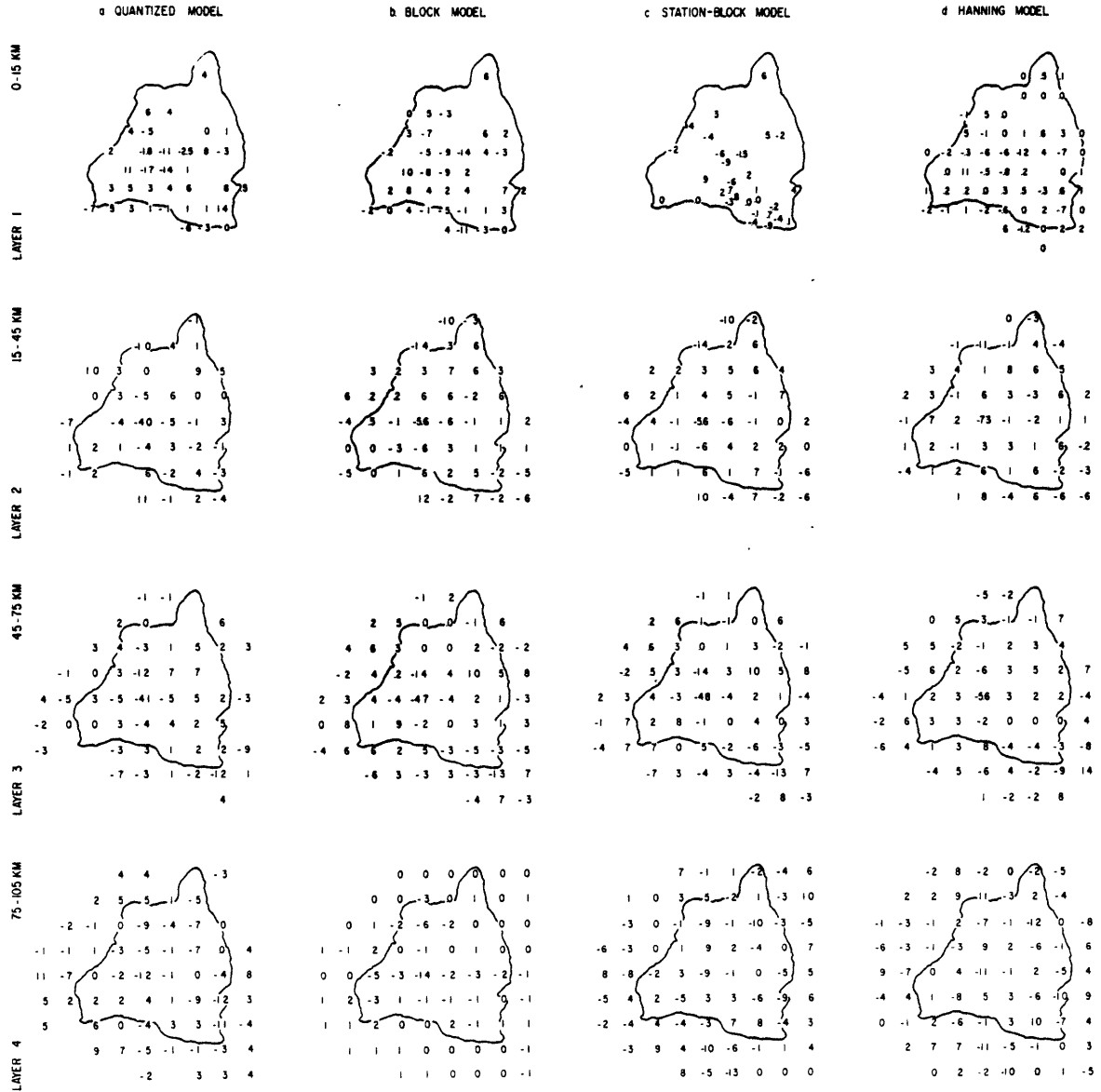
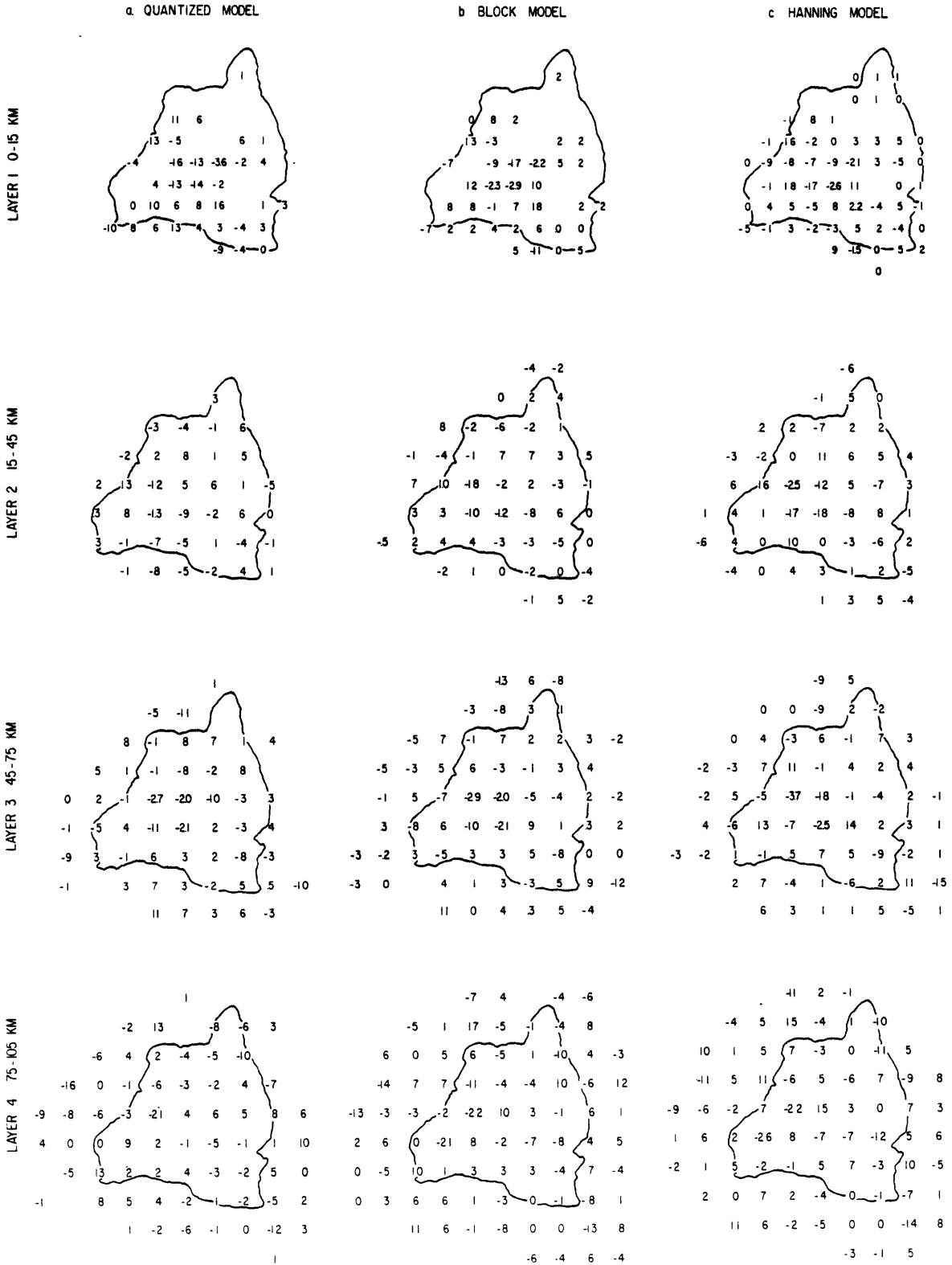


Figure B.16

SOLUTION ON A TRANSLATED GRID



BIOGRAPHICAL NOTE

The author was born in Tulsa, Oklahoma, on September 22, 1948, and was raised there. He attended Stanford University from 1966 to 1971 and graduated with degrees in Physics (B.S.) and Geophysics (M.S.). Between 1971 and 1974 he worked as a geophysicist at the National Center for Earthquake Research, U.S. Geological Survey, in Menlo Park, California. During this interlude in his academic study he met Nancy Marx whom he married in January, 1975. In September, 1974, he returned to graduate study in the Department of Earth and Planetary Sciences at M.I.T. The Ellsworths now make their home in Menlo Park, California, where the author is employed with the U.S.G.S.

Publications

- Wesson, R.L., R.O. Burford, and W.L. Ellsworth, Relationship between seismicity, fault creep, and crustal loading along the central San Andreas fault, in Proceedings of the Conference on Tectonic Problems of the San Andreas Fault, Stanford, Calif., Stanford Univ. Pubs. Geol. Sci., v. 13, 303-321, 1973.
- Wesson, R.L., and W.L. Ellsworth, Seismicity preceding moderate earthquakes in California, J. Geophys. Res., 78, 8527-8545, 1973.
- Ellsworth, W.L., R.H. Campbell, D.P. Hill, R.A. Page, R.W. Alewine, III, T.C. Hanks, T.H. Heaton,

- J.A. Hileman, H. Kanamori, B. Minster, and J.H. Whitcomb, Point Mugu, California, earthquake of 21 February 1973 and its aftershocks, Science, 182, 1127-1129, 1973.
- Robinson, Russell, R.L. Wesson, and W.L. Ellsworth, Variation of P-wave velocity before the Bear Valley, California, earthquake of 24 February 1972, Science, 184, 1281-1283, 1974.
- Ellsworth, W.L., Bear Valley, California, earthquake sequence of February-March, 1972, Bull. Seis. Soc. Am., 65, 483-506, 1975.
- Stierman, D.J. and W.L. Ellsworth, Aftershocks of the February 21, 1973, Point Mugu, California earthquake, Bull. Seis. Soc. Am., 66, 1931-1952, 1976.
- Kirkman, S.L. and W.L. Ellsworth, Catalog of earthquakes in the Santa Monica Mountains area, U.S. Geol. Surv. Open-File Report 77-301, 1977.
- Kirkman, S.L. and W.L. Ellsworth, Catalog of earthquakes in the Santa Barbara Channel area, U.S. Geol. Surv. Open-File Report 77-302, 1977.
- Ellsworth, W.L. and R.Y. Koyanagi, Three-dimensional crust and mantle structure of Kilauea volcano, Hawaii, J. Geophys. Res., in press, 1977.
- Wesson, R.L., R. Robinson, C.G. Bufe, W.L. Ellsworth, J.H. Pfluke, J.A. Steppe, and L.C. Seekins, Search for seismic forerunners to earthquakes in central California, Tectonophysics, 42, 111-126, 1977.